

200
N64-20889
N64-20889
NASA CONTRACTOR
REPORT



NASA CR-46

NASA CR-46

SUNFLOWER SOLAR COLLECTOR

Prepared under Contract No. NAS 5-462 by
THOMPSON RAMO WOOLDRIDGE, INC.
Cleveland, Ohio
for

NATIONAL AERONAUTICS AND SPACE ADMINISTRATION • WASHINGTON, D. C. • MAY 1964

SUNFLOWER SOLAR COLLECTOR

This paper is photographically reproduced
from copy supplied by contractor.

Prepared under Contract No. NAS 5-462 by

THOMPSON RAMO WOOLDRIDGE, INC.

Cleveland, Ohio

for

NATIONAL AERONAUTICS AND SPACE ADMINISTRATION

For sale by the Office of Technical Services, Department of Commerce,
Washington, D.C. 20230 -- Price \$3.00

TABLE OF CONTENTS

	Page
1.0 INTRODUCTION	1
2.0 SUMMARY	3
3.0 COLLECTOR SPECIFICATION	4
3.1 CONTRACT SPECIFICATION	4
3.1.1 Mission	4
3.1.2 Operating Life	4
3.1.3 Envelope	4
3.1.4 Launch Environment	4
3.1.5 Space Environment	5
3.2 CONVERSION SYSTEM REQUIREMENTS	6
3.2.1 Concentrator Geometry	6
3.2.2 Receiver Geometry	6
3.2.3 Concentration Ratio	7
3.2.4 Collector Performance	7
3.2.5 Stowage and Deployment	7
3.2.6 Concentrator Structure	7
3.2.7 Weight	8
3.3 DESIGN SPECIFICATION REVISIONS	8
4.0 ANALYTICAL INVESTIGATIONS	9
4.1 PERFORMANCE ANALYSIS	9
4.1.1 Concentrator Performance	11
4.1.1.1 Combined Surface Errors	11
4.1.1.2 Analytical Models of Surface Deviations	11
4.1.1.3 Measured Surface Deviation Characteristics	12
4.1.1.4 Calculated Flux Profile in the Focal Plane	19
4.1.1.5 Predicted and Measured Concentrator Performance	19
4.1.2 Receiver Performance	24
4.1.3 Combined Collector - Receiver Performance	33
4.2 ENVIRONMENTAL ANALYSIS	36
4.2.1 Launch Environment Analysis	36
4.2.2 Vibration Analysis	36
4.2.3 Deployment Analysis	39

TABLE OF CONTENTS (Continued)

	Page
4.2.4 Deployed Paraboloidal Position Structural Analysis	39
4.2.5 Orbital Thermal Environment Investigation	42
4.2.5.1 Transient Temperature Characteristics	42
4.2.5.2 Steady State Temperature	47
4.2.5.3 Thermoelastic Structural Analysis	49
4.2.5.4 Effects of Thermal Distortion on Optical Performance	57
4.2.5.5 Thermal Environment Investigation Supporting Test Description	60
4.2.5.6 Summary of Thermal Distortion Control Concepts and Associated Design Consideration for the Sunflower Solar Collector	69
4.2.6 Collector Materials Space Environment Reliability	71
5.0 COLLECTOR DESIGN	74
5.1 COLLECTOR STRUCTURAL DESIGN	74
5.2 STOWAGE AND DEPLOYMENT DESIGN CONCEPT	74
5.3 SUB-COMPONENT DESIGN	79
5.3.1 Sector Design	79
5.3.2 Hinge-Torsion Spring Design	79
5.3.3 Lock Design	82
5.3.4 Center Mounting Ring Design	87
5.3.5 Stacking Ring Design	87
5.3.6 Vibration Isolation Design	87
5.3.6.1 Stowed Vibration Isolation Design	89
5.3.6.2 Deployed Position Vibration Isolation Design . .	89
5.4 WEIGHT CONSIDERATIONS IN THE COLLECTOR DESIGN	89
5.5 REFLECTIVITY CONSIDERATIONS	92
5.5.1 Surface Improvement	92
5.5.2 Reflective and Transparent Coating	100
5.5.3 Summary of Reflectivity Investigations	100
6.0 COLLECTOR FABRICATION	102
6.1 SECTOR ADHESIVE BONDING	102
6.1.1 Tooling	102
6.1.2 Sector Fabrication Process	106

TABLE OF CONTENTS (Continued)

	Page
6.2 SURFACE IMPROVEMENT COATING	106
6.3 REFLECTIVE AND TRANSPARENT COATING VACUUM	
DEPOSITION EQUIPMENT AND PROCESS	107
6.4 PREPROTOTYPE COLLECTOR FABRICATION TECHNIQUE	
DEVELOPMENT	115
6.5 PREPROTOTYPE COLLECTOR ASSEMBLY	117
7.0 INSPECTION AND OPTICAL TESTS	121
7.1 GENERAL COMMENTS ON OPTICAL TESTING	121
7.2 TEN FOOT DIAMETER COLLECTOR MODEL OPTICAL	
INSPECTIONS	121
7.3 SECTOR INSPECTION	123
7.3.1 Types of Surface Deviations	123
7.3.2 Sector Optical, Inspection Facility Description	123
7.3.3 Sector Optical Inspection Results	126
7.3.4 Honeycomb Markoff Inspection Results	126
7.3.5 Reflective Coating Results	133
7.4 OVERALL GEOMETRIC QUALITY OF THE SUNFLOWER	
SOLAR COLLECTOR	133
8.0 DEVELOPMENTAL TESTING	139
8.1 PERFORMANCE TESTING	139
8.1.1 Single Panel Performance Testing	139
8.1.1.1 Test Rig Description	139
8.1.1.2 Instrumentation	139
8.1.1.3 Test Description and Results	141
8.1.2 Full Size Sunflower Solar Test Facility	145
8.2 OPTICAL TESTS OF THE PREPROTOTYPE COLLECTOR	149
8.3 ENVIRONMENTAL TESTING	149
8.3.1 Dead Weight Structural Testing	150
8.3.2 Collector Deployment Testing	154
8.3.2.1 Deployment Simulation Harness Description	154
8.3.2.2 Deployment Test Instrumentation and	
Procedure	154
8.3.2.3 Deployment Test Results	154

TABLE OF CONTENTS (Continued)

	Page
8.3.3 Collector Vibration Testing	159
8.3.3.1 Stowed Collector Vibration Tests	163
8.3.3.2 Deployed Collector Vibration Tests	170
8.3.4 Optical and Structural Effects of Environmental Testing .	176
8.3.4.1 Effects of Dead Weight Structural Testing . . .	176
8.3.4.2 Effects of Deployment and Vibration Environments	176
9.0 CONCLUSIONS	183
10.0 RECOMMENDATIONS	184
APPENDIX A REFERENCES	A-1
APPENDIX B NOMENCLATURE	B-1

LIST OF FIGURES

Figure No.		Page
1.0-1	Sunflower System	2
4.1-1	Typical Concentrator Receiver Geometry	10
4.1-2	A Comparison of Surface Error Distribution Curves	13
4.1-3	Paraxial Plus Profile Geometry	14
4.1-4	Paraxial Plus Profiles Due to Specific Error Distribution Curves	15
4.1-5	Effects of Various Surface Error Models on Surface Geometric Efficiency	16
4.1-6	Honeycomb Markoff Geometric Characteristics	17
4.1-7	Comparison of Measured Distribution with Normal Distribution Models	18
4.1-8	Calculated Flux Profiles in Focal Plane	20
4.1-9	Relationship of ϕ_{\max} to σ	21
4.2-10	Predicted vs Measured Concentrator Performance, Hukuo-Mii Analysis	22
4.1-11	Predicted vs Measured Concentrator Performance, Normal Distribution Surface Model	23
4.1-12	Effects of Misorientation on Concentrator Performance	25
4.1-13	Effects of Temperature on Receiver Retention Efficiency	28
4.1-14	Effects of Receiver Surface Radiation Characteristics on Retention Efficiency	29
4.1-15	Effects of Receiver Surface Area on Retention Efficiency	30
4.1-16	Effects of Shade Time Reradiation on Receiver Retention Efficiency	31
4.1-17	Sunflower Concentrator Receiver Performance	35
4.2-1	Collector Sector Stress Analysis Computer Program	37
4.2-2	Axial Vibration Specifications	38
4.2-3	Collector Vibration System Schematic	40
4.2-4	Sunflower Sector Kinetics	41
4.2-5	Heat Transfer Characteristics of Composite Sandwich Material	43
4.2-6	Orbit Geometry	44
4.2-7	Transient Temperature Characteristics - Original Concept	45
4.2-8	Transient Temperature Characteristics - Thermal Control Design	46
4.2-9	Collector Temperature Gradients at the End of the Sun Period	50
4.2-10	Collector Temperature Gradients at the Beginning of the Sun Period	51
4.2-11	Collector ΔT Through the Thickness at the End of the Sun Period	52
4.2-12	Collector ΔT Through the Thickness at the Beginning of the Sun Period	53

<u>Figure No.</u>		<u>Page</u>
4.2-13	Computed Thermal Distortion Modes, Single Sector Gridwork . .	55
4.2-14	Computed vs Measured Dead Weight Deflection	56
4.2-15	Computed Thermal Distortion Surface Rotations from the True Paraboloid	58
4.2-16	Optical Quality of Thermally Distorted Collector	59
4.2-17	Temperature Drop Test Set-Up Exploded Views	61
4.2-18	Composite Materials Heat Transfer Results	62
4.2-19	Adhesive Thermal Conductivity Test Rig	63
4.2-20	Sandwich Material Thermal Distortion Test Schematic	65
4.2-21	Sandwich Material Thermal Distortion Test Rig - General View	66
4.2-22	Sandwich Material Thermal Distortion Test Rig - Specimen View	67
4.2-23	Test I - Ribbon Perpendicular to Length, Deflection vs Length and Deflection vs ΔT	68
4.2-24	Thermal Distortion Control Concepts Weight Comparison	70
5.1-1	Sunflower Concentrator Sandwich Material Cross Section	76
5.2-1	Geometric Relationship for Petaline Stowage.	77
5.2-2	Collector - Receiver Geometry - Sunflower I System	78
5.3-1	Hinge and Torsion Bar Hardware.	80
5.3-2	Hinge and Torsion Bar Hardware (Disassembled).	81
5.3-3	Combination Shock Absorber-Lock	83
5.3-4	Typical Sector Lock	85
5.3-5	Lock Detent	86
5.3-6	Viscous Damper Arrangement	88
5.3-7	Bottom View of Collector Bundle	90
5.5-1	Proficorder for Surface Quality Measurements	94
5.5-2	Proficorder Roughness Graphs of Aluminum Foils.	95
5.5-3	Specularity Curves and Reflectometer Composite	96
5.5-4	Specularity Curves for Various Surfaces	97
5.5-5	Reflectance vs Wavelength.	98
5.5-6	Reflectance vs Wavelength.	101
6.1-1	General View of Sector Fabrication Area	103
6.1-2	Environmental Test Group - Sunflower Sector Molding	104
6.1-3	Sunflower Collector Master Tooling Pattern	105
6.3-1	Vacuum System.	108
6.3-2	Filament Types	110
6.3-3	Silicon Oxide Evaporator	110
6.3-4	Deposition Chamber Interior.	112
6.3-5	Glow Discharge with Shutter Open	112
6.3-6	Temperature Distribution	113
6.3-7	Relationship of Film Thickness to Observed Color Changes . . .	116

<u>Figure No.</u>		<u>Page</u>
6.5-1	Collector Assembly Area	118
6.5-2	Assembled Sunflower Preprototype Collector	119
6.5-3	Sunflower Preprototype Collector-Stowed Position	120
7.2-1	Collimated Light Source - Exploded View	122
7.3-1	Classification of Surface Deviations from the True Paraboloid.	124
7.3-2	Single Sector Optical Inspection Rig	125
7.3-3	Projection Grid Inspection Results	127
7.3-4	Sector SPTR-1	128
7.3-5	Optical Inspection Results - Radial Deviations	129
7.3-6	Optical Inspection Results Circumferential Deviations	130
7.3-7	Radial Deviations.	131
7.3-8	Proficorder Trace of Honeycomb Markoff	132
7.3-9	Reflectivity Results.	134
7.4-1	Individual Characteristics of Surface Deviations	136
7.4-2	Combined Surface Deviations of the Sunflower Solar Collector	137
7.4-3	Distribution of Radial Angular Errors for the Sunflower Collector	138
8.1-1	Test Rig for Performance Testing of the Sunflower Solar Collector	140
8.1-2	Focal Plane Image	142
8.1-3	Temperature Plot in the Focal Plane and Temperature Profile	143
8.1-4	Sunflower Collector, Solar Testing Results, Single Panel Test Rig	144
8.1-5	Solar Collector Test Facility	146
8.1-6	Fabrication of 40 Ft. Diameter Paraboloid Sector	147
8.1-7	Completed Segment of 40 Ft. Diameter Paraboloid	148
8.3-1	Dead Weight Test Arrangement.	151
8.3-2	Dead Weight Deflection	153
8.3-3	Deployment Harness Calibration	155
8.3-4	Deployment Harness Calibration Data	156
8.3-5	Deployment Test Setup Prior to Deployment	157
8.3-6	Sunflower Collector Deployment Dynamics	158
8.3-7	Sunflower Collector Deployment Test No. 2	160
8.3-8	Sunflower Collector Deployment Non-Symmetry	161
8.3-9	TRW 21,500 lb Sine and Random Shaker System	162
8.3-10	Stowed Collector Vibration Test Installation	164
8.3-11	Sunflower Collector-Stowed Configuration Vibration Test 3/8/63 and 3/11/63, Profile of Actual Input "g"-Levels at Component Mounting Pad	165
8.3-12	Structural Support Rings, Mid Span Transmissibility	166
8.3-13	Sunflower Collector - Stowed Vibration Test 3/11/63, Petal No. 13, Center X-X Axis	167

<u>Figure No.</u>		<u>Page</u>
8.3-14	Sunflower Collector - Slowed Vibration Test 3/11/63, Petal No. 13, Center Z-Z Axis	168
8.3-15	Deployed Collector Vibration Test Installation	171
8.3-16	Sunflower Collector - Deployed Configuration Vibration Test, 3/14/63 to 3/16/63	172
8.3-17	Sunflower Collector - Deployed Vibration Test, 3/14/63 to 3/16/63 - Sector Response at Mid Span Axial Direction.	173
8.3-18	Sunflower Collector - Deployed Vibration Tests, 3/14/63 to 3/16/63 - Sector Response at Rim Axial Direction .	174
8.3-19	Optical Inspection Results - Dead Weight Testing.	177
8.3-20	Radial Slope Changes - Dead Weight Testing.	178
8.3-21	Optical Inspection Results Before and After Environment Testing	179
8.3-22	Radial Slope Changes - Environmental Testing.	180
8.3-23	Waviness Shape Change due to Environmental Testing	181

LIST OF TABLES

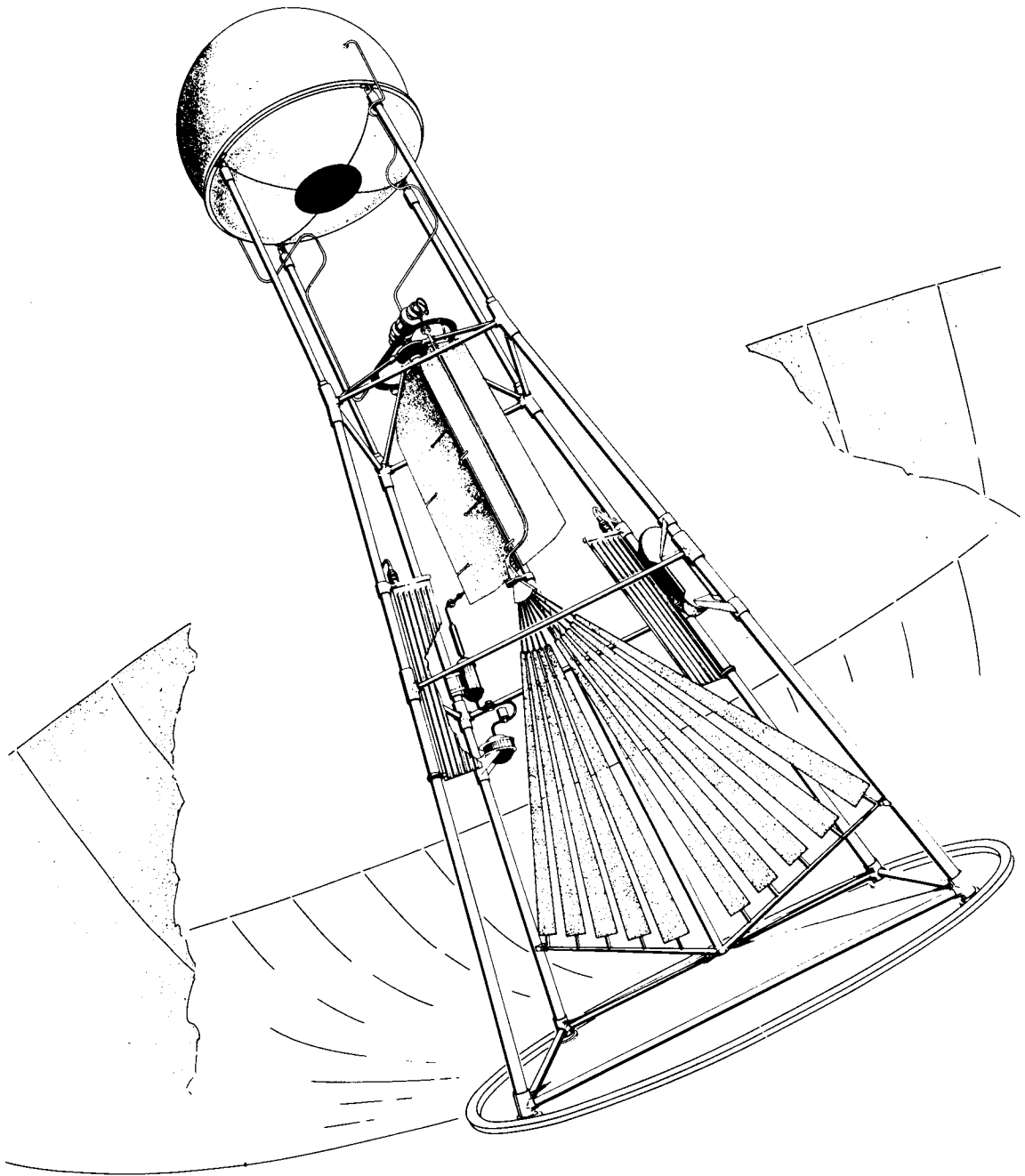
<u>Table No.</u>		<u>Page</u>
4.1-1	Receiver Study Parameters	27
4.1-2	Parametric Study Results	34
4.2-1	Transient Heat Balance Characteristics	48
4.2-2	Computed vs. Measured Reactions and Stresses	54
4.2-3	Adhesive Thermal Conductivity Test Results.	64
5.1-1	Solar Concentrator Materials Comparison.	75
5.4-1	Sunflower Collector Weight	91
8.3-1	Dead Weight - Structural Test Results	152
8.3-2	Stowed Vibration Resonance Points	169
8.3-3	Cyclic Stresses at Resonant Points - Deployed Collector Vibration	175

1.0 INTRODUCTION

The Sunflower system, illustrated in Figure 1.0-1, is a mercury Rankine cycle solar powered engine. Solar energy is collected and focused on the boiler by the solar collector. The boiler then transfers heat to the working fluid, mercury. Mercury vapor flowing in the loop drives the turbo-alternator with the turbine exhaust flowing through a radiator-condenser in which heat is removed, thus condensing and subcooling the fluid. The condensate pump returns the liquid mercury to the boiler to complete the cycle.

Collection of the solar energy is accomplished with a paraboloidal reflector in combination with a cavity receiver.

The purpose of this report is to describe the analysis, design, and development of the solar collector for the Sunflower system.



SUNFLOWER SYSTEM

2.0 SUMMARY

20889

A

Based upon specified orbital missions and associated environments, a paraboloidal solar concentrator was designed. The design was such that deployment to the final geometric shape was accomplished from the Centaur vehicle nose cone volume.

A full size 32.2 foot diameter collector composed of thirty deployable segments was fabricated and assembled as a preprototype model for structural integrity investigations.

This preprototype collector was successfully deployed in a simulated zero gravity environment. Also, environmental tests of launch vibration and orbital transfer vibration and acceleration were conducted with no major structural damage. Optical inspections of the paraboloid were performed to determine the effect of these environmental loadings upon the optical quality.

Single sectors of the collector were fabricated and reflective-coated in a specially designed vacuum deposition facility, for optical and performance testing. Optical quality of these preprototype segments was measured and compared with results of calorimetric efficiency measurements using solar energy.

A full collector solar performance test facility was designed and built for combinations of collector and collector-receiver testing and ultimately for full system testing.

Author

3.0 COLLECTOR SPECIFICATION

The specification to which the collector has been designed was established by virtue of (1) the contract specification of power requirements and usage, and (2) conversion system parametric considerations.

The system parameters were initially viewed to provide the maximum conversion efficiency where other trade-off factors such as stowage volume, weight, environment, etc., must also be considered. Some modifications to the specifications are outlined at the end of this section. All of the requirements of the collector specification and only those system or component requirements as they affect the collector design are included in this report.

3.1 CONTRACT REQUIREMENTS

3.1.1 Mission

The collector shall deliver a sufficient heat rate to the boiler/heat storage component so that a useful power output of 3000 watts shall be obtained from the integrated system when used between orbital altitudes of 300 to 20,000 nautical miles or for a lunar vehicle. Modifications to the collector shall be minimized for operation in the vicinity of Mars or Venus.

3.1.2 Operating Life

The system shall be developed for ultimate attainment of 95% reliability for 1 year missions.

3.1.3 Envelope

The collector and power conversion system shall be packaged in a volume comprised of a 9.5 foot diameter by 8 foot long right circular cylinder topped by a conical section of 15° half angle. No reliance shall be placed on the nose fairing for mechanical support of the power system.

3.1.4 Launch Environment

3.1.4.1 External power: None

3.1.4.2 Temperature: 0° to 200°F

3.1.4.3 Pressure: 0 to 1 atmosphere

3.1.4.4 Relative humidity: 0 to 100%

3.1.4.5 Linear acceleration: 10 "g" maximum along the longitudinal axis and 1 "g" maximum lateral.

3.1.4.6 Vibration: 10 minutes between 20 to 2000 cps at .05 inch double amplitude or 10 "g" acceleration level, whichever is less.

3.1.4.7 Fairing separation: Stowed collector shall withstand aerodynamic loads and stagnation temperatures after jettisoning of the fairing at an altitude of 400,000 feet minimum and a maximum velocity of 13,000 ft/sec at a flight angle of attack of up to 6 degrees.

3.1.5 Space Environment

3.1.5.1 Deployment: The collector shall be capable of automatic deployment to the operating position upon a command signal.

3.1.5.2 Energy: The collector shall be capable of delivering sufficient energy to the boiler/heat storage unit during a 60 minute sun phase (300 nautical mile orbit) to provide continuous boiler operation during a 96 minute orbit period.

3.1.5.3 Pressure: The minimum value for cislunar and interplanetary space.

3.1.5.4 Linear acceleration during orbital transfer periods: Up to 1 "g" in any direction for three periods of 5 minutes each. The collector need not meet performance requirements during these periods but shall not sustain permanent performance deterioration due to such conditions.

3.1.5.5 Linear acceleration during normal operation: 0.001 "g" continuous in any direction.

3.1.5.6 Vibration: Vibration shall be the same as for launch environment except that it will be for three 5 minute periods.

3.1.5.7 Rotational acceleration and velocity: Up to 1 degree/sec² and up to 10 degrees/sec about any axis during six periods of up to five minutes each. Three of these periods may be simultaneous with the acceleration and vibration requirements in 3.1.5.4 and 3.1.5.6. The remaining three periods of rotational orientation shall be required with the collector in the open position.

3.1.5.8 Inertia loads: Zero "g" for most of life except for 3.1.5.5 during sun orientation corrections.

3.1.5.9 Meteoroid, Van Allen radiation, and cosmic radiation consistent with the latest scientific data.

3.1.5.10 Orbital transfer: Transfer period shall not exceed 5 minutes while in the sun phase of a 300 nautical mile orbital. Transfer periods during the shade phase may be longer. Collector shall be in the open position during transfer periods.

3.1.5.11 Collector re-stowage: The collector shall not be required to re-stow after it is once deployed to the open position.

3.1.5.12 Performance: The collector shall maintain performance to meet mission requirements after exposure to launch, deployment, orbital transfer, and stabilization environments. The collector shall meet the performance requirements while exposed to the orbital space environment.

3.2 CONVERSION SYSTEM REQUIREMENTS

A complete evaluation of system parameters to select the optimum trade-off in collector design was not available at the time of the Sunflower proposal effort. The optimum design has since been more substantially established. However, there are still some parameters, such as sun orientation limits or allowable conversion system weights, which are not well defined and could have a considerable effect on the optimum collector design. The specification as it initially existed is listed in this sub-section. Changes as a result of the program efforts will be discussed in the subsequent sub-section. Justification for the specification as initially and presently stated will be discussed throughout the body of this report, and reference shall be to the specification and any changes that have been made.

3.2.1 Concentrator Geometry

3.2.1.1 Type: Paraboloid, having the equation of $R = \frac{Y^2}{816}$ (in inches)

3.2.1.2 Outside diameter: 32.2 feet for the near earth distance from the sun.

3.2.1.3 Inside diameter: 9.2 feet

3.2.1.4 Focal length: 17.0 feet

3.2.1.5 Rim angle: $50^{\circ} 41'$

3.2.1.6 Intercepted area to solar flux: 747 ft^2

3.2.2 Receiver Geometry

3.2.2.1 Type: Cavity

3.2.2.2 Shape: Spherical segment of 1.4 ft radius with center displaced from the focal point to reduce reflection losses.

3.2.2.3 Aperature diameter: 1.2 ft

3.2.3 Concentration Ratio

3.2.3.1 Nominal area concentration ratio, $\left(\frac{32.2}{1.2}\right)^2$: 720

3.2.3.2 Actual intercepted area concentration ratio, $\frac{D_o^2 - D_1^2}{D_a^2}$: 660

3.2.4 Collector Performance

3.2.4.1 Concentrator efficiency: 73.6% at.

Reflectivity: 0.92

Solar misorientation: $3/4^\circ$ max

Surface slope deviation: $\pm 1/2^\circ$ max

Surface translation deviation: ± 1 inch max

Solar constant: 130 watts/ft²

3.2.4.2 Receiver efficiency: 90.3%

3.2.4.3 Overall collection efficiency: 66.5%

3.2.5 Stowage and Development

The concentrator shall be stowed in the envelope defined in a petaline manner.
Deployment upon achieving orbit shall be as follows:

3.2.5.1 A restraining hoop shall be severed upon command.

3.2.5.2. Preloaded torsion bar springs in each petal hinge shall accelerate the petals toward the open position.

3.2.5.2 The petals shall be decelerated to and locked in the open position by a locking device at the petal tips.

3.2.6 Concentrator Structure

The materials and construction of the petals shall be of adhesive bonded aluminum honeycomb sandwich. The dimensions and fabrication of face, core, and sandwich cross section shall provide the concentration efficiency defined in Section 3.2.4.1.

3.2.7 Weight

The entire concentrator, including actuation and lock devices, shall be 186 pounds or 0.25 pound/ft² of intercepted solar flux area.

3.3 DESIGN SPECIFICATION REVISIONS

During the course of the development program, there have been some interim changes in the contract specifications, as well as basic revisions in the detailed design due to parametric optimization derived from developmental investigations.

The major revisions are in environmental loading conditions where the lateral acceleration was changed from 1 "g" to 3 "g". Also, the following suggested revisions to the vibration specifications have been investigated during environmental testing:

<u>Sinusoidal</u>		<u>Axial (z-z)</u>	<u>Lateral (x-x and y-y)</u>
1	- 2 cps	---	2.5 s. a.
2	- 4 cps	---	0.625 s. a.
4	- 8 cps	0.30 s. a.	0.155 s. a.
8	- 16 cps	2.0 "g"	1.0 "g"
16	- 64 cps	2.5 "g"	2.0 "g"
64	- 512 cps	5.0 "g"	2.0 "g"
512	-2056 cps	7.5 "g"	---

(4.5 minutes)

logarithmic sweep, two octaves per minute

<u>Random:</u>	<u>Axial</u>	<u>Lateral</u>
15 - 2000 cps	{ 0.033 "g" ² /cps 5.5 Minutes	0.017 "g" ² /cps 5.5 Minutes

<u>Acoustic (white noise)</u>	<u>Total</u>
20 - 9600 cps (Progressive wave)	155 db

Some of the major changes in the system requirements which resulted from parametric studies are discussed in Section 4.1.3.

In January 1962, a NASA redirection of the Sunflower program occurred which had a significant effect upon the design objectives of the preprototype collector. At that time, it was decided to freeze the design of the major system components. Since the collector project was in the process of optimizing tooling and fabrication processes to meet geometric quality, it was decided to relax the optical quality specifications for the preprototype design and investigate primarily structural integrity.

4.0 ANALYTICAL INVESTIGATIONS

Analytical investigations of the Sunflower system were conducted during the course of the development program. Performance of the paraboloidal concentrator in combination with the cavity receiver was analysed to establish and optimize basic geometric, optical, and thermal design parameters. Investigation of environmental requirements were conducted to establish structural design criteria and to insure long life space compatibility.

4.1 PERFORMANCE ANALYSIS

The solar energy collection performance for the Sunflower system has been separated into concentrator and receiver (absorber) performance for two reasons. First, it allows analysis of the concentrator and receiver as components; thereby, the specific design parameters may be evaluated more easily and effectively. Second, it allows convenience in testing, especially for the concentrator. The following efficiency factors are thus defined * (See Figure 4.1-1):

$$\eta_{CR} = \eta_C \eta_R = \frac{\dot{Q}_C}{\dot{Q}_i} \quad (4.1-1)$$

The concentrator and receiver efficiency factors are functions of the following parameters;

$$\eta_C = f(\phi, \delta, \Omega, \theta, R, \alpha) \quad (4.1-2)$$

$$\eta_R = a_{sa} - \frac{\mu F_r A_s \sigma T_s^4}{q_s A_C \eta_C} \quad (4.1-3)$$

The concentrator efficiency cannot be conveniently expressed in one equation because of the difficulty in integrating the geometric, surface deviation, and solar misorientation effects. However, as will be shown in Section 4.1.2, the influence of these parameters can be determined through the use of several families of curves. Equation 4.1-1 can then be expressed as:

$$\eta_{CR} = \eta_C a_{sa} - \frac{\mu F_r A_s \sigma T_s^4}{q_s A_C} \quad (4.1-4)$$

Finally, the overall power conversion system efficiency is;

$$\eta_s = \eta_E \eta_{CR} \quad (4.1-5)$$

*Symbols are explained in Appendix A, Nomenclature

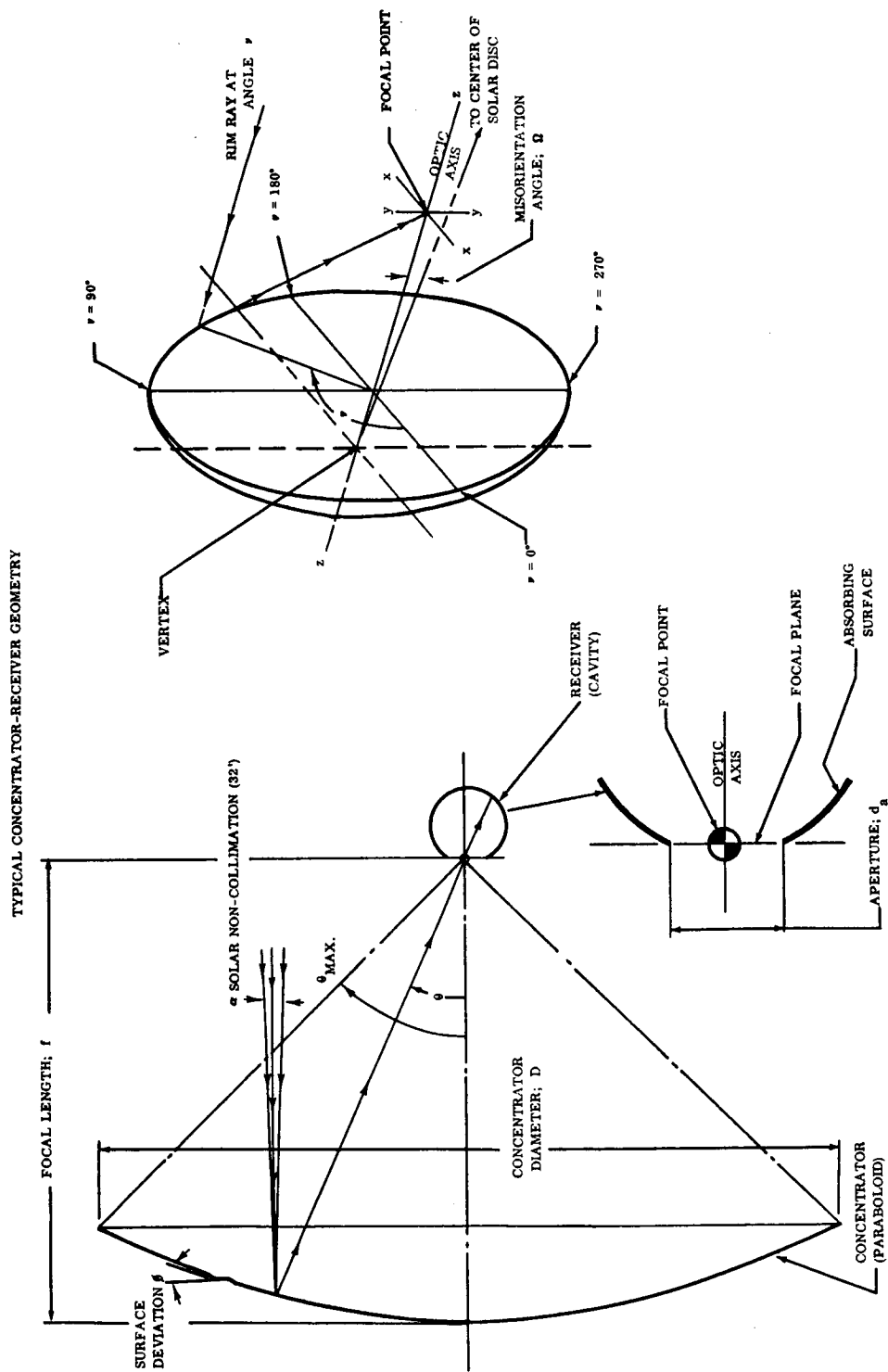


FIGURE 4.1-1

A more detailed discussion on collector performance is given in a TRW publication.⁴

4.1.1 Concentrator Performance

The concentrator efficiency is difficult to evaluate because of the need to know detailed surface dispersion characteristics. In a large multi-piece construction, deviations from a true surface are caused by:

- a. Surface finish imperfections
- b. Reinforcing structure mark-off
- c. Panel fabrication errors
- d. Concentrator assembly deviations
- e. Concentrator deployment inaccuracy
- f. Thermal distortion

4.1.1.1 Combined Surface Errors

The concentrator efficiency is a function of the maximum cumulative surface error and the distribution or probability of occurrence for these cumulative surface errors for the entire concentrator. The first property can be obtained by measuring the individual surface errors and summing the maximum values. However, the distribution of these combined errors is difficult to determine. Knowing the maximum surface error categorizes the concentrator, but knowing the distribution curve allows accurate prediction of performance. Unfortunately, the distribution curve cannot be determined accurately until a complete concentrator is built and thoroughly inspected. The characteristics of the errors due to petal fabrication, assembly, deployment, and thermal distortion can also vary significantly from one area of the concentrator to another. Such characteristics make computation of concentrator performance complex, even after a convenient method of mathematically expressing the errors is developed. A technique has been developed for computing the flux distribution in the focal plane.¹⁵ Several other methods, generally using various models of surface deviations to predict the performance of paraboloidal solar concentrators, have also been proposed.^{17, 23}

4.1.1.2 Analytical Models of Surface Deviations

In order to illustrate the influence of slope error distribution on the flux profile, several analytical models of surface error distribution which have been proposed or observed for paraboloidal collectors will be discussed. However, to avoid unnecessary complication, the cases will be treated separately and independent of the geometry of the paraboloid. Also, the distribution of non-parallel rays from the sun is treated independently by considering it as an equivalent surface deviation.

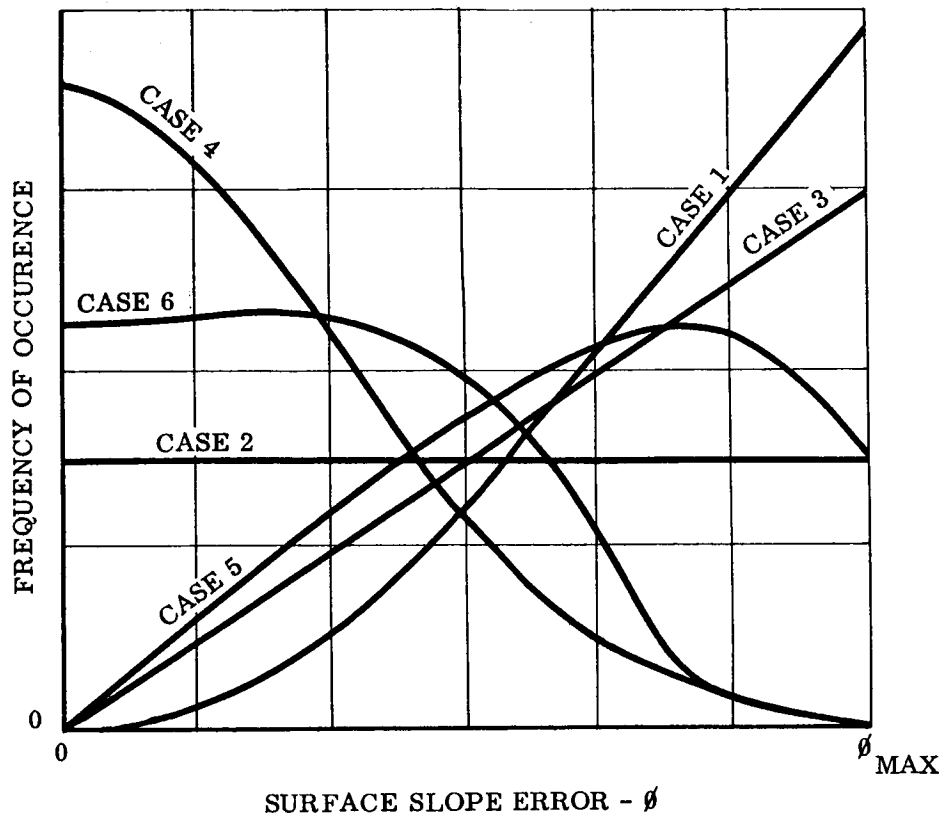
Figure 4.1-2 shows the curves of various analytical models and the measured Sunflower error distribution for comparison, where equal error population and equal maximum errors are assumed. Note that they differ considerably. If the paraxial profile, as defined in Figure 4.1-3, produced by these cases is calculated, the profile in Figure 4.1.4 result. From the profiles, the paraxial concentrator efficiency (η_{PA}) versus aperture diameter (d_a) is obtained and plotted in Figure 4.1-5 for each case. The normal distribution provides the highest efficiency and the " π cosine" distribution the lowest for any given aperture size. The plots in these figures do not consider the effect of the paraboloid geometry. When the profiles from all other portions of the concentrator (where $\theta \neq 0$ degrees, Figure 4.1-3) are summed to provide the entire concentrator efficiency, the same rank of performance would result. The general shape of the profile for a given distribution would be similar when comparing the paraxial case with the entire concentrator case. However, the profiles from points other than $\theta = 0^\circ$ extend over a larger area, because of the cosine effect of the angle θ and the longer ray length from concentrator surface to focal point. When the solar non-parallelism effect is combined with any of the other four cases, the profiles change from those shown in Figure 4.1-5. Results of calculations based upon the previously mentioned analytical approaches, which include the paraboloid geometry for several of these surface error models, will be presented after a brief discussion of the actual error distributions which were observed and measured for the Sunflower preprototype collector.

4.1.1.3 Measured Surface Deviation Characteristics

Error distribution curves similar to cases 1, 2, 3, or 4 have been measured. For example, the errors due to honeycomb core mark-off were measured (see Section 7.3.4). Typical error distribution plots of these data are shown in Figure 4.1-6, indicating either a π or 2π cosine characteristic. The less desirable π distribution is encountered if too much adhesive is used to bond the face to the core. By controlling adhesive application, the maximum slope error is about 6 minutes and the error distribution follows the 2π characteristic.

Although the honeycomb markoff has a specific deviation characteristic, the combination with other modes of geometric errors may result in completely different distributions. The combined error distribution for the Sunflower solar collector was obtained from the analytical and test results of the development program. This curve, obtained from Figure 7.4-3, was presented in Figure 4.1-2 for comparison with the various analytical surface models. It is seen that it is related most closely to the geometric error model surface having a normal distribution. Comparison with various standard deviations (68 percent of the reflector area has smaller absolute angular error than the standard deviation value σ) is shown in Figure 4.1-7. It is seen that the standard deviation of 15 minutes approximates the measured curve. The fact that this model ($\sigma = 15'$) exceeds the observed maximum gross error of approximately 30 minutes is compensated for by the fact that honeycomb markoff is not included in Figure 4.1-7; thus, the distribution would be modified to include the equal probability for the markoff characteristic. This would increase the maximum deviation to approximately 36 minutes and approach the $\sigma = 15'$ standard deviation curve.

A COMPARISON OF SURFACE ERROR DISTRIBUTION CURVES

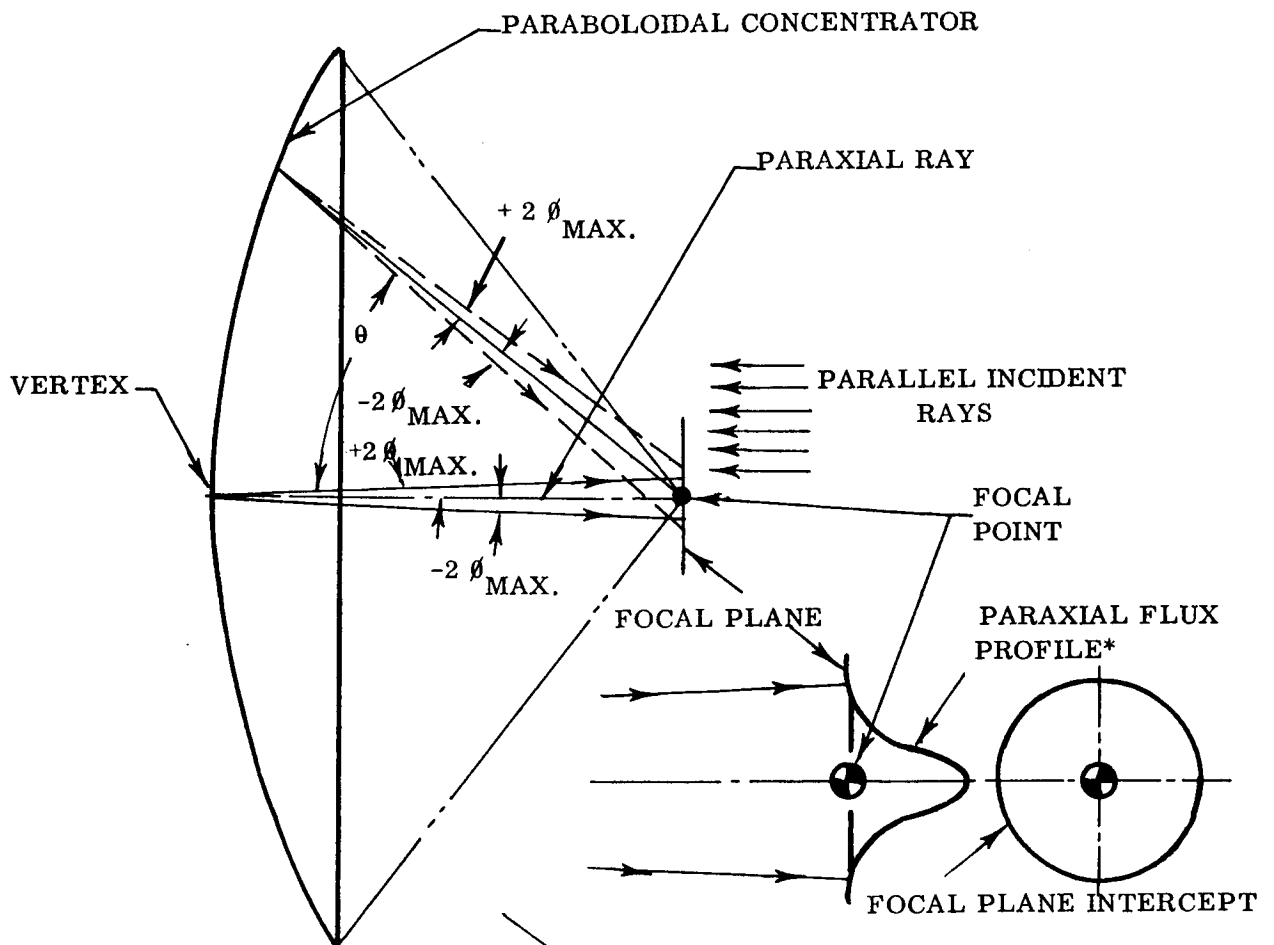


- CASE 1; π COSINE (HANSON, REF. 15)
- CASE 2; 2π COSINE (TYPICAL OF HONEYCOMB MARKOFF)
- CASE 3; PROPORTIONAL (HUKUO-MII, REF. 17)*
- CASE 4; NORMAL OR GAUSSIAN (SILVERN, REF. 23)
- CASE 5; SOLAR LIMB DARKENING (CONSIDERED AS AN EQUIVALENT SURFACE DEVIATION)
- CASE 6; SUNFLOWER (FIG. 7. 4-3)

*ALTHOUGH THE REFERENCE IS NOT EXPLICIT AS TO THE SURFACE CHARACTERISTICS, THE DISTRIBUTION SHOWN WOULD BE REQUIRED TO SATISFY THE "UNIFORM ILLUMINATION" IN THE FOCAL PLANE SCATTERING CIRCLE AS STATED BY THE AUTHORS.

FIGURE 4. 1-2

PARAXIAL FLUX PROFILE GEOMETRY



*THE PARAXIAL FLUX PROFILE IS:

THE PROFILE OF FLUX INTENSITY IN THE FOCAL PLANE WHICH RESULTS FROM REFLECTING THE INCIDENT RAYS FROM AN ASSUMED SURFACE DISPERSION CHARACTERISTIC AT THE VERTEX; THE INCIDENT RAYS ARE PARALLEL AS IF FROM A STAR SOURCE

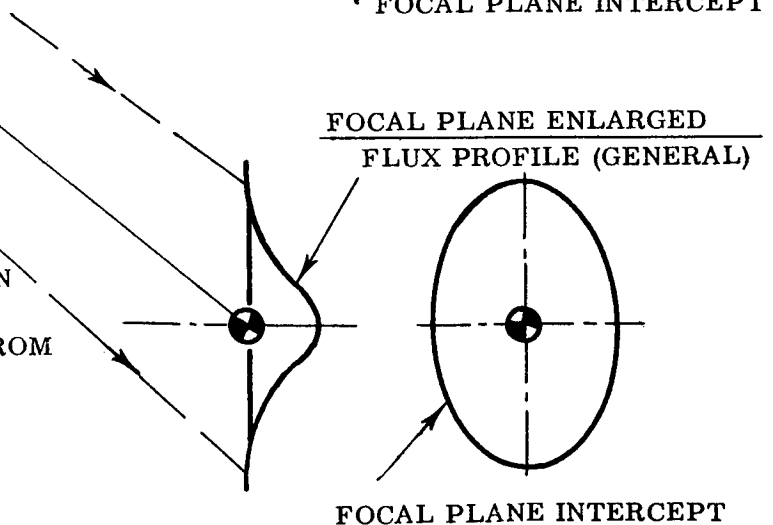


FIGURE 4.1-3

PARAXIAL FLUX PROFILES
DUE TO SPECIFIC ERROR DISTRIBUTION CURVES

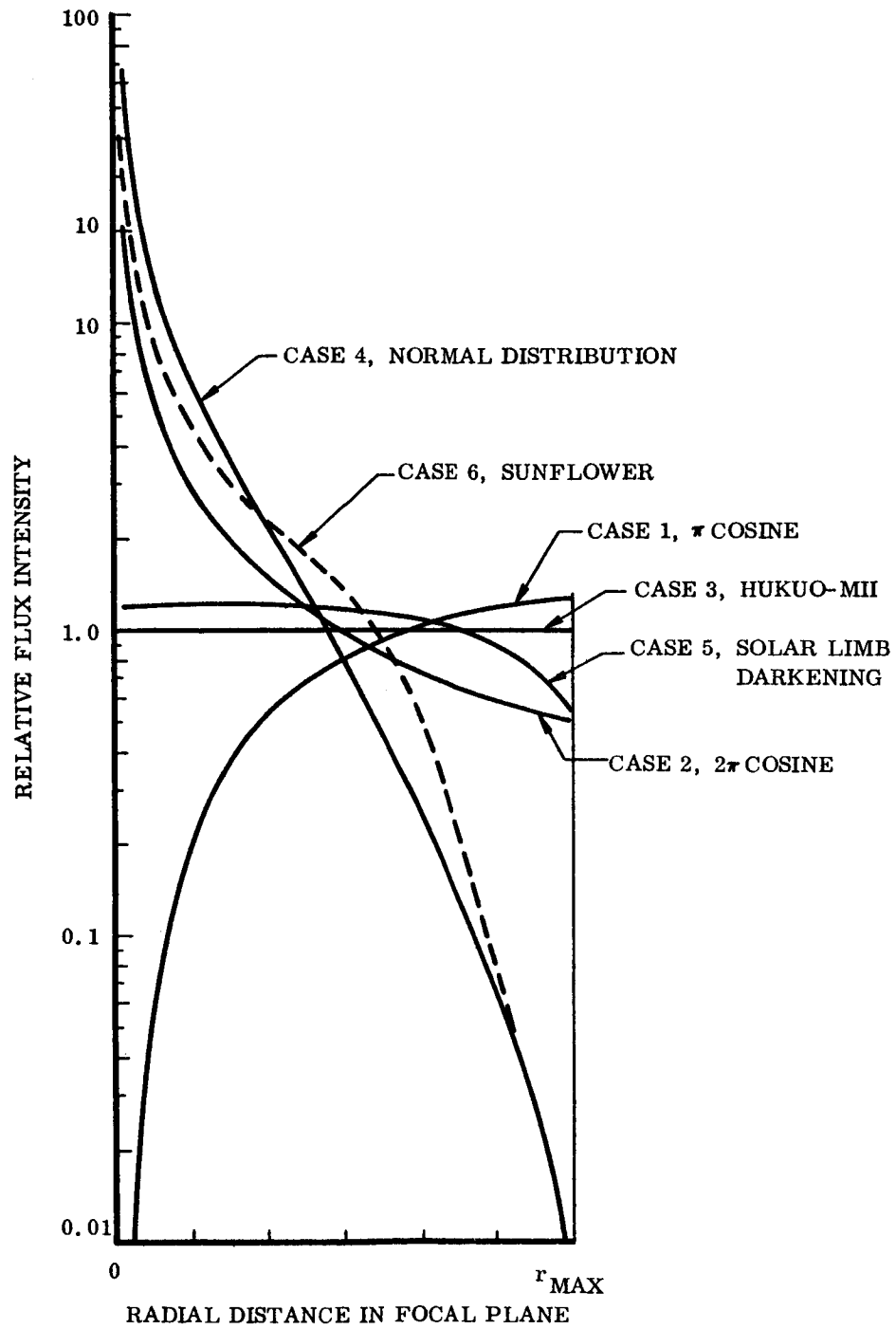


FIGURE 4. 1-4

EFFECTS OF VARIOUS SURFACE ERROR MODELS ON SURFACE GEOMETRIC EFFICIENCY

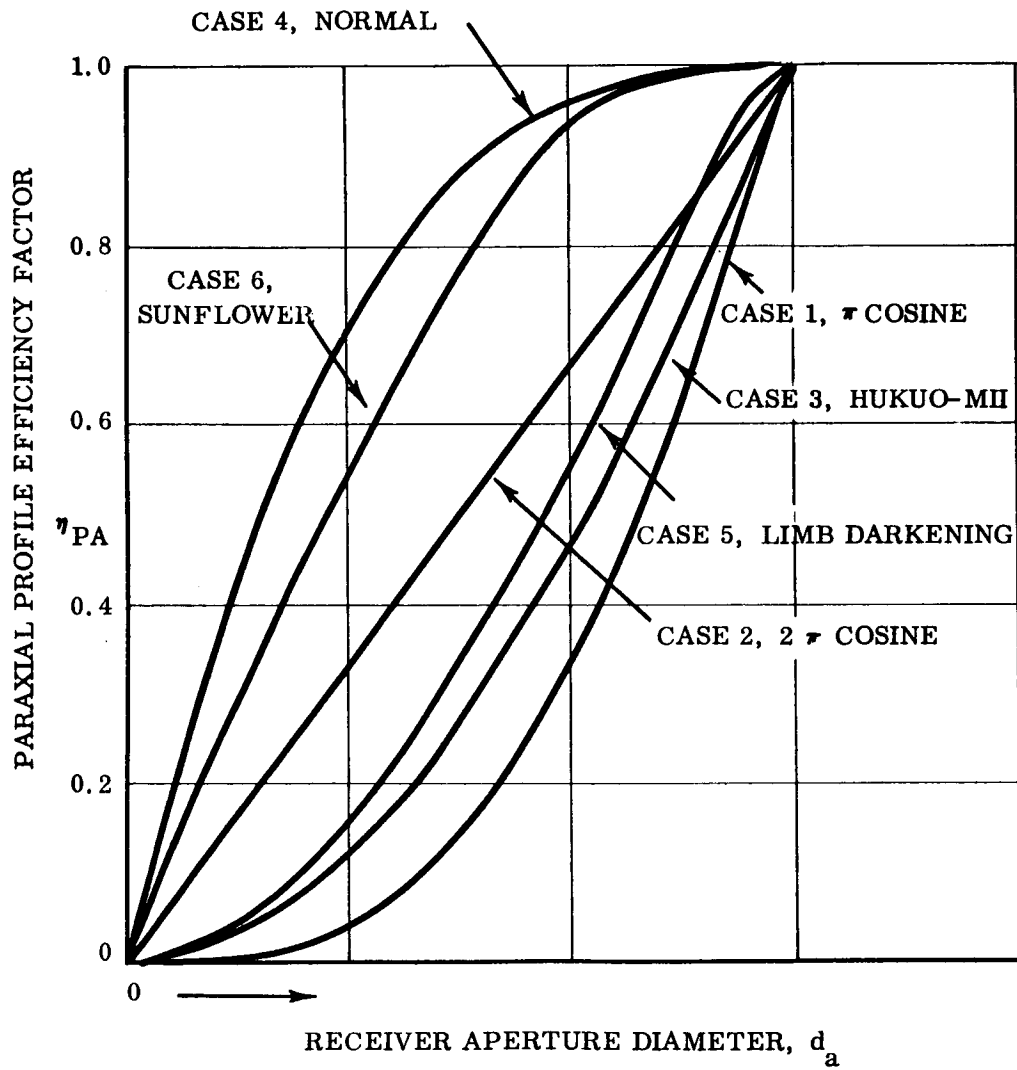


FIGURE 4.1-5

HONEYCOMB MARKOFF GEOMETRIC CHARACTERISTICS

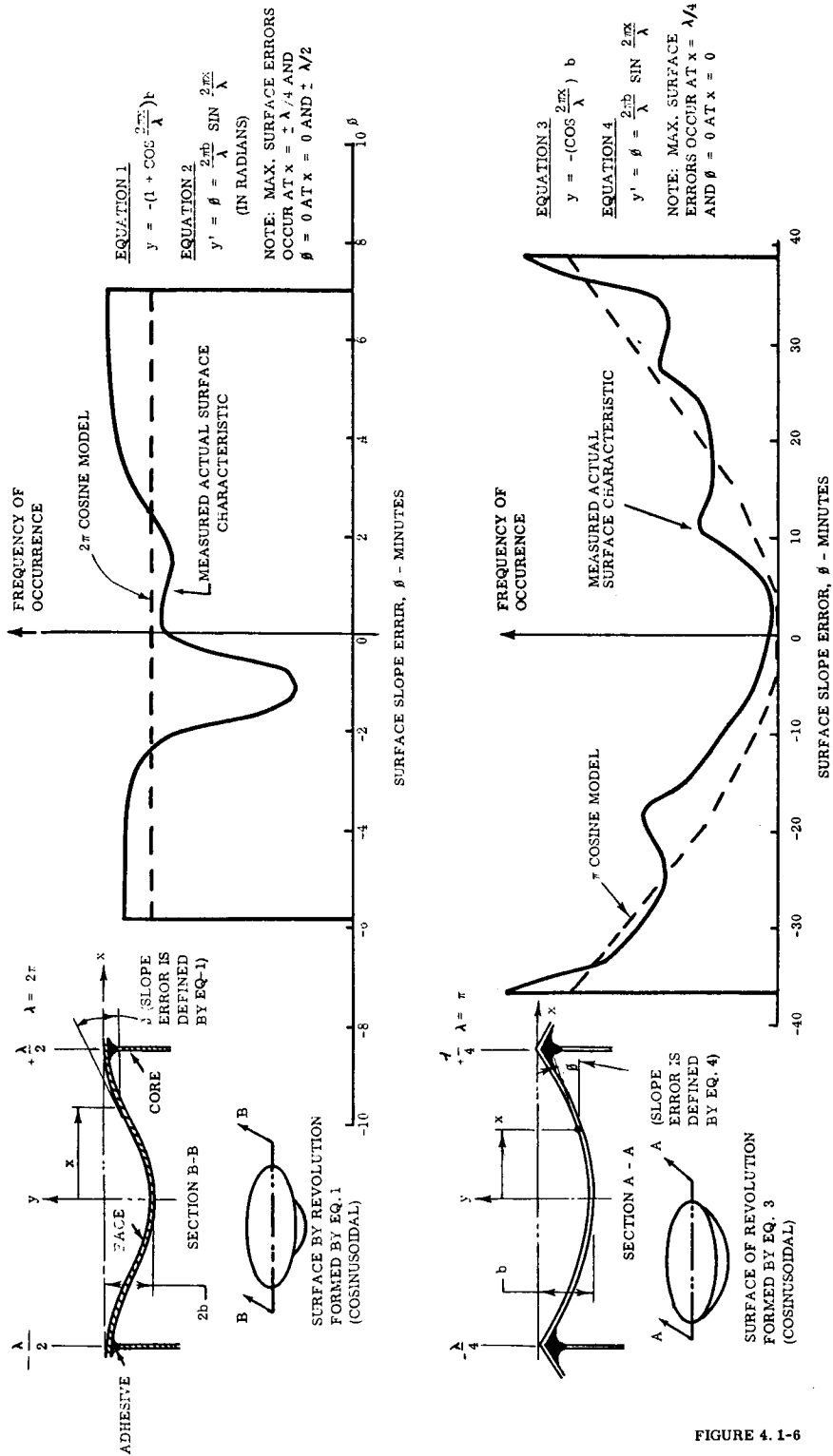


FIGURE 4.1-6

COMPARISON OF MEASURED DISTRIBUTION
WITH NORMAL DISTRIBUTION MODELS

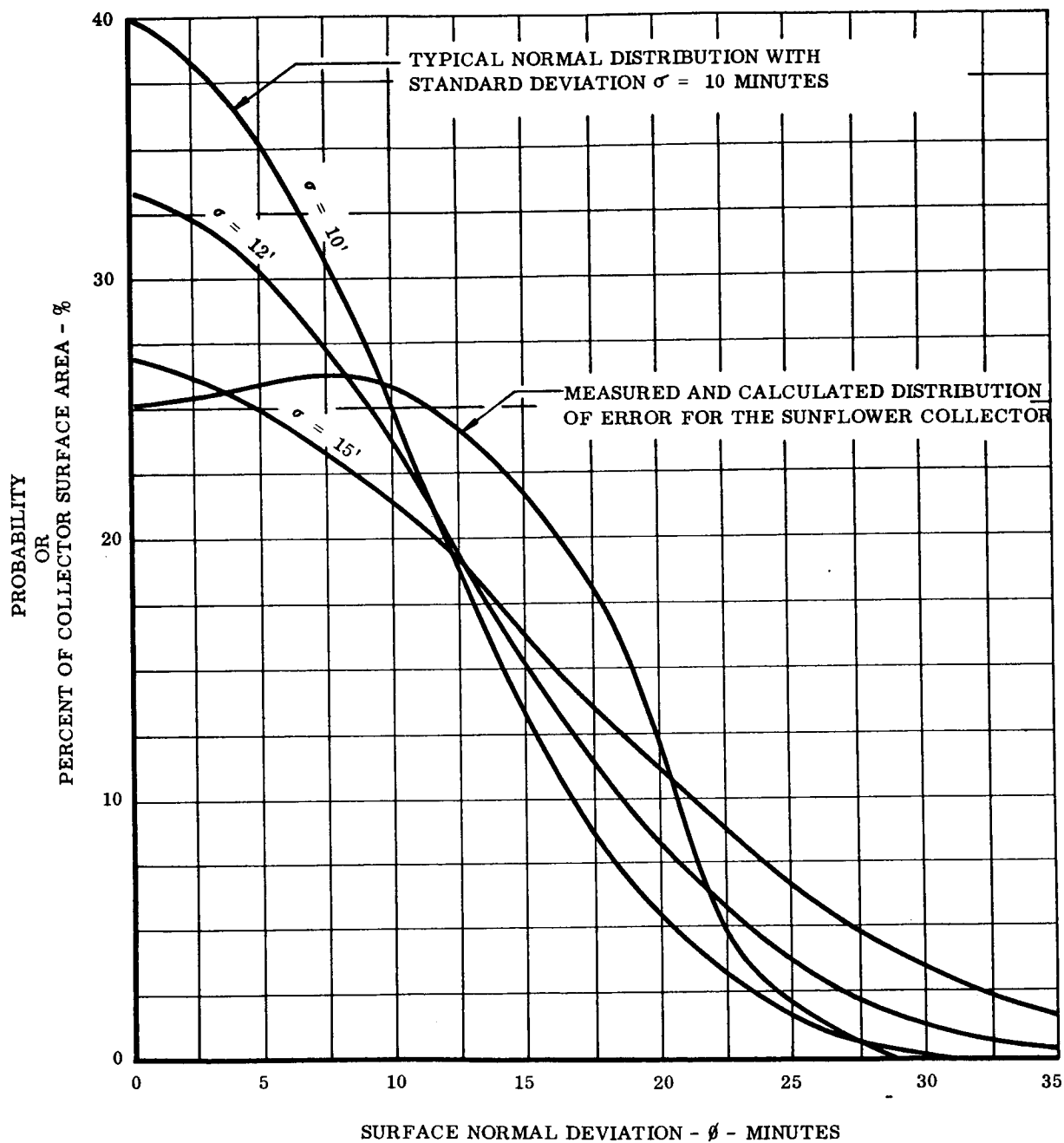


FIGURE 4.1-7

4.1.1.4 Calculated Flux Profile in the Focal Plane

In the initial Sunflower concentrator analysis, the flux profile was based primarily upon the results of solar tests conducted on a ten foot diameter concentrator model. To evaluate various design parameters, the Hukuo-Mii¹⁷ analysis was originally used. However, based upon the observed characteristics of the Sunflower preprototype collector, the analytical surface model proposed by Silvern²³ appears to be more accurate.

Calculated flux profiles comparing results of these two surface models is shown in Figure 4.1-8. Also shown for comparison is the originally estimated flux profile. All curves are based on a reflectivity of 100%. It should be noted that the calculated curves must be modified to account for the Sunflower geometrical characteristic that the collector is an annulus. In effect, the flux from a "virtual" collector which represents the central open section of the Sunflower concentrator is subtracted from the total flux calculated for a full paraboloid. The standard deviation ($\sigma = 15$), is based upon the discussion of the previous section while the $b/d = 6$ value is based upon the criterion suggested by Dresser⁸ for the maximum deviated nominal light ray. By referring to Figure 7.4-2, it can be seen that this occurred not at the collector rim but at a radial location of approximately 160 inches. The six minute deviation due to the honeycomb markoff was also added to this combined gross deviation value in establishing the b/d parameter.

Actually the maximum deviated light ray is not of major interest since it is seen that a very small portion of the collector surface area is involved. Of major interest in collector analysis is the distribution of surface errors which, if it has a normal distribution characteristic, is best defined by the standard deviation parameter (σ).

It is obvious that the defining values of angular deviation in the two analytical approaches which have been discussed (maximum angular error in Hukuo-Mii and standard deviation σ in Silvern) cannot be compared directly. The approximate relationship of σ to the maximum deviated ray as described by normal probability is shown in Figure 4.1-9 and must be defined as to the degree to which the model is extended.

From the calculated flux distribution curves presented in this section, concentrator performance can be evaluated for various size apertures.

4.1.1.5 Predicted and Measured Concentrator Performance

Concentrator performance for various size apertures, as predicted by the previously mentioned analytical approaches, is presented in Figures 4.1-10 and 4.1-11. Also shown for comparison is the observed performance of the preprototype segments as measured during solar testing. These single panel solar tests are described in detail in Section 8.1.1.

Figure 4.1-10 shows the results of solar tests as compared to the Hukuo-Mii predicted performance. Figure 4.1-11 is a comparison with the normal distribution model and shows a closer curve shape correlation, thus supporting the previously stated conclusion based on geometric inspection that the normal distribution of surface errors is the more accurate analytical model.

CALCULATED FLUX PROFILES IN FOCAL PLANE

REFLECTIVITY = 100%

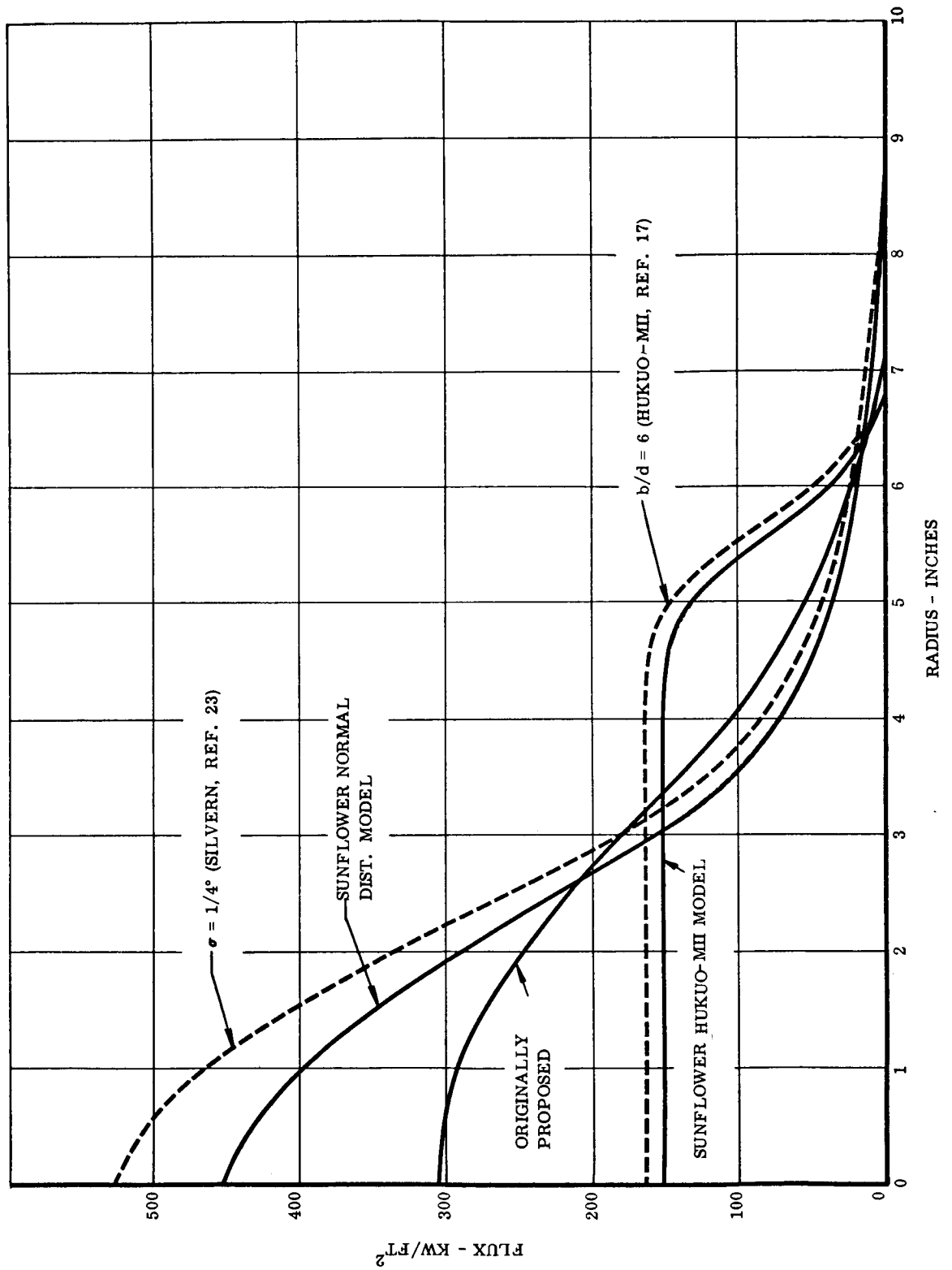


FIGURE 4. 1-8

RELATIONSHIP OF ϕ_{MAX} TO σ

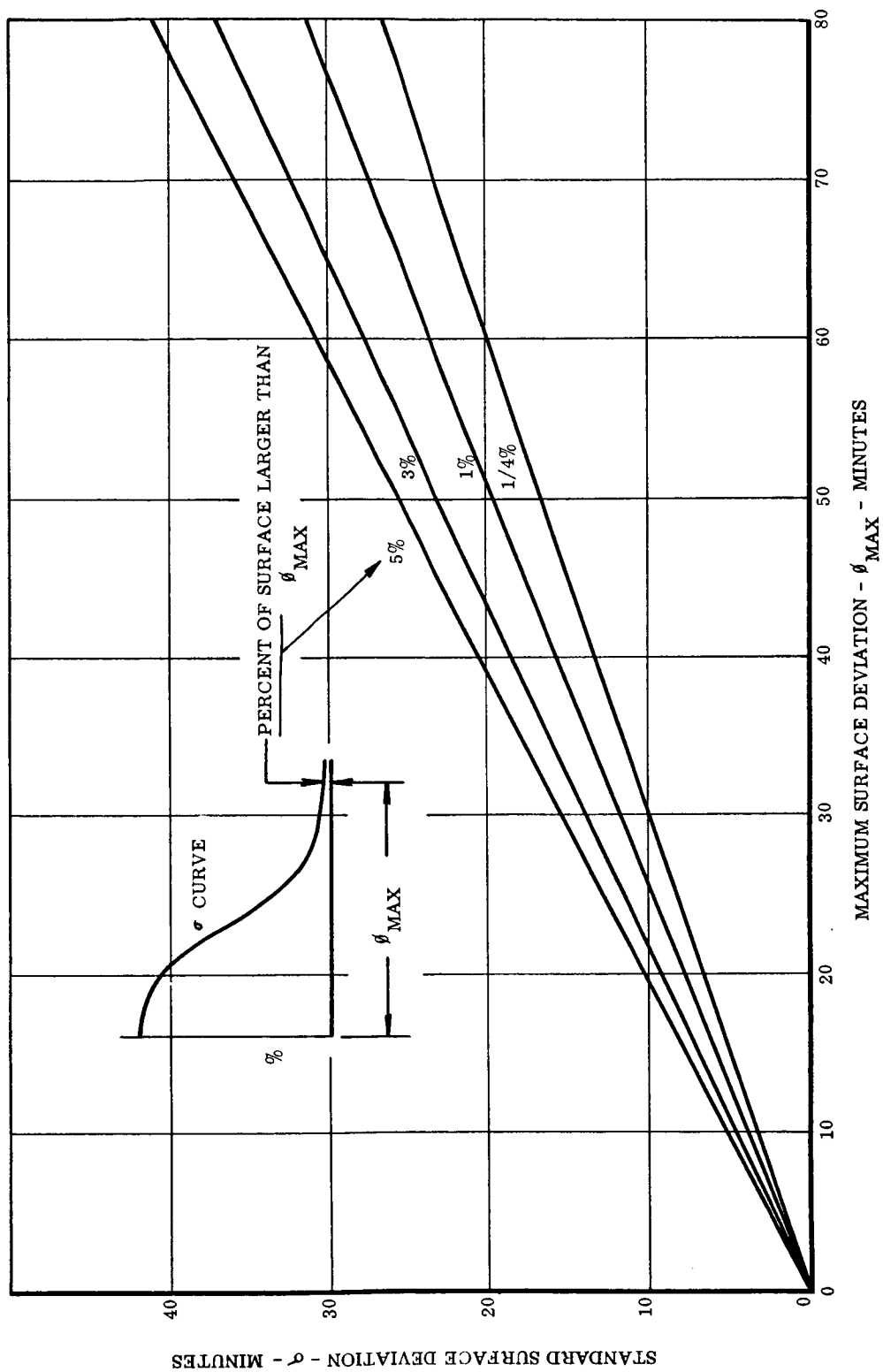


FIGURE 4. 1-9

PREDICTED VS MEASURED CONCENTRATOR PERFORMANCE
HUKUO-MII ANALYSIS
ZERO MISORIENTATION

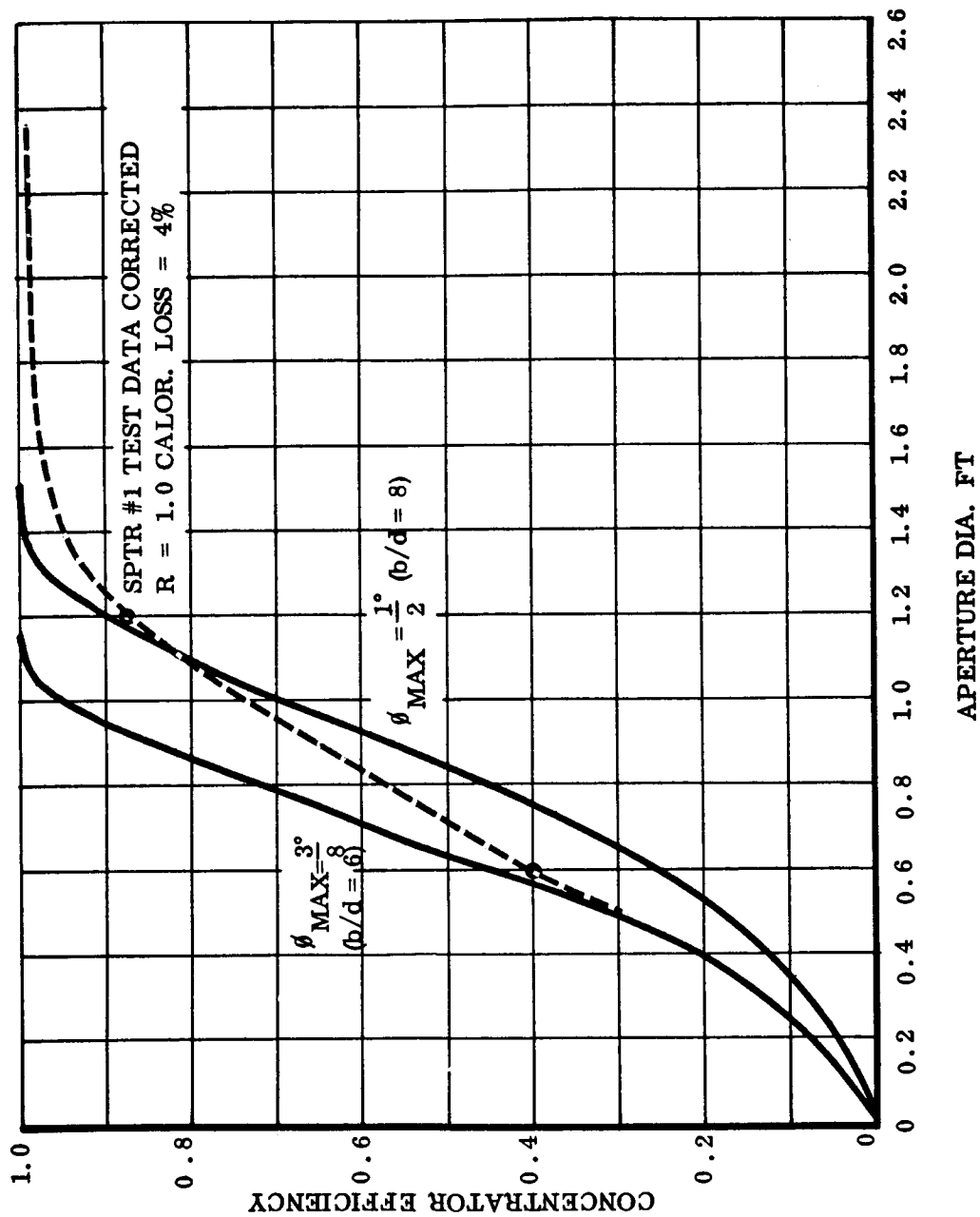


FIGURE 4. 1-10

PREDICTED VS MEASURED CONCENTRATOR PERFORMANCE
 NORMAL DISTRIBUTION SURFACE MODEL
 ZERO MISORIENTATION

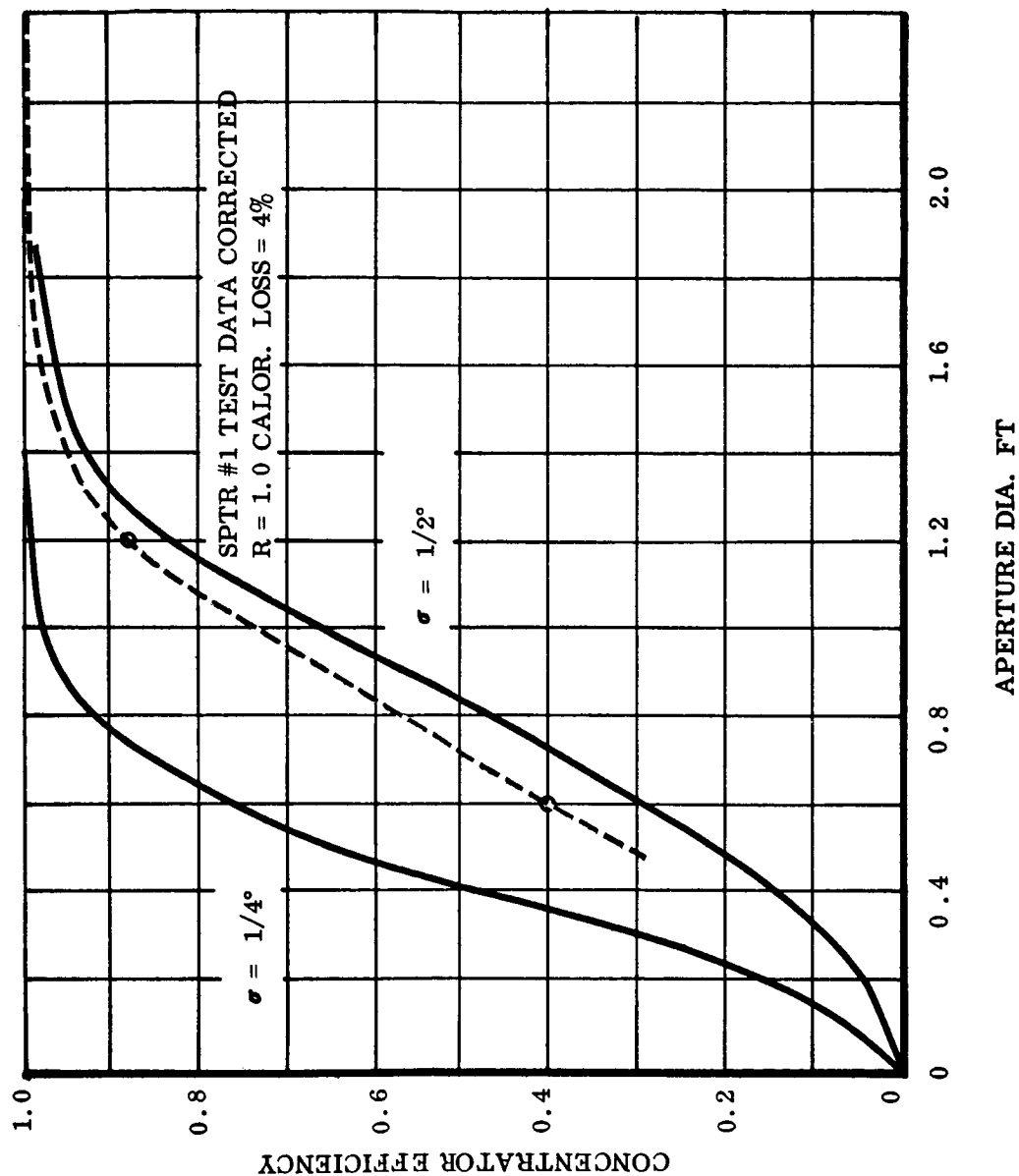


FIGURE 4. 1-11

It is seen that the performance displayed by the preprototype collector is represented by a standard surface error deviation of 25 to 30 minutes. This high value is primarily caused by the honeycomb markoff condition of SPTR #1 which is described in Section 7.3.4. As mentioned previously, a standard deviation value of 15 minutes can be expected in the Sunflower prototype design.

In the early Sunflower parametric analysis, the Hukuo-Mii flux profile characteristic was assumed. With modifications, the profile shape was related to a maximum surface error value which made analysis more convenient. These data were further analyzed to evaluate the solar misorientation parameter⁴. The resulting parametric curves are presented in Figure 4.1-12 for various misorientations. Based upon the subsequent test and inspection information, the actual flux profile of the Sunflower collector would be expected to fall somewhere between the normal distribution and the Hukuo-Mii profiles. Thus, higher efficiencies than are shown in Figure 4.1-12 can be anticipated. Parametric calculations using the normal distribution model must be made during a prototype design period.

4.1.2 Receiver Performance

This section treats a parametric analysis of the receiver retention efficiency. Receiver efficiency is expressed by equation (4.1-3), where the first term on the right hand side establishes the absorption factor and the second term establishes the thermal radiation factor. The objective in obtaining a high receiver efficiency is therefore to approach an η_R of 1.0 by making the first term large and the second small. For the purpose of this analysis, several assumptions have been made:

- a. The receiver surface reflects and emits solar or thermal radiation according to the classical cosine law.
- b. The receiver surface temperature is uniform over the entire area.
- c. The concentrator efficiency factor (η_C) is equal to 1.0 for all values of aperture diameter.

The second assumption is valid since the temperature profiles computed for the receiver surface²⁸ are near to being uniform. The third assumption was made so that the receiver efficiency would be independent of the effect of concentrator efficiency. However, the combined concentrator-receiver efficiency will be obtained in the subsequent section.

From equation (4.1-3), it can be seen that the parameters of q_s , A_c and η_c cannot be varied in this analysis. But the parameters of μ , a_{as} , F_r , A_s^c and T_s^c can be handled to optimize the receiver efficiency. The temperature T_s^s is established primarily by the heat storage media melting temperature. However, the temperature will vary to values above the melting temperature due to the heat transfer characteristics of the boiler/heat storage design. The temperature is not expected to decrease below

EFFECTS OF MISORIENTATION ON CONCENTRATOR PERFORMANCE

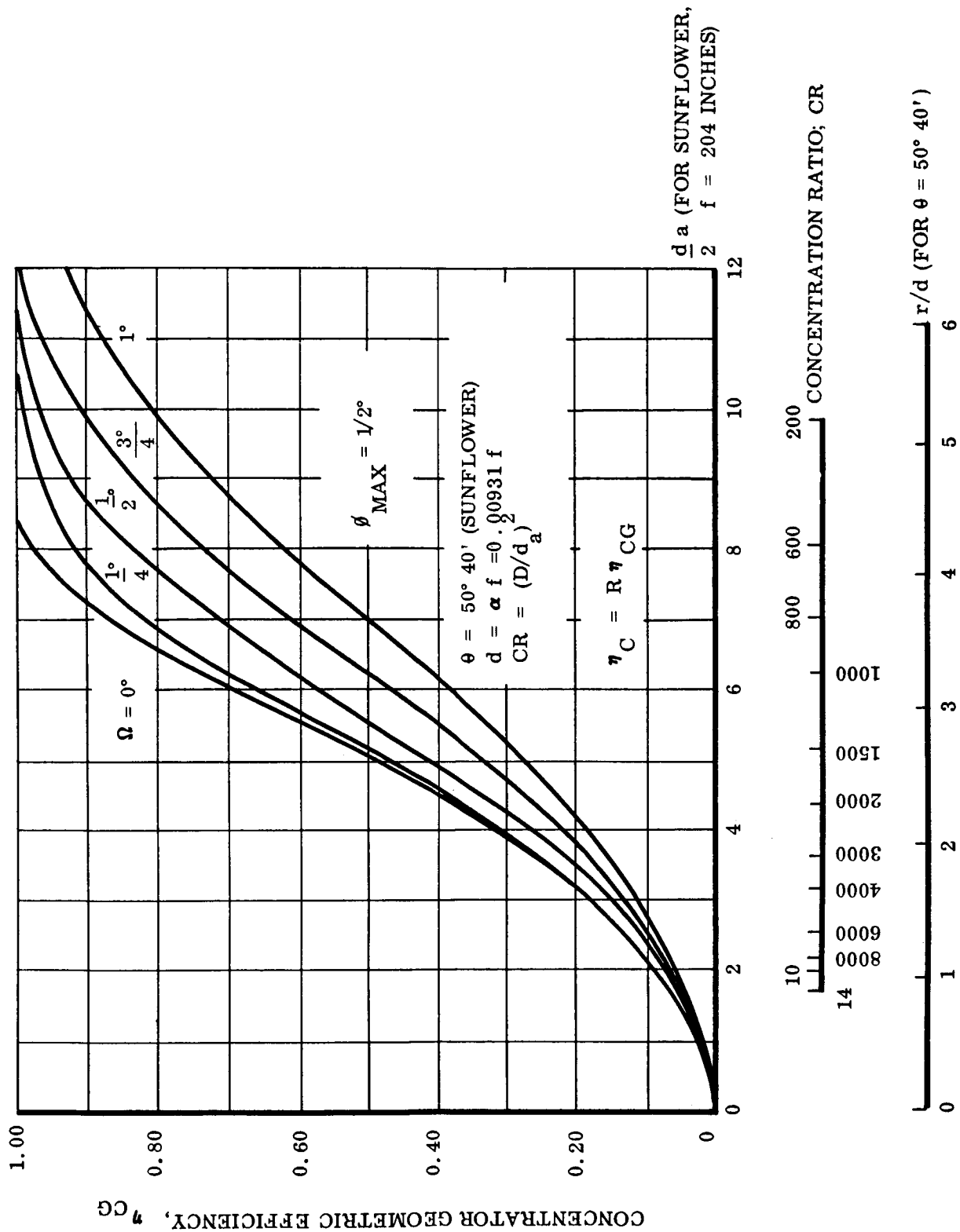


FIGURE 4. 1-12

1250°F, which will be the temperature just as the shade phase of an orbit ends. The upper limit has been set at 1600°F; this will be the case at completion of the sun phase of a 300 nautical mile orbit. In order to obtain a mean temperature for these receiver calculations, a typical temperature-time profile was chosen and the fourth root of the fourth power arithmetic mean value was calculated to be 1450°F.

It should be noted that the parameters a_{as} and F_r are functions of other parameters as follows:

$$a_{as} = F(a_{cs}, T_s, \frac{A_r}{A_s}), \quad \text{the directional reflecting characteristics of the receiver surface, and the view factor of the surface with respect to the cavity aperture.} \quad (4.1-6)$$

$$F_r = G(a_{ct}, \text{and the same parameters as in (4.1-6) except } a_{cs}) \quad (4.1-7)$$

The parameters a_{as} and F_r are in effect the apparent absorptivity of the aperture to solar radiation incident over that area and the radiation loss factor associated with the entire receiver surface, respectively. The parameter F_r includes the radiation which passes directly out of the aperture as well as radiation reflected from other areas of the interior to the aperture and out. The receiver area (A_s) is in most cases sized by the heat flux required by the conversion device. For the Sunflower boiler/heat storage component the heat flux (q_B) is approximately 10,000 Btu/hr ft².

The combinations of parametric values chosen for the Sunflower receiver evaluation are shown in Table 4.1-1, where a total of ten different cases are treated. The results are plotted in Figures 4.1-13 to 4.1-16 as receiver efficiency versus cavity aperture diameter. It will be shown in the following section that the 15 to 17 inch aperture diameters form the range of optimum aperture sizes for the cases chosen. Therefore, for this analysis, that same range should receive the most attention.

Figure 4.1-13 shows the effect of receiver temperature on retention efficiency. The predicted mean temperature of 1450°F is representative of the expected performance, whereas the curves of 1250° and 1600°F are the limits of conceivable performance. As can be seen, the efficiency can differ by 15% at a 17 inch aperture size. The conclusion is that if the receiver design is changed to allow a reduced maximum temperature (1600°F on these curves), an improvement of about 5% in efficiency might be achieved.

Figure 4.1-14 shows the effect on efficiency as the parameters of a_{cs} and a_{ct} (equations (4.1-6) and (4.1-7)) are varied. Here a 10% spread exists between the extreme cases at the 17 inch aperture size. For this example, the cases of 2a and 2b may not be realistic because of the assumption of a non-gray characteristic, where the a_{cs}/a_{ct} ratios are 2.0 and 0.5, respectively. Although many surfaces exhibit

TABLE 4.1-1
RECEIVER STUDY PARAMETERS

Case	Receiver Temperature T_s (°F)	Receiver Surface Solar Absorptivity a_{cs}	Receiver Surface Thermal Absorptivity at T_s a_{ct}	Receiver Surface Area A_s (ft ²)	Reradiation Time to Sun Time Ratio μ	Plotted in Figure
1a b c	1250 1600 1450					4.1-13
2a b c d* e		1.0 0.5 0.5 0.9 0.375	0.5 1.0 0.5 0.9 0.3			4.1-14
3a b c*				20 30 26		4.1-15
4a b*					1.0 1.6	4.1-16

*Same as case 1c

$$A_c = 747 \text{ ft}^2$$

$$q_s = 440 \text{ Btu/hr ft}^2$$

$$\eta_c = 1.0$$

$$a_{cs} = 0.9 \text{ Except as in cases 2a, b, c, and e}$$

$$a_{ct} = 0.9 \text{ Except as in cases 2a, b, c, and e}$$

$$A_s = 26 \text{ ft}^2 \text{ Except as in cases 3a and b}$$

$$T_s = 1450^\circ\text{F} \text{ Except as in cases 1a and b}$$

$$\mu = 1.6 \text{ Except as in case 4a}$$

EFFECTS OF TEMPERATURE ON RECEIVER RETENTION EFFICIENCY

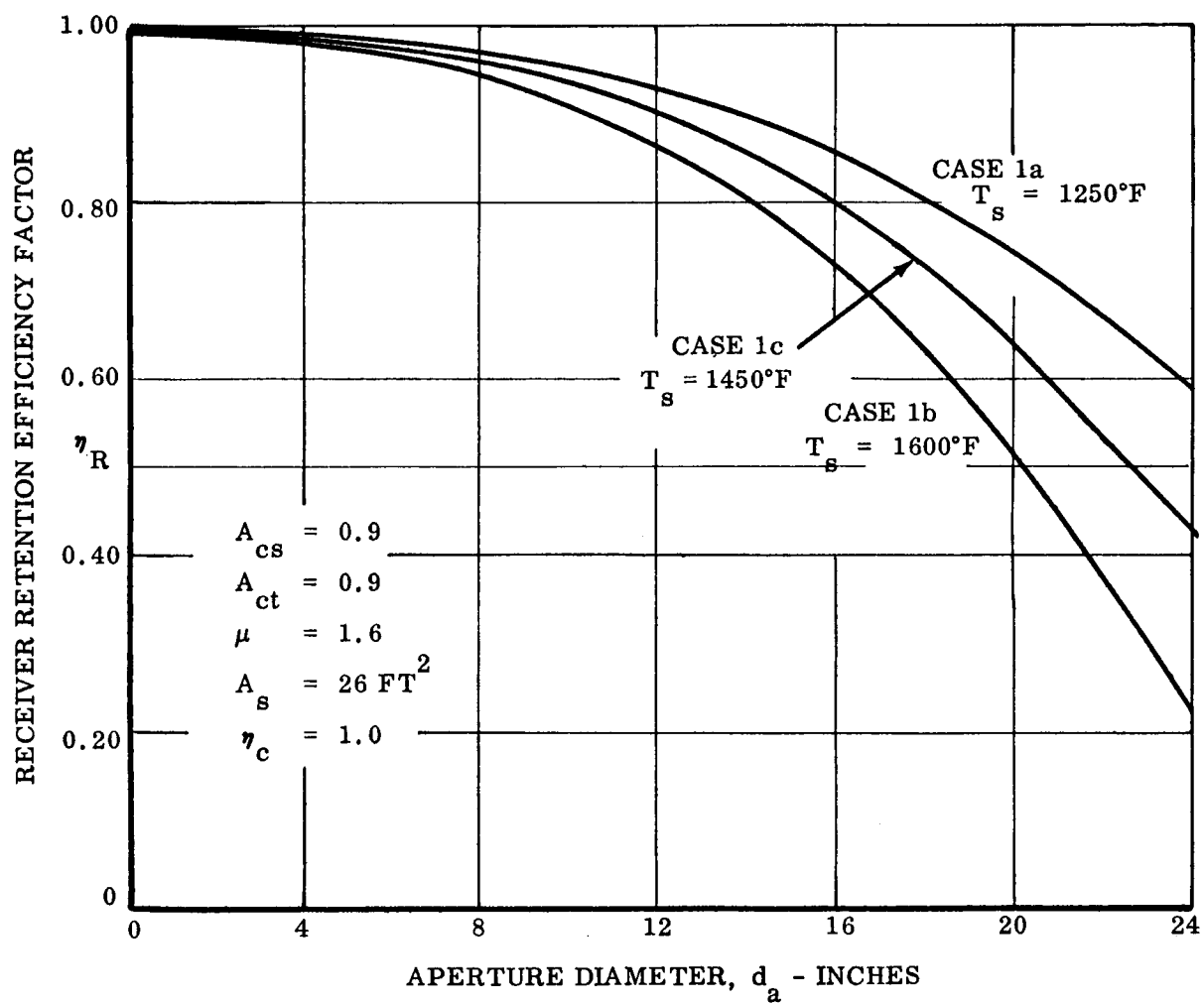


FIGURE 4.1-13

EFFECTS OF RECEIVER SURFACE RADIATION CHARACTERISTICS ON RETENTION EFFICIENCY

CASE	a_{cs}	a_{ct}
2a	1.0	0.5
2b	0.5	1.0
2c	0.5	0.5
2d	0.9	0.9
2e	0.375	0.30

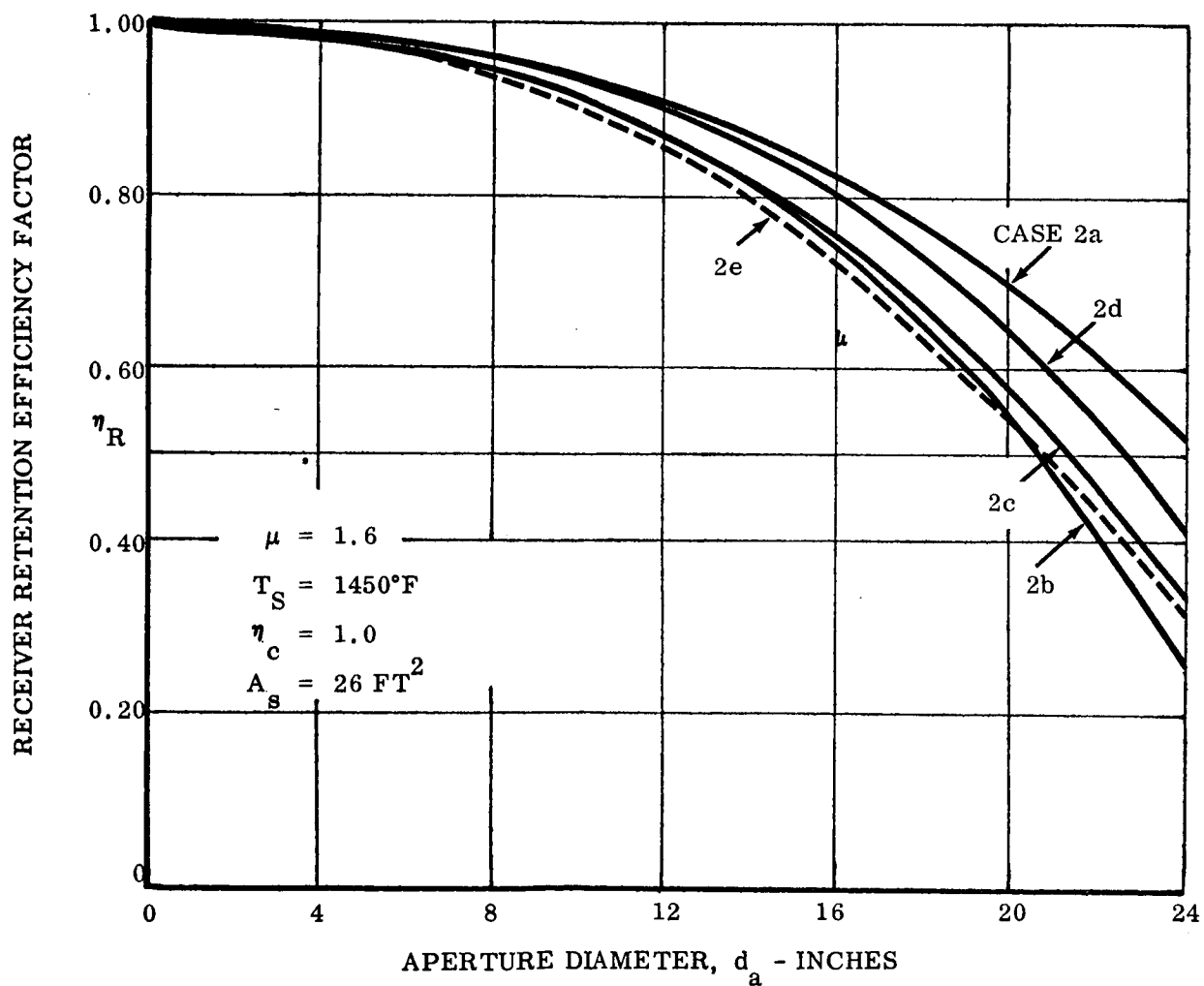


FIGURE 4.1-14

EFFECTS OF RECEIVER SURFACE AREA ON RETENTION EFFICIENCY

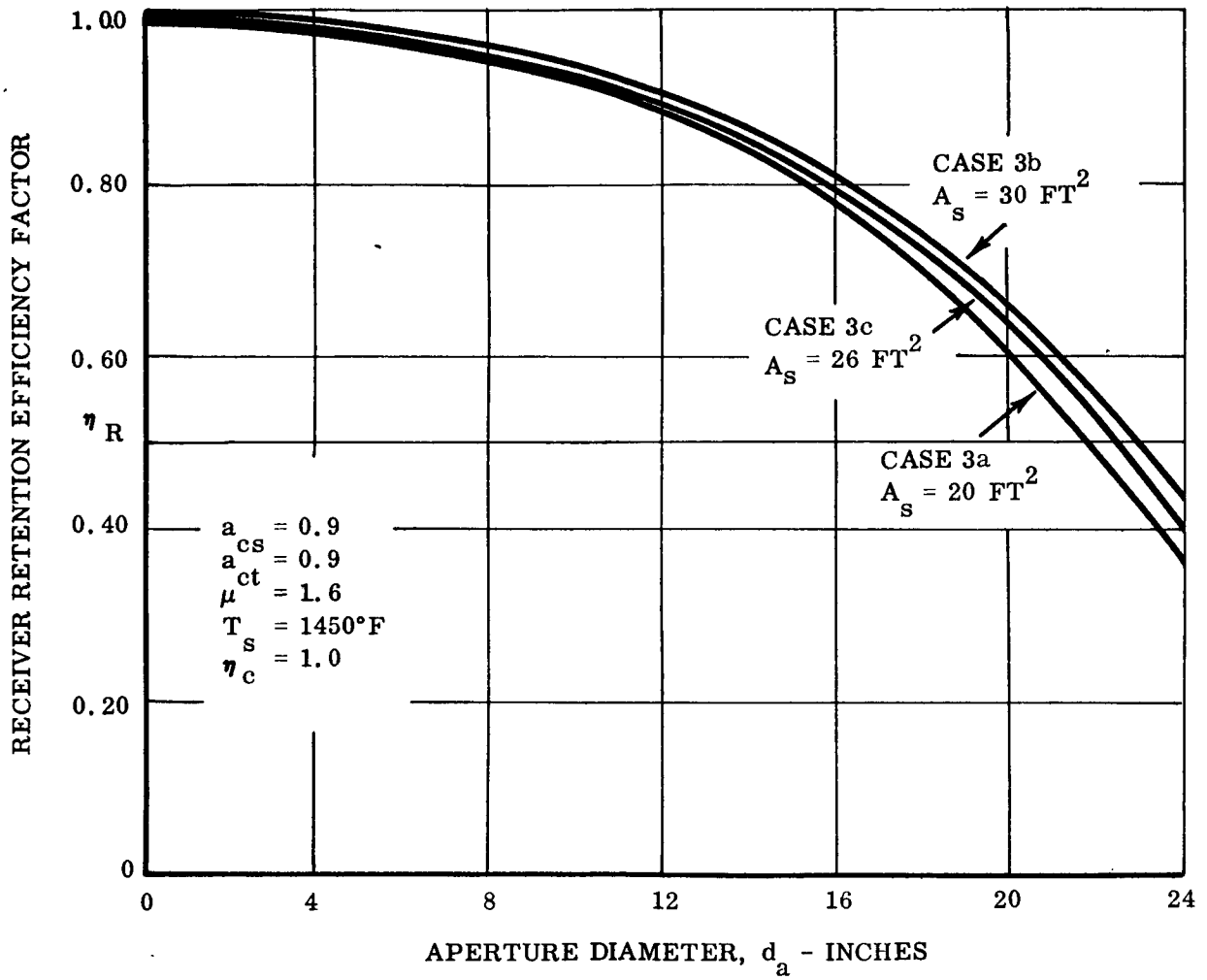


FIGURE 4.1-15

EFFECTS OF SHADE TIME RERADIATION ON RECEIVER RETENTION EFFICIENCY

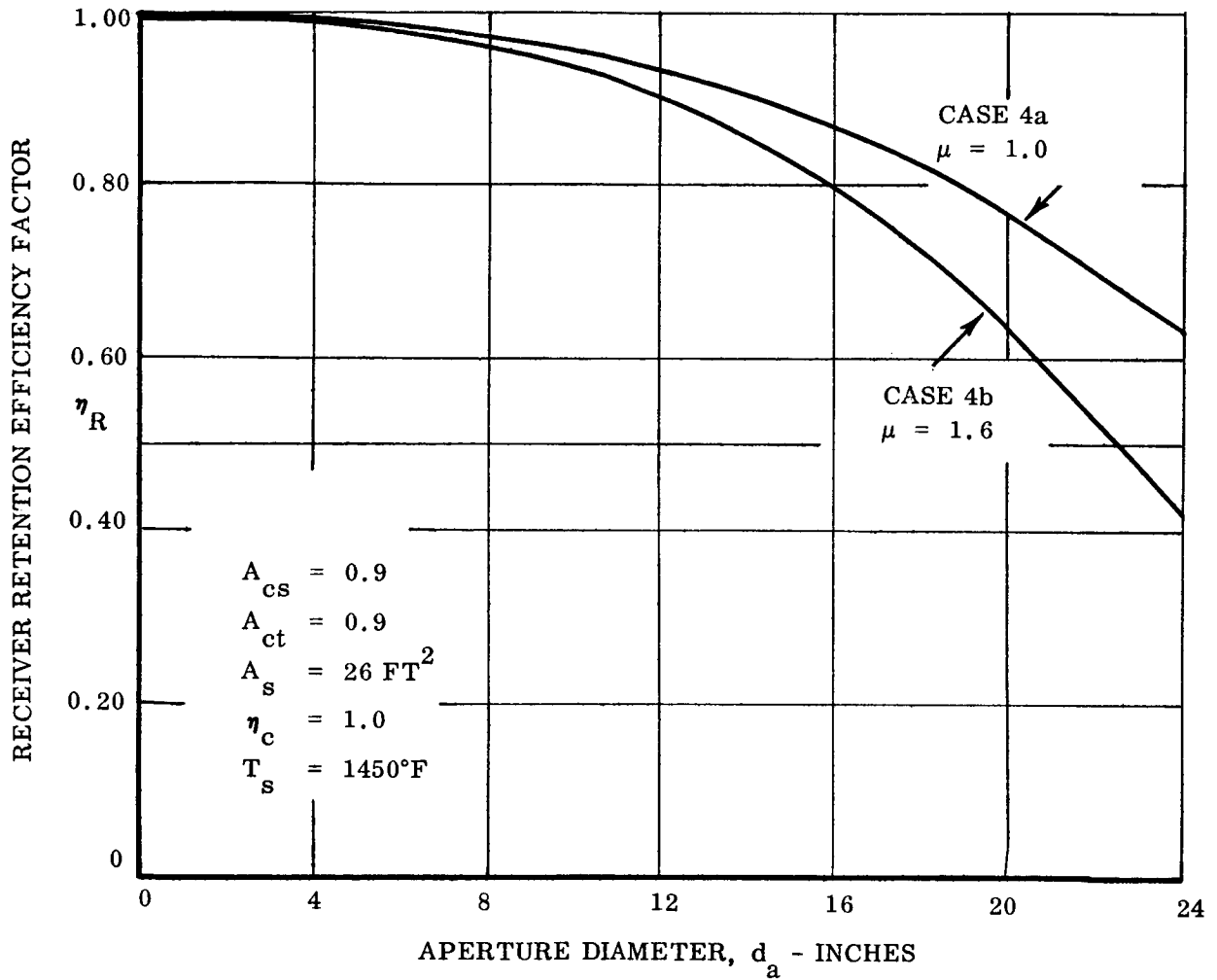


FIGURE 4.1-16

these spectrally dependent characteristics, it is expected that the ratio of a_{cs}/a_{ct} for the receiver surface will be close to one. For one reason, the wavelength ranges of the solar and 1250° to 1600°F thermal radiation are more alike than the ranges of solar and 100° to 200°F thermal radiation.

Case 2a shows the most desirable receiver surface absorptivity properties where $a_{cs}/a_{ct} = 2.0$, and case 2b shows the case where the ratio is 0.5. Case 2c shows the results of using $a_{cs}=0.375$ and $a_{ct}=0.3$ values, and in the 15 to 17 inch diameter range this combination results in the lowest receiver efficiency. This last case could be typical of the Haynes alloy used in the shell construction if it is heated in a vacuum. The change in absorptivity when heated in the presence of air is not known. However, the case 2d curve shows the desirability of having a high value of a_{cs} and accepting the fact that the a_{ct} value will be the same. A high a_{cs} value makes the first term in equation (4.1-3) large. As case 2a shows, the need for an $a_{cs}/a_{ct} = 2.0$ ratio does not markedly improve receiver efficiency. Besides, such a tailored surface may be difficult to attain.

Figure 4.1-15 shows the influence of receiver surface area on efficiency; however, this parameter cannot be changed too drastically because of the heat flux requirements resulting from the boiler/heat storage design. Of the four parameters which have been varied, the surface area has the least effect on efficiency, being only 3% at the 17 inch aperture.

Figure 4.1-16 shows a larger change of 8% at the 17 inch aperture as the parameter μ is changed from 1.6 to 1.0. To achieve a μ of 1.0 for a 300 nautical mile orbit, it will be necessary to close the receiver aperture during the shade period, thus eliminating the radiation loss for that phase.

The conclusions of this analysis are, therefore, that the highest receiver efficiency can be obtained by:

- a. Reducing receiver temperature.
- b. Increasing the absorptivity of solar radiation.
- c. Increasing the receiver interior area.
- d. Closing the aperture during the shade phase.

The quantitative changes will be shown in the following section.

Since a solaramic coating (glass) is being proposed for purposes of hydrogen containment in the heat storage design, it is expected that an investigation into additives or modifications would show that higher absorptivities could be achieved. This, of course, has to be done without degrading the hydrogen containment property.

4.1.3 Combined Collector-Receiver Performance

The combined collector-receiver performance was studied parametrically during the development program. Since the correlation of the Sunflower collector surface errors to the normal distribution characteristic was not obtained until late in the development program, the parametric studies are based upon flux distributions in the focal plane as predicted by the Hukuo-Mii analytical approach. In particular, the curves that show the effect of solar misorientation on collector efficiency are based on the Hukuo-Mii model. The fact that the actual Sunflower surface characteristic is between the Hukuo-Mii and a normal distribution model means that the efficiencies predicted here are conservative. Thus, higher efficiencies are expected.

Because of the many parameters, an infinite number of optimum collector-receiver efficiencies can be obtained. An optimum efficiency for any combination exists at a finite value of aperture diameter, because the collector efficiency increases with aperture whereas the receiver efficiency decreases.

Based on the conclusions regarding surface errors, it is anticipated that maximum cumulative slope errors will not exceed $1/2^\circ$ in the Sunflower collector. This being the case, the curves in Figure 4.1-12 can be used to predict Sunflower collector-receiver performance.

Utilizing the analyses in sections 4.1.1 and 4.1.2, the five cases in Table 4.1.2 have been selected as logical parametric combinations for study. As can be seen in Figure 4.1-17, the concentrator-receiver efficiency increases as each case is considered, starting with the first. This increase is due to the choice of parameters that tend to increase efficiency. The highest efficiency achieved in Case 5 does not involve any major developmental programs but would entail the following:

- a. Maintain solar misorientation to $1/4^\circ$ maximum.
- b. Design an aperture door for closure in the shade phase.
- c. Provide a high surface absorptivity to solar radiation.

If one or more of these conditions are not acceptable, the remaining 4 cases reveal the degree of reduction in efficiency.

The boiler/heat storage component requires a total heat input of 190,200 btu per orbit period at 300 nautical miles, including 4020 btu for thermal losses from the exterior of the unit. The intercepted solar flux with a 32.2 foot outside diameter, 9.2 foot inside diameter concentrator is 329,000 btu/hr. Since the sun phase is 60 minutes, then 329,000 btu will be intercepted per orbit period. The minimum collector-receiver efficiency is therefore 190,200 divided by 329,000, or 57.8%. As can be seen in Table 4.1-2, case 3 is just below this limit for the 32.2 ft diameter collector design and cases 4 and 5 allow a reduction in collector size. For the first and second cases, a collector larger than 32.2 ft would be necessary.

TABLE 4.1-2

PARAMETRIC STUDY RESULTS

Case	Solar Mis-orientation Ω max. (degrees)	Reradiation Time to Sun Phase Ratio μ	Receiver Surface Solar Absorp. a_{cs}	Receiver Surface Thermal Absorp. a_{ct}	Collector Receiver Efficiency η_{CR}	Receiver Aperture Diameter d_a (inches)	Area Concentration Ratio CR	Heat into Boiler/Heat Storage Unit During Sun Phase * Q_B (Btu)	Collector Diameter Required For 190,200 Btu To Boiler D (Ft.)
1	3/4	1.6	0.5	0.5	0.445	17.3	496	146,500	34.3
2	1/2	1.6	0.5	0.5	0.535	16.8	526	176,000	32.8
3	1/2	1.6	0.9	0.9	0.570	17.2	504	187,500	32.3
4	1/4	1.6	0.9	0.9	0.630	15.5	620	207,000	31.4
5	1/4	1.0	0.9	0.9	0.705	16.5	546	231,000	30.4

* D = 32.2 ft

$$\phi_{\max.} = 1/2^\circ$$

$$R = 0.90$$

$$A_s = 26 \text{ ft}^2$$

$$A_c = 747 \text{ ft}^2$$

$$T_s = 1450^\circ \text{F}$$

$$q_s = 440 \text{ Btu/hr ft}^2$$

$$\eta_{CR} = a_{as} \eta_c - \frac{\mu F_s A_s \sigma T_s^4}{q_s A_c}$$

SUNFLOWER CONCENTRATOR RECEIVER PERFORMANCE

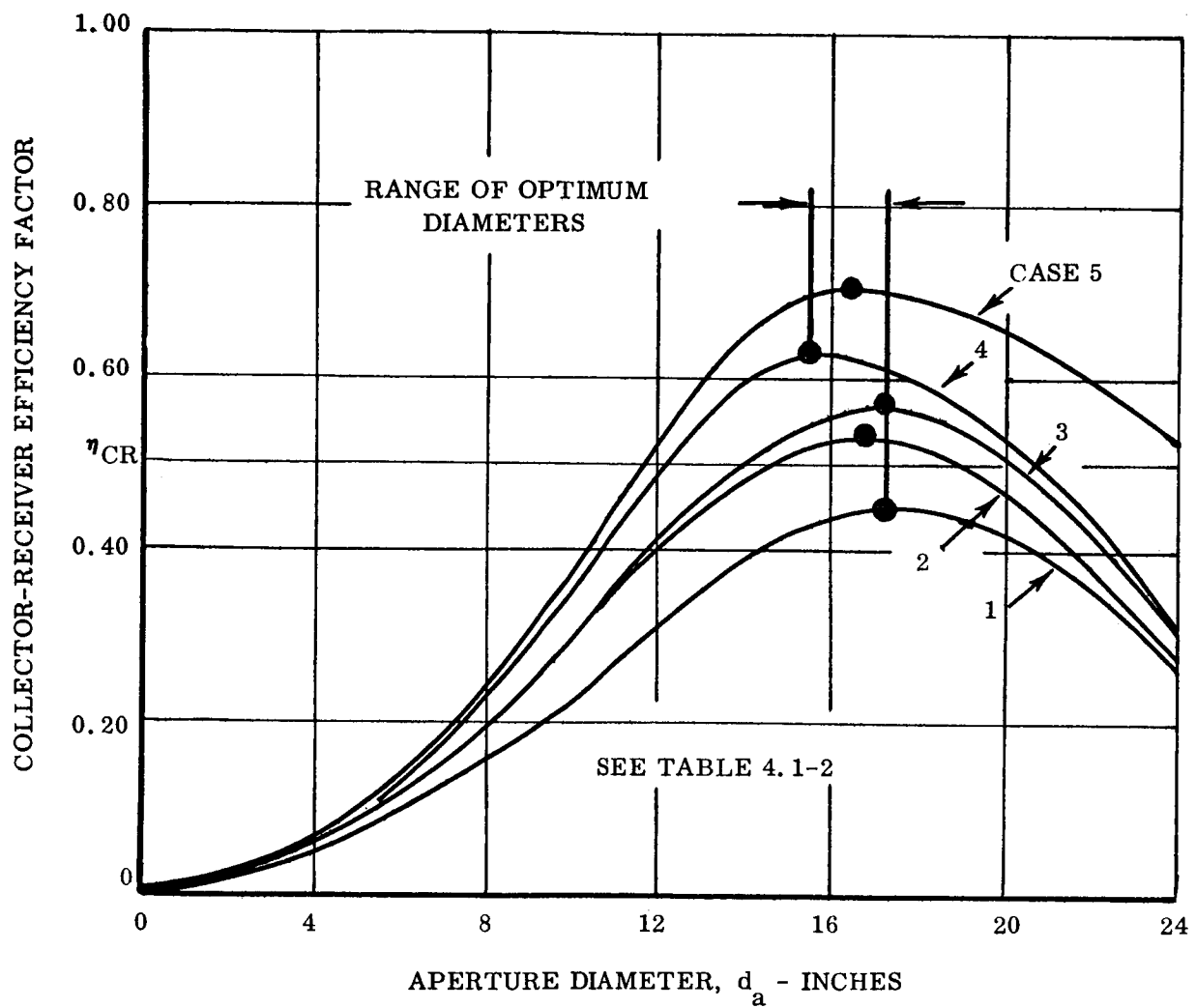


FIGURE 4.1-17

4.2 ENVIRONMENTAL ANALYSIS

Analytical investigations of the Sunflower systems were conducted to determine the structural and other design requirements for the solar collector. These analyses included launch environments of acceleration, aerodynamic loading, and vibration for the stowed structural arrangement. Deployed position environments of orbital transfer acceleration and vibration as well as space conditions of vacuum, meteorite bombardment etc., and thermal environment were investigated. Also analyzed were deployment dynamics and kinetics.

4.2.1 Launch Environment Analysis

In the launch position, the collector sectors are bundled around the system structure and held in position by restraining bands at several locations. A structural analysis of the sectors as conjugate beams was programmed on a Burroughs 205 digital computer. The program computes the deflections of a parabolic shape sector under the influence of acceleration and arbitrarily imposed forces along the sector length, and considers that the sector is supported at the hinge end and by contact with a support ring whose position may be specified. Any desired moment may be imposed at the hinge, and a single restraining band (in addition to that at the support ring) may be located as desired.

Primary deflections are calculated and inertia and aerodynamic loads are again placed on this new shaped sector. Secondary deflection is computed and added to the primary. This iteration is repeated until the newly-found deflection increment is less than 1% of the primary deflection at the point of maximum deflection.

The computer prints out deflections, stresses, shear forces, support ring reactions, and band forces. Typical computed results for the launch inertia loading are shown plotted in Figure 4.2-1.

This computer program was used to establish the honeycomb material crosssection and to optimize support and band locations for minimum deflection and stress. Computed reactions and band forces were used as a criterion for the design of sub-components.

4.2.2 Vibration Analysis

Certain vibration specifications have been established for the Sunflower system. Figure 4.2-2 shows the original vibration specifications and also the more recent revised specification. The original specifications apply to both launch (stowed) and orbital transfer (deployed) positions of the collector.

Vibration analysis during the initial investigation period consisted of calculating the fundamental frequency of a single sector simply supported. As might be expected for a large flexural element, this frequency was low—approximately 2 to 3 cps.

COLLECTOR SECTOR STRESS ANALYSIS COMPUTER PROGRAM
2057 JOB #13 LAUNCH ACCELERATION LOADING

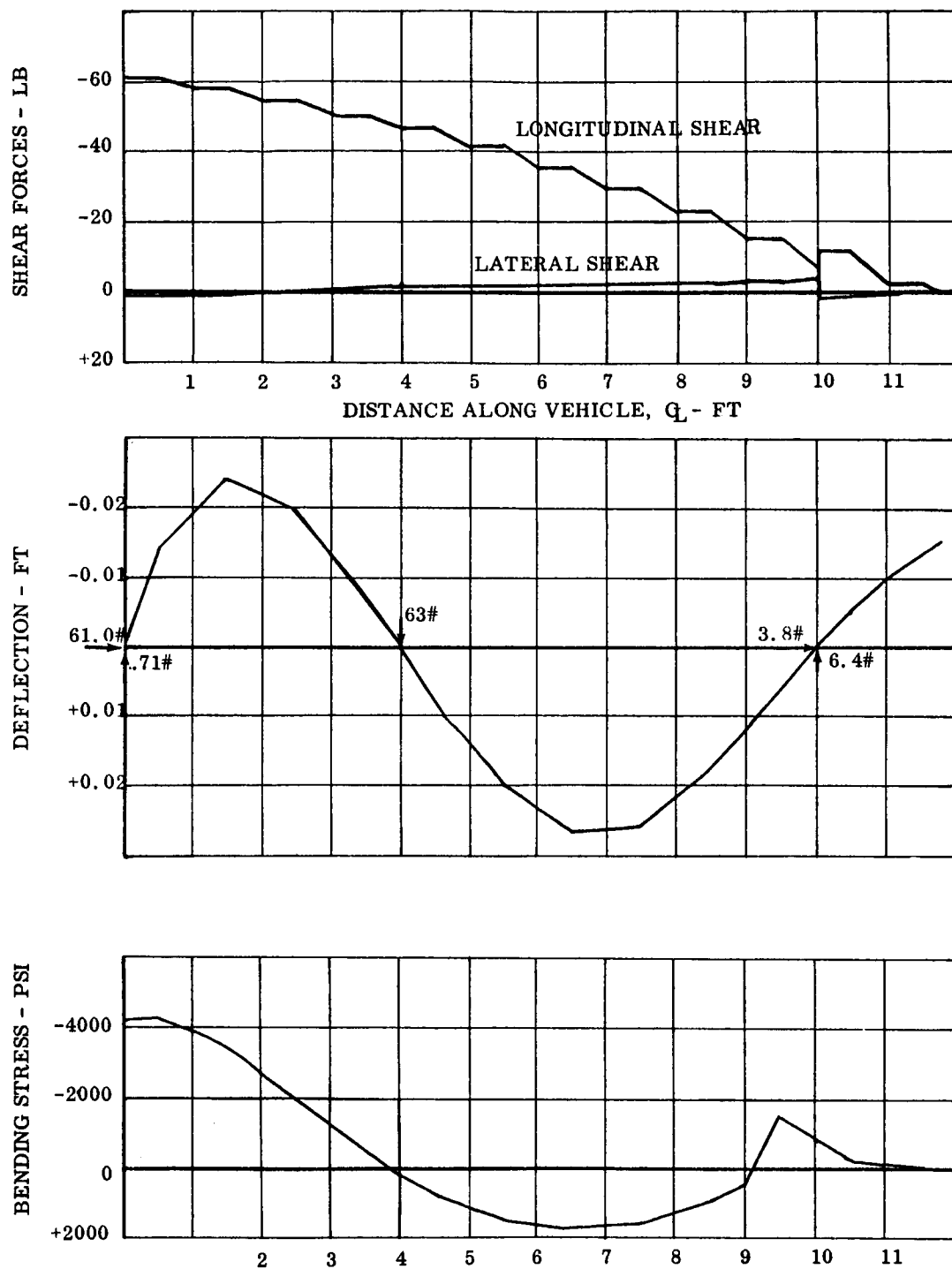


FIGURE 4.2-1

AXIAL VIBRATION SPECIFICATIONS

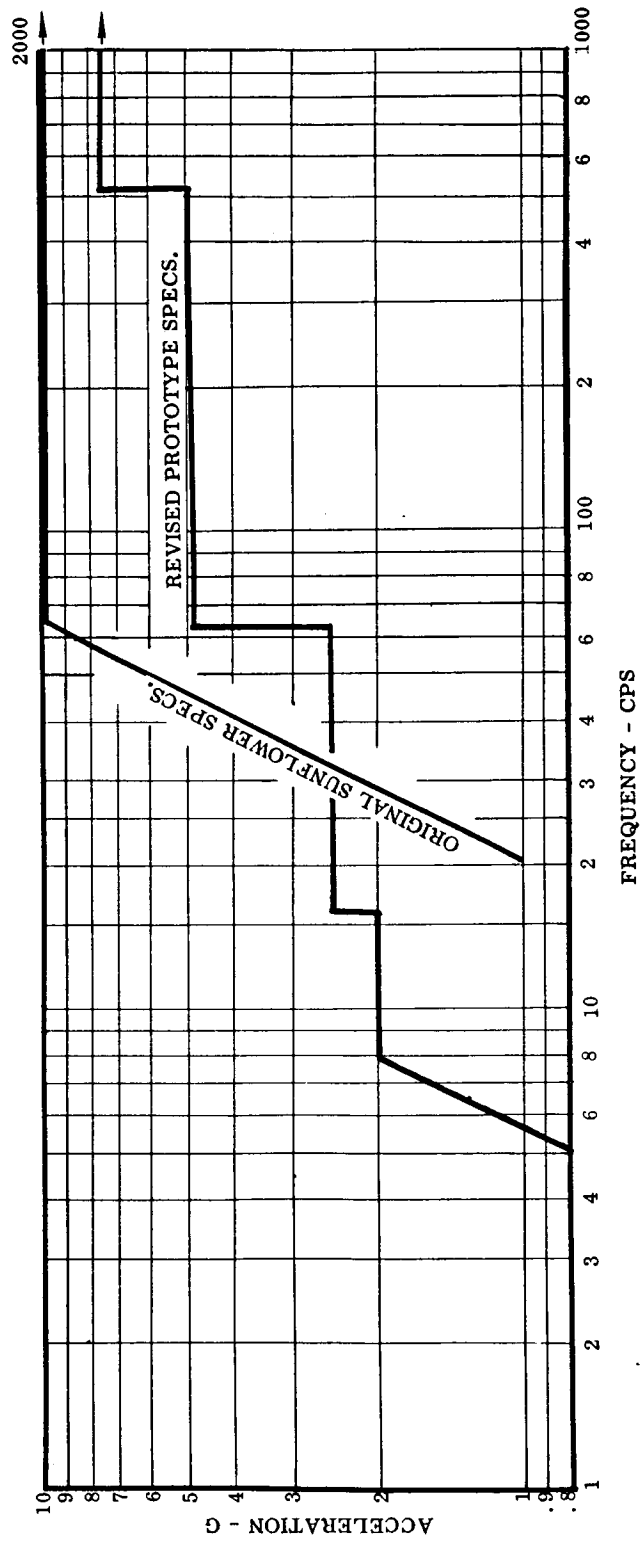


FIGURE 4.2-2

The sectors are subjected to different degrees of vibration in the stowed and deployed configurations. Figure 4.2-3 is a schematic representation of the relationship of the vehicle vibration inputs to that transmitted to the collector supports.

Based upon this preliminary analysis and low level vibration testing, a vibration isolation system was established for the Sunflower collector and will be described in Section 5.3.6.

4.2.3 Deployment Analysis

The Sunflower collector deployment concept may be briefly stated as follows:

- a. Torsion spring actuation from the stowed position
- b. Motion to the full open paraboloidal position
- c. Stop and lock in the full open position

The motion of the collector sectors, as well as the forces involved in the locking sequence, were analytically investigated.

Orbital deployment of the collector will occur in a zero gravity environment where the only driving force will be the torsion spring. Motion due to the spring will be damped by sliding friction forces between sectors. Since these forces are difficult to predict accurately, a range of frictional values was investigated.

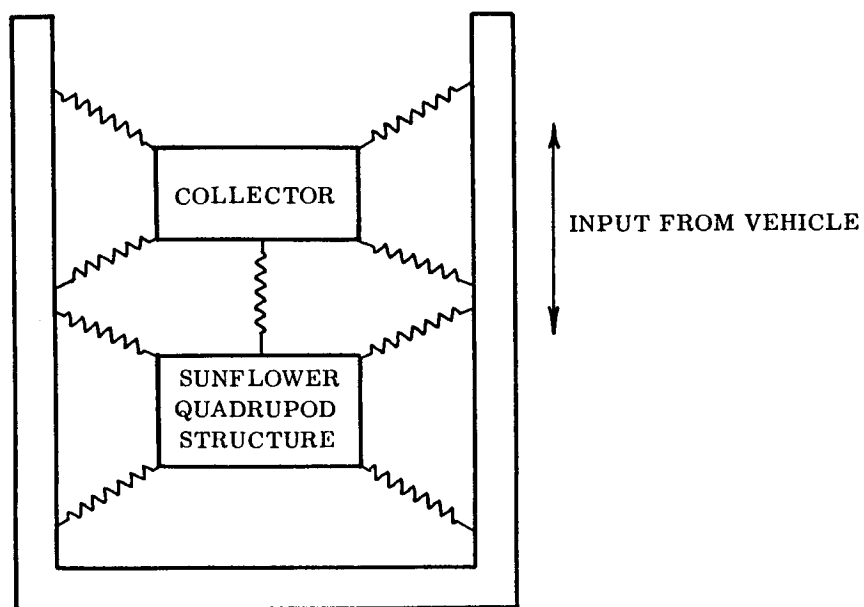
To avoid excessive kinetic energy build-up in sector inertia, a viscous damping arrangement at the hinge was also investigated over the range from no damping to critical damping. The equations of motion for such an arrangement were solved and typical results will be presented in section 8.3.2 for comparison with test data.

The kinetics of such a system were also analyzed and typical results are shown in Figure 4.2-4. It is seen that as the damping coefficient (γ) approaches critical damping ($\gamma = 1.0$), the level of final kinetic energy decreases and yet a wide range of frictional torques can be accommodated. Thus, stopping and locking forces can be controlled by the proper design of a damping device.

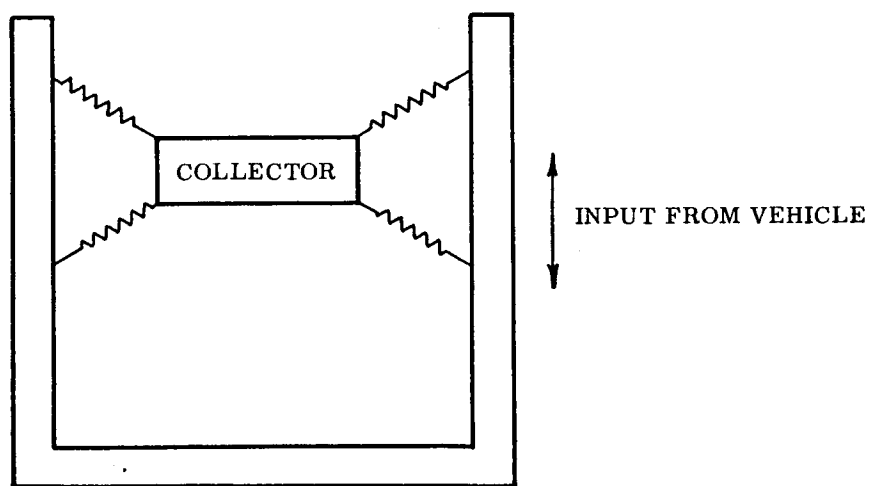
4.2.4 Deployed Paraboloidal Position Structural Analysis

Several methods were used to analyze deflections and stresses of the deployed collector. As mentioned previously, the Burroughs 205 computer program was used to establish the honeycomb sandwich material cross-section for launch loads on a single sector analysis. Stresses and deflections for a simply supported sector were also computed on the 205. However, the effect of the structure of revolution could not be handled. A membrane analysis of a paraboloid of revolution showed small deflections which, of course, did not include bending.

COLLECTOR VIBRATION SYSTEM SCHEMATIC



STOWED LAUNCH



DEPLOYED

FIGURE 4.2-3

SUNFLOWER SECTOR KINETICS
DRIVING TORQUE = 6 FT-LB/SECTOR - MAX.

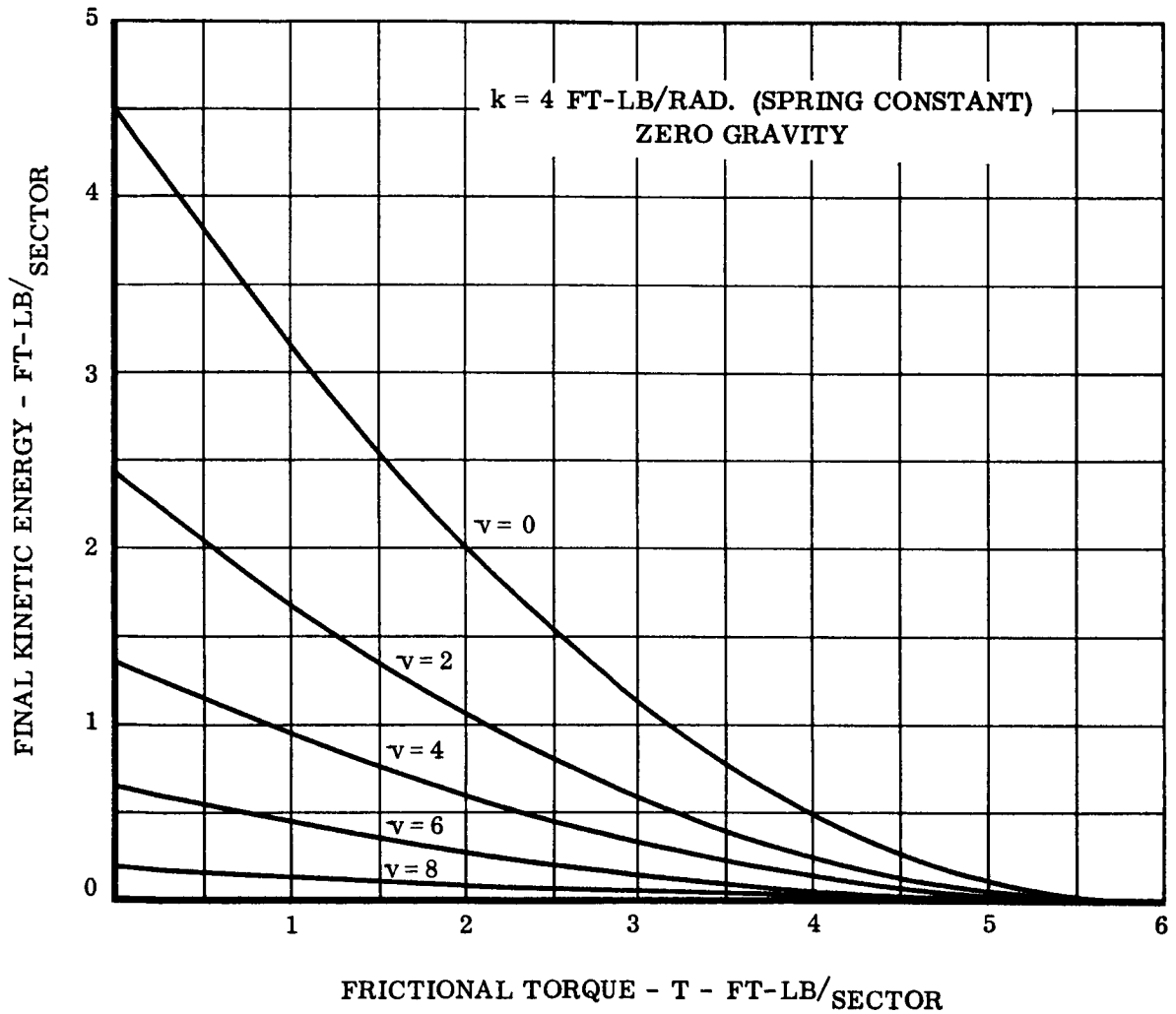


FIGURE 4.2-4

A satisfactory structural analysis of the deployed collector was obtained in conjunction with the thermoelastic structural analysis programmed on an IBM 704 computer. Further description of the analytical model and results will be presented in Section 4.2.5.

Calculations were also made for anticipated inertia loadings due to satellite attitude control and stabilization maneuvers; these were shown to be negligible.

4.2.5 Orbital Thermal Environment Investigation

The Sunflower power conversion system must be capable of operation in any earth orbit between 300 miles and 20,000 miles normal altitude. The resulting sun-shade environment and changing irradiation conditions of a near-earth orbit will impose temperature variations on the solar collector. Theoretical and supporting experimental investigations of the effects of orbital thermal environment on the performance of the Sunflower solar collector were conducted and resulted in specific structural design considerations.

4.2.5.1 Transient Temperature Characteristics

Variations in temperature experienced by an object in a near-earth orbit are primarily caused by its passages into and out of the earth's shadow. The resulting cooling and heating trends are controlled by the orbit elements, the intensities of solar and terrestrial radiation fluxes, and a combination of several parameters of the satellite material and its surface structure, including albedo, emissivity, heat conductivity, and heat capacity.

For the Sunflower system, the largest variations in temperature can be expected from the wide range of radiation intensities encountered in a low earth orbit. For this reason, the 300 mile orbit with approximately 60 minutes of sun and 35 minutes of shade time was investigated.

Transient Heat Balance

The Sunflower collector is composed of adhesive bonded aluminum honeycomb sandwich material with a typical cross-section as shown in Figure 4.2-5 (a). The thermal characteristics of this material in a space environment are represented in Figure 4.2-5 (b) by a simplified diagrammatic thermal network.

The solution of this network for an increment of collector material as the surface progresses through an orbital period (see Figure 4.2-6) was calculated.

Results of these calculations are shown in Figure 4.2-7 for the originally proposed honeycomb material. Results for the minimum weight thermal control design are shown in Figure 4.2-8. This concept uses transparent silicon oxide radiation control films which increase or decrease the emissivity in a certain temperature range. The thick

HEAT TRANSFER CHARACTERISTICS OF COMPOSITE SANDWICH MATERIAL

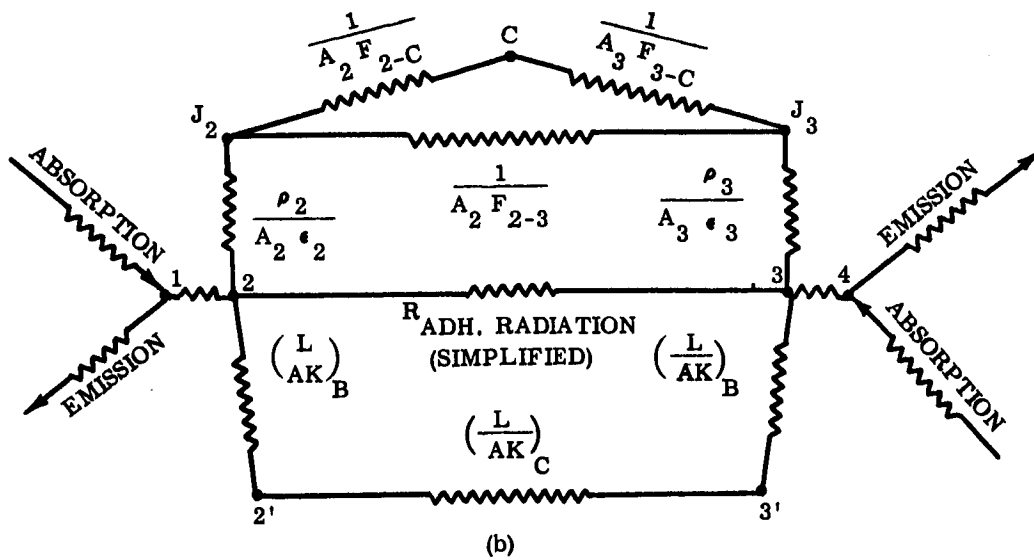
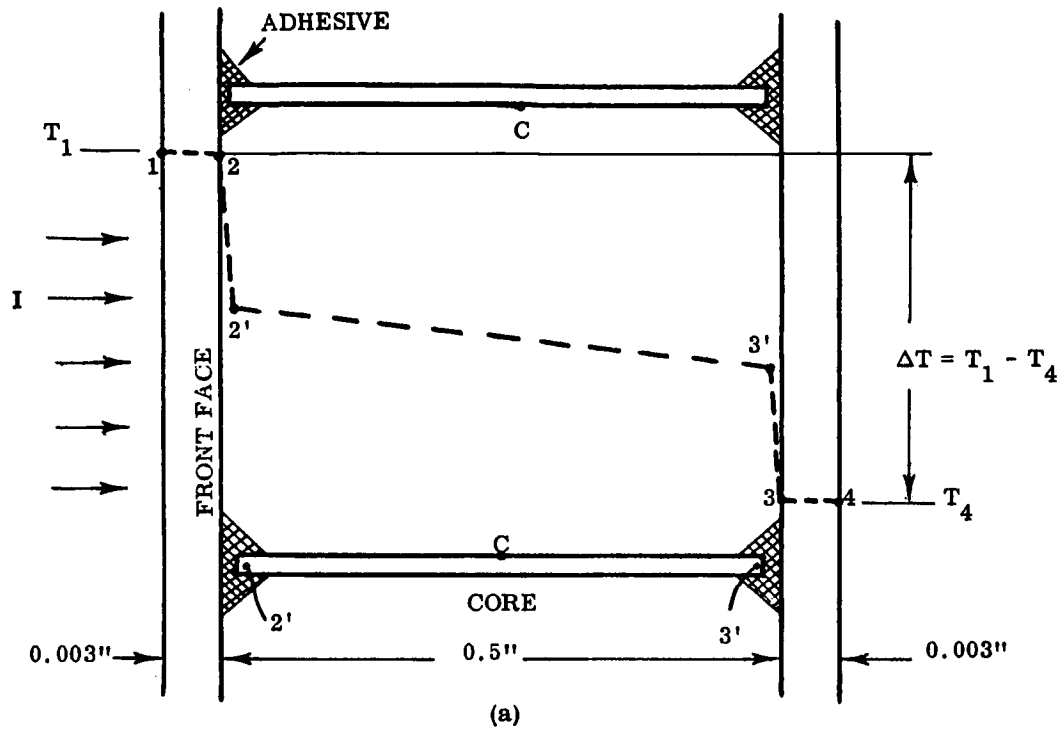


FIGURE 4.2-5

ORBIT GEOMETRY

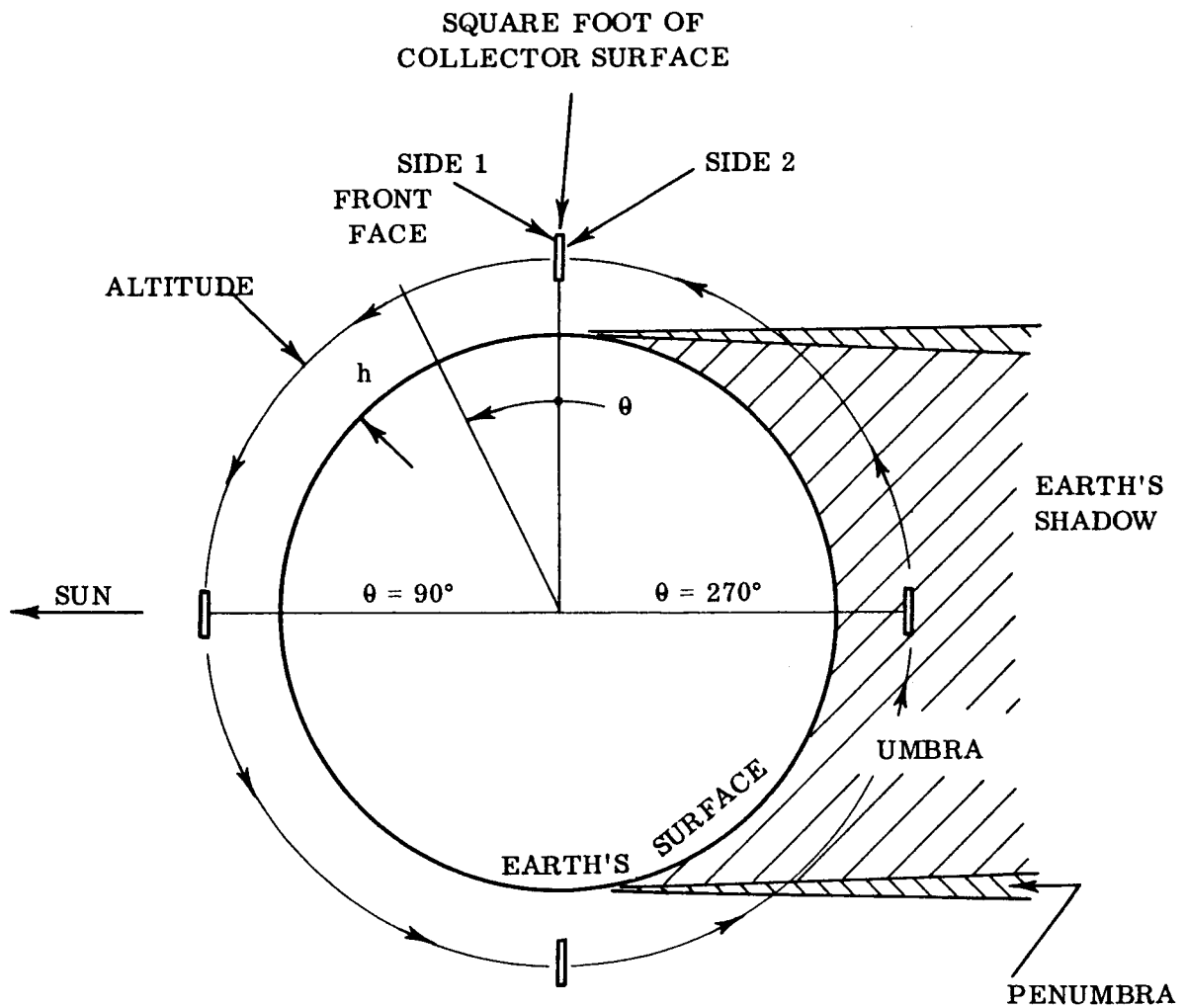


FIGURE 4.2-6

TRANSIENT TEMPERATURE CHARACTERISTICS, ORIGINAL CONCEPT

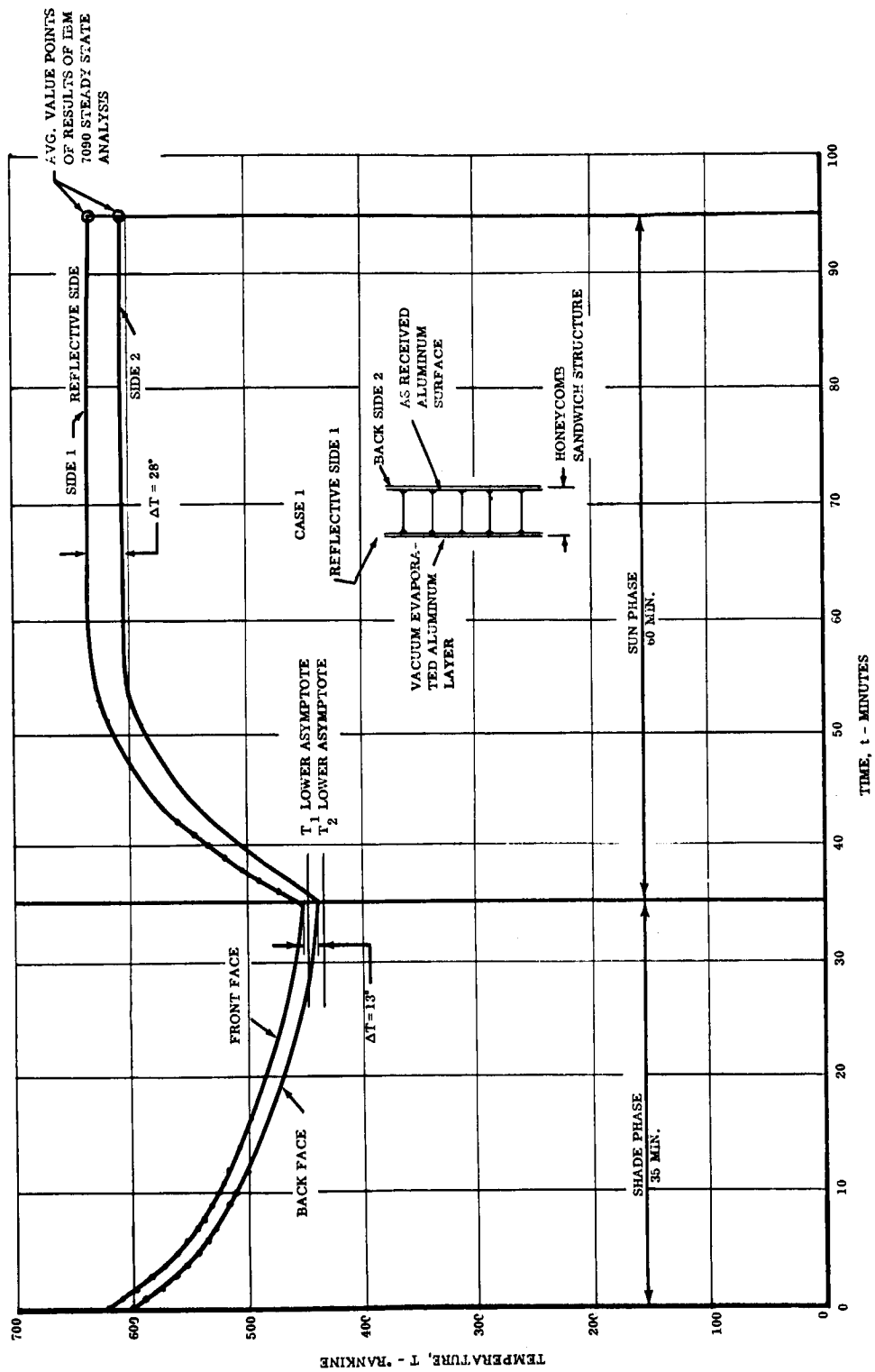


FIGURE 4.2-7

TRANSIENT TEMPERATURE CHARACTERISTICS THERMAL CONTROL DESIGN

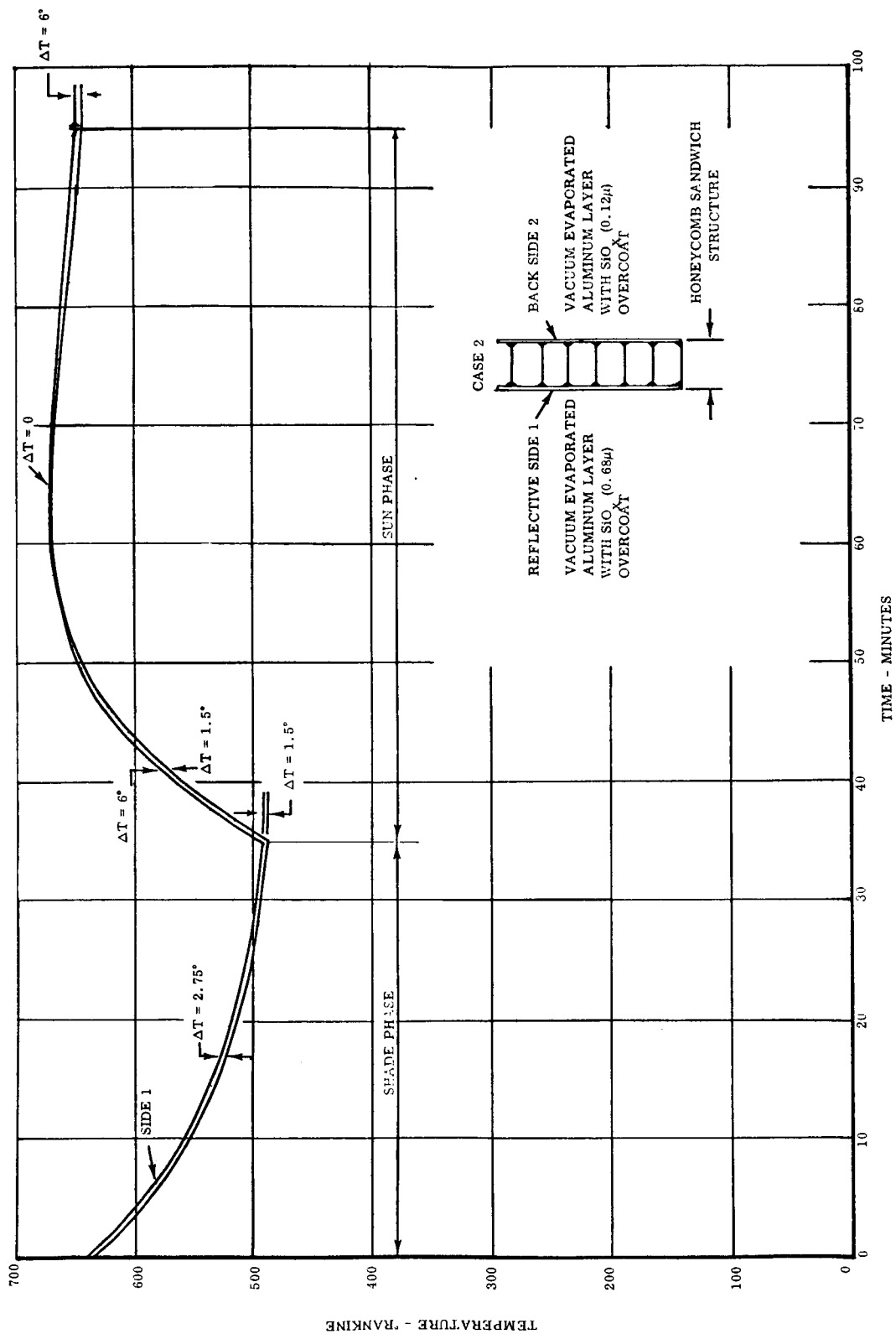


FIGURE 4.2-8

silicon oxide layer on the front face of the collector increases the emissivity of thermal radiation in the 0° to 200°F temperature range. Therefore, any energy absorbed on the front face will have an increased tendency to be reradiated from that face rather than being transferred to the back side for radiation, thus minimizing the ΔT . This thermal control concept will be discussed further in Section 4.2.5.6.

Transient characteristics which were calculated for other material and surface combinations are shown in Table 4.2-1. The heat transfer from front to back face of the collector material was considered in these heat balance calculations. Values of appropriate thermal conductivity were obtained experimentally for various combinations of materials and fabrication techniques. A description of this testing and results will be presented in Section 4.2.5.5.

4.2.5.2 Steady State Temperature Gradients

Figure 4.2-7 shows that, in general, the transient curve has two extreme points—one at the beginning of the sun period and one at the end. Therefore, the Sunflower system thermal map was computed for the approximate steady state conditions at the beginning and end of the sun period of the orbit.¹¹

Each component of the system is represented by a network of descriptive steady-state energy balance equations based on nodal points. A three-dimensional network is used in analyzing the collector, thus including the radial and circumferential temperature gradients as well as the temperature difference through the thickness of the honeycomb sandwich material. Due to the symmetry of irradiation and view factors, an analysis model of only one-half of the collector was established.

The primary energy inputs and factors contributing to temperature gradients in the solar collector are:

- a. Absorbed energy from the sun varying with the ratio of the incremental projected normal area to the actual surface area due to the dished shape.
- b. Directly absorbed energy of the earth's albedo, including the varying view factors from points on the collector to the earth's illuminated portion.
- c. Thermal radiation from the earth to the collector, including the varying view factor from points on the collector to the entire earth.
- d. Infra-red diffuse energy emission and reflection to other components of the system and appropriate view factors.
- e. Energy emitted from the boiler cavity to the collector, including varying view factor.

TABLE 4. 2-1

TRANSIENT HEAT BALANCE CHARACTERISTICS

Case	Radiation Coefficients		Calculated Results			
	Side 1 Surface Treatment	Side 2 Surface Treatment	θ Degree	ΔT °F	T_1 °F	T_4 °F
1 Originally Proposed Material	Vacuum evaporated aluminum overcoated with SiO_x approx. 0.12μ thick ($\epsilon = 0.05$) ($\alpha = 0.10$)	As received surface of aluminum foil ($\epsilon = 0.2$) ($\alpha = 0.2$)	0 90 270	24 28 14	80 172 10	56 144 -4
2 Desired Thermal Control Design	Vacuum evaporated aluminum overcoated with SiO_x of about 0.68μ thickness ($\epsilon = 0.2$) ($\alpha = 0.12$)	Vacuum evaporated aluminum overcoated with SiO_x of about 0.12μ thickness ($\epsilon = 0.05$) ($\alpha = 0.2$)	0 90 270	6.0 0 2.75	120 210 71	114 210 68.25
3	Vacuum evaporated aluminum overcoated with SiO_x of approx. 0.72μ thickness ($\epsilon = 0.22$) ($\alpha = 0.12$)	Same as Case 2 above ($\epsilon = 0.05$) ($\alpha = 0.2$)	0 90 270	11.4 -1.7 5.5	171.5 193.3 55	160.1 195 49.5
4	Vacuum evaporated aluminum overcoated with SiO_x of approx. 3 to 6μ thickness ($\epsilon = 0.5$) ($\alpha = 0.12$)	Vacuum evaporated aluminum back face with 4 thickness radiation barrier over back face ($\epsilon = 0.0056$) ($\alpha = 0.2$)	0 90 270	0.7 1.3 0.6	72.7 70.0 47.6	72.0 68.7 46.9
5	Same as 4 above ($\epsilon = 0.5$) ($\alpha = 0.12$)	As received surface of aluminum foil ($\epsilon = 0.2$) ($\alpha = 0.2$)	0	15.0	47.0	32.0
6	Vacuum evaporated aluminum overcoated with SiO_x of about 0.12μ thickness ($\epsilon = 0.05$) ($\alpha = 0.10$)	Vacuum evaporated aluminum overcoated with SiO_x of about 0.12μ thickness ($\epsilon = 0.05$) ($\alpha = 0.10$)	0	18.8	282.0	263.2
7	Same as 4 above ($\epsilon = 0.5$) ($\alpha = 0.12$)	Vacuum evaporated aluminum overcoated with SiO_x of about 3 to 6μ thickness ($\epsilon = 0.5$) ($\alpha = 0.2$)	0	22.5	11.0	-11.5

- f. Energy emitted from the boiler control doors and bottom face.
- g. Conduction through the sector thickness and along the skins.

Again, the experimental results for thermal conductivity were used in the computations. (See Section 4.2.5.5.)

The collector will achieve an equilibrium temperature so that all absorbed energy is reradiated to space. Solution of the steady-state energy balance equations was accomplished on an IBM 7090 digital computer. Results for the collector portion of the Sunflower system are shown in Figures 4.2-9 and 4.2-10 for the two extreme points mentioned previously. Resulting ΔT 's through the thickness of the collector material are shown in Figures 4.2-11 and 4.2-12. These calculations were based on the heat transfer characteristics of the originally proposed honeycomb material.

The average values of the steady-state computer solution are shown in Figure 4.2-7 for comparison with the transient solution. Note the excellent correlation even though no geometry considerations exist in the transient analysis.

4.2.5.3 Thermoelastic Structural Analysis

The maximum thermal gradients of the originally proposed structural material were presented in Figures 4.2-9 and 4.2-11. To analyze the thermal distortions and associated optical errors caused by these temperature gradients, a structural analysis of the Sunflower collector was made.

Analysis Model Description

The analysis model of the paraboloidal collector utilized two major idealizations:

- a. The composite sandwich material (see Figure 4.2-5 (a)) is idealized as a homogenous plate with special properties.
- b. These plates are further idealized as a gridwork of beams having elastic properties which simulate the continuous plate.

The first idealization was necessary due to the extreme lightweight of the composite material and the nature of the thermal gradient through the thickness (see Figure 4.2-5 (a)). This gradient is caused by the low thermal conductivity of the adhesive bond and results in a reduced coefficient of thermal expansion for the composite material when compared to an aluminum plate using a linear temperature drop and the classical approach of bending to a spherical shape. In other words, the thermal distortion of the honeycomb sandwich material was described by the use of an apparent coefficient of thermal expansion with a linear ΔT through the thickness. This apparent coefficient was obtained from tests of thermal distortion of sandwich material specimens which will be described in Section 4.2.5.5.

COLLECTOR TEMPERATURE GRADIENTS
AT THE END OF THE SUN PERIOD

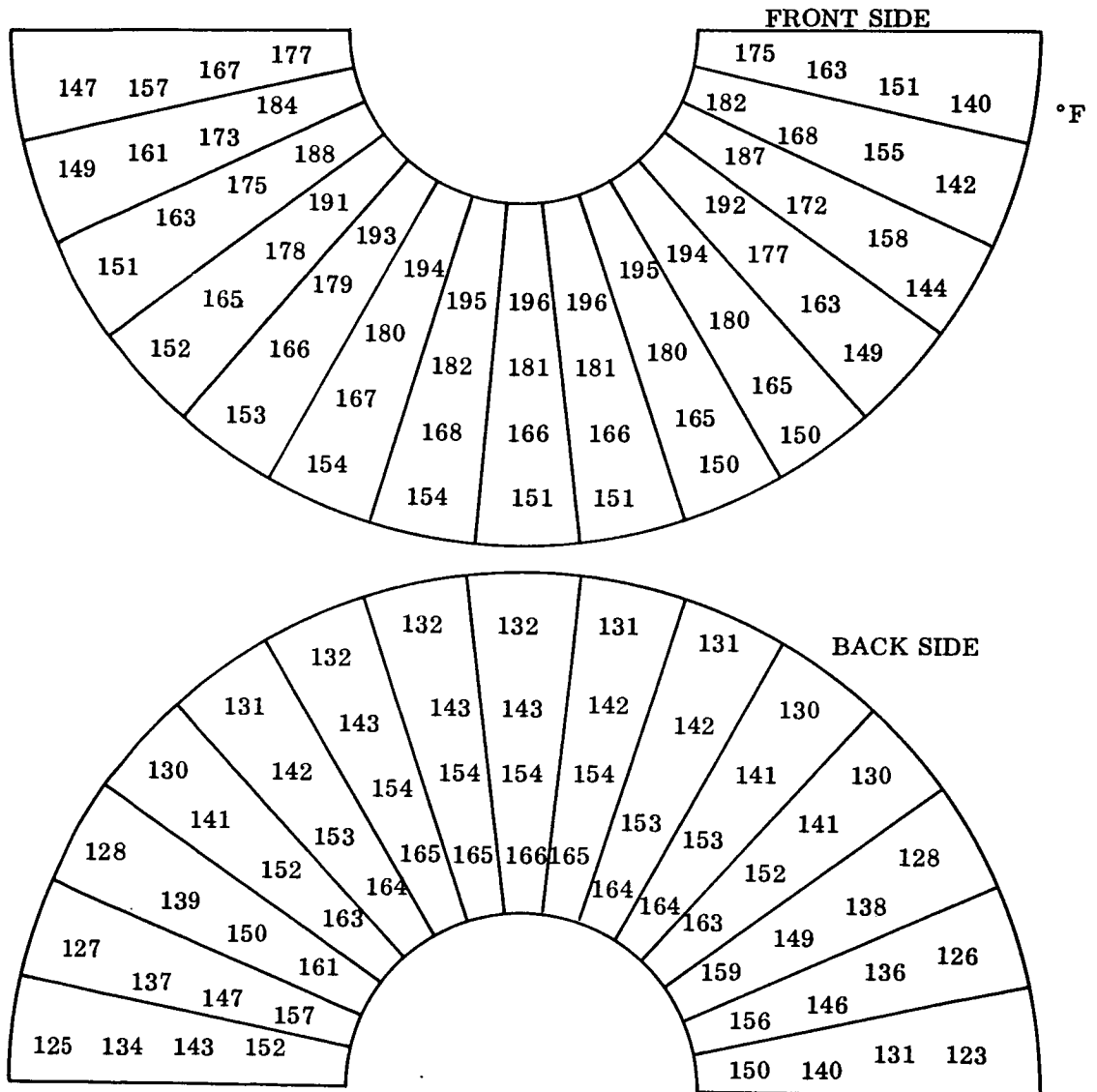


FIGURE 4. 2-9

COLLECTOR TEMPERATURE GRADIENTS AT THE BEGINNING OF THE SUN PERIOD

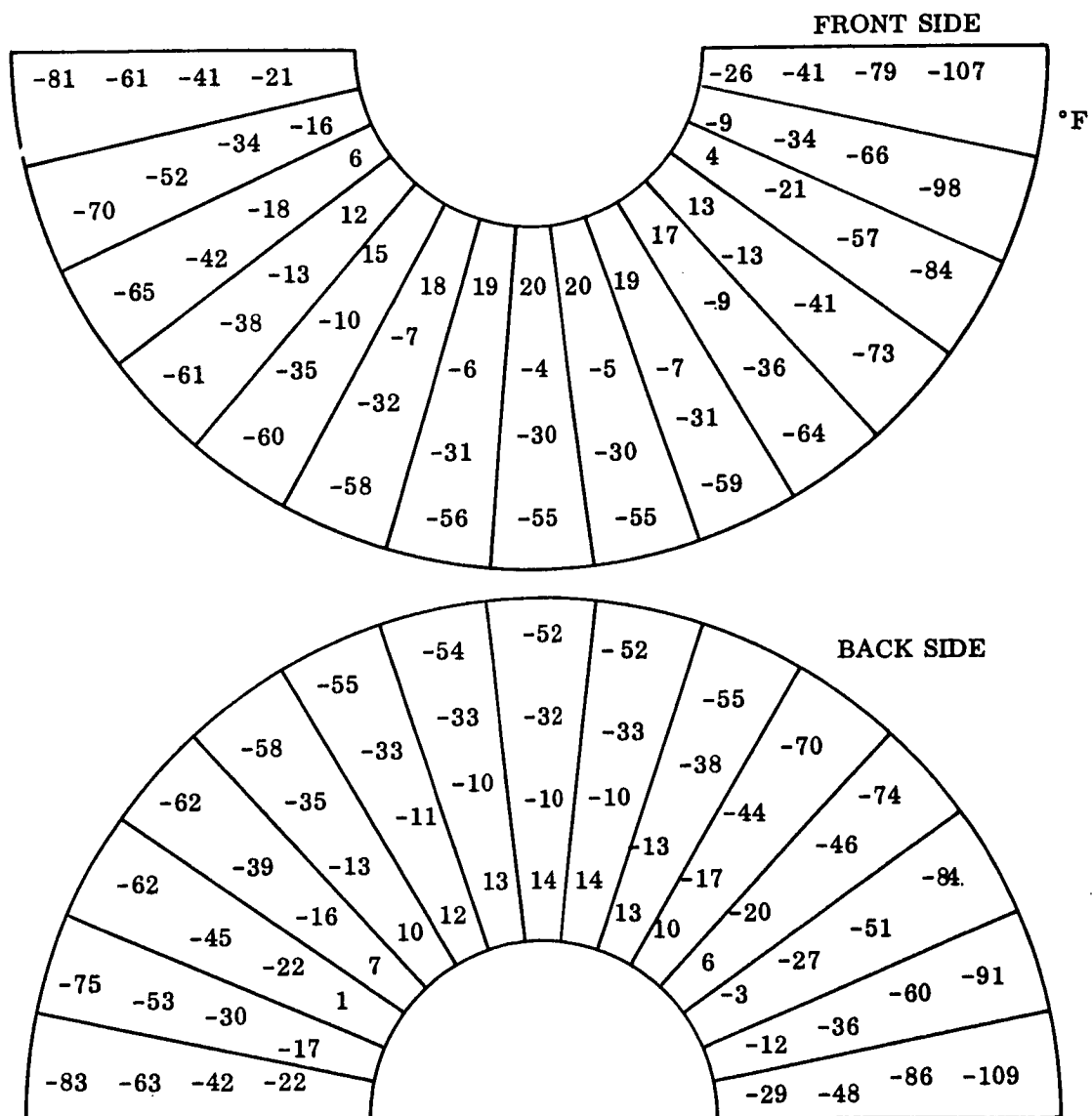


FIGURE 4.2-10

COLLECTOR AT THROUGH THE THICKNESS
AT THE END OF THE SUN PERIOD

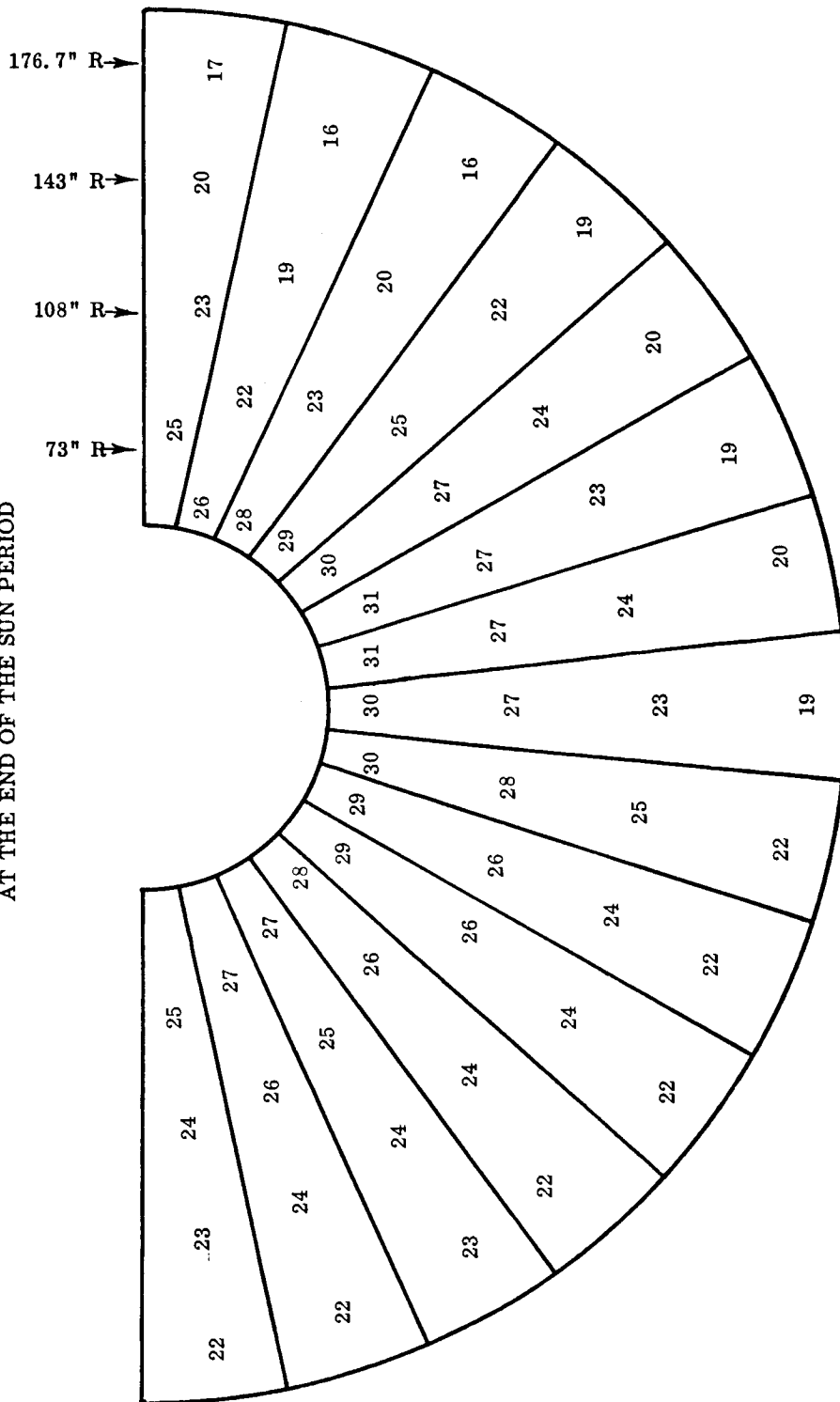


FIGURE 4. 2-11

COLLECTOR ΔT THROUGH THE THICKNESS
AT THE BEGINNING OF THE SUN PERIOD OF ORBIT

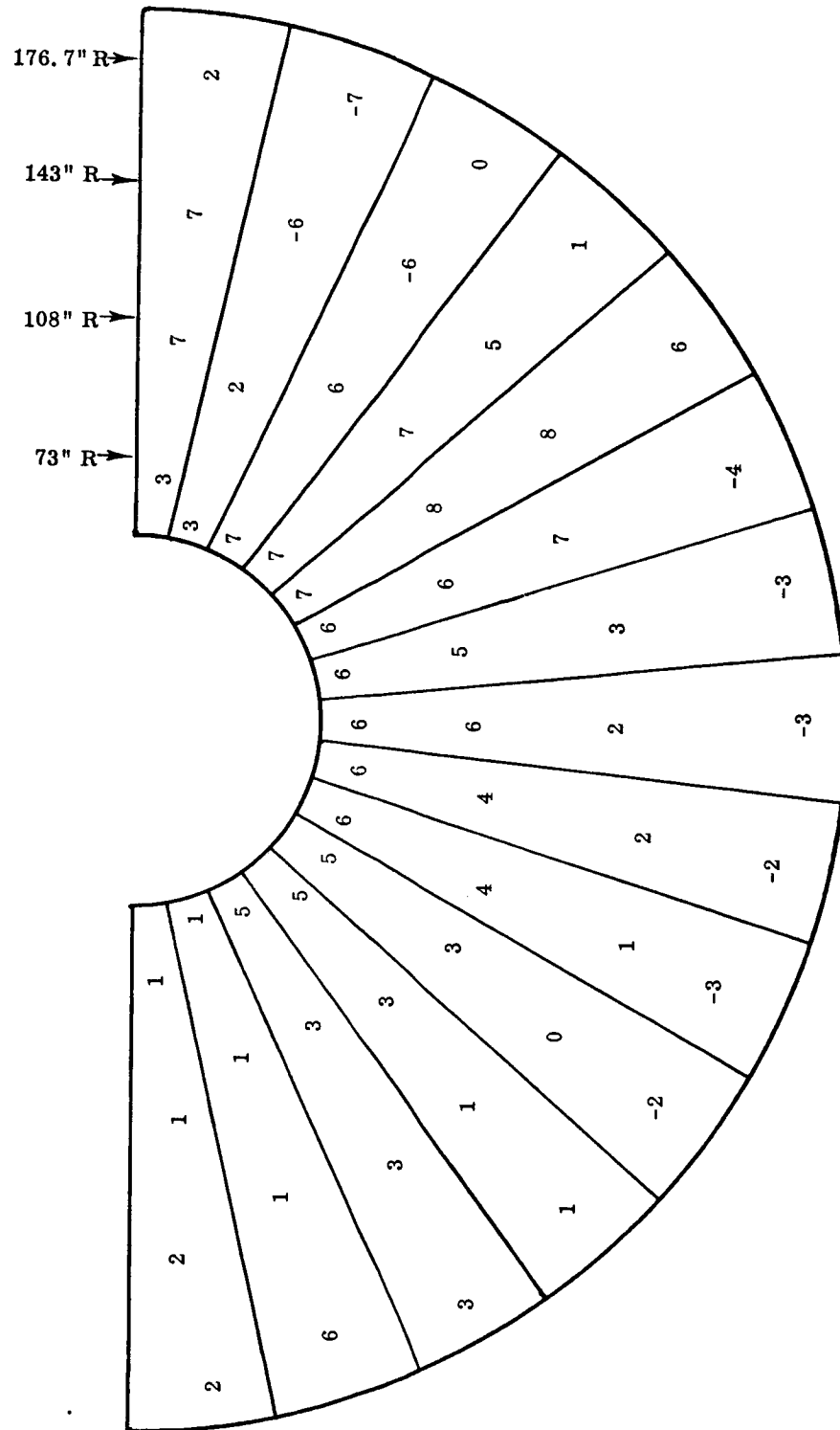


FIGURE 4.2-12

The second idealization is made to allow solution of the problem by digital computation using established general structural analysis computer programs.⁵ Essentially, the continuous material of the elastic body is replaced by a three-dimensional gridwork of equivalent straight elastic beams and diagonal members interconnected at joints called nodal points.

A further description of the idealized structural model is presented in TRW ER 5028¹⁹.

Since the collector is composed of 30 sectors, both a single sector and a quadrant of the collector were programmed for solution. The quadrant was selected since ΔT 's are approximately symmetrical on a quadrant basis. The equations representing the mathematical model were formulated by a stiffness matrix approach based upon small deflection theory. These equations were automatically formed and solved in terms of deflections at nodal points and constraint forces using General Dynamics/Electric Boat Division's IBM 704 general structural analysis computer program.

Thermoelastic Analysis Results

Computed results for thermal distortion modes are shown in Figure 4.2-13 for the various cases which were investigated. Before presenting the effects of these distortions on optical performance, the structural analysis will be discussed further.

As a check on the accuracy of the analysis model, solutions for the dead weight deflection of the collector were computed for comparison with measured data obtained from developmental testing of the full scale preprototype collector (see Section 8.3.1). Results of these comparisons are shown in Table 4.2-2 and Figure 4.2-14. Reactions and stresses were obtained from strain gage measurements during dead weight testing. It can be seen that reasonable correlation is obtained except for the compressive stress in the upper skin.

TABLE 4.2-2
COMPUTED VS MEASURED REACTIONS AND STRESSES

	Computed IBM 704	Measured Preprototype COL II-2
Rim Lock Constraints		
Force	49.3 lb	50 lb
Moments	15.8 in-lb	13.7 in-lb
Stresses		
Upper Skin	4500 psi (compressive)	1285 psi (compressive)
Lower Skin	3600 psi (tensile)	3210 psi (tensile)

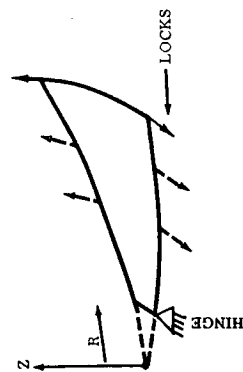
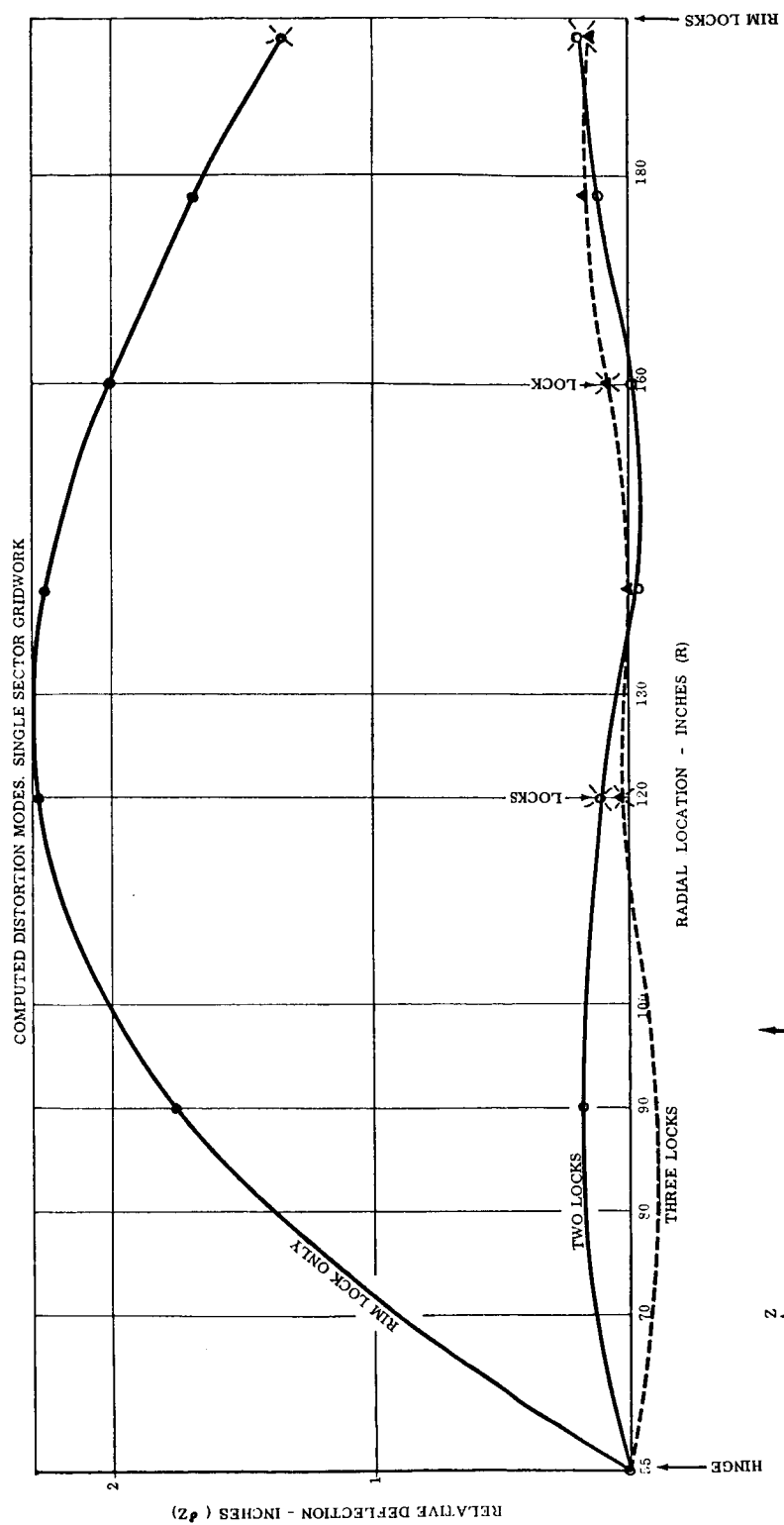


FIGURE 4.2-13

COMPUTED VS. MEASURED DEAD WEIGHT DEFLECTION

Δ - COMPUTED - IBM 704
 O - MEASURED - PREPROTOTYPE COLLECTOR

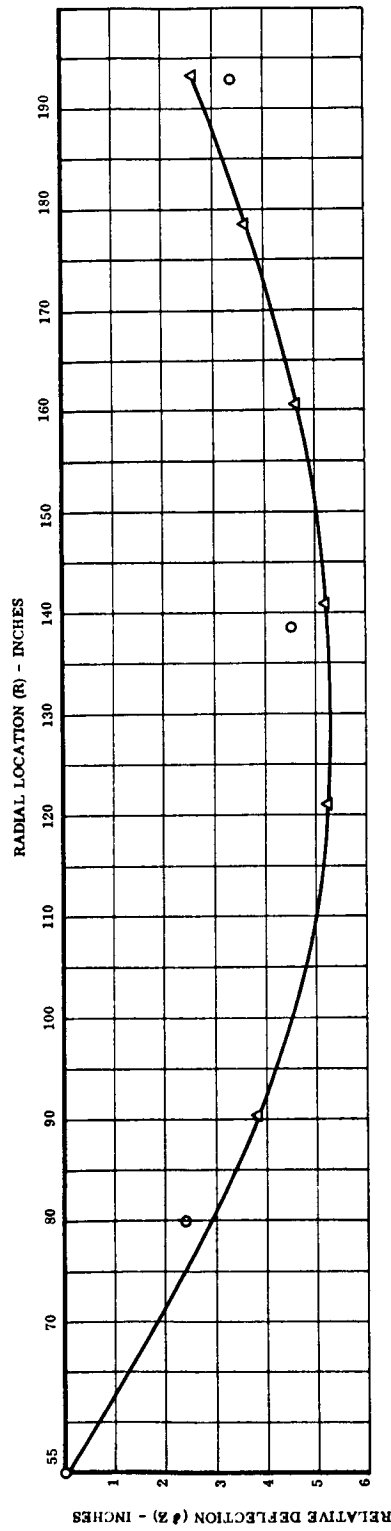


FIGURE 4.2-14

The originally proposed locking arrangement provided for locks only at the rim for simplicity and increased reliability. However, it can be seen in Figure 4.2-13 that excessive thermal distortion results. Considerable increased restraint is obtained from the cases of one and two additional locking points. Comparison of the optical errors associated with each case will also be discussed in Section 4.2.5.4.

The structural analysis model of a quadrant of the collector was established to investigate the effects of the circumferential gradients (see Figures 4.2-9 and 4.2-11). However, the computer results of the thermal analysis of the quadrant model are considered to be inaccurate. The conditions of static equilibrium and the boundary conditions specified at the points of constraint were not completely satisfied. The unsatisfactory solutions of the quadrant analysis are due mainly to the inherent flexibility of the structure, the mechanics of the procedure used to form the equilibrium equations, and the round-off errors due to the numerical process. Corrections to the program were not attempted at this time. However, comparison of solutions of the quadrant model for the case of no circumferential gradient versus the gradient shown in Figure 4.2-11 showed similar deflections within 0.050 inches for the single lock case. This indicates, as might be expected, that the primary distorting gradient is through the thickness of the honeycomb sandwich material.

Further structural analysis results are presented by Aldrich, Kiritis, and Bond¹.

4.2.5.4 Effects of Thermal Distortion on Optical Performance

Figure 4.2-13 shows that the various methods of constraint result in different deviations. To relate these deviations to optical quality, radial surface rotations from the true paraboloid are plotted in Figure 4.2-15 as a function of radial location. These rotations were calculated directly by the structural analysis computer program. From this information, a measure of the optical quality of a geometrically perfect collector which is thermoelastically distorted can be obtained by relating surface area to surface deviations. Figure 4.2-16 shows the percentage of collector surface area which is within various degrees of optical quality. The improvement in quality obtained with increased restraint is apparent. One curve is an extrapolation of computed results for the improved thermal control design indicated in Figure 4.2-8.

Circumferential deviations were also computed in the structural analysis; however, they are small deviations which would add a maximum of one-half minute to the absolute deviation.

To determine the effect of thermal distortion on collector overall efficiency, it must be remembered that this surface deviation is only one of the many factors which enter into the overall optical performance. Comparison and summation of all types of errors will be presented in Section 7.4. Also important is that these thermal distortions will vary from zero to the maximum during the sun portion of the orbit as the ΔT varies from zero to 6°F (see Figure 4.2-8).

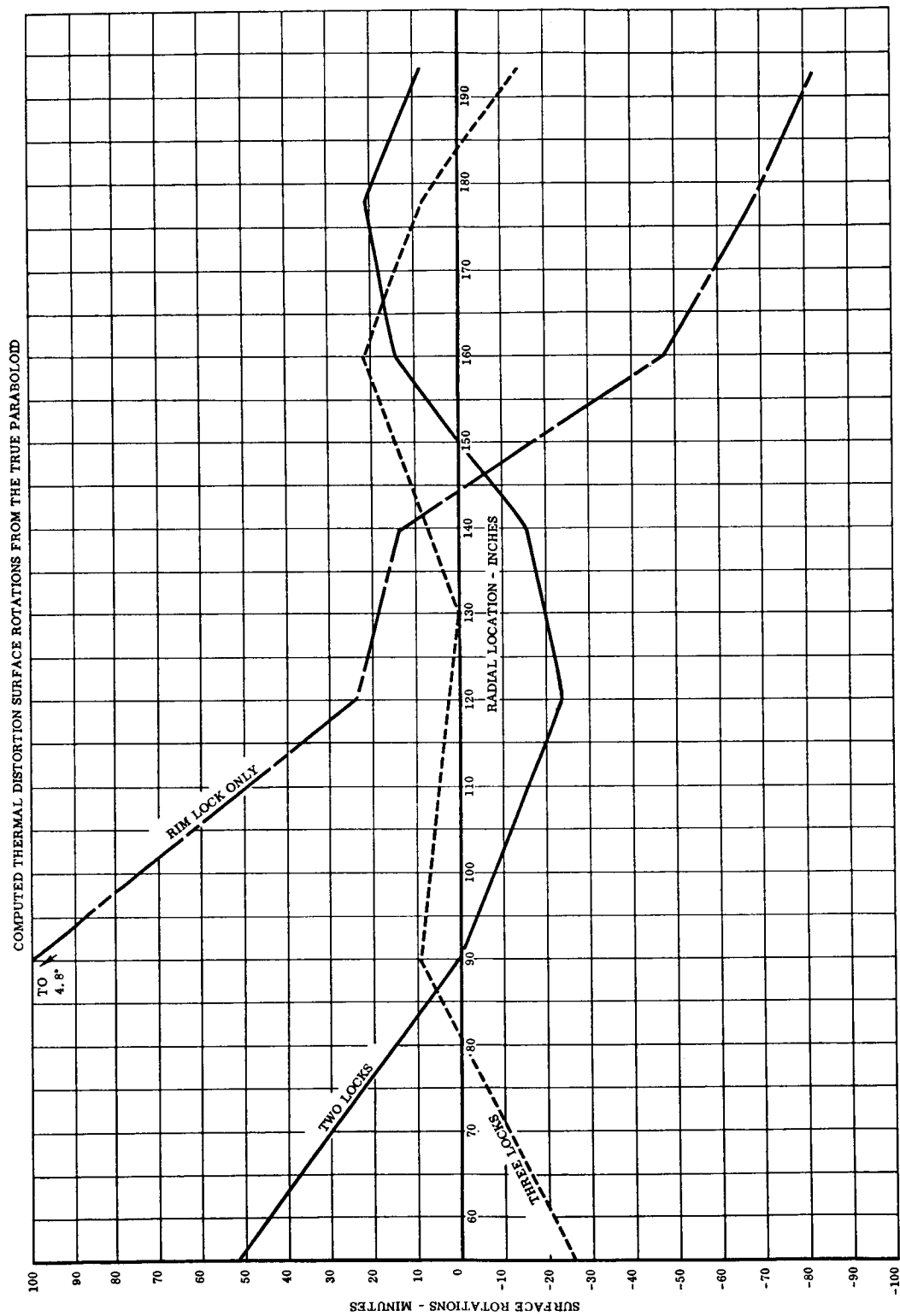


FIGURE 4.2-15

OPTICAL QUALITY OF THERMALLY
DISTORTED COLLECTOR

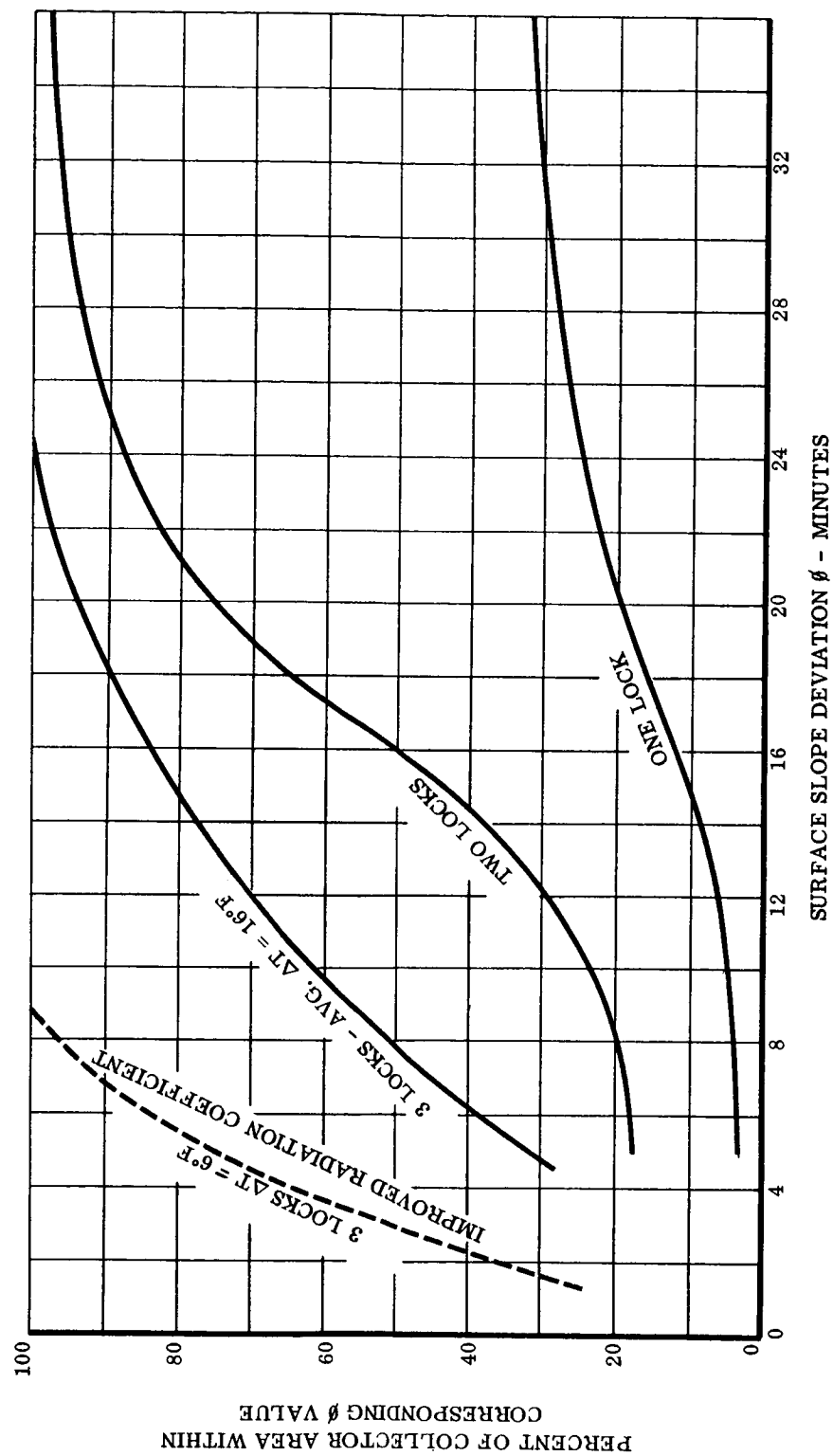


FIGURE 4.2-16

4.2.5.5 Thermal Environment Investigation Supporting Tests Description and Results

To obtain pertinent information regarding thermal distortion of the Sunflower solar collector, testing on a small specimen basis was accomplished. Test facilities for the following areas of investigation were designed, built, and utilized.

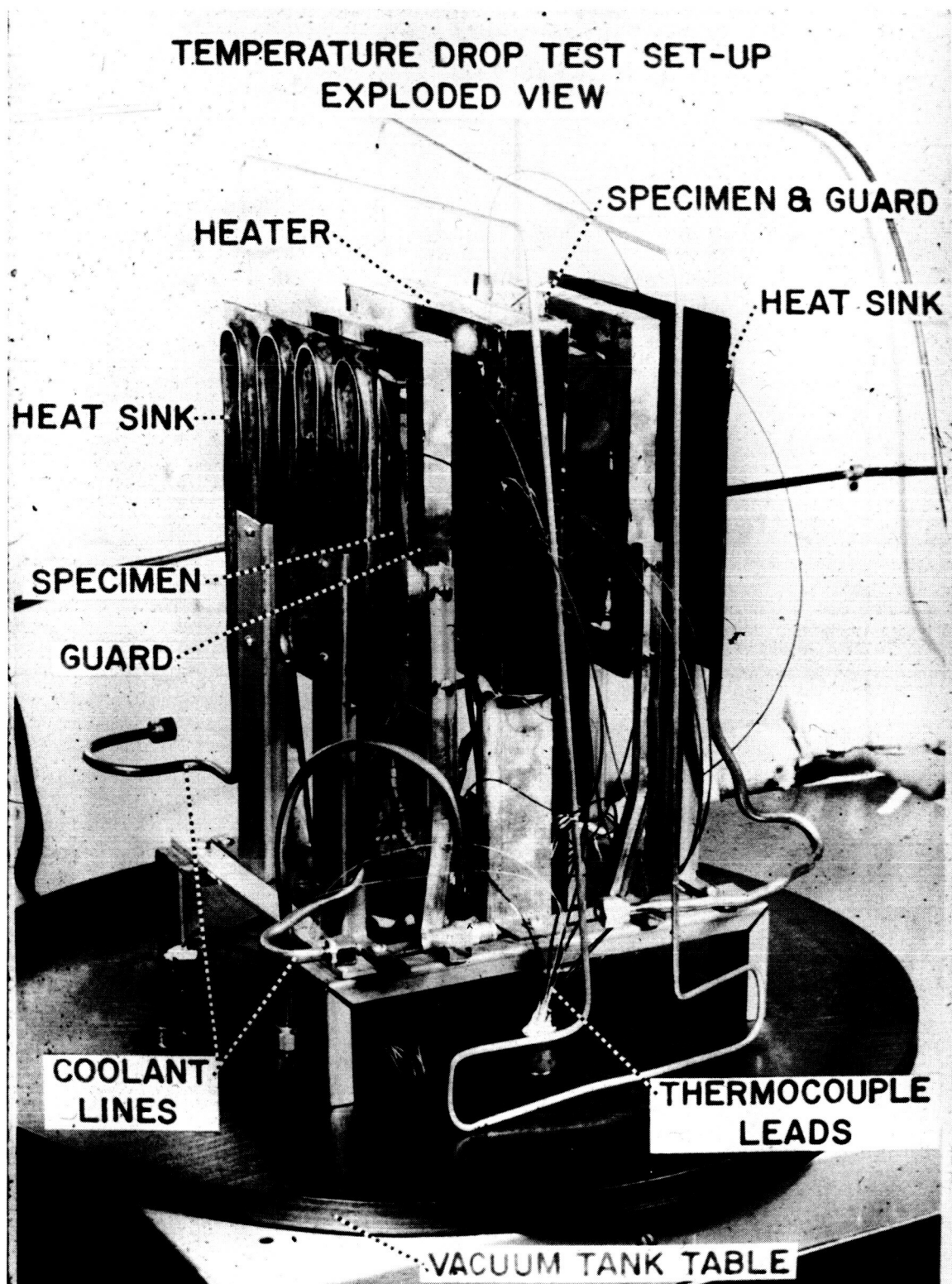
- a. Honeycomb sandwich composite material heat transfer tests.
- b. Adhesive thermal conductivity tests.
- c. Composite material thermoelastic distortion tests.
- d. Mechanical testing.

Composite Material Heat Transfer Tests

The composite sandwich material heat transfer tests were accomplished on the test set-up shown in Figure 4.2-17. Specimens, five and one-half inches square, are mounted on each side of a guarded hot plate type electrical resistance heat source. The heat sinks consist of water or liquid nitrogen-cooled copper plates. This arrangement provides a controlled temperature differential across the specimen thickness as well as insuring that all the measured electrical input energy passes through the specimens. Iron-constantan thermocouples were used to measure temperature levels and differentials. The entire set-up is enclosed in an 18 inch bell jar vacuum chamber and tests were conducted in the 10^{-5} mm mercury vacuum range. General results of this series of tests is shown in Figure 4.2-18. This information was used in the heat balance calculations of Section 4.2.5.1. Comparison of results will be discussed in Section 4.2.5.6.

Adhesive Thermal Conductivity Tests

Figure 4.2-18 shows that one of the important parameters in the thermal characteristics of the collector material is the conductivity of the adhesive used in the bonding process. To investigate this parameter, the adhesive thermal conductivity test rig shown in Figure 4.2-19 was designed and built. The test set-up utilized two bars of aluminum, with a known thermal conductivity, which are bonded together with the adhesive being tested. An electrical resistance heat source is used to heat one end while the other end is water-cooled. The entire assembly is insulated and iron-constantan thermocouples are used to measure temperatures. With this arrangement, the known thermal conductivity of the aluminum bars gives the heat rate passing through the adhesive; an accurate extrapolation to the temperature at the bonded interfaces is also obtained. Results for the various adhesive systems which were tested are shown in Table 4.2-3. Although K is given in standard units, it is made up of the actual conductivity of the test specimen plus the effect of the two bond interfaces. Depending upon the thickness of the test material and the relative effect of the interface resistance, K could vary significantly. However, the results were used as a guide for the selection of adhesives to be used in honeycomb sandwich material bonded assemblies for other testing.



TEMPERATURE DROP TEST SET-UP EXPLODED VIEW

FIGURE 4.2-17

COMPOSITE MATERIALS HEAT TRANSFER RESULTS

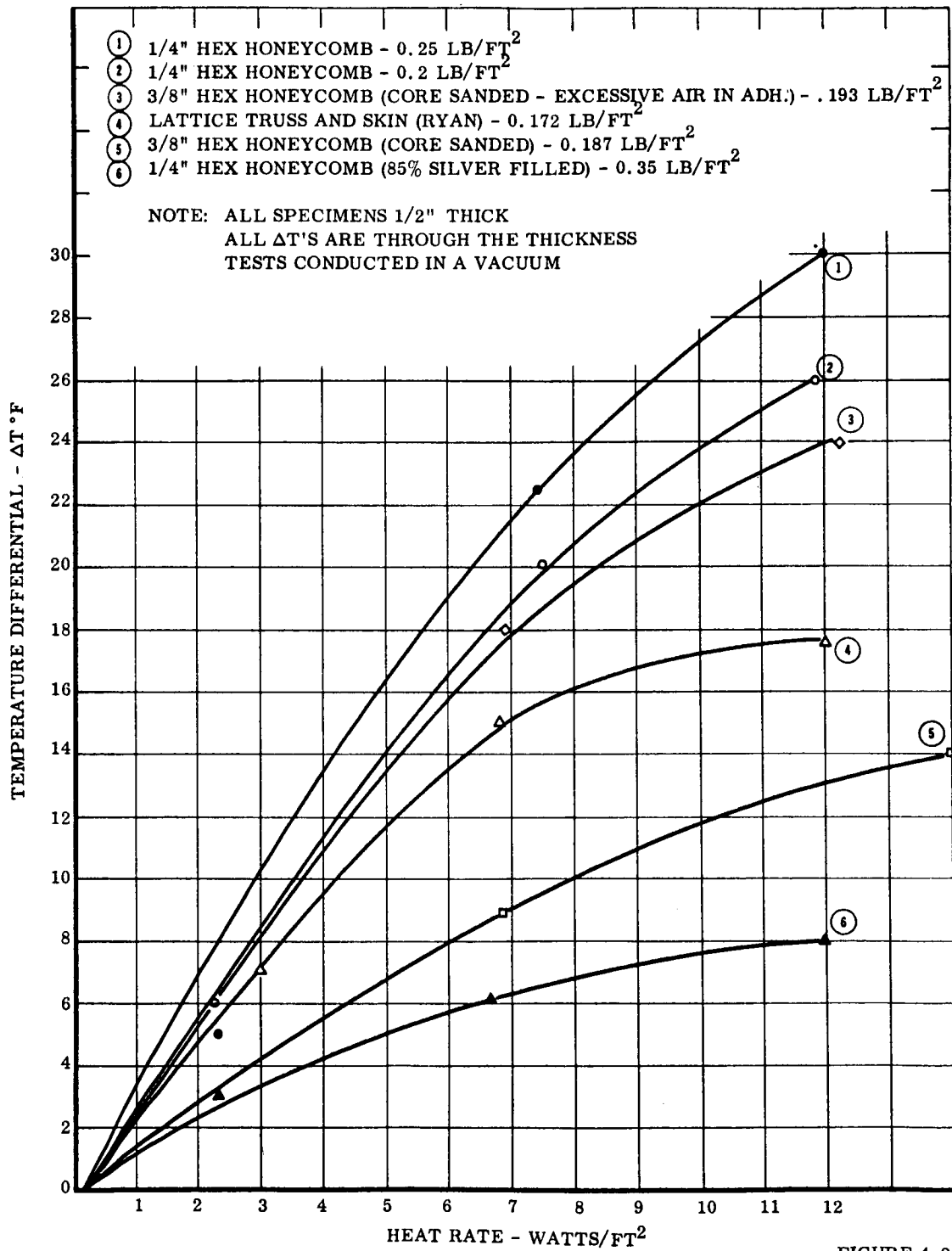
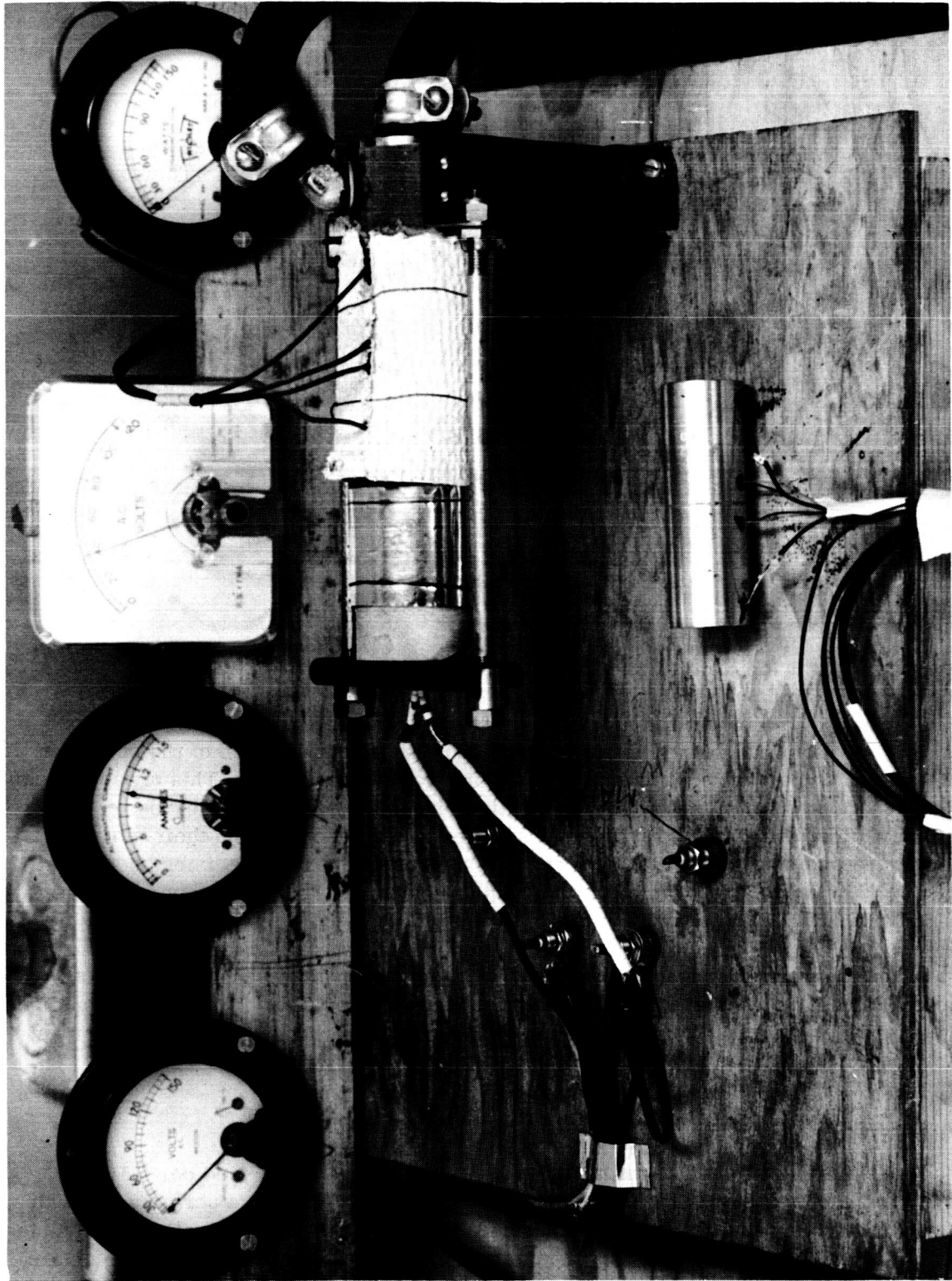


FIGURE 4.2-18



ADHESIVE THERMAL CONDUCTIVITY TEST RIG

TABLE 4.2-3
ADHESIVE THERMAL CONDUCTIVITY TEST RESULTS

Adhesive System	K	Specimen Bond Thickness Inches
Plain epoxy (Bondmaster 688)	0.14	0.018
Epoxy with 70% by weight Ag	0.34	0.028
Epoxy with 80% by weight Ag	0.45	0.011
Epoxy with 85% by weight Ag	0.51	0.009
Epoxy with A1 filler (Raymond R-86002)	0.29	0.006
Epoxide based adhesive (Eccobond 57C)	1.10	0.120

Note: "K" is the thermal conductivity in Btu/hr-ft²-°F-ft

Composite Material Thermal Distortion Tests

Honeycomb sandwich composite material thermoelastic distortion testing was accomplished on the rig shown in Figures 4.2-20, 4.2-21, and 4.2-22. This test set-up consists of a mount for holding the test sample in a vertical position attached only at the bottom end. An electrical heater is used to heat one face of the specimen with a water cooled copper plate as the heat sink for the back face. This arrangement provides a controlled temperature differential across the specimen thickness. To observe deflections, optical targets are attached to the specimen and their movement is observed and measured with a micrometer microscope. The specimen, heaters, and cold plate are enclosed in a specially built vacuum chamber and tests are conducted in a high vacuum.

Typical results are shown in Figure 4.2-23 for the prototypical sandwich material. These test results were used to calculate an apparent coefficient of thermal expansion of the sandwich material for the thermoelastic structural analysis of the collector as mentioned previously in Section 4.2.5.3.

Composite Material Mechanical Testing

Mechanical testing of the composite sandwich material was performed per MIL-STD 401 A for short beam specimens. Also, long plate beam tests were performed. Values for flexural rigidity and shear modulus were obtained and correlated well with formulas given in MIL-STD 401 A. These values were used in the structural analysis to define the elastic characteristics of the sandwich material.

SANDWICH MATERIAL THERMAL DISTORTION TEST SCHEMATIC

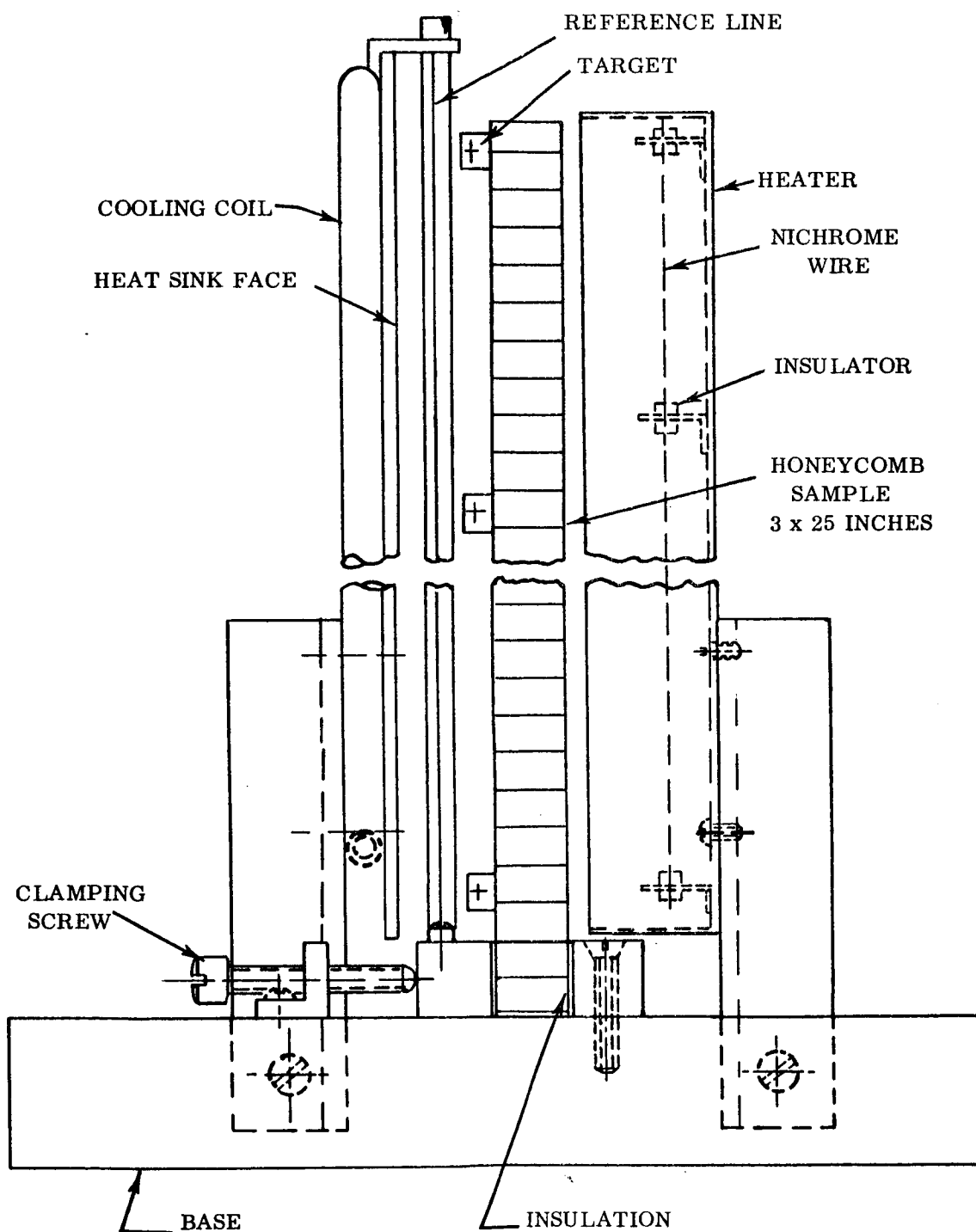
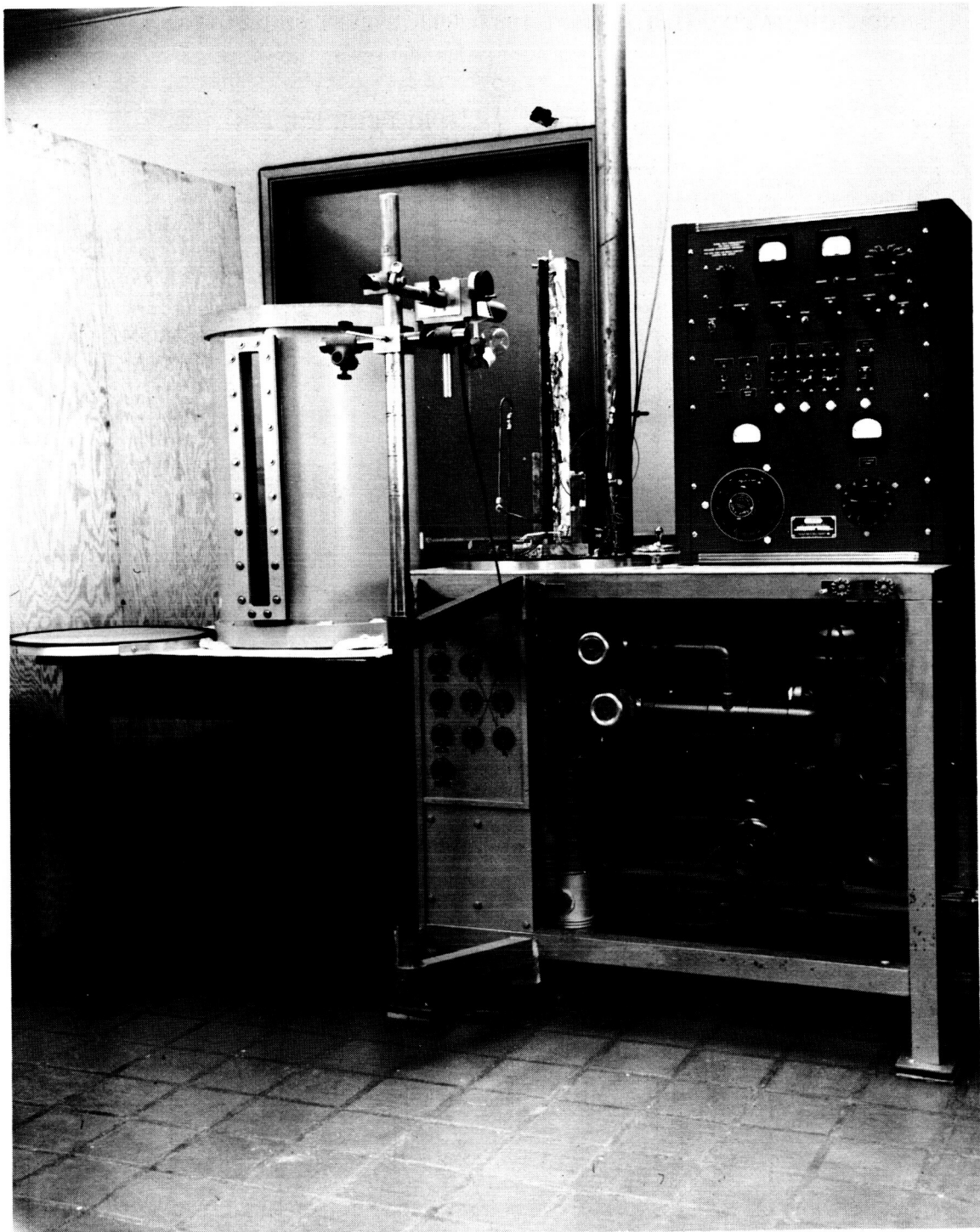


FIGURE 4. 2-20



SANDWICH MATERIAL THERMAL DISTORTION TEST RIG GENERAL VIEW

FIGURE 4. 2-21



SANDWICH MATERIAL THERMAL DISTORTION TEST RIG SPECIMEN VIEW

FIGURE 4. 2-22

TEST I
RIBBON PERPENDICULAR TO LENGTH
DEFLECTION VS LENGTH AND
DEFLECTION VS ΔT

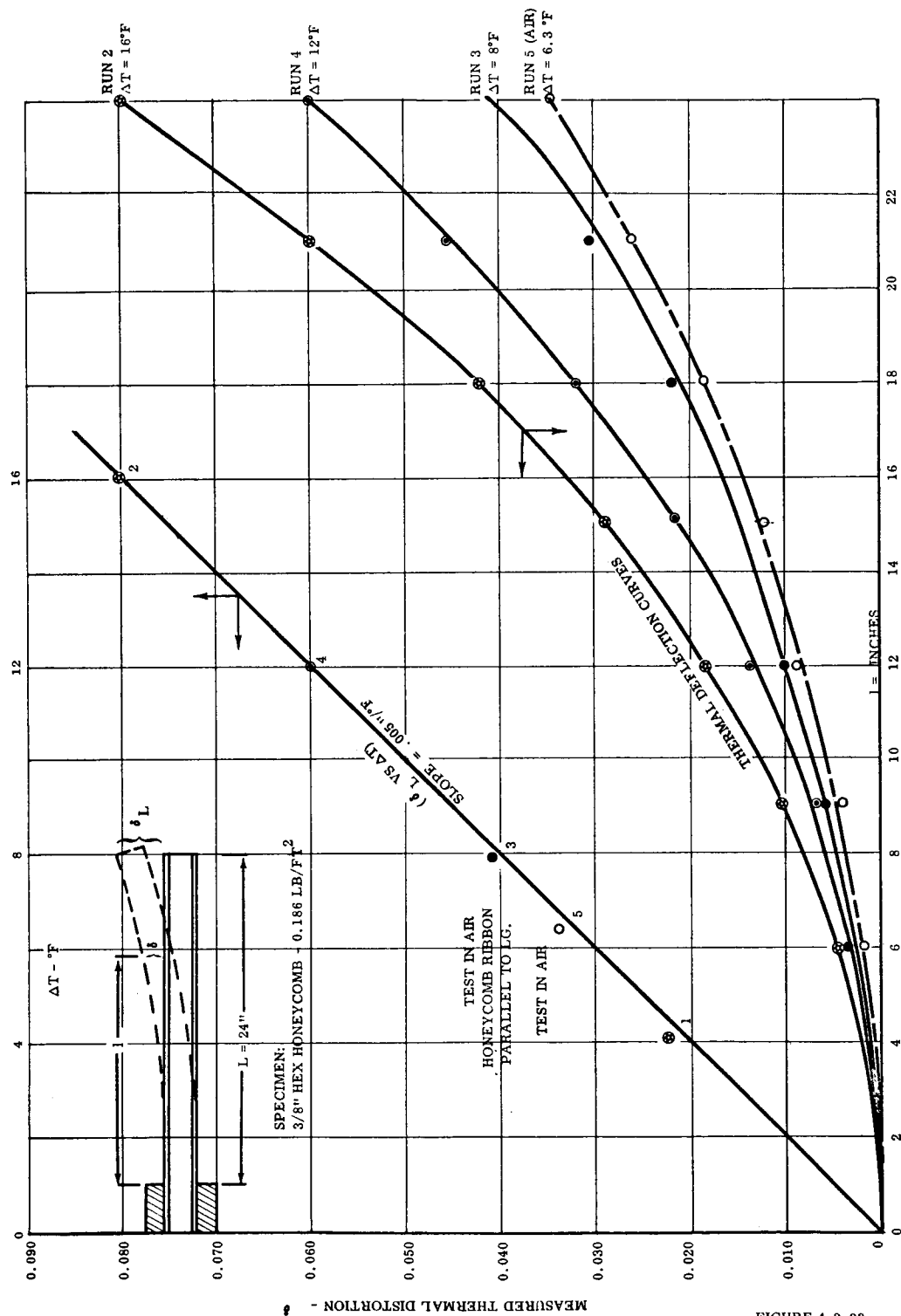


FIGURE 4.2-23

4.2.5.6 Summary of Thermal Distortion Control Concepts and Associated Design Consideration for the Sunflower Solar Collector

The following are the primary parameters which affect the thermal distortion characteristics of the solar collector:

- a. Radiation coefficients: α and ϵ
- b. Thermal conductivity through the sandwich material thickness.
- c. Structural stiffness of the collector assembly.

It is seen in the presentation of the previous sections that various single parameters and combinations of these parameters have been investigated, resulting in varying degrees of distortion control. Associated with these concepts of control are weight increases for the solar collector. Based on the overall results of the thermal control investigations, the comparison shown in Figure 4.2-24 was calculated. Case "C" accomplishes a high degree of thermal distortion control with a minimum of additional weight; for this reason, it has been selected as the thermoelastic design concept for the Sunflower collector. This concept involves the following three design areas:

- a. Three rows of locking points around the collector to restrain distortion.
- b. Fabrication and process control of factors affecting thermal conductivity of the sandwich material.
- c. Selective radiation film applications to the front and back surfaces of the collector to improve radiation characteristics.

Front: 0.65 to 0.70 microns of silicon oxide (transparent).

Back: Reflective coated plus 0.12 microns of silicon oxide.

Three rows of locks reduce thermal distortions, as indicated in Figure 4.2-16; also, during other phases of environmental testing of the preprototype collector, it was established that three lock restraint is necessary for reasons other than thermal distortion. Environments of one "g" orbital transfer and vibration require the additional restraint to lower stress levels.

During thermal conductivity investigations for typical honeycomb sandwich material, it was found that conductivity is quite sensitive to the type and conditions of the adhesive, the geometry of the adhesive fillet, and the surface finish of the core material. Figure 4.2-18 showed the effects of some of these parameters as measured during thermal conductivity testing. By controlling the fillet uniformity, the mixing of the adhesive, and the surface finish of the core material, maximum conductivity is obtained.

THERMAL DISTORTION CONTROL CONCEPTS
WEIGHT COMPARISON

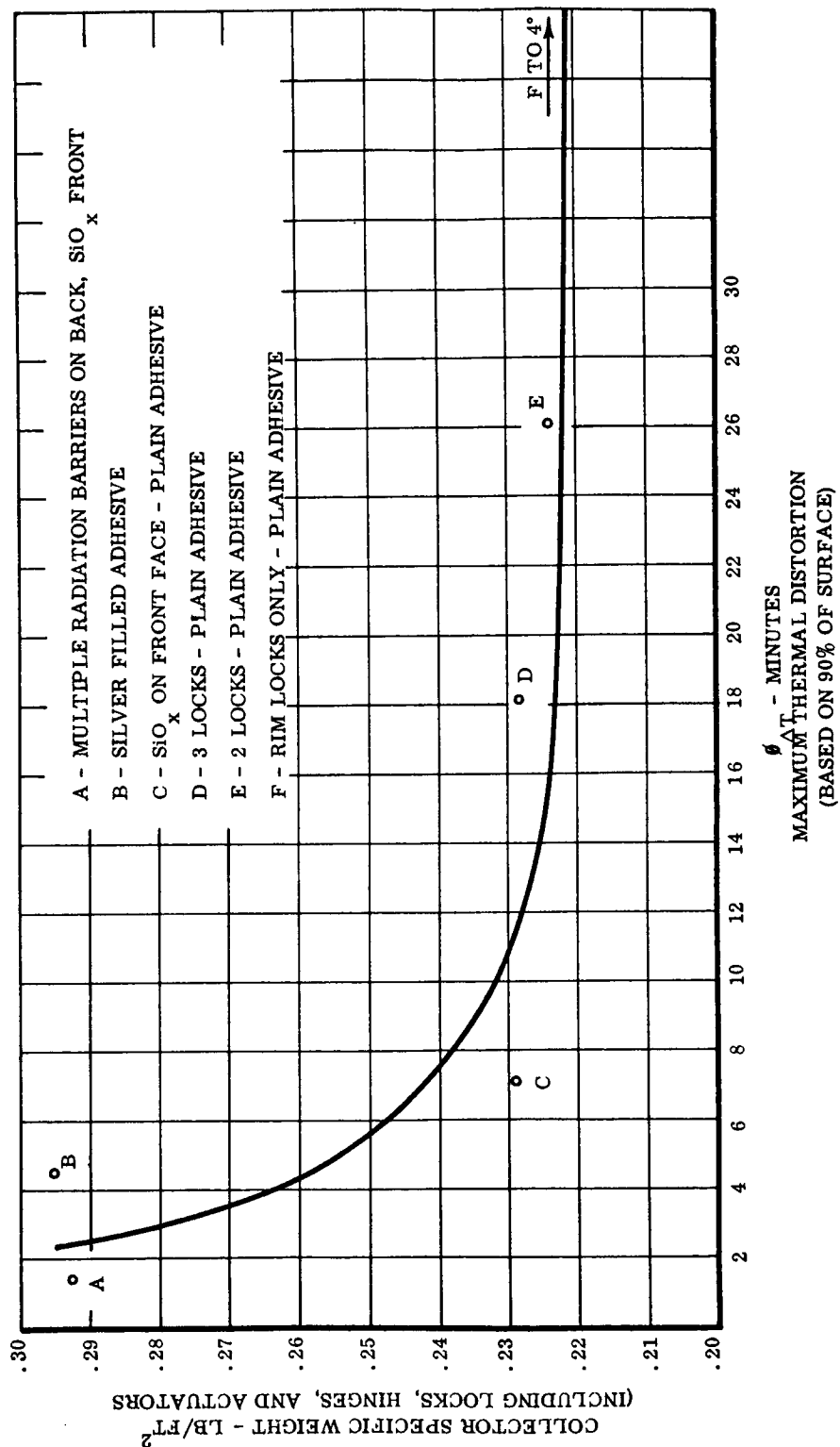


FIGURE 4.2-24

Radiation control films allow a large range of thermal control with a negligible increase in weight and a small loss in reflectivity. Use of these films has been adopted in the collector thermal control design, based on the available optical and thermal characteristics information in the literature.^{10, 25, 27} Further investigation is required concerning specific application to the Sunflower solar collector.

Should closer investigation of silicon oxide films eliminate their use, due to ultraviolet radiation degradation of optical and thermal characteristics, silver filled adhesives can be incorporated into the Sunflower solar collector design. With a more detailed investigation of the higher conductivity adhesives and their application to honeycomb sandwich materials, it is felt that specific weights in the neighborhood of 0.25 lb/ft² can be accomplished.

One other method of distortion control which was briefly considered was that of modifying the collector shape in order to attain the paraboloidal shape when thermally distorted. This approach requires a high degree of analytical accuracy in predicting both thermal gradients and thermoelastic deformations. Also, since the temperature differential varies during the sun portion of the orbit (see Figure 4.2-7), optical deviations would still be present and would vary about an optimum modified shape.

4.2.6 Collector Materials Space Environment Reliability

The space environment of the Sunflower collector will involve varying degrees of high vacuum, penetrating and ultra-violet radiation, and meteorites.

During the collector development program, no active tests or evaluation of materials space compatibility were conducted; however, continued monitoring of the materials investigations performed in the general space technology build-up was maintained to provide the greatest degree of reliability in material selections.

Some of the general conclusions and comments which can be made at this time will now be presented.

High vacuum will have its primary effect upon the lubrication of the sliding surface involved in the collector deployment and locking. Dry film lubricants are considered entirely satisfactory for the lightly loaded sliding surfaces of the hinge and locks, especially considering the short exposure time (maximum six hours) before orbital deployment.^{20, 21} The vacuum environment can also affect adhesives used in spacecraft bonding. Epoxys in general have been found to have good vacuum stability and specific types which have been tested by various investigators^{18, 20} are recommended for reliable spacecraft structural bonding, especially for internal applications. Since the adhesives used in the bonding of the Sunflower collector honeycomb sandwich material are enclosed by the aluminum skins and aluminum edge close-outs, this use of epoxy is considered an internal application and reliable vacuum compatibility is anticipated.

Penetrating radiation is encountered in varying forms.²⁰ Cosmic ray-induced damage is not a hazard. Trapped (Van Allen) electron and proton damage is a function of dose rate, and the degree of degradation which could occur is not well defined at this time. Auroral proton flux is negligible from the standpoint of material damage but may cause cumulative damage to optical surfaces and thermal control surfaces. However, exposure to auroral radiation is dependent upon the orbit since it is localized at the poles. Solar flare proton radiation occurs in intense fluxes but are periodic and relatively short. Any radiation damage to the epoxy adhesives would be minimized by the shielding provided by the aluminum skins.

Ultraviolet radiation degradation of certain thermal control surface coatings has been measured by various investigators.^{7, 22, 25} Specimens of transparent silicon oxide similar to the proposed Sunflower collector thermal control film have been reported to discolor and increase absorptivity in several laboratory tests. However, most investigators were not dependent upon the transparency of the thermal control film and could turn their attention to more favorable coatings rather than trying to improve the stability of the silicon oxide. Several factors indicate that the stability can be improved. It is believed that the discoloration is produced when radiation displaces electrons which become trapped in "color centers," thereby changing the isotropy of the film. If this is the case, color formation can be greatly retarded by the addition of a small amount of cerium oxide.²⁴ Also, when the radiation is removed, trapped electrons will migrate back to their normal position and color will disappear. This migration increases with increased temperature and when illuminated by white light. Laboratory degradation tests of silicon oxide simulate only the ultraviolet radiation; therefore, observed degradation may be highly accelerated, especially since both the sun and shade portions of a true orbital environment would tend to remove discoloration. The stability of the aluminum₂ reflective film itself has been demonstrated by recently reported results. Brozdowicz states: "It appears that the aluminum reflective coating is not affected by high-energy electromagnetic radiation, regardless of substrate material, underlying coatings, or SiO₂-fast deposited on the top." These tests were conducted in a vacuum for 1000 hours at 3.5 to 4 solar intensities and results show little difference in reflectivity when compared to control specimens which were not irradiated.

Only detailed investigation of silicon oxide films for the specific Sunflower application will determine the reliability of its use. The optical and thermal characteristics, i. e., transparency, wide α/ϵ range, light weight, make it an ideal control coating for space mirror applications. This potential indicates that increased effort is needed in establishing its space compatibility.

Meteorites can cause damage by penetration or surface erosion. Any penetrations of the collector material would involve very small areas and thus would not affect performance or structural integrity.²⁰ The possibility of penetration in a critical structural area represents a hazard on very infrequent and unpredictable occasions.

Calculations of the average area affected by micrometeorites in one year show erosion is not significant.

Spacecraft-borne experiments to investigate space compatibility of materials are planned by several agencies and will provide increased information for the final selection of reliable long-term materials in the collector design.

5.0 COLLECTOR DESIGN

Based on the performance and environmental analyses, the preprototype collector was designed with the following major objectives:

- a. Minimum weight within optical and structural integrity requirements.
- b. Stowage for launch in the Centaur vehicle nose fairing.
- c. High reliability in deployment and locking actions.

5.1 COLLECTOR STRUCTURAL DESIGN

Early in the development program, a review of light weight structural materials and structural concepts was made to evaluate all possible design approaches. General results are summarized in Table 5.1-1.

As originally proposed, aluminum sandwich material was used in the Sunflower design. Several types of core material were investigated but hexagonal honeycomb was found to be technologically well advanced and readily available.

Based on the various environmental structural analyses (see Section 4.2), the sandwich material crosssection shown in Figure 5.1-1 was established.

The 3 mil face material is epoxy adhesive bonded to the aluminum core. Adhesive is used only at the core cell walls where the fillet forms an adequate shear tie with minimum adhesive weight.

5.2 STOWAGE AND DEPLOYMENT DESIGN CONCEPT

The Sunflower collector stowage arrangement is based on a "flower-petal" or petaline concept for folding segments of the paraboloid. This concept was adopted because of its inherent kinematic simplicity and because it is well suited to the Centaur nose cone envelope. Figure 5.2-1 shows the approximate geometric relationship of the number of sectors required for various vehicle and collector sizes. Naturally for maximum reliability and optical quality, the number of sectors should be kept at a minimum.

The Sunflower collector stowing envelope and resulting configuration are shown in Figure 5.2-2. It is seen that the number of sectors was minimized to 30 by scalloping the tips to clear the coned portion of the envelope.

Each sector is hinged at a center structural support ring. In the stowed position, the sectors are folded against an upper structural support ring and bands around the outside restrain the bundle during launch. A torsion spring at each sector hinge is fully torqued in the stowed position. At the time of deployment, the restraining bands release and the springs actuate the deployment. When the open paraboloidal position is

TABLE 5.1-1
SOLAR CONCENTRATOR MATERIALS COMPARISON

MATERIAL	ADVANTAGES	DISADVANTAGES
Aluminum	<ol style="list-style-type: none"> 1. Light Weight 2. Non magnetic 3. Good replication by stretch forming 4. Does not require highly polished master 	<ol style="list-style-type: none"> 1. Surface finish must be improved by over coat layer 2. Thermal conductivity of sandwich sections must be improved for sectioned concentrators
Nickel	<ol style="list-style-type: none"> 1. Good replication by electroforming 	<ol style="list-style-type: none"> 1. Heavy 2. Sandwich sections difficult to make without sacrificing weight 3. Requires highly-polished master 4. Magnetic
Polymers	<ol style="list-style-type: none"> 1. Light weight 2. Non-magnetic 3. Low stowage volume 	<ol style="list-style-type: none"> 1. Must be inflated, foamed, rigidized, and separated in orbit reliably 2. Surface quality poor because of foam bubbles 3. High (200°F) thermal gradients across thickness 4. Reflectivity of mylar surface lower than metal surfaces.

SUNFLOWER CONCENTRATOR SANDWICH MATERIAL CROSSSECTION

(NOT TO SCALE)

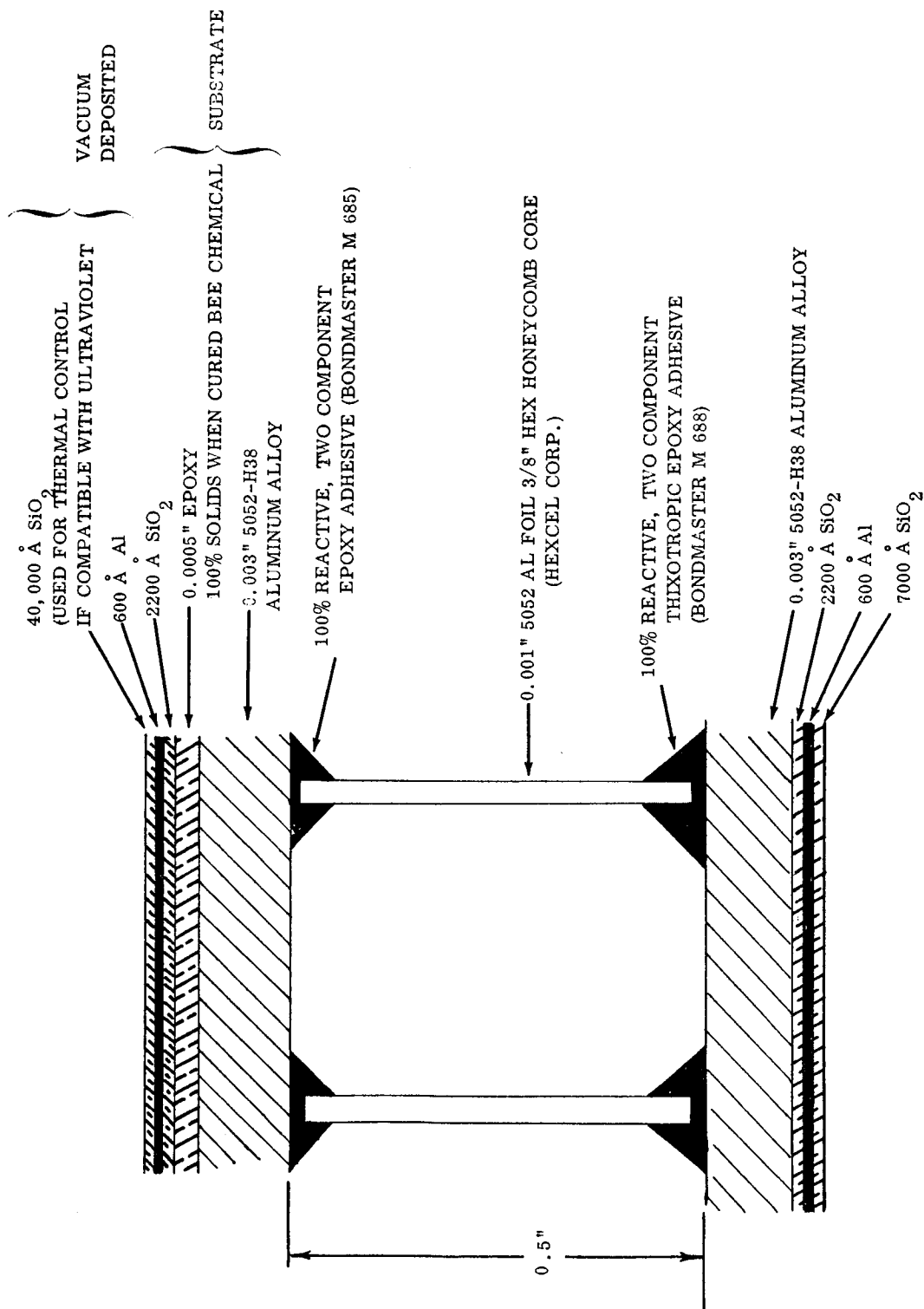


FIGURE 5.1-1

GEOMETRIC RELATIONSHIP FOR PETALINE STOWAGE

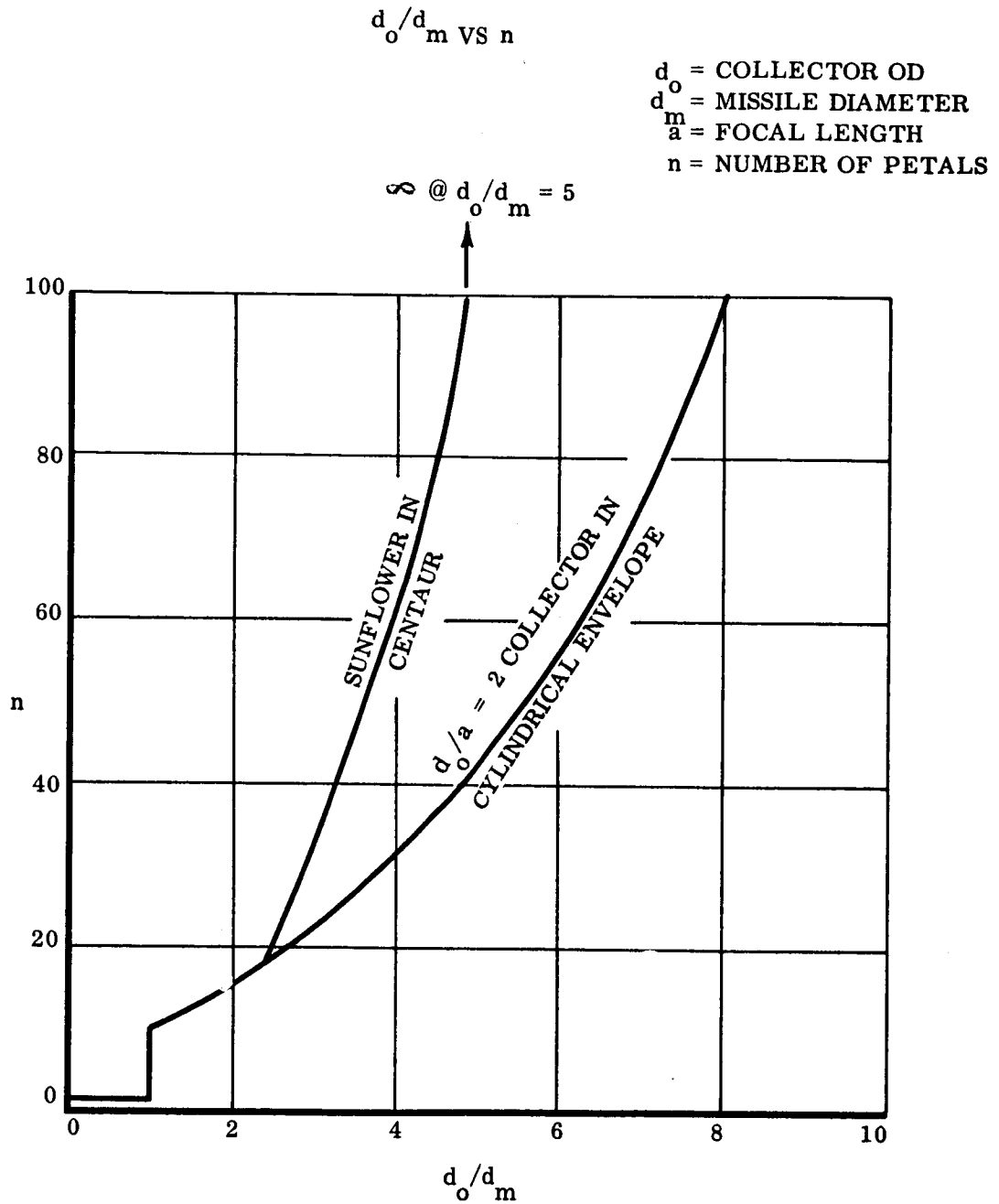


FIGURE 5.2-1

COLLECTOR - RECEIVER GEOMETRY - SUNFLOWER I SYSTEM

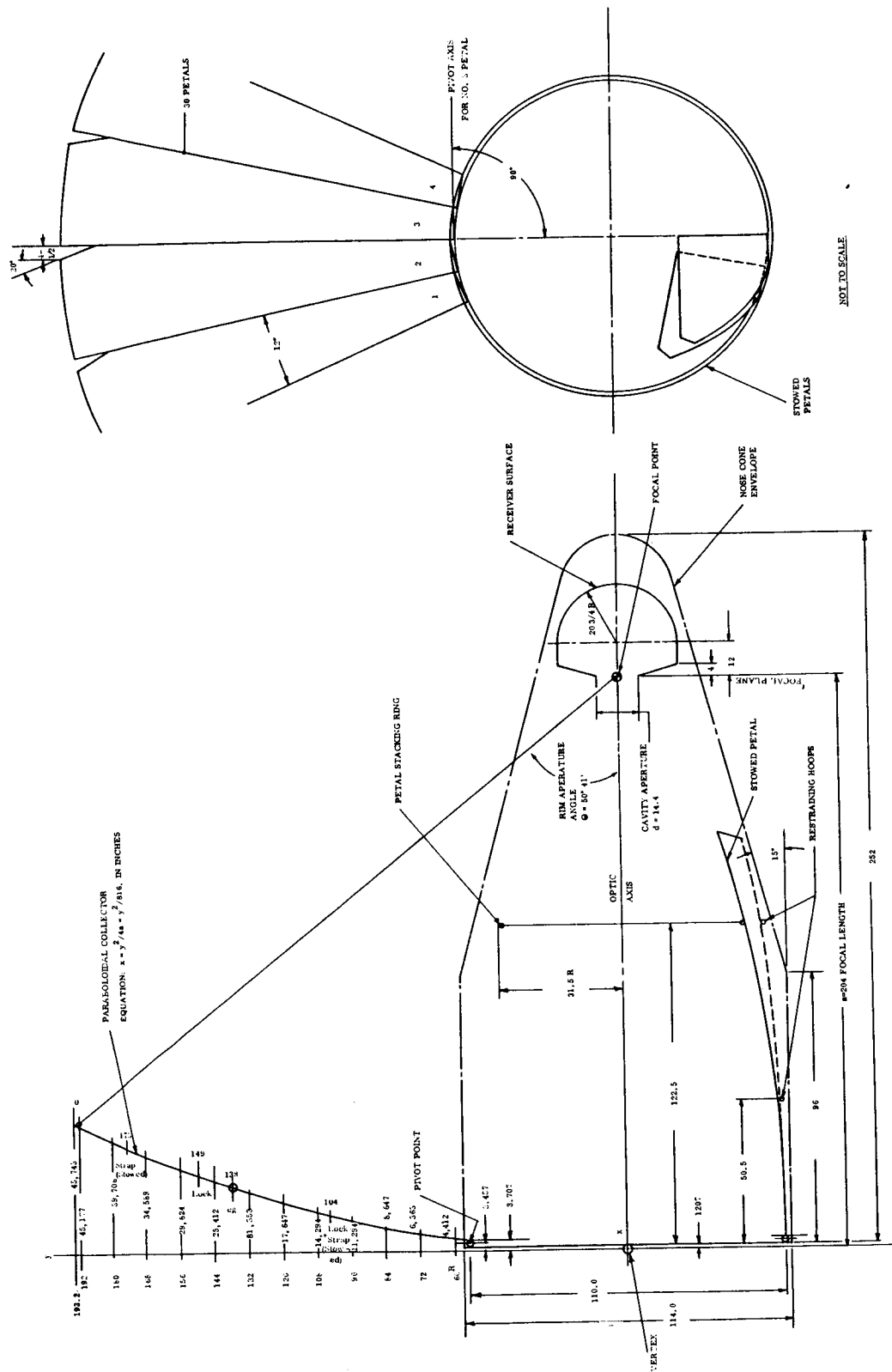


FIGURE 5.2-2

reached, the spring is in the free position and locking devices along the sectors connect adjacent sectors into a structure of revolution.

5.3 SUB-COMPONENT DESIGN

It is seen that the solar collector is composed of various major sub-components. Detailed design descriptions of these components follow.

5.3.1 Sector Design

Each sector is constructed of aluminum honeycomb sandwich material which is adhesive bonded. Based on considerations of strength, surface finish, and availability, 5052-H38 aluminum alloy was used in the preprototype design. The adhesive system selection is a 100% reactive, two component epoxy adhesive and was based upon consideration of strength, ease of handling, and application and curing characteristics.

Edge close-outs for the sectors consists of three mil aluminum "Z" sections which are lap joint bonded to the skins. This provides an all metal edging on the part which minimizes edge losses due to markoff and distortion.

Components such as hinges and locks are attached to the sector by threaded fasteners. For these attachments, metal inserts are bonded into the honeycomb core during fabrication of the sector. Potting-in of adjacent cell areas around the insert provides a reliable shear tie to the skins.

Mechanical testing of both insert connections and the sandwich material itself was conducted to optimize strength and weight for various adhesive application methods.

5.3.2 Hinge-Torsion Spring Design

The hinge and torsion bar hardware is shown in Figures 5.3-1 and 5.3-2. The torsion spring is a rectangular spring-metal torsion bar which runs through the hollow hinge pin. Connections on each end fix the bar to the sector and mounting ring. A rectangular crosssection torsion bar was used to obtain the proper relationship between required angle of twist, torque, and stress. This shape bar is also much more economical to fabricate compared to a circular bar with adequate end connections.

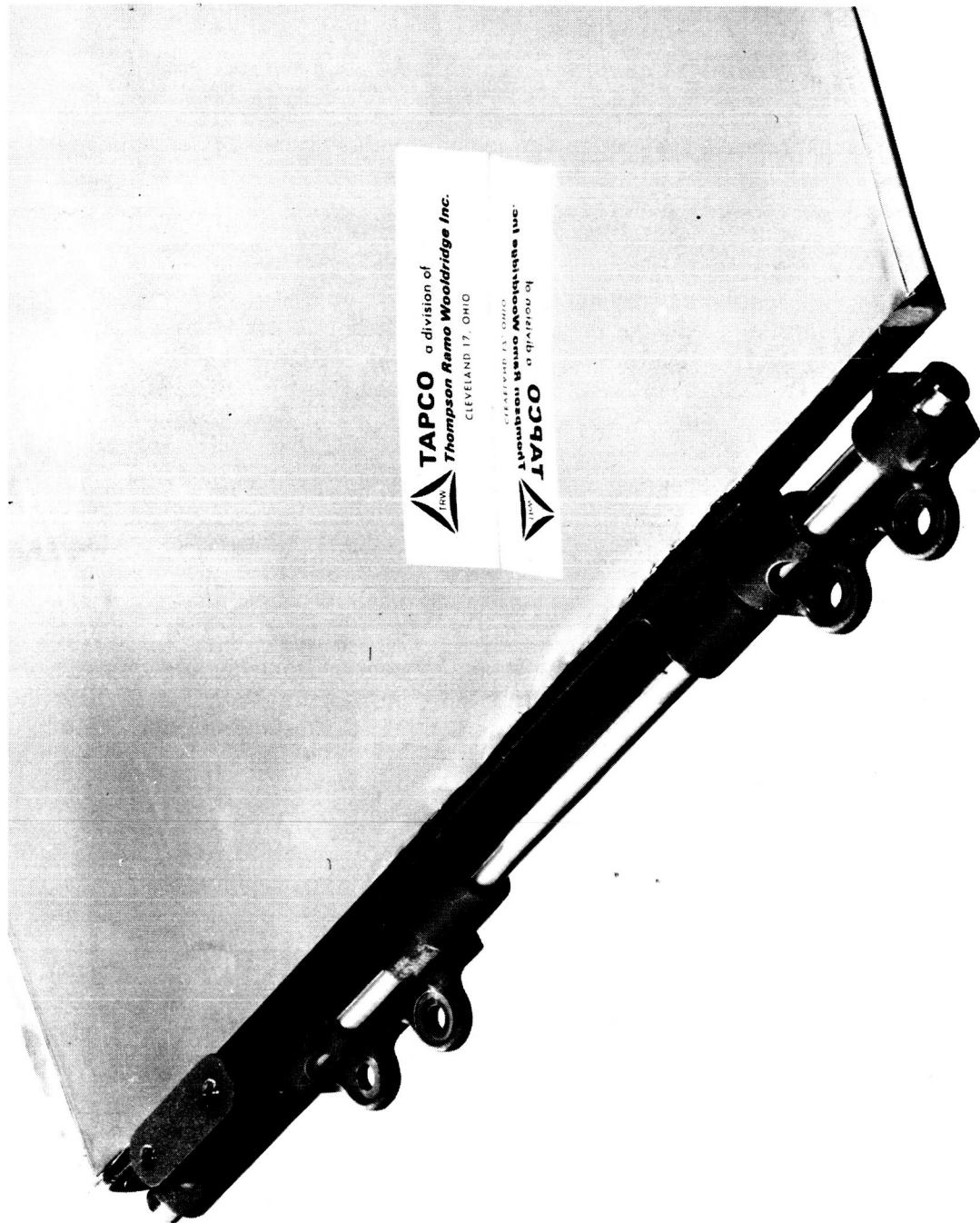
The hinge itself is made of cast aluminum alloy and has integral torsion bar end connections and a mounting pad for attachment of a damping device linkage. As shown in Figure 5.3-2, the hinge assembly is edge mounted to the honeycomb sector by threaded fasteners. The hinge attaches to the center structural ring also using threaded fasteners. This arrangement allows for adjustment during assembly and ease of disassembly.

The torsion bar-hinge arrangement is designed so that the torsion bar can be torqued or released with a hand tool when the sector is in the stowed position, thus eliminating the necessity of deploying the collector to load the actuating springs.



HINGE AND TORSION BAR HARDWARE (DISASSEMBLED)

FIGURE 5.3-1



HINGE AND TORSION BAR HARDWARE

FIGURE 5.3-2

5.3.3 Lock Design

Two basic approaches to a locking device were investigated during the design phase:

- a. Combination shock absorber-lock
- b. Detent lock - continuous viscous damping

The differences in the two design requirements are based on the kinetic characteristics of the deployment dynamic system. If the deployment design is such that the actuating spring energy is absorbed only by the sliding friction between sectors, then the kinetic energy remaining in the system must be absorbed by the lock.

On the other hand, if a viscous damping device is used in conjunction with the spring actuator, torque is absorbed continuously by the damper, thus requiring only a detenting lock in the open positions.

The combination shock absorber - lock which was investigated is shown in Figure 5.3-3 and a sequence of operation is shown in Figures a through f. The device performs two functions in the final phase of the collector deployment sequence: it decelerates the petal so as to prevent excessive forces from developing and it locks the petal in the correct open position. There is a locking device for each sector of the collector.

During the locking sequence there are four events:

- a. Initial detent
- b. Diaphragm puncture
- c. Deceleration
- d. Final detent

Figure 5.3-3a shows the probe of one petal as it approaches the dash pot assembly of another petal. The initial detent springs are tapered as shown so as to guide the probe into the socket if there is any misalignment between the two.

This initial detent, Figure 5.3-3b, requires only a small portion of the kinetic energy of the petal to operate. The intent is to positively engage the probe and dash pot to avoid disengagement before final locking occurs. Once the initial detent is made, the probe forces the piston against the pressure (P_1) inside the dash pot cavity. The pressure P_1 will be greater than P_2 by some 14.7 psi or more since operation will occur in orbit where P_2 is a near vacuum. When the piston advances far enough, the puncture point, Figure 5.3-3c, punctures the diaphragm. This allows the pressure P_1 to relieve itself through the orifice, thus preventing a large pressure rise and the resulting large deceleration forces.

COMBINATION SHOCK ABSORBER - LOCK

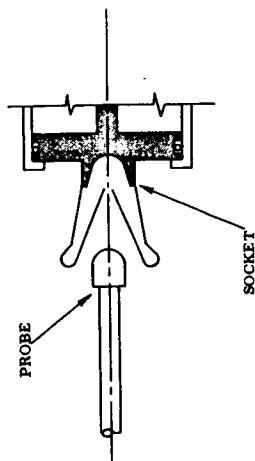


FIGURE 5.3-3(a)

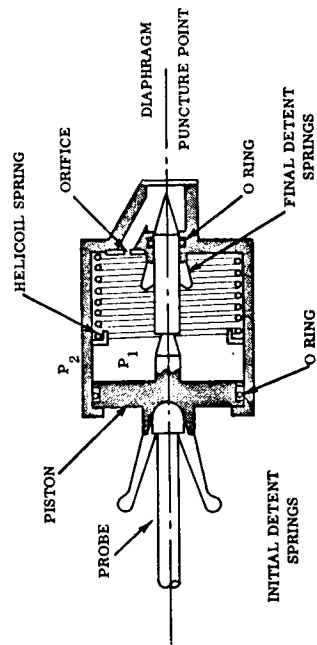


FIGURE 5.3-3(b)

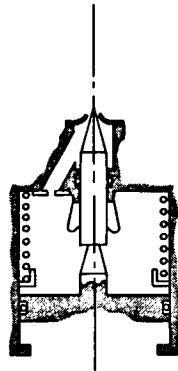


FIGURE 5.3-3(c)

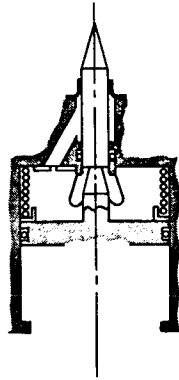


FIGURE 5.3-3(e)

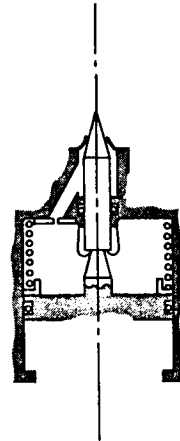


FIGURE 5.3-3(d)

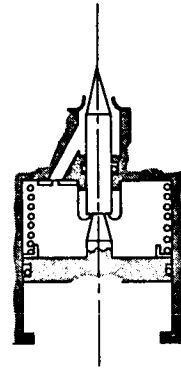


FIGURE 5.3-3(f)

When the piston reaches the position shown in Figure 5.3-3d, the collector has reached its full open position and the final lock detent occurs as shown. But an additional feature is built into the dash pot; it can absorb minimum and maximum amounts of petal kinetic energy which are an order of magnitude different from one another. If the petal kinetic energy happens to be the minimum, then the piston merely advances to the final detent and stops. If any value of kinetic energy up to the maximum is encountered, the piston continues to advance as in Figure 5.3-3e until the energy is absorbed. The petals must rotate beyond the full open position of the collector to do this. Therefore, the helical spring, which was engaged by the piston even prior to reaching the full open position in Figure 5.3-3d, forces the piston backwards until the final detent springs prevent further reversal of the sequence. The helical spring is not intended to have any shock absorbing features, although it does act against the piston as the pressure P_1 does. It must only have force enough to return the piston to the full open position as in Figure 5.3-3f.

The second lock design which was investigated involves separating the dash pot portion of the device from the detent portion. The detents would remain at the tips of the petals, but the dash pots would be placed at the pivot points of the petals. In this way, two advantages could be realized:

- a. Fewer dashpots could be used where each one would act on a set of 3 petals, thus reducing hardware requirements
- b. A control of petal kinetic energy could be maintained over the entire deployment sequence; thus, the forces developed in the final locking phase would be reduced.

This second deployment system was selected for preprototype design.

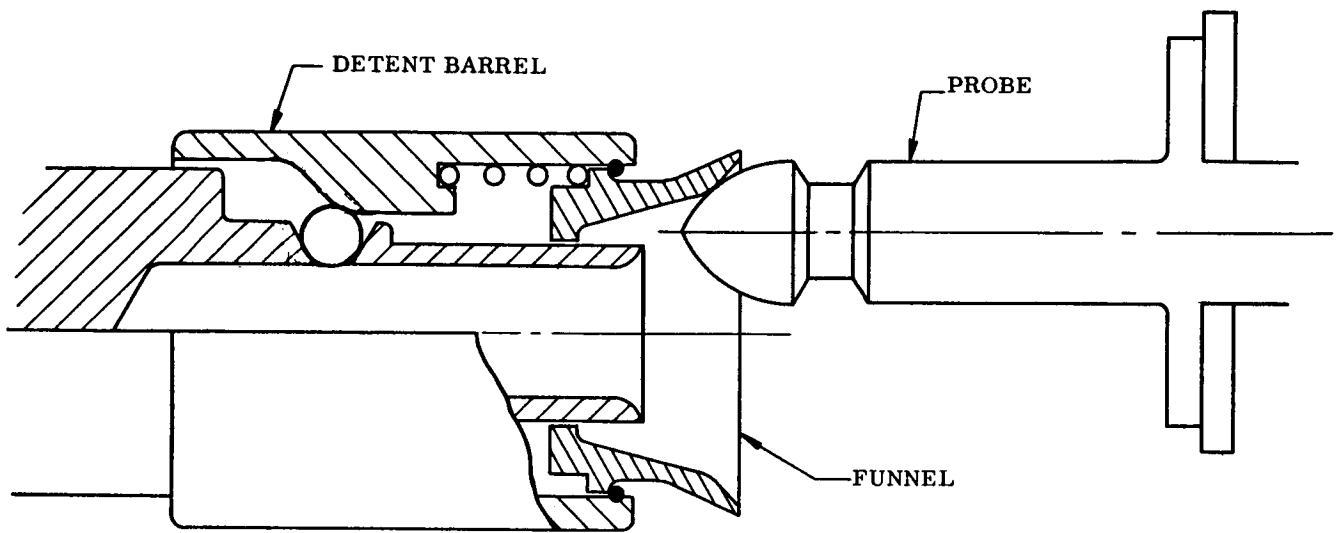
Typical lock hardware is shown in Figure 5.3-4. The lock consists of a probe and a detent barrel which has a funnel opening to pilot the probe. To span the scallop at the sector tips, a flat spring strap is used. This spring section, in combination with the pivot at the mounting bracket, allows for the kinematic discontinuity which occurs at the end of the deployment sequence due to the thickness of the sector. A guide shoe is also part of the lock. It rides along the edge of the sector to provide a link and guide during the entire deployment sequence. A detail of the detent portion of the lock is shown in Figure 5.3-5. In operation, the probe is piloted to the detent portion by the funnel. Upon engagement, the probe shoulder pushes the barrel over the detent balls which drop into the probe relief, thus locking the two adjacent sectors. The lock can be released only by pushing the detent barrel against the compression spring, thus relieving the detent balls. With this locking arrangement, the primary function is the detenting action; however, a small amount of shock absorption is obtained when the probe compresses the detent barrel compression spring.



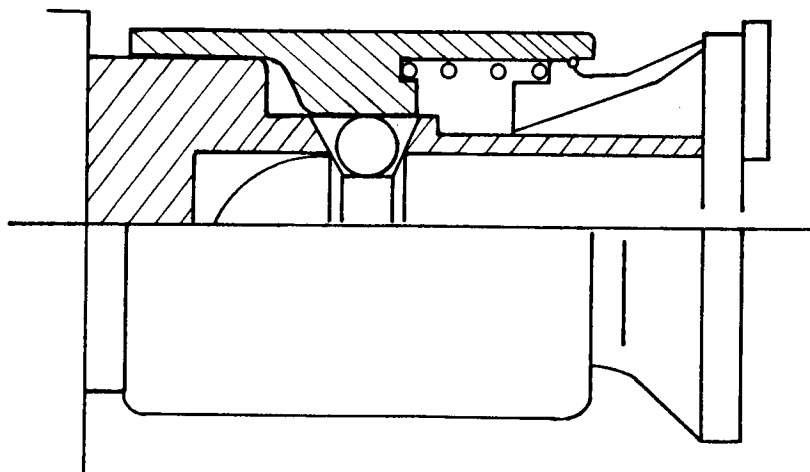
TYPICAL SECTOR LOCK

FIGURE 5. 3-4

LOCK DETENT



(a) INITIAL ENGAGEMENT



(b) LOCKED POSITION

FIGURE 5.3-5

The primary motion controlling device in this deployment concept is a viscous damper. Since the damping of this type of device is proportional to velocity, high initial torques can be designed into the actuating torsion bars to reliably deploy the collector under a large range of inter-sector friction; yet with a properly sized viscous-damper, high velocities and final kinetic energies are not imparted to the locking sequence.

A damper, such as the one shown in Figure 5.3-6, was sized for the initial estimates of inter-sector friction. Detailed design and fabrication was not performed in this portion of the development program, however, since accurate frictional values would be obtained in the scheduled deployment simulation testing. Based on these deployment test results, the motion control concept would be finalized.

5.3.4 Center Mounting Ring Design

The Sunflower collector structural concept requires a continuous structural ring for supporting the individual honeycomb sectors. The design of this ring for the pre-prototype collector was based on the calculated launch environment loading. Various numbers of support points were investigated and resulted in the use of the four attachment points at the Sunflower structure quadripod. No intermediate bracing was used. A square cross section tubular aluminum alloy member was used to obtain a flat reference surface for mounting and adjustment of the hinges and sectors. The square section provided the most efficient box design for both bending and torsion.

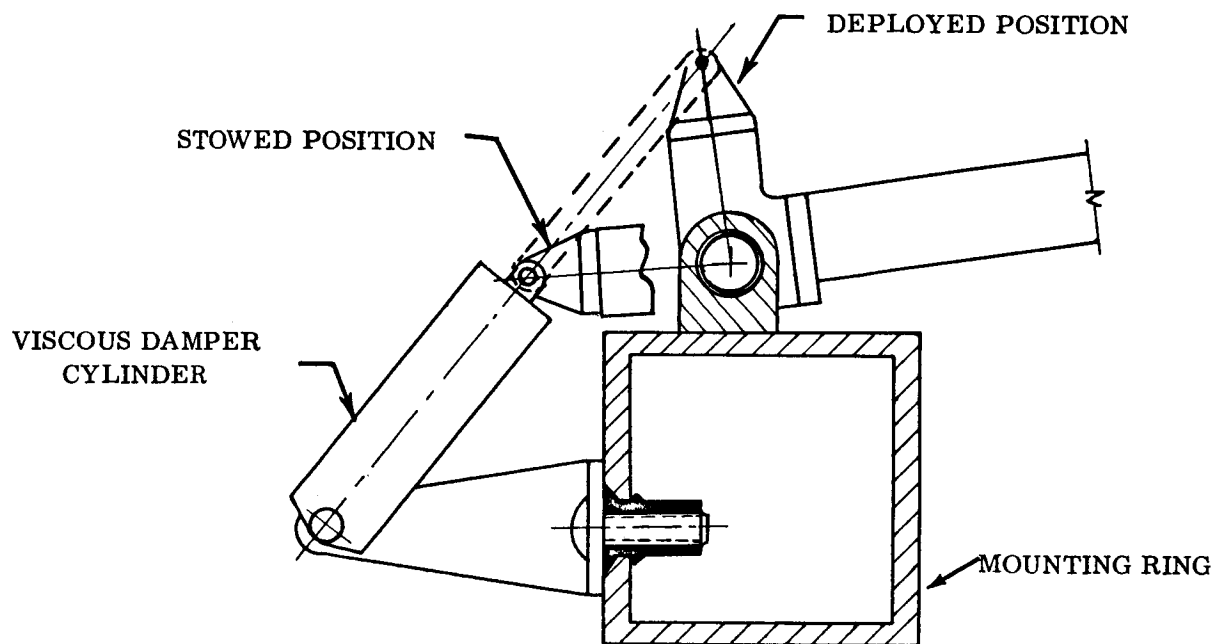
In the flight hardware design, it is anticipated that a more efficient weight design can be obtained by closer integration of this structural ring with the payload structure and/or launch vehicle structure. In this way, deep section structural design, or at least additional support points to relieve long curved beam spans and at the same time accomplish a more evenly distributed load transfer to the launch vehicle structure, can be obtained.

5.3.5 Stacking Ring Design

The stacking ring is located approximately ten feet from the mounting ring (see Figure 5.2-2). It provides support for the sector bundle during the launch environment. A circular tubular cross section was used with four attachment points to the quadripod and no additional bracing. The primary design consideration for this ring was vibration isolation and damping.

5.3.6 Vibration Isolation Design

The vibration environment of the relatively flexible honeycomb sectors is the primary factor in the vibration design considerations. As represented in Figure 4.2-3, the sectors are subjected to different degrees of vibration in the stowed and deployed configurations.



VISCOUS DAMPER ARRANGEMENT

FIGURE 5.3-6

5.3.6.1 Stowed Vibration Isolation Design

In the stowed position, the sectors are supported by:

- a. The lower mounting ring
- b. The upper stacking ring
- c. The intermediate bands

Vibration transmitted to the sectors can be reduced by a vibration isolation system. Based on the results of preliminary low level vibration testing of the collector and simulated system structural response, military standard isolators were modified for mounting the upper stacking ring. Also, the ring was structurally damped by visco-elastic damping tape (see Figure 5.3-7).

Thus, during the launch vibration environment, the sector bundle will be isolated from any amplifications or resonances which may occur in the system structure at the stacking ring location. Final design of these isolators must be based upon a detailed knowledge of the vibrational response characteristics of the system structure.

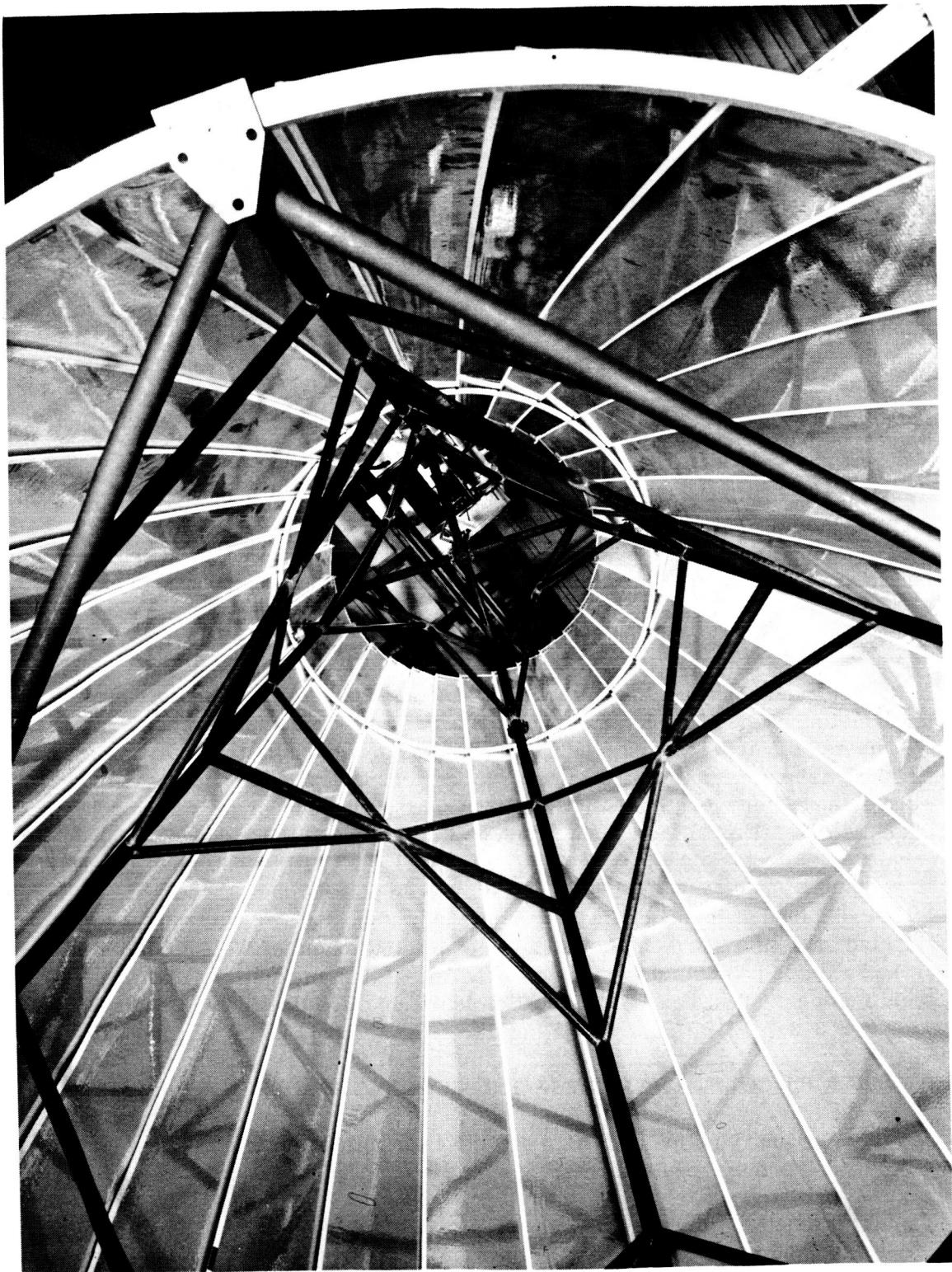
5.3.6.2 Deployed Position Vibration Isolation Design

In the deployed position, the collector is supported only at the mounting ring. Low level testing of the ring alone was again used as an isolation design basis. Large transmissibilities were observed. Since the deployed orbital transfer vibration specifications are quite severe (the same as those generated by the launch engines), isolators were selected for vibration isolating the mounting ring supporting the 1 "g" weight of the collector. This is the weight which will be experienced by the collector due to acceleration during orbital transfer. These isolators will be bottomed-out under the 10 "g" launch load of the collector in the stowed position; thus, no vibration isolation will be obtained at the mounting ring in the stowed position. The isolators which were selected are stiff enough so that no appreciable movement of the collector with respect to the boiler is possible under orbital conditions, thus maintaining optical performance specifications. Test results of vibration isolation effectiveness will be presented in Section 8.3.3.

5.4 WEIGHT CONSIDERATIONS IN THE COLLECTOR DESIGN

One of the primary collector design objectives is minimum weight within optical and structural integrity requirements.

Weight, strength, and geometric accuracy are all closely inter-related. The amount of adhesive and the face thickness used in the sandwich material not only affects weight and strength, but also optical quality of the collector surface due to the tendency of this type of construction to dimple in the core cell areas. This honeycomb markoff



BOTTOM VIEW OF COLLECTOR BUNDLE

FIGURE 5.3-7

TABLE 5.4-1
SUNFLOWER COLLECTOR WEIGHT

	PRE-PROTOTYPE			FLIGHT DESIGN
	ACHIEVED PRE-PROTOTYPE COLLECTOR (AVG)	ACHIEVED SECTORS S/N 7 through 12 (AVG)		
Honeycomb sandwich material	AL face foil	0.0840 lb/ft ²	0.0840	0.0840
	AL core material	0.0667 lb/ft ²	0.0667	0.0667
	Adhesive	0.0343 lb/ft ²	0.0343	0.0343
	Composite Sandwich	0.185 lb/ft ²	0.185 lb/ft ²	0.185 lb/ft ²
SECTOR WEIGHT	Sandwich Material	4.75 lb	4.75 lb	4.75 lb
	Close-outs & inserts	0.25 lb	0.25 lb	0.25 lb
	Doublers	0.9 lb	NONE	NONE
	Total Sector Weight	5.9 lb	5.0 lb	5.0 lb
LOCK WEIGHT PER SECTOR	Rim Lock	0.24 lb	0.24 lb (STL)	0.09 lb (AL)
	Intermediate Locks (2)	NONE	NONE	0.06 lb (AL)
HINGE-ACTUATOR WEIGHT PER SECTOR	Hinge-torsion bar	0.46 lb	0.46 lb	0.3 lb
	Damper	NONE	NONE	0.05 lb
TOTAL COLLECTOR WEIGHT		198 lb	171 lb	165 lb
COLLECTOR SPECIFIC WEIGHT BASED ON INTERCEPTED AREA		0.26 lb/ft ²	0.23 lb/ft ²	0.22 lb/ft ²

pattern can be controlled by proper processing in bonding the honeycomb part, the critical factors being uniformity and amount of adhesive. However, adhesive amount must be satisfactory for obtaining adequate shear-tie for the skins and core.

Achieved and extrapolated flight design weights are shown in Table 5.4-1. The specific weight break-down for the honeycomb sandwich material was found to result in optimum trade-off between weight, strength, and geometric quality. It should be noted that the achieved average sector weight of 5.9 lb for the preprototype collector is due to an interim design change which incorporated a reinforcing double strip along the edges of the sector front face. This was required to support stresses formed in the skins during layup. As shown in Table 5.4-1, sectors without doublers have been fabricated within weight specifications. However, honeycomb markoff along the edges is out of spec due to the residual layup stress relief and resultant distortion.

The indicated weight reductions shown in the flight design of lock and hinge hardware are based upon results of preprototype hardware tests and can be accomplished by reduction in wall thickness and material changes.

Center support ring weights are not included in this weight summary since efficient weight design of this member is closely related to integration with the payload and vehicle structures. The center support ring which was fabricated for the preprototype collector assembly weighs 21 lb and could be reduced by approximately 40% in a specially extruded aluminum shape.

5.5 REFLECTIVITY CONSIDERATIONS

Reflectivity is commonly separated into specular and diffuse reflectivity, where the latter has only detrimental effects on solar collectors. Ideally, a truly specularly reflecting surface would be desirable. However, actual surfaces, especially of large sizes, will produce a certain amount of scattering and thereby reduce specularity. Scattering is produced by small surface areas having a different slope than the average microscopic surface. These slope variations are the results of fabrication and mechanical or chemical treatments and are evident as roll marks, scratches, and etch effects. It then becomes necessary to either eliminate or reduce these slope variations to acceptable limits.

Having achieved an acceptable, flat surface, the next requirement is to reflect the maximum amount of the incoming radiation.

5.5.1 Surface Improvement

Since surfaces of materials come with various finishes, an evaluation of the finish and its effect on the specular reflectance is important. Since specularity is a theoretical concept, actual measurement values depend greatly on the instrument and its geometry.

Micro-finish deviations of the surfaces were investigated by obtaining profiles on a Proficorder. The instrument is shown in Figure 5.5-1 and sample traces in Figure 5.5-2. Although no precise correlation exists between these traces and the RMS values which were obtained using a standard RMS indicator, there is a relationship as indicated by the results of the two samples shown. Generally, the greater the RMS reading, the higher the amplitude on the Proficorder graph. However, this is dependent on the direction of the trace. The highly directional nature of the surface roughness of the samples is a function of the rolling process. The circumferential grinding marks of the rolls are duplicated on the sheet in the rolling direction.

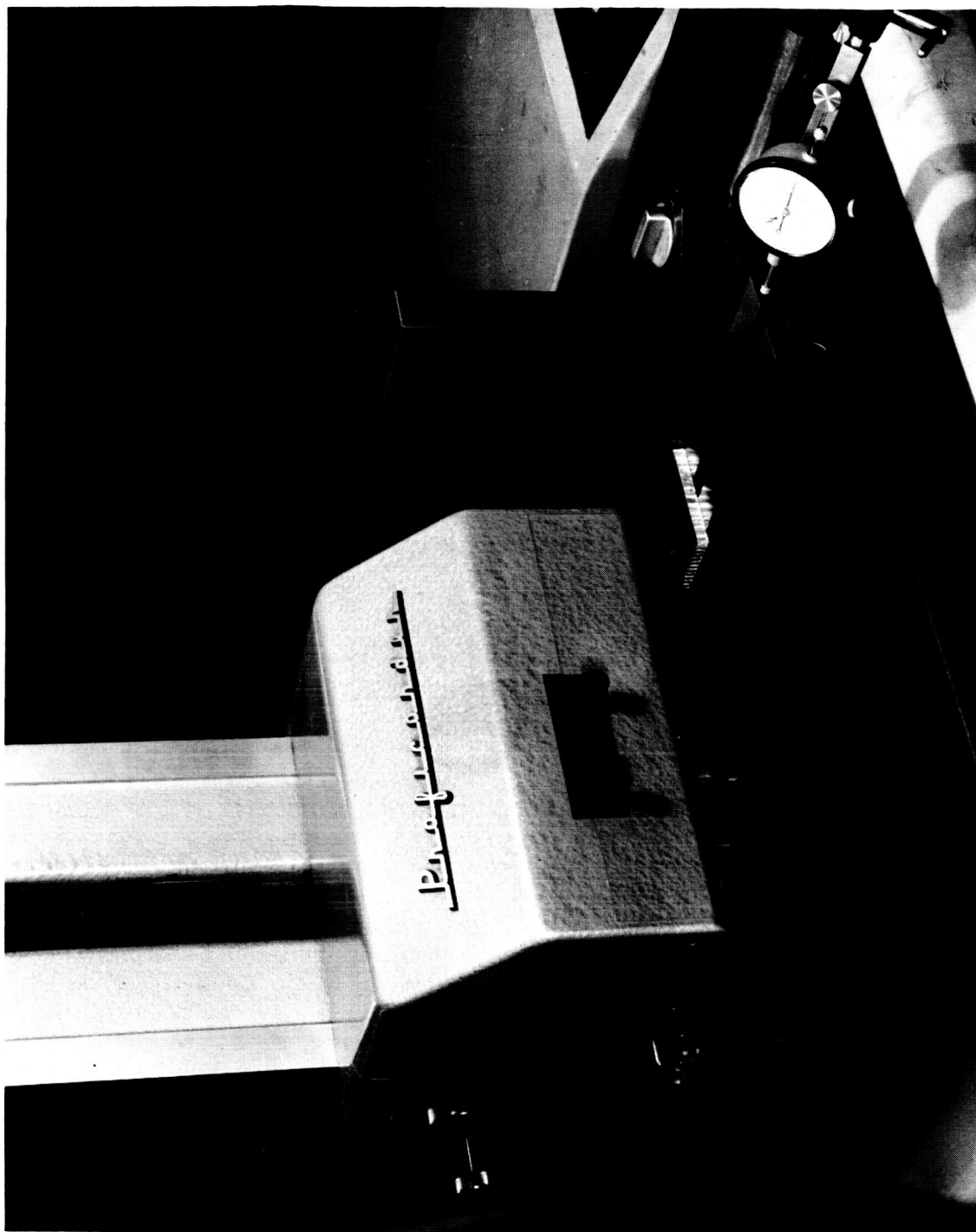
To reduce the surface roughness, the final roll or rolls are then required to have the best finish obtainable. Inquiries to aluminum fabricators as to their capability and willingness to produce high surface quality sheet resulted in only one favorable response, from ALCOA. The important findings were: of the high strength alloys, 5052 will yield the best surface finish but not as good as the lower strength alloy 1145 with a special process. Applicability of this process to other alloys is doubtful.

Proficorder graphs served well in the initial screening of the submitted samples; however, when surface finishes of 1-2 micro inch RMS were investigated, the practical limit of a stylus type instrument was reached and an optical arrangement was required.

A reflectometer (Figure 5.5-3) was built to continue evaluation of the finer surface finishes. The basic parts are a monochromator with light source, a pivot with sample holder, a rotating arm with an attached iP22 phototube, and a photomultiplier micro-photometer. The combination of geometry and slit adjustments permitted scanning the resultant light beam in increments of 0.1 degree for intensity measurements. Green light of 5000 Angstrom wavelength was used in initial screening of specimens since it represented the maximum intensity plateau of the light source.

First, the source intensity distribution was obtained in the position shown in Figure 5.5-3, then the sample holder with a sample retained by vacuum was placed on the pivot, the arm rotated to the scanning position, and the reflected beam intensity distribution obtained. Because of absorption losses, the reflected beam intensity will not reach the 100% mark. This point is illustrated by the aluminized glass surface specimen on the graph of Figure 5.5-3, which has a maximum intensity of 92%. The reflectometer was designed to evaluate scattering effects and will not yield total reflectivities. However, all samples must have the same total reflectivity for a valid comparison. This is accomplished by aluminizing the surface with 99.99% pure aluminum, by the vacuum deposition process.

Figures 5.5-3 and 5.5-4 show resulting specularly characteristic curves of various surface finishes. The highly directional nature of the surface roughness was again visible by the different intensity profiles obtained when scanning parallel or perpendicular to the roll marks. The directional effect is not apparent from the reflectance curves shown in Figure 5.5-5 which were obtained with an integrating



PROFICORDER FOR SURFACE QUALITY MEASUREMENTS

FIGURE 5.5-1

PROFICORDER ROUGHNESS GRAPHS OF ALUMINUM FOILS

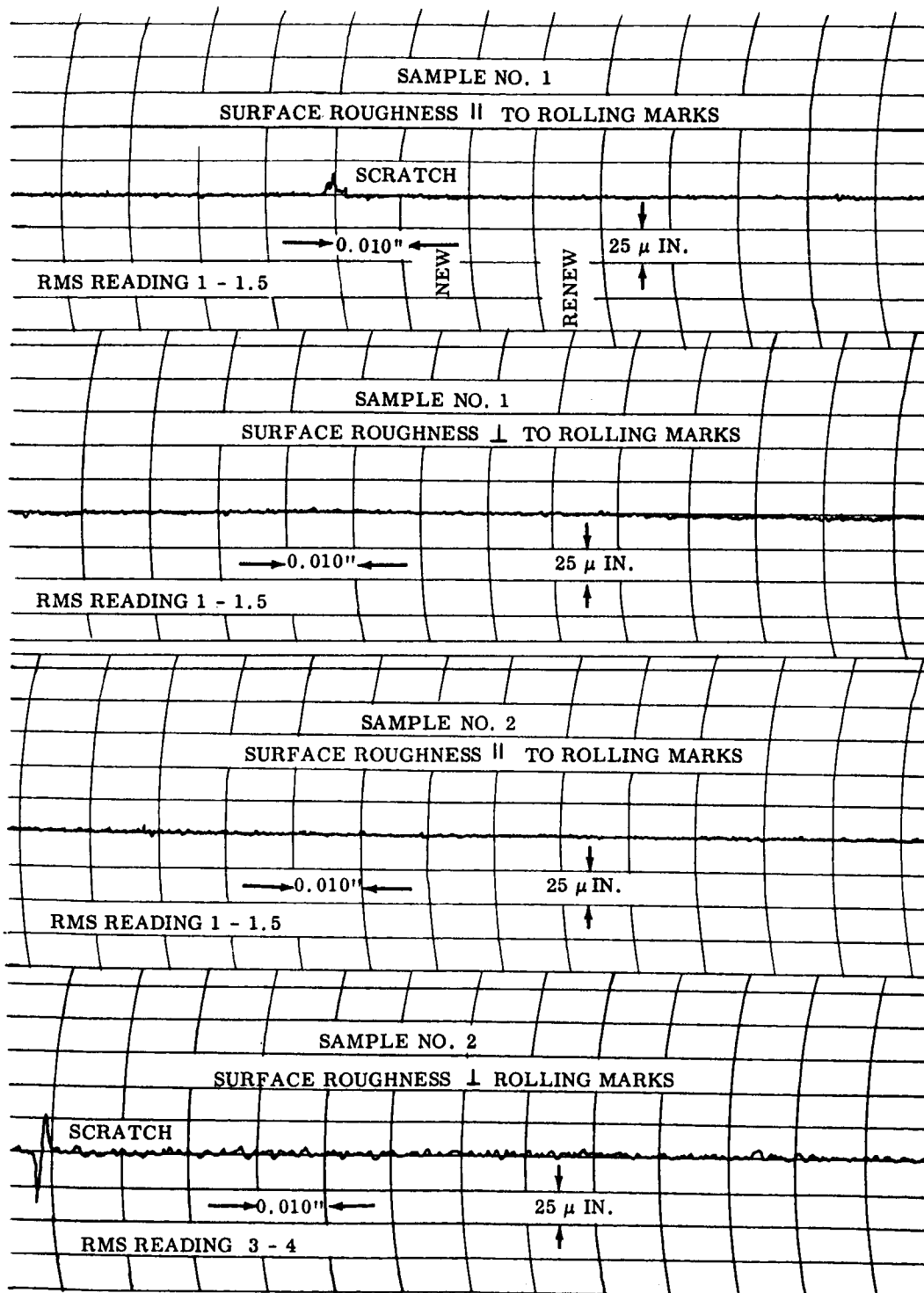
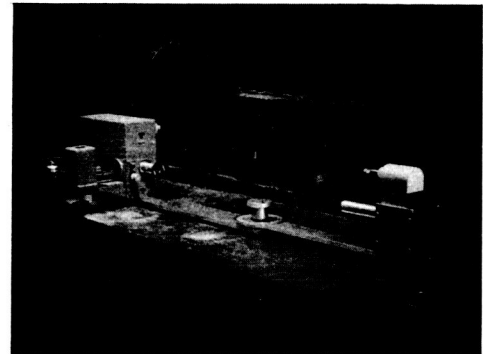
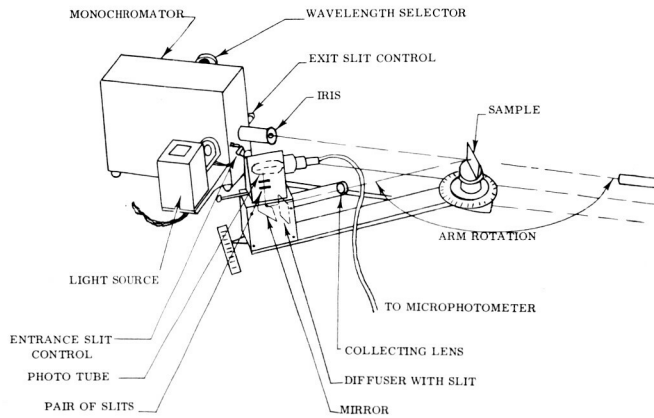
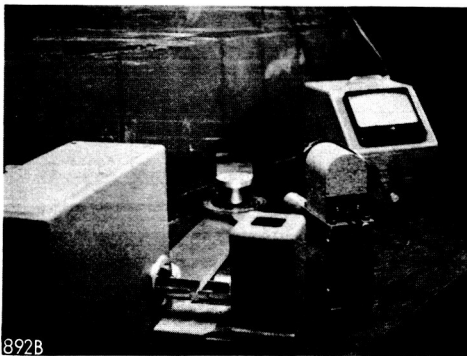


FIGURE 5.5-2

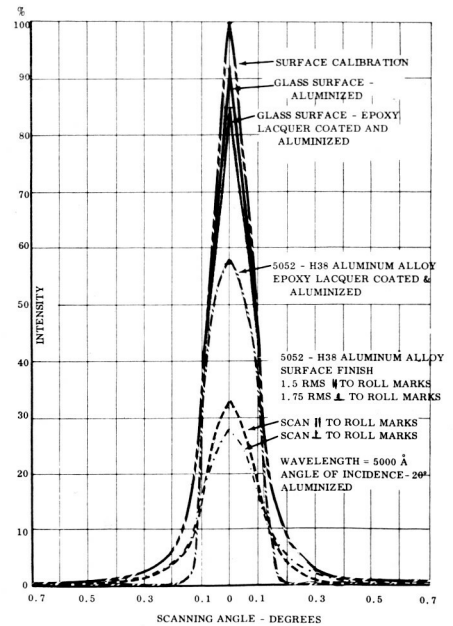
SPECULARITY REFLECTOMETER



SOURCE CALIBRATION POSITION



12° ANGLE OF INCIDENCE
MEASUREMENT



SPECULARITY CURVES FOR VARIOUS SURFACES

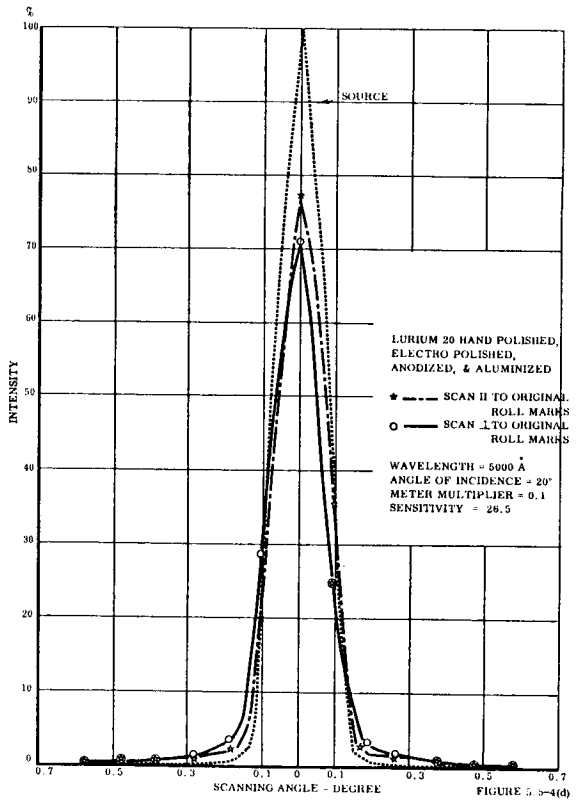
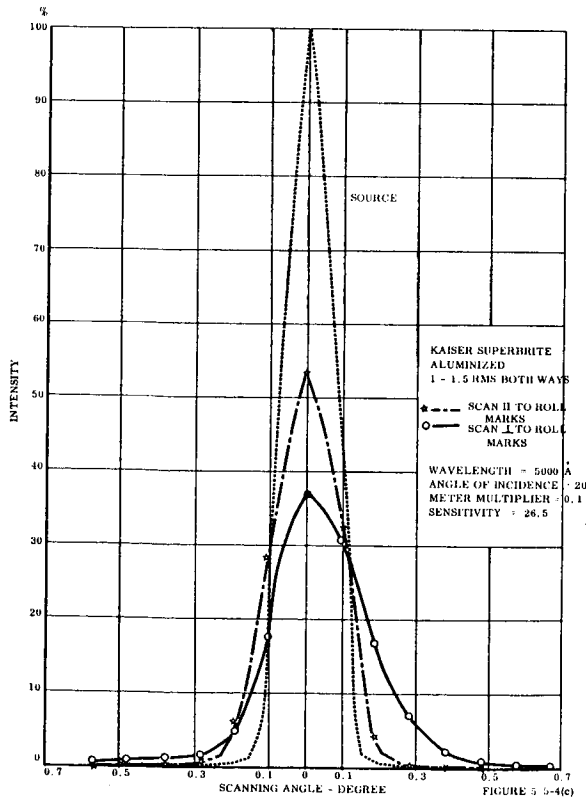
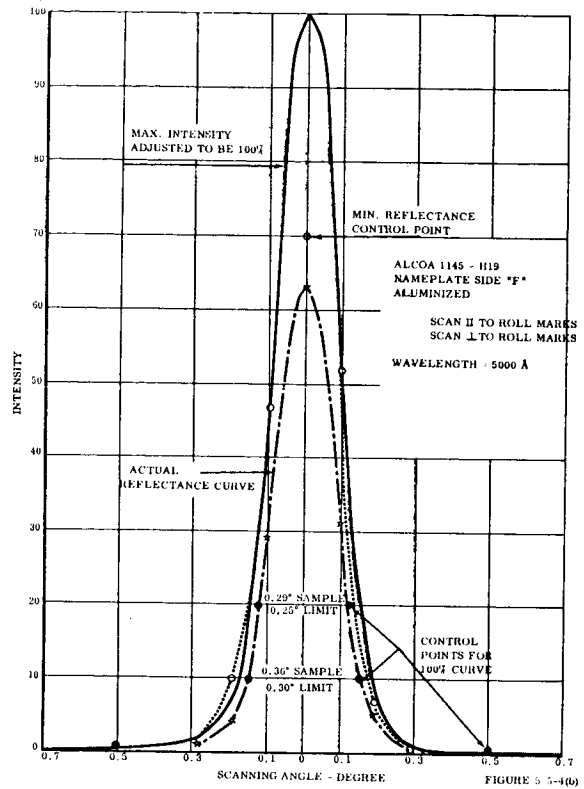
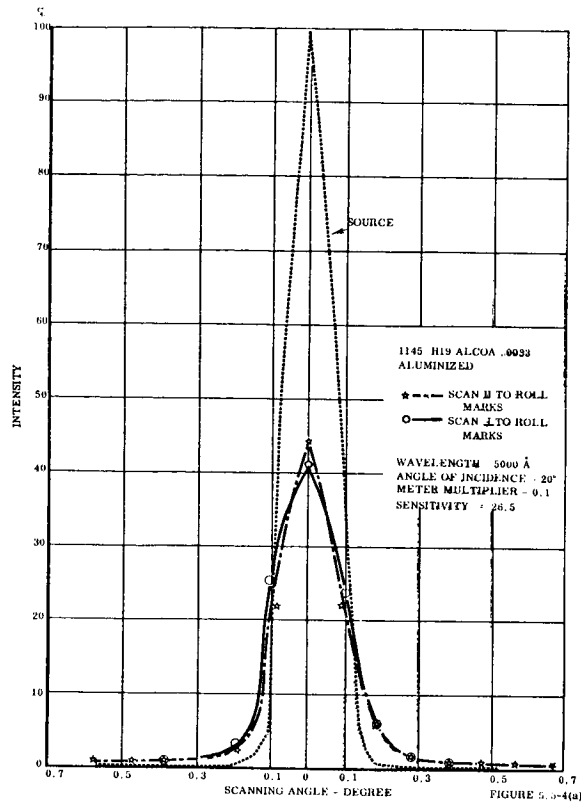


FIGURE 5.5-4

REFLECTANCE VS WAVELENGTH

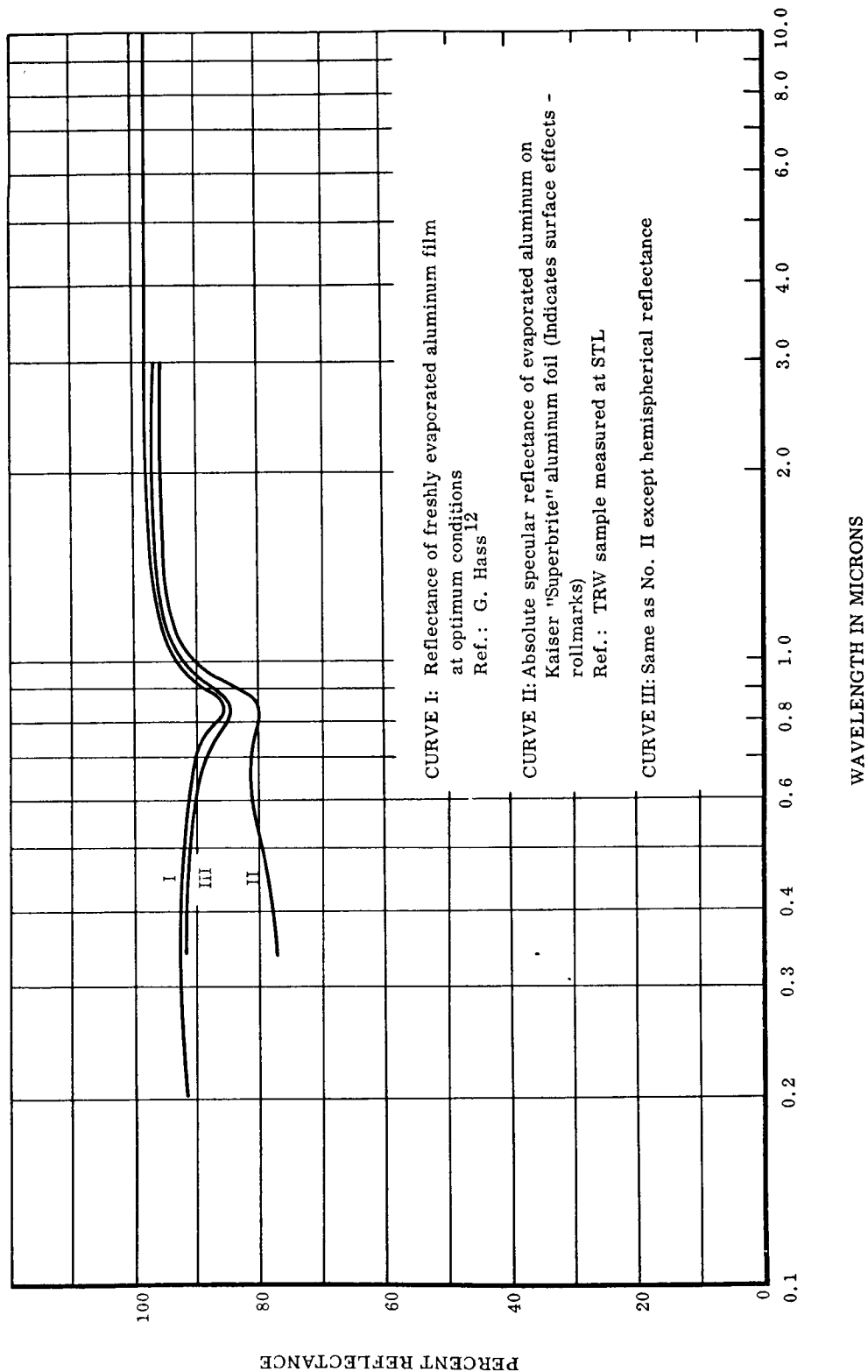


FIGURE 5. 5-5

sphere of a conventional reflectometer. Curve II of Figure 5.5-5, however, shows the substantial reduction in specularity due to the roll mark effect. The directional dependency decreases as the general surface finish improves as shown on Figure 5.5-4b. This figure also shows the control points of the surface quality inspection. Although this sample represented the best surface finish obtainable from the mill, it did not yet meet the minimum specifications; consequently, other methods of surface improvements were investigated.

Hand polishing, although tried and proved to be effective, was ruled out because of the large surface areas involved and the difficulty experienced in polishing 0.003 inch thick foil.

The other alternatives were chemical and electro-polishing. The latter method produced a surface quality just meeting the specifications (See figure 5.5-4). However, an acceptable surface quality can only be obtained with higher purity aluminum and not with the usually stronger alloys. Also, the large surface areas involved were outside the equipment capabilities.

Since a satisfactory surface finish could not be obtained on the chosen material by the discussed means, attention was focused on producing a flat substrate for the evaporated reflective film by lacquer coating. A 100% solid epoxy lacquer was chosen. Although the lacquer polymerized and dried at room temperature, an elevated temperature cure could be applied to insure complete loss of all volatiles. This particular feature would increase space compatibility and prevent any potentially detrimental effect on the reflective and protective coating. Although all organic materials are more or less affected by the space environment, epoxies are in the more suitable category. The degree to which the material would be affected, however, depends on local space conditions, such as Van Allen radiation belt and the protection afforded by the reflective and protective films. Long term space compatibility of the complete coating system should be experimentally determined.

Sample measurements proved the effectiveness of the coating by increasing the peak intensity and reducing the wide angle scattering losses. Figure 5.5-3 shows a comparison of an uncoated and coated material. The amount of improvement depends on the original surface roughness, the thickness of the lacquer, the lacquer-solvent mixing ratio, and the effects introduced due to the method of application and environment. Comparison of coated and uncoated glass surfaces shows a small reduction in peak intensity on the lacquered surface. This is probably due to some of the mentioned factors and quite possibly can be eliminated. The imperfections of the lacquered surface showed up in various forms. Dust particle inclusions and some conformity to surface variations, depending on lacquer thickness, could easily be separated. Another common imperfection experienced was the tendency to produce an orange peel-like surface texture. In addition, cloudiness was found on some samples or on some areas of larger pieces. Under a lower power microscope, this cloudiness resolved into a great number of small hemispherical elevations. It is believed that they are produced by air or solvent entrapment and or by condensed

moisture from the atmosphere. Surface improvement coating of full sized sectors will be discussed in Section 6.2.

5.5.2 Reflective and Transparent Coating

To obtain the highest collector efficiency, the surface reflectivity must be maximum. Since the solar radiation covers a relatively broad spectrum and reflectivity is a function of wavelength, both factors must be considered in obtaining total reflectivity. Reflectance curves for some metals are shown in Figure 5.5-6. Integration of the reflected solar energy results in a 95% reflectivity for silver and 92% for aluminum. All other materials were far below this percentage. Although silver has a higher reflectivity, several undesirable properties, such as poorer adhesion, tarnishing, and oil vapor effects in the vacuum system, precluded its use for the time being. Aluminum was therefore chosen for the reflective film.

To obtain maximum reflectivity, pure aluminum should be evaporated in a suitable vacuum chamber under certain conditions. A special vacuum evaporator, capable of handling the large Sunflower panels, was acquired. Besides permitting the evaporation of an aluminum film, the capability to evaporate SiO_x was also required. SiO_x was to be evaporated on top of the pure soft aluminum not only to control orbital thermal characteristics but also to protect it from atmospheric effects, scratching, etc. and to permit cleaning during prolonged outdoor testing. The vacuum deposition facility and process will be discussed in Section 6.3. Measured reflectivity results will be presented in Section 7.3.5.

5.5.3 Summary of Reflectivity Investigations

Investigations of the surface finish of commercial foil pointed out the need for surface improvement. Mechanical and chemical means could not be employed because of the large surface areas involved and equipment size limitations. Good results were obtained with an epoxy lacquer as a substrate. However, some improvement in the method of applying the lacquer should be made to obtain the desired surface flatness. The specially built vacuum evaporator met the design goals and permitted evaporation of the reflective and protective films. The pure aluminum film reflectivity duplicated the maximum values obtainable. The SiO_x protective coat showed, at its best, a 4% increase in absorptivity (See Figure 7.3-9). This is about twice the anticipated rate and probably can be reduced by changing the film thickness and providing more oxygen during the evaporation to obtain a higher percentage of fully oxidized molecules.

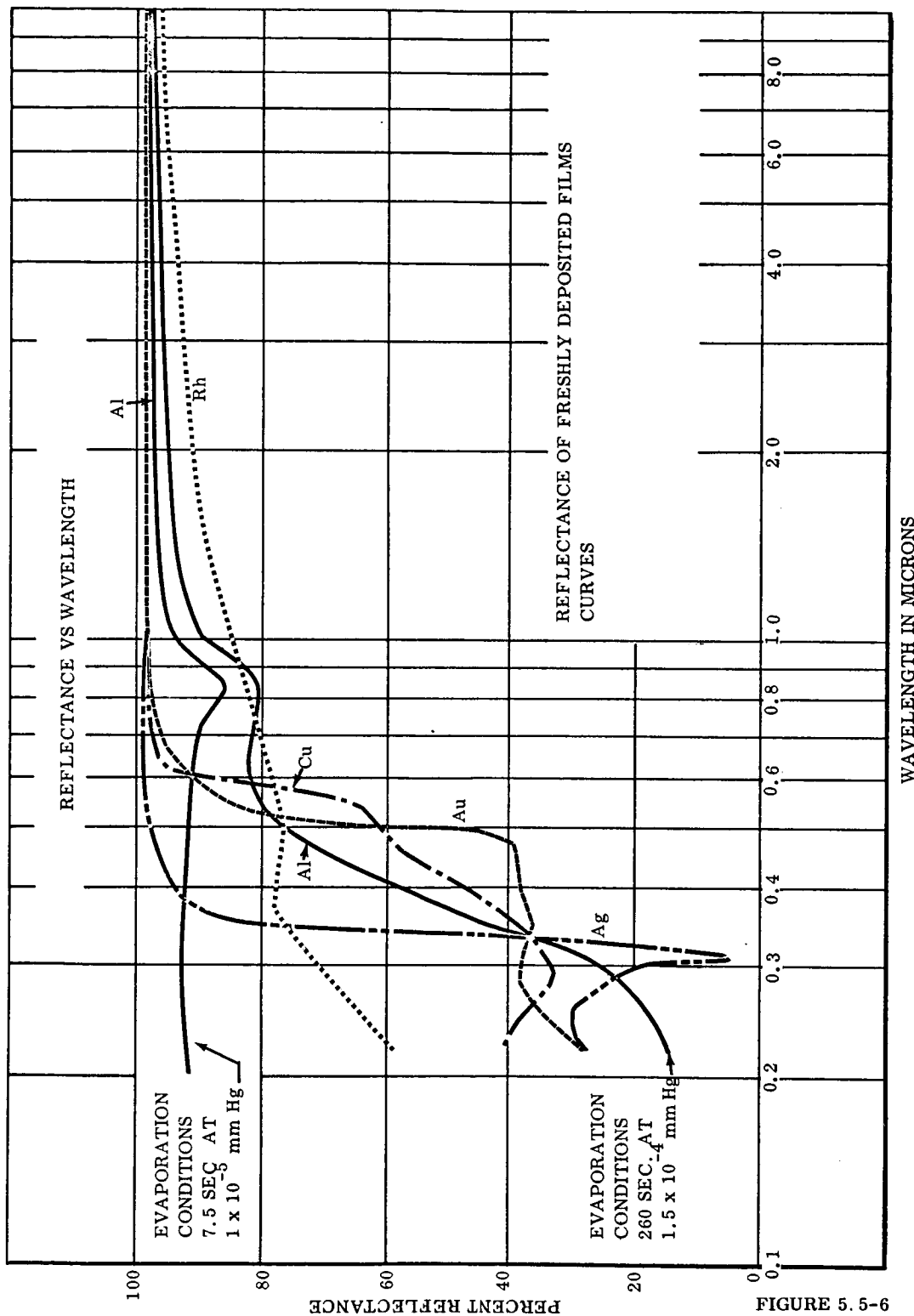


FIGURE 5-5-6

6.0 COLLECTOR FABRICATION

The thirty sectors which make up the collector are fabricated individually and involve adhesive bonding, surface improvement coating, and reflective coating. A general view of the fabrication area is shown in Figure 6.1-1.

6.1 SECTOR ADHESIVE BONDING

Of primary interest in reporting the collector fabrication is the honeycomb sandwich layup and curing techniques. Sectors were fabricated as individual parts on a single tool, using vacuum bagging and electrical resistance heat curing.

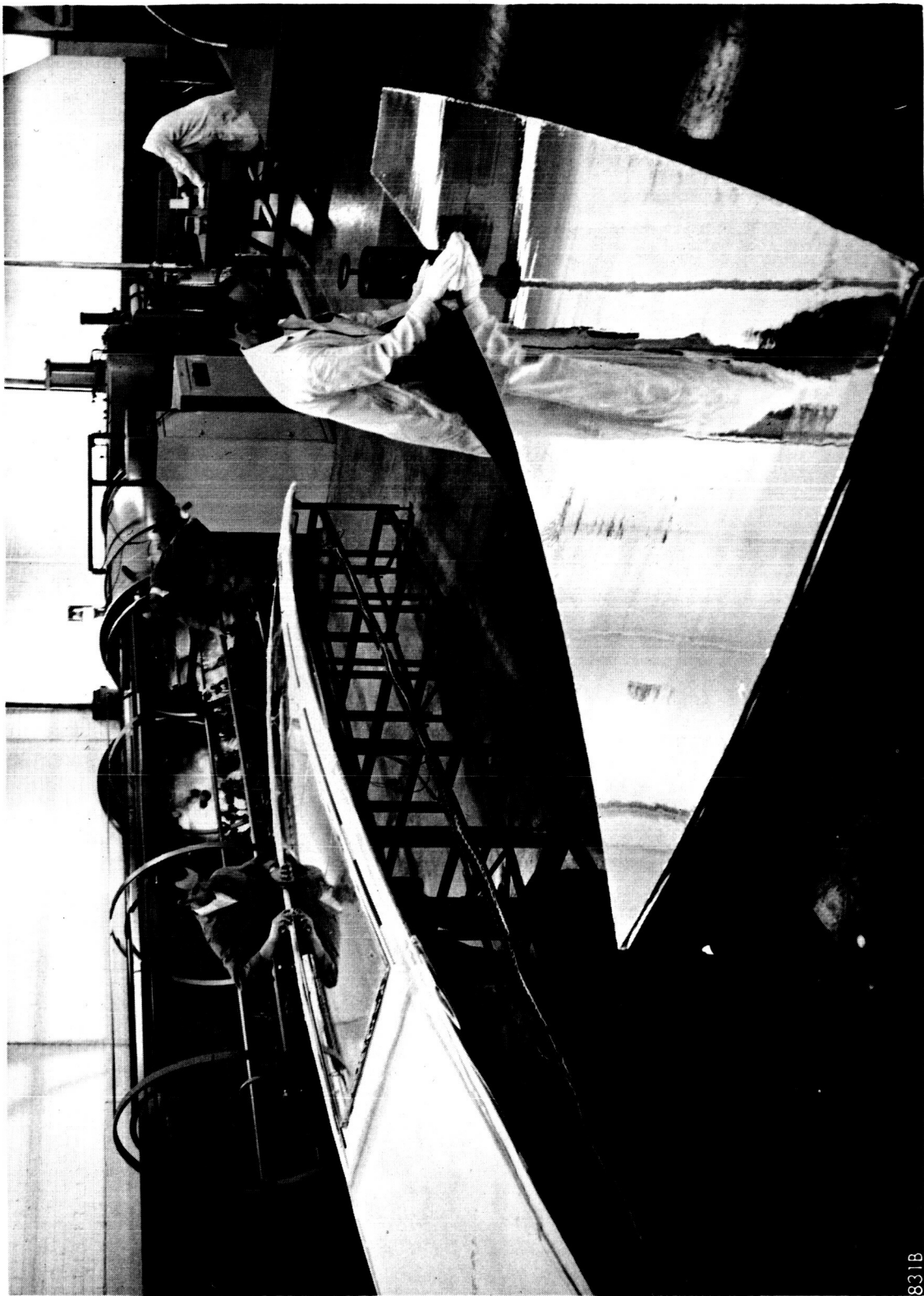
6.1.1 Tooling

The layup tool is shown in Figure 6.1-2. The surface is made up of reinforced epoxy and has a floating mounting attachment to the metal support frame to allow differential thermal expansion. This male tool was replicated from the master female pattern which is shown in Figure 6.1-3.

The master pattern was generated by sweeping out the paraboloidal shape using a master template pivoted at the optic axis. Progressively finer sweeps were made using a quick drying plaster compound. Prior to replication of the male tool, the master pattern was optically inspected using a collimated light source and the optical characteristics of the paraboloid. Metallized polystyrene with adhesive backing was temporarily applied to the plaster surface at various points and the reflected image of the collimator light beam was recorded on targets in the focal plane. The collimator can be seen in Figure 6.1-3. Areas of deviation were located and corrected. General surface deviations in the areas that were inspected showed that the master pattern was geometrically accurate within nine minutes surface normal rotation from the true paraboloid.

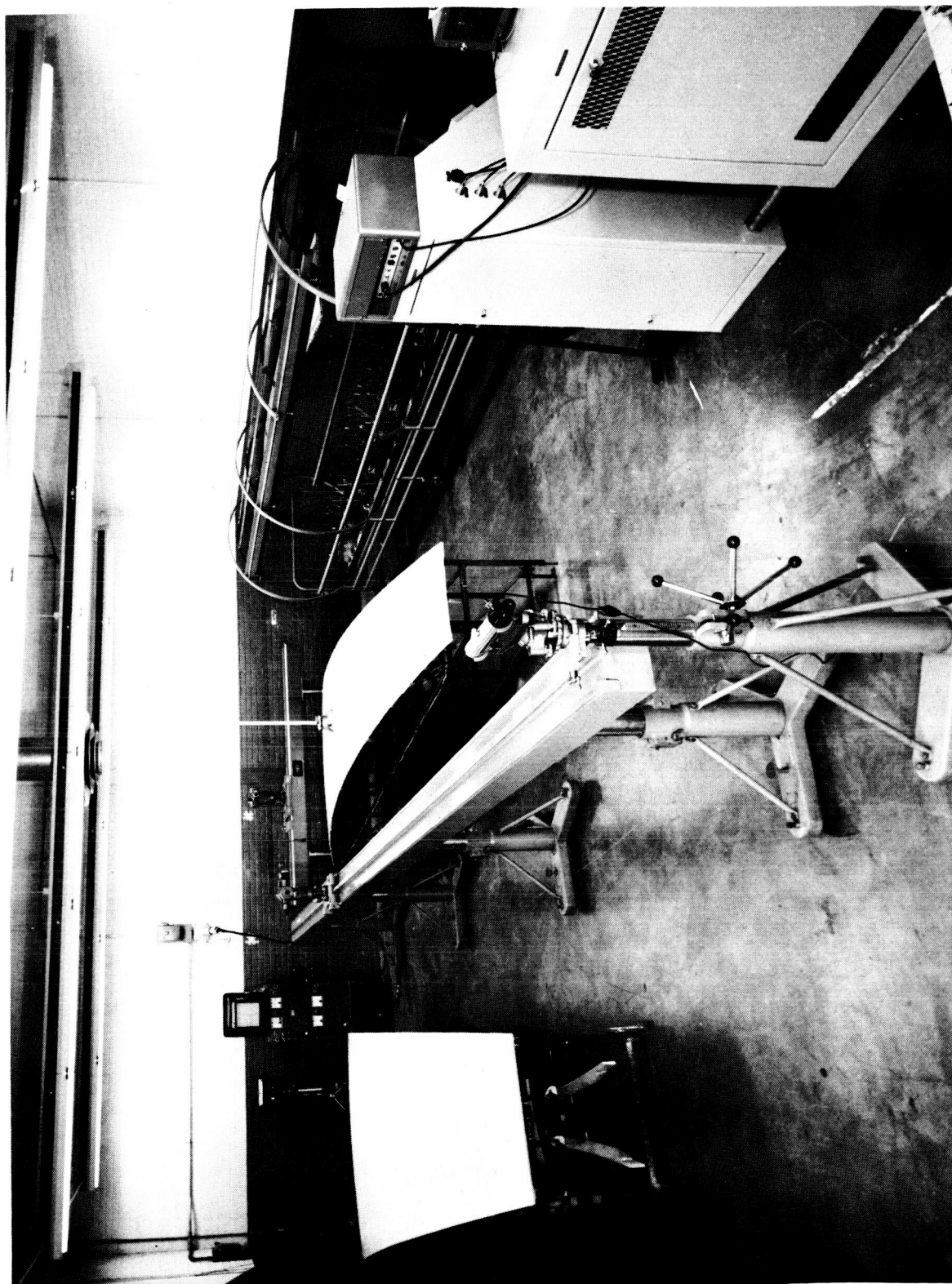
The male tool surface was layed-up directly on the master pattern in successive laminates of epoxy and reinforcing glass cloth. Electrical resistance heater blankets were also imbedded in the lay-up for later use in curing the honeycomb sectors. Also imbedded were vacuum lines and ports. Attachment lugs were bonded directly into the epoxy tool back surface, the prefabricated metal frame was attached after curing, and the completed male tool was lifted from the master pattern.

The tool design is such that the tool surface is supported by closely spaced adjustable attachments. By a combination of adjustment and barbering of the surface, the tool shape can be corrected or modified as determined by the inspection of fabricated honeycomb sectors. Initial tool leveling and alignment was accomplished using the optical tooling arrangement shown in Figure 6.1-2.



GENERAL VIEW OF SECTOR FABRICATION AREA

831B



SECTOR FABRICATION TOOL

FIGURE 6.1-2

SUNFLOWER COLLECTOR
MASTER TOOLING PATTERN

Collimated
Light Source



FIGURE 6.1-3

6.1.2 Sector Fabrication Process

The sector layup is accomplished by successive applications of face material, adhesive, and core with final heat curing to obtain the composite sandwich material. The process may be outlined as follows: The front skin aluminum foil is pulled from the roll as received from the rolling mill and is laid over the tool. The foil is trimmed to the proper shape and tape sealed around the edges. Vacuum is pulled beneath the foil through the integral vacuum ports and the foil forms to the tool. Creases which form in the foil are kept outside the part trim line. The foil surface is then cleaned for proper adhesive bonding. Honeycomb core material is expanded to the proper cell size and trimmed to the sector shape.

As mentioned in Section 5.1, adhesive is used only at the core cell walls. To accomplish this, an adhesive dip application technique was developed. Adhesive is spread on a flat table to an accurate depth. The trimmed core is dipped in the adhesive film and then placed directly on the aluminum foil already in place on the tool.

Edge closeouts and fastener inserts are fixtured to the layup and potted.

Back face adhesive is roller-coated on the exposed edges of the core. The previously trimmed and formed back face foil is applied to the layup. The entire layup is covered with a polyvinyl bag which is then sealed at the edges. A vacuum is pulled beneath this bag and the sandwich layup is thus held to the tool by atmospheric pressure.

In addition to the heaters imbedded in the tool, electrical heating blankets are placed over the bagged layup. Curing is accomplished at 175°F for approximately two hours.

After curing, the vacuum bag is removed and the part is removed from the tool. Finish hand trimming is performed along trim lines which were scored in the foil while on the tool.

Special techniques of material handling, bagging, fixturing, and adhesive application were developed to optimize the considerations of weight, strength, and geometric quality.

6.2 SURFACE IMPROVEMENT COATING

As mentioned in Section 5.6.1, a 100% solids epoxy lacquer is used to improve the specularity of the optical face before reflective coating. This coating process was accomplished on full size sectors by flow coating. A tray-like container was formed by the sector itself by adding temporary side rails. The proper mixture of epoxy and thinner was applied to the sector and flow-coated over the entire surface; the excess was permitted to run off. Epoxy application and heat curing was accomplished in a positive pressure booth. Radiant electrical heaters were used for curing.

6.3 REFLECTIVE AND TRANSPARENT COATING VACUUM DEPOSITION EQUIPMENT AND PROCESS

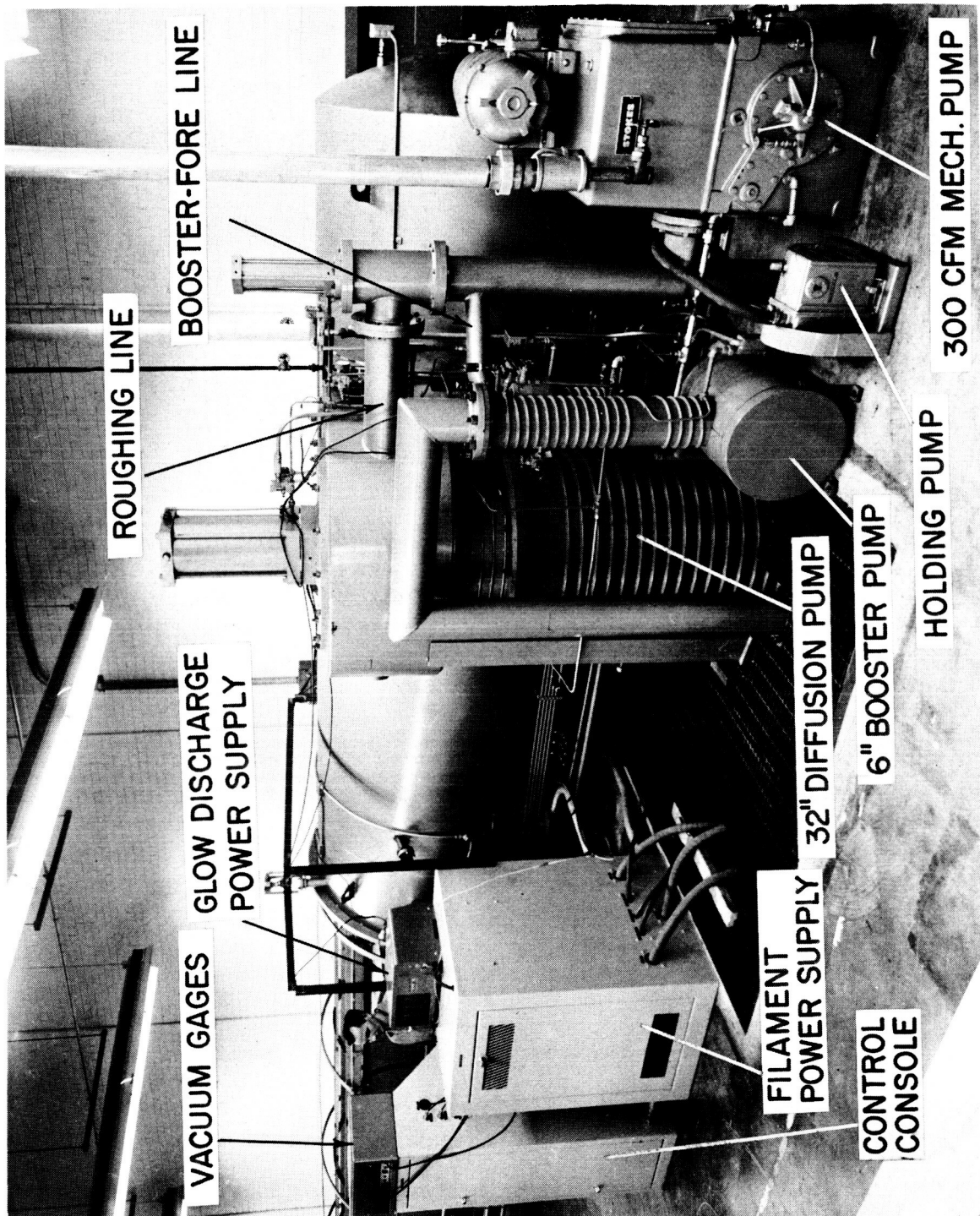
Figure 6.3-1 shows a photograph of the installed vacuum deposition facility. The chamber is a 16.5 ft long, 5 ft diameter horizontal cylinder. To have the chamber at a convenient elevation for servicing, a pit was provided for the diffusion pump. It was anticipated that during an 8 hour day, not more than 2 sectors would be coated. Since the effect of the work load on the pumping cycle could not easily be established, a 3 hour limit to obtain a vacuum of 1×10^{-9} mm Hg with an empty chamber was specified. Also, the pump capacity was to be high enough to prevent excessive pressure rise during evaporation. To meet these conditions, the manufacturer chose the following pumping system:

- a. Rough pumping through a separate line by a 300 cfm mechanical pump.
- b. Fine pumping by a 32 inch fractionating diffusion pump backed by a 6 inch diffusion-booster pump and the 300 cfm mechanical pump.
- c. When hot and valved off, diffusion pumps held under vacuum by a small mechanical pump.

All valves are pneumatically operated and controlled from the instrument panel. During the glow discharge or SiO evaporation, vacuum can be held at the required levels by bleeding air into the chamber through a needle valve. A micrometer head aids in the valve setting. This arrangement permits continuous pumping during the process cycle.

Pumping can be done by manually selecting rough or fine pumping or by setting the controls at automatic. The system performed well within design limits. The empty and clean chamber was evacuated to 1×10^{-5} mm Hg in 2 hours. A typical process cycle can be completed in 3-5 hours. The time required depends largely on the workload and atmospheric conditions. A cycle consists of the following:

- a. Evacuation into the 10^{-4} mm Hg range.
- b. Bleeding of air into the chamber to about 40 microns.
- c. Glow discharge cleaning for 10 minutes.
- d. Continuation of pumping to 1×10^{-5} mm Hg.
- e. Evaporation of aluminum.
- f. Bleeding of air into the chamber to 4×10^{-4} mm Hg.
- g. Evaporation of SiO.



VACUUM SYSTEM

FIGURE 6. 3-1

The only requirement for the aluminum film is that it reflects the maximum amount of the incident radiation. This can only be achieved if several factors are considered.

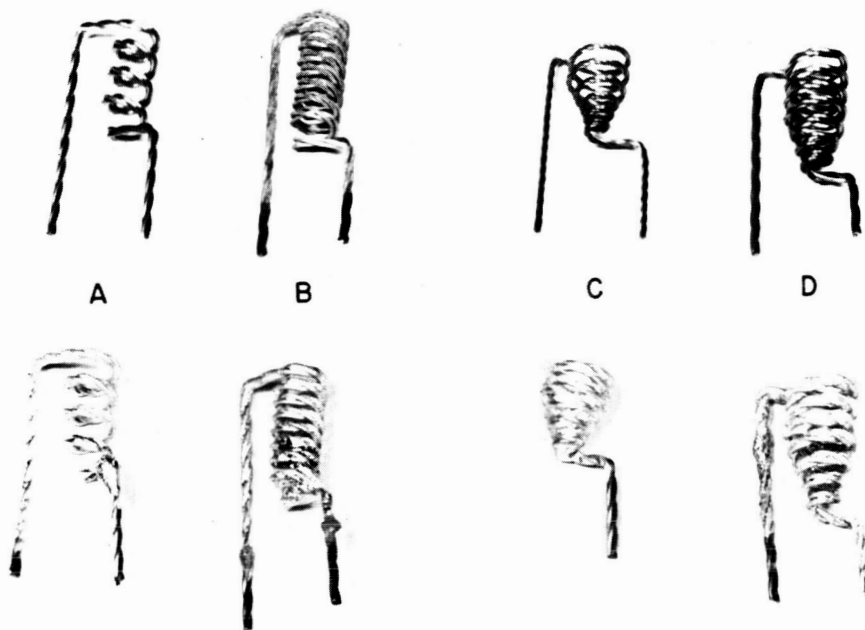
- a. The film must be opaque to solar radiation. The corresponding thickness is about 600 Å or slightly over 2 millionths of an inch.¹⁴
- b. The film should not be more than a few times the required thickness or otherwise the resultant large grains and surface roughness would decrease the specular reflectance.
- c. The angle of incidence of the aluminum vapor on the substrate should not exceed 45°. Greater angles also produce rough surfaces with the same result as item b.^{13, 16}
- d. The film should be evaporated in the shortest time, preferably below 20 seconds. Long evaporation rates tend to increase the substrate temperature with the same result as the other items.^{12, 14}
- e. Evaporation pressure should be in the low 10^{-5} mm Hg range. At high pressures, a marked decrease in reflectance (especially with lower evaporation rates) has been observed.^{12, 14}

The easiest method to check for opaqueness was found by looking at the sun through the deposited aluminum film on a glass substrate. If no light is visible, the film is opaque. If the sun appears as a pale disc without any discomfort to the eye, the transmissivity is about 0.01%. This is about the brightness of the moon. A transmissivity of 0.1% is already too much for the eye. These comparisons were obtained by measuring the transmissivities of green light, 5000 Å wavelength, with a photometer.

To obtain an opaque film, several evaporation filament types were tried. Figure 6.3-2 shows the various configurations. Types A and B are cylindrical with their center line in the direction to the substrate. Type A did not produce an opaque film. Type B improved the situation only a little, although it had twice as many windings.

To increase the amount evaporated in an upward direction, basket type filaments were tried. Type C made from thinner tungsten wire collapsed but type D proved satisfactory. The necessary power is supplied by a 50 KW saturable core reactor with an output of 2850 amperes. The lines carrying the current are rubberized braided copper hoses with internal water cooling. The angle of incidence of the vapor atoms is controlled by stainless steel sleeves around the filaments.

SiO is evaporated from tantalum crucibles (Figure 6.3-3). They are made from three concentric cylinders, the innermost holding the SiO granules around the filament and the outer two serving as radiation heat shields. The filament ends pass through insulators at the bottom to the conductors.

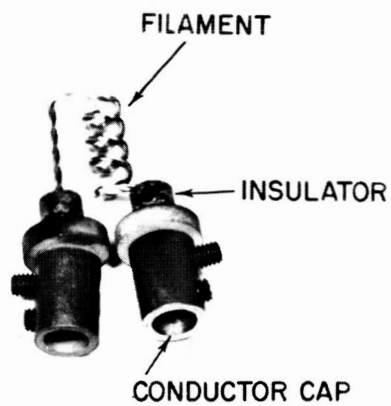


FILAMENT TYPES

FIGURE 6.3-2



TANTALUM CRUCIBLE



SILICON OXIDE EVAPORATOR

FIGURE 6.3-3

Evaporated silicon monoxide has an amber-brown color. At certain conditions, all colors of the spectrum were produced. To obtain a transparent non-absorbing coat, silicon monoxide must be evaporated in an oxidizing atmosphere to obtain a chemical composition of Si_2O_3 to SiO_2 .^{6,9} By bleeding air into the chamber during evaporation and adjusting the needle valve to obtain a pressure of $2 - 4 \times 10^{-4}$ mm Hg, sufficient oxygen is supplied for oxidation.

Maximum reflectance from a protected surface is obtained if the coat thickness is one half of the wavelength of the radiation. Since the solar radiation covers a broad band and the angle of incidence to the paraboloid varies from the inside to the rim diameter, optimum thickness and permissible tolerances were calculated. Optical constants were only available for the range from 4000 Å to 9500 Å of the solar spectrum and the corresponding thickness was found to be $1000 \text{ Å} \pm 20\%$. This would result in a 3/4% reflectance variation from the high to the low point. However, it seems improbable on such a large structure that all points could have a thickness bordering the tolerance band. Reflectance tests to verify these calculations and to extend the values beyond the calculated spectrum width should be conducted.

To meet the tolerance requirement, 37 filaments were spaced (Figure 6.3-4) so that their evaporation patterns blended into each other. Locating the evaporators at elevations similar to the curvature of the sector permitted even spacing for the full length. Having determined the location of the SiO sources and letting the aluminum sources share the same common power line determined the number and location of the aluminum filaments. This insured a fairly uniform thickness of the aluminum film.

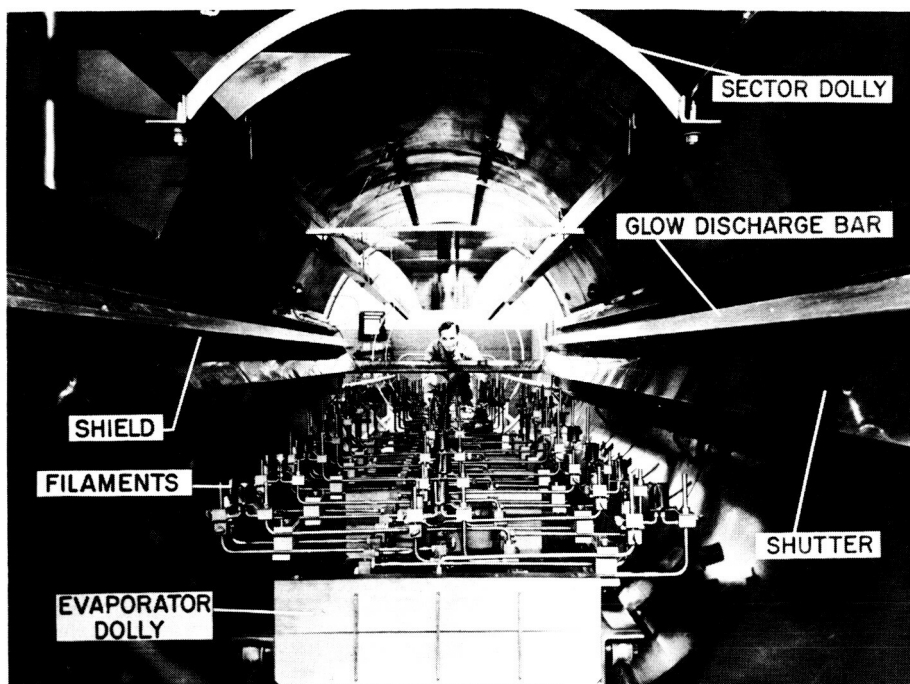
Initial heating of the filaments and charges results in some outgassing. At the evaporation pressures, the outgassed vapors will travel in a straight line and condense on the substrate. To prevent contamination, a shutter, running the full length of the chamber, is closed until deposition is started.

On top of the shutter are two electrically insulated aluminum bars serving as cathodes for glow discharge. The bars are 16 ft long, 2 in. wide and 1/4 in. thick. An evaporation shield was added toward the center of the chamber so that evaporated SiO will not deposit on the bars. Otherwise, the glow will quickly diminish and render the attempted cleaning process useless. Figure 6.3-5 shows the glow as seen through the lower sight port.

Ionized gas will heat the substrate it bombards. Measuring the temperature will therefore give an indication of the effectiveness and uniformity of the cleaning process.

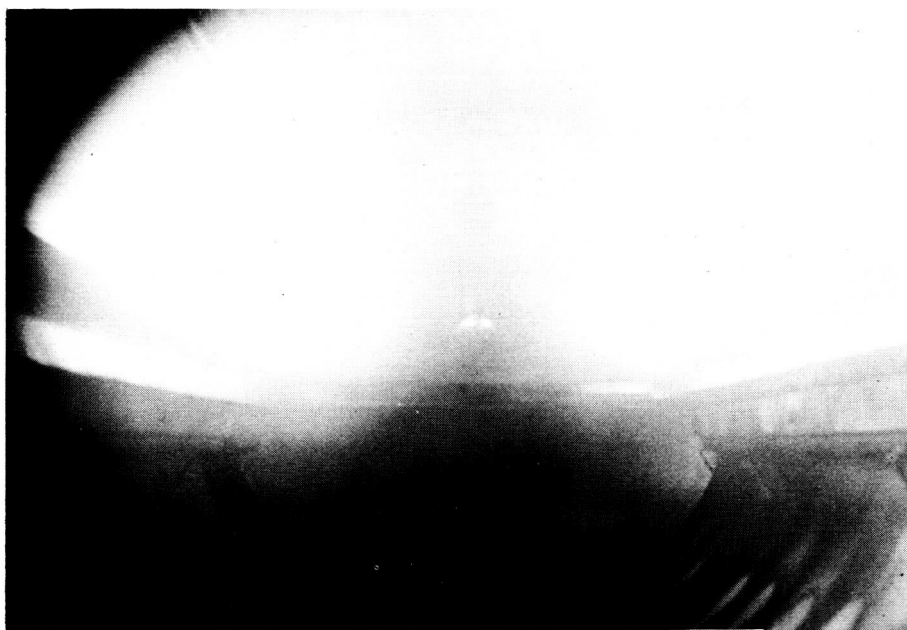
Figure 6.3-6 shows the temperature distribution for some test runs. Ideally, a flat temperature curve is desirable. However, having a doubly curved surface with varying widths makes the attainment of this goal rather difficult. An improvement can be expected by twisting the aluminum bars at the wide end of the sector toward the outside to reduce overlapping of the ion pattern in the center.

As can be seen, the resultant temperature rise at constant current is also a function of the residual air pressure. Higher pressure tends to carry more of the heat away



DEPOSITION CHAMBER INTERIOR

FIGURE 6.3-4



GLOW DISCHARGE WITH SHUTTER OPEN

FIGURE 6.3-5

TEMPERATURE DISTRIBUTION

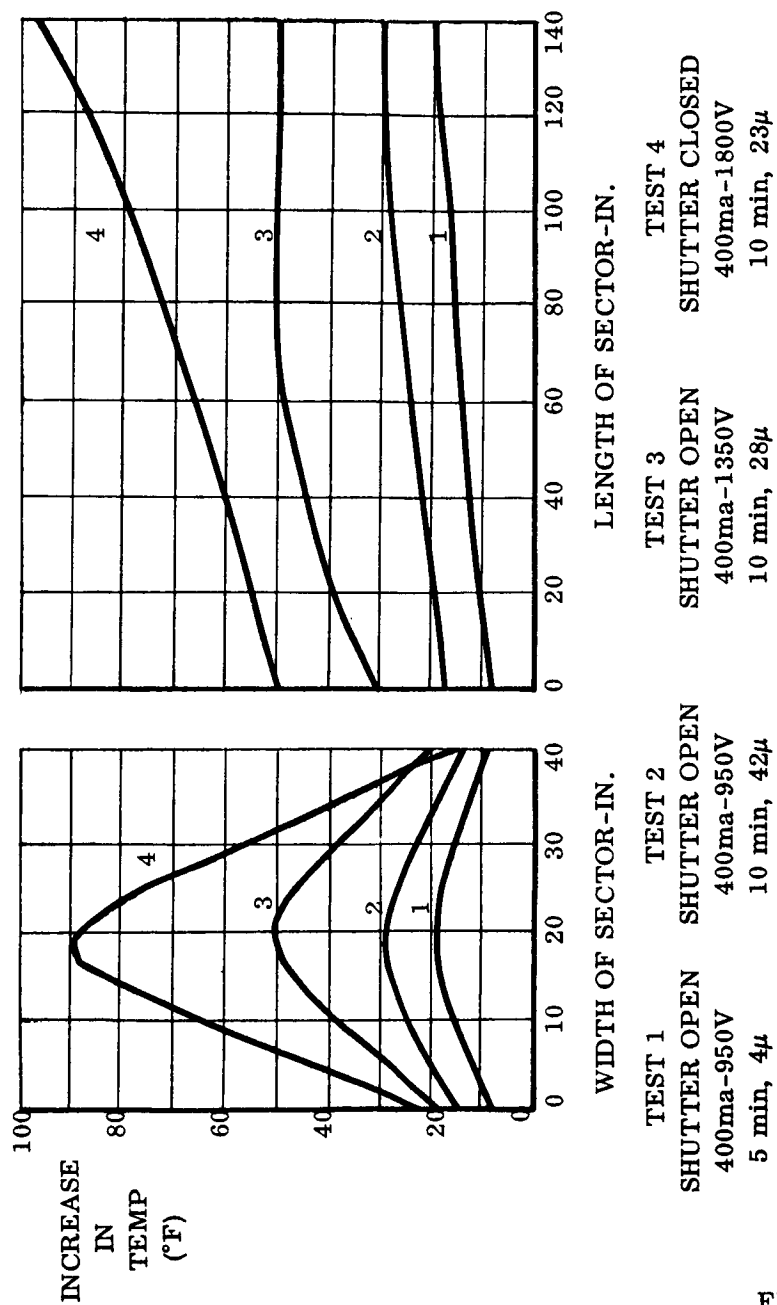


FIGURE 6.3-6

by air conduction and convection. The glow pattern greatly diminishes as the pressure is reduced below 20μ and stops at about 8μ when the maximum potential of 5000 volts dc is reached. In this range, the current drops also, requiring constant adjustment.

Glow discharge cleaning cannot be relied upon as the primary substrate cleaning technique. It will only remove contaminations usually left after other cleaning processes. It was therefore necessary to clean the substrate carefully before placing it into the vacuum chamber. Many cleaning processes are described in literature. They are designed to obtain utmost cleanliness but were developed for rather small substrates of a few square inches. Trying to apply these methods to about 30 square feet is, from an economic point of view, not possible. Chemical cleaning could not be employed since most chemicals would attack the substrate and degrade the surface finish. The best results obtained so far employed washing with a 2% Aerosol OT solution in distilled water until no water breaks were observed. This was followed by several rinses of distilled water.

Several port holes were provided in the evaporation tank to observe the various processes and to afford control.

Eliminating potential personnel hazards and protecting the equipment were two of the many considerations in the design of this unit. The following safety features were incorporated.

- a. Internal lighting.
- b. Circuit cut off switch in chamber flange to prevent opening of valves when door is open.
- c. Safety chain to prevent closing of door. One end is permanently fastened to the outside and the other end is hooked up by the operator when inside the chamber.
- d. A one minute time delay switch in the valve opening circuit.
- e. A dead man switch on the inside of the door, again to interrupt the valve open circuit.
- f. Pressure limit switch to prevent accidental closing of high voltage and filament power when door is open.
- g. Coolant flow limit switch to cut off vapor pump heater during low flow or water failure.
- h. Critical valves in fail safe position, closing during air pressure failure.

For ease of servicing, the evaporator assembly, shutter, and sector fixture can be rolled out of the chamber onto a carriage as needed. The carriage wheels are guided

inside a channel track to insure alignment of the individual dolly tracks on the carriage with those inside the chamber.

Since the concurrently running surface improvement efforts indicated, toward the end of the program, the need for a lacquer coating, a change had to be made in the evaporation cycle. It was found that an intermediate film of SiO_x between the lacquer and the pure aluminum film increased the adhesion of the aluminum and decreased the susceptibility to thermal shock flaking during hot water tests. The SiO_x film also would provide an effective diffusion barrier for any volatiles still present in the cured epoxy lacquer.

The thickness of evaporated SiO_x films could be continuously checked during the evaporation by observing the color spectrum of light which it reflected. A diffuse, low intensity white light beam was reflected from the substrate at an angle of 80° from the normal. The reflected light was observed through a viewing port. Initially, the light only reflected and appeared white. But with increasing film thickness, refraction and interference produced colors cycling through the visible spectrum. To initially establish the color-to-thickness relationship, optical flats were coated until a particular color appeared. The thickness was then measured with an interferometer and plotted as a function of color and spectrum number. The resultant plot, Figure 6.3-7, was then used to predict film thicknesses.

Measured results of the reflective coatings obtained will be presented in Section 7.3.5.

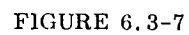
6.4 PREPROTOTYPE COLLECTOR FABRICATION TECHNIQUE DEVELOPMENT

During the fabrication of the thirty sectors for the preprototype collector, improvements in the processing and handling techniques were continually being made. In many cases, however, these developmental improvements were not made because they were beyond the reduced scope of the Sunflower program redirection of January 1962, which defined the preprototype collector as primarily a structural integrity development copy.

Some of the compromises which were made during the fabrication period will be listed here to qualify the inspection and test results to be presented later.

- a. Only nominal adjustment and barbering of the tool surface was made to optimize geometric quality.
- b. Reinforcing doublers were added, as stated in Section 5.5, to prevent markoff and peeling due to over-stressed edge condition.
- c. No reflective coating was put on the majority of the sectors. Only sectors which were solar tested were reflective coated.
- d. Preprototype detenting locks were used only at the tips of the sectors. The intermediate locks were simulated by aluminum straps.

COLOR OF
REFLECTED
LIGHT



6.5 PREPROTOTYPE COLLECTOR ASSEMBLY

Accurate assembly of the thirty segments of the paraboloid is accomplished by a combination of optical and geometric references. Figures 6.5-1 shows the collector assembly area and partially assembled preprototype collector. It is seen that the entire area is covered by a circular over-head crane arrangement for use in optical inspection and for access to the upper areas of the stowed collector. Mounted on the observation platform of the crane is a grid-screen arrangement for optical inspection and a ten-inch diameter collimated light source for optical alignment.

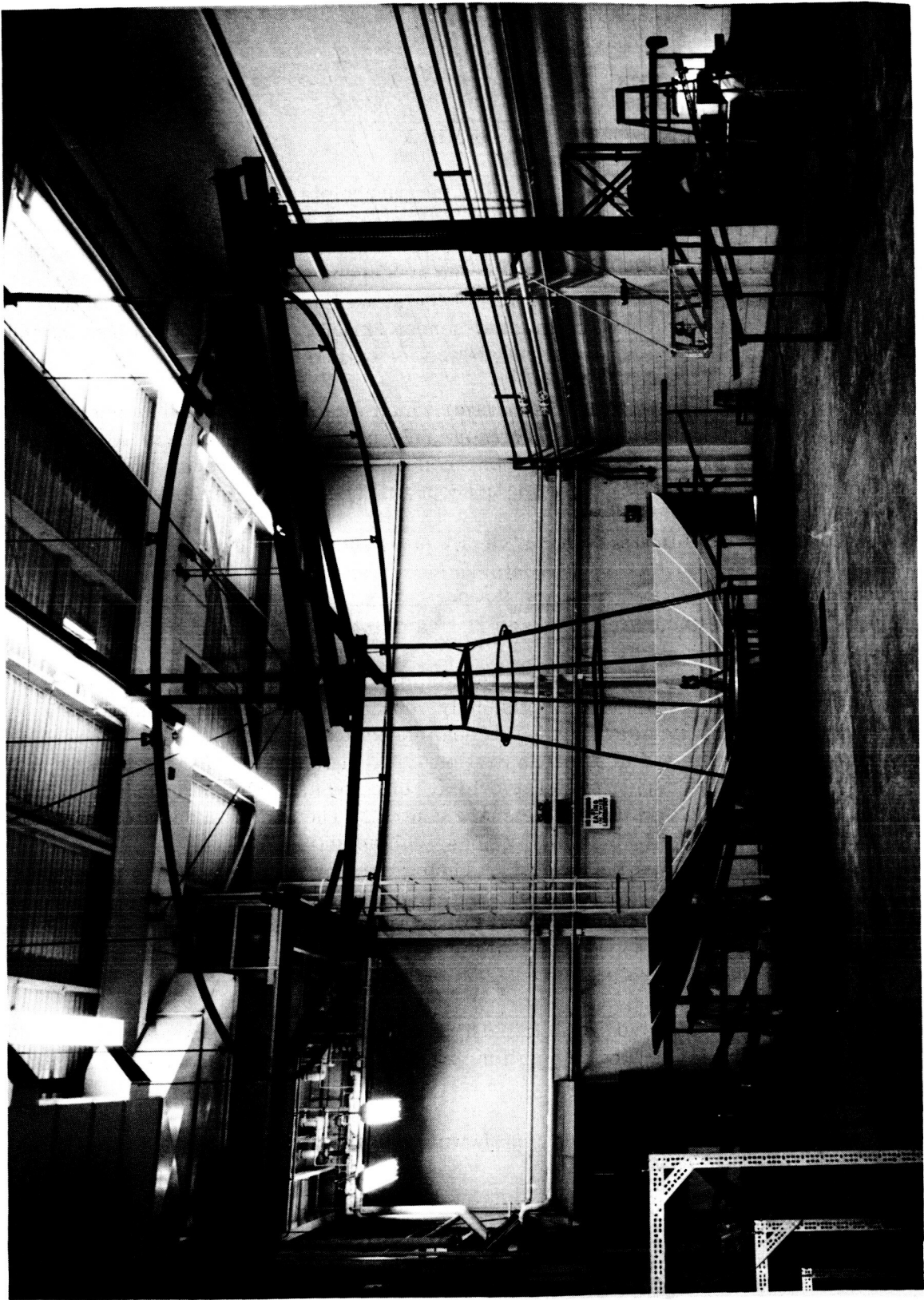
Located at the focal point is a projection lamp which illuminates the collector surface. Reflected light from the collector will be nominally parallel to the optic axis. Deviation from the true parabolic surface can be observed using the grid-screen arrangement. Additional discussions of this inspection concept will be presented in Section 7.0.

Sector-hinge subassemblies are geometrically positioned on the center support ring by sighting reference targets on the sector using a transit. During assembly, the sectors are supported by fixtures from the floor. The collimator is used for final alignment to optimize the optical characteristics of the individual sectors.

The entire assembly concept is designed to establish the optimum zero gravity shape for the assembled collector. Before assembly, each sector is optically inspected in its free or zero "g" shape using a grid-screen inspection similar to that on the assembly rig. This will be discussed in detail in Section 7.0. Photographs of the grid pattern are taken to record the inspection. The orbital collector assembly can then be made by using the inspection photographs as the shape control. The sector support fixtures are used to prevent sector dead weight deflections; with adjusting screws, the sector is adjusted to match the free position inspection photographs by comparison with the grid-screen arrangement on the assembly rig. As the sectors are positioned in their zero "g" position, the locks are attached without distorting the sectors. In this way, stresses induced in the sectors by the assembly will be minimized; thus, the zero gravity optical characteristics can be controlled.

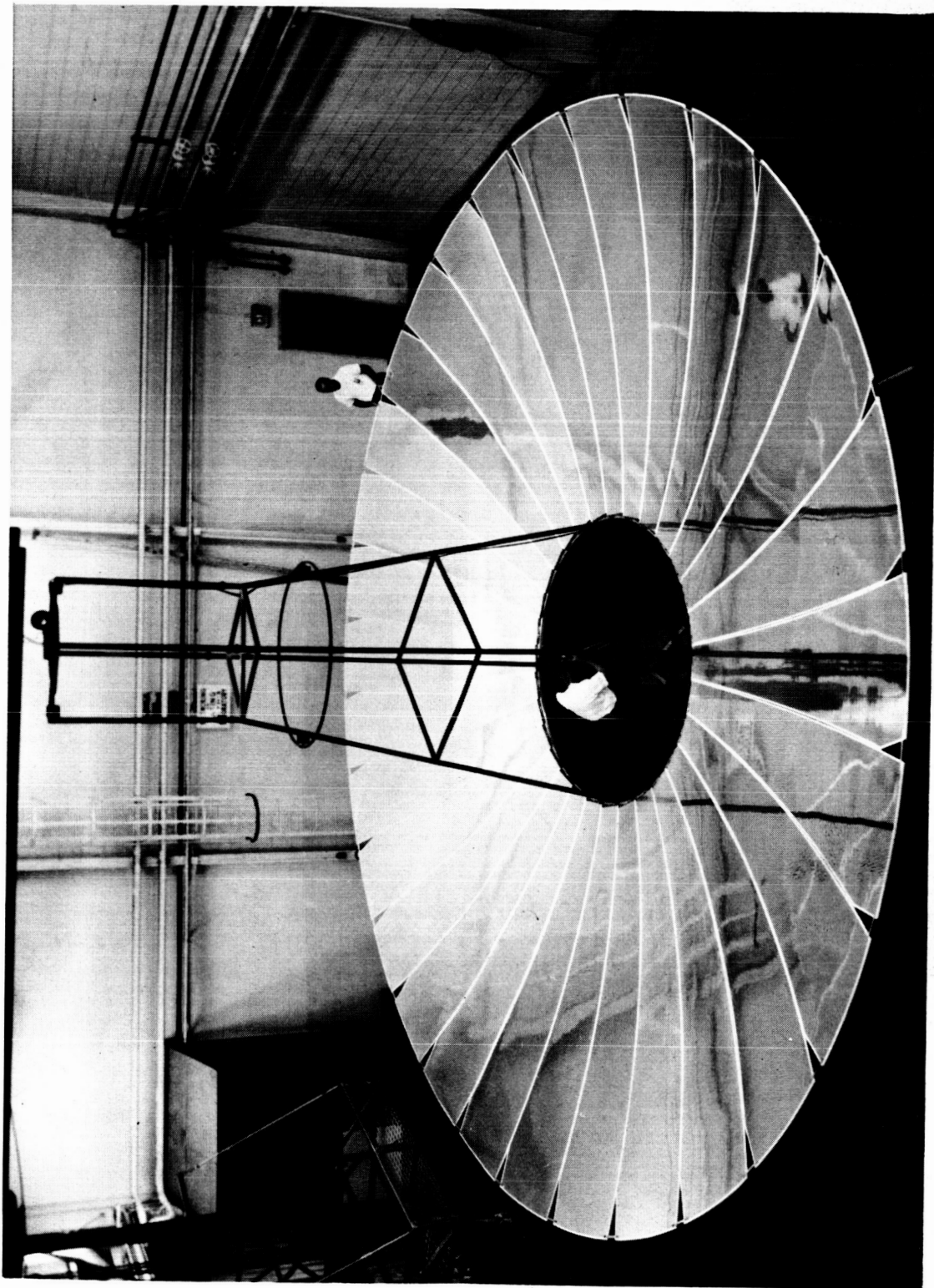
Intermediate to the optical and geometric alignments in the parabolic shape are periodic checks of the sectors in the stowed position for symmetry and additional hinge adjustments.

The assembled preprototype collector is shown in Figures 6.5-2 and 6.5-3.

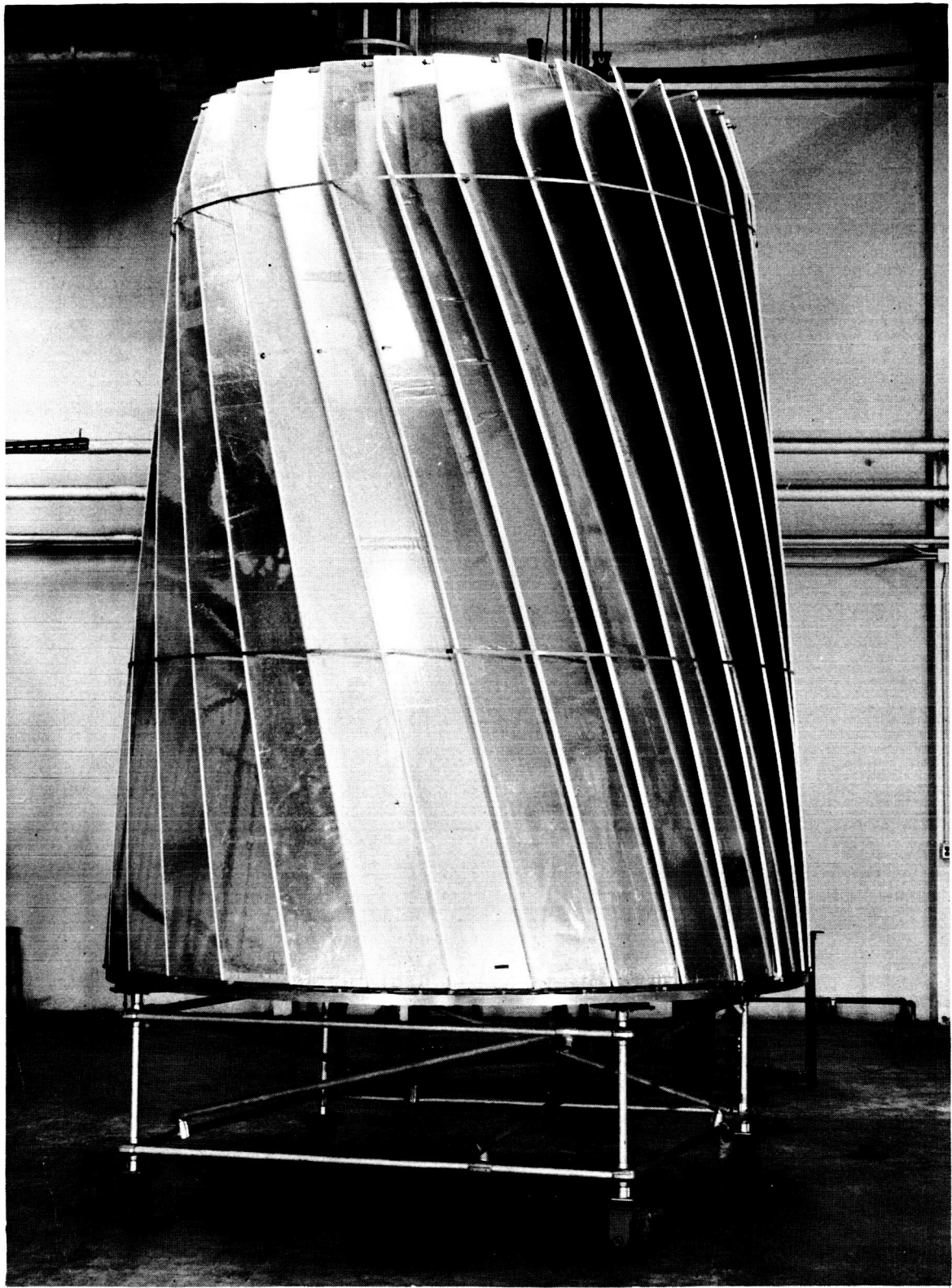


COLLECTOR ASSEMBLY AREA

FIGURE 6.5-1



ASSEMBLED SUNFLOWER PREPROTOTYPE COLLECTOR



SUNFLOWER PREPROTOTYPE COLLECTOR STOWED POSITION

FIGURE 6.5-3

7.0 INSPECTION AND OPTICAL TESTS

7.1 GENERAL COMMENTS ON OPTICAL TESTING

Evaluation of paraboloidal mirrors can be easily determined using the optical characteristics of the mirror. Various approaches to optical testing using these characteristics can be pursued. In the Sunflower development program, two specific optical test approaches were selected and adapted to the collector characteristic of large size and relative optical quality range. These two approaches are:

- a. The use of a collimated light source parallel to the optic axis, which will ideally reflect to the focal point.
- b. The use of a point source of light at the focal point to illuminate the collector and ideally reflect collimated light.

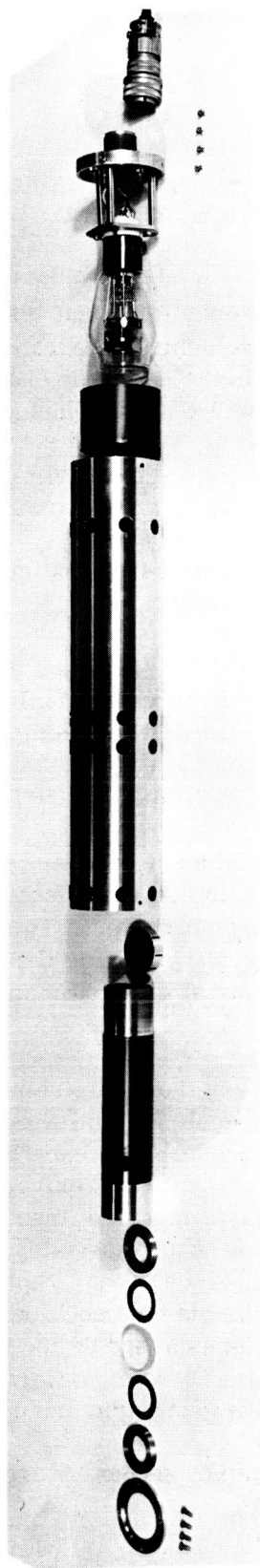
Several collimators were built and used for alignment and testing. A point source - grid screen system of inspection was designed and built as the primary inspection device for both single sectors and the complete collector.

7.2 TEN FOOT DIAMETER COLLECTOR MODEL OPTICAL INSPECTIONS

Early in the Sunflower collector development program, optical inspection tests were performed on a ten foot diameter petaline solar collector which was previously fabricated on a company-sponsored research program. The collimated light source shown in Figure 7.2-1 was used in a ray trace type test to determine geometric accuracy; a photometer was used to investigate optical characteristics such as reflectivity and concentration effects.

The primary results of this testing were the establishment of test procedures and data analysis methods suitable for the full scale Sunflower collector. It was established that the collimated light ray trace procedure was excellent for optical alignment and positioning during assembly; but for inspection of extremely large surface areas such as the Sunflower collector, a more rapid means of inspection was desirable. Also, even a collimator for use as an alignment and assembly tool should have a large aperture to average a greater portion of surface area. Photometer measurements established that reflectivity of the composite surface could not be determined accurately due to the curvature and local concentrations caused by the honeycomb cells. Using these conclusions and based upon the specific characteristics of the Sunflower collector, the following general areas and methods of geometric and optical inspection was established:

- a. Measurement of gross geometric errors by use of the point source - grid screen method.
- b. Measurement of honeycomb markoff and surface finish with a profilometer.



COLLIMATED LIGHT SOURCE EXPLODED VIEW

FIGURE 7.2-1

- c. Reflectivity measurements on a flat specimen basis using standard spectral reflectometers.

7.3 SECTOR INSPECTION

7.3.1 Types of Surface Deviations

The following specific areas of surface deviations have been identified and measured:

- a. Spring - back
- b. Gross waviness
- c. Honeycomb - markoff
- d. Random markoff
- e. Surface micro-finish

These types of deviations are represented in Figure 7.3-1. Spring-back was observed as a general longitudinal flattening-out of the sector. It is caused by relief of stresses built-up during the fabrication process. Gross waviness deviations are in the form of large period waves along the sector length or of flat spots in the parabolic shape; they are caused by errors in the tooling master or replication.

Honeycomb markoff, as mentioned previously, is characteristic of the Sunflower collector sandwich material. Random markoff is the term used for effects such as edge discontinuities, core splice areas, and fastener area markoff. This random markoff was found to involve very small amounts of surface area and, when proper consideration is given in design, processing, and handling, this source of error can be considered negligible. Surface micro-finish is a deviation which is associated with reflectivity more than geometric accuracy. It was discussed in Section 5.6.1.

7.3.2 Sector Optical Inspection Facility Description

Gross waviness inspection of the finished sectors is made by using the optical characteristics of the paraboloid. The part is mounted in the inspection fixture shown in Figure 7.3-2 using a template referencing system.

Since the individual sectors are quite flexible in a direction normal to the optical surface, the part is supported on edge at both ends in pivoting supports. This allows the sector to assume its free position, thus simulating a zero gravity inspection. Located at the focal point of the sector is a small light source which illuminates the sector. The reflected light from the sector is nominally parallel to the optic axis by virtue of the optical characteristics of a paraboloid. By viewing the grid-screen arrangement which is aligned to be parallel, deviations of the reflecting surface of the sector are observed as misalign-

CLASSIFICATION OF SURFACE DEVIATIONS
FROM THE TRUE PARABOLOID

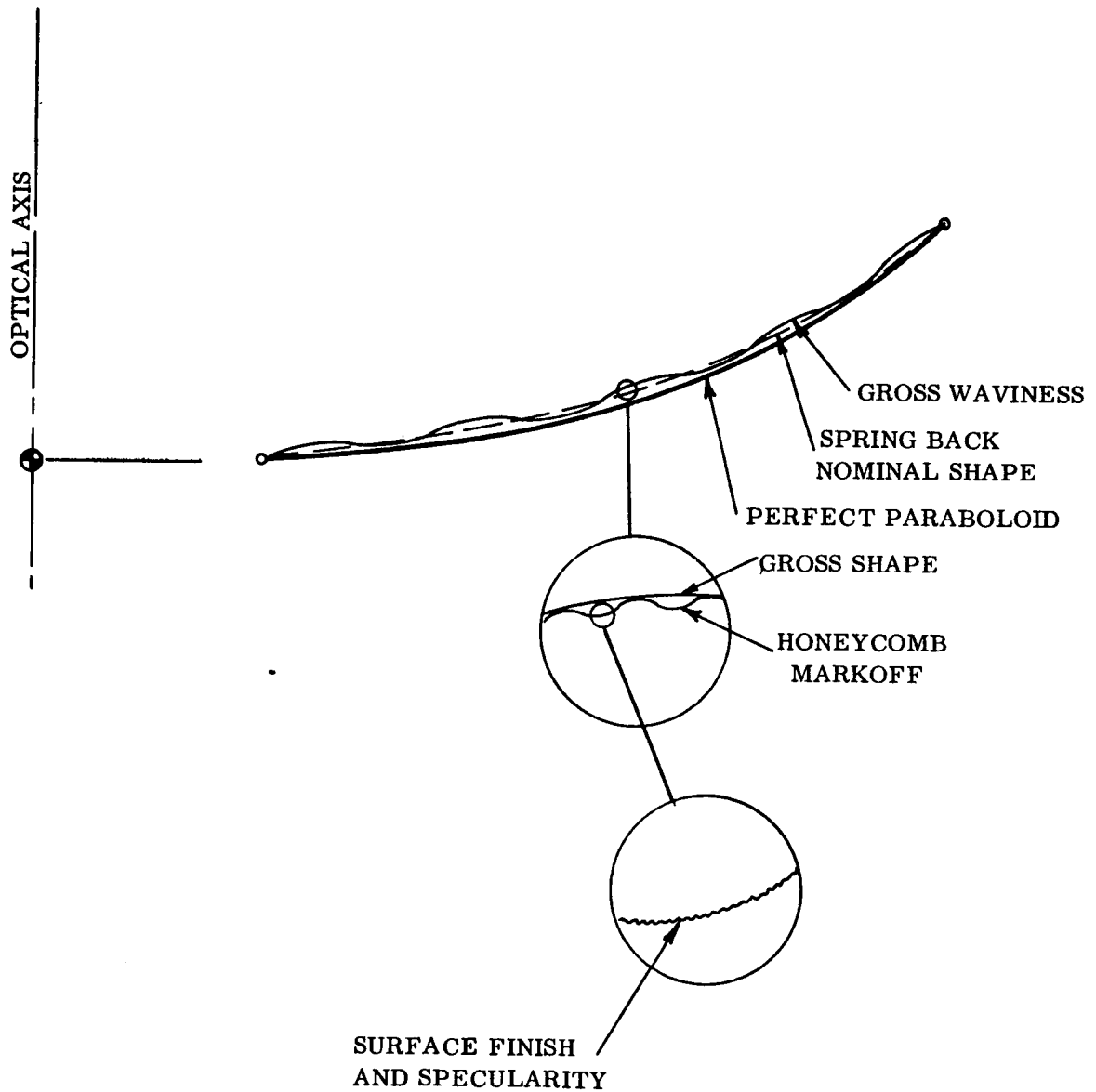
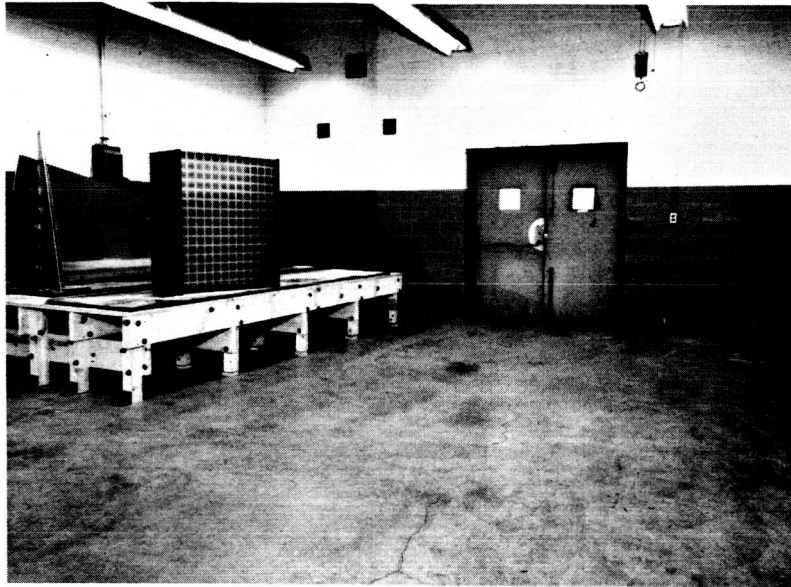
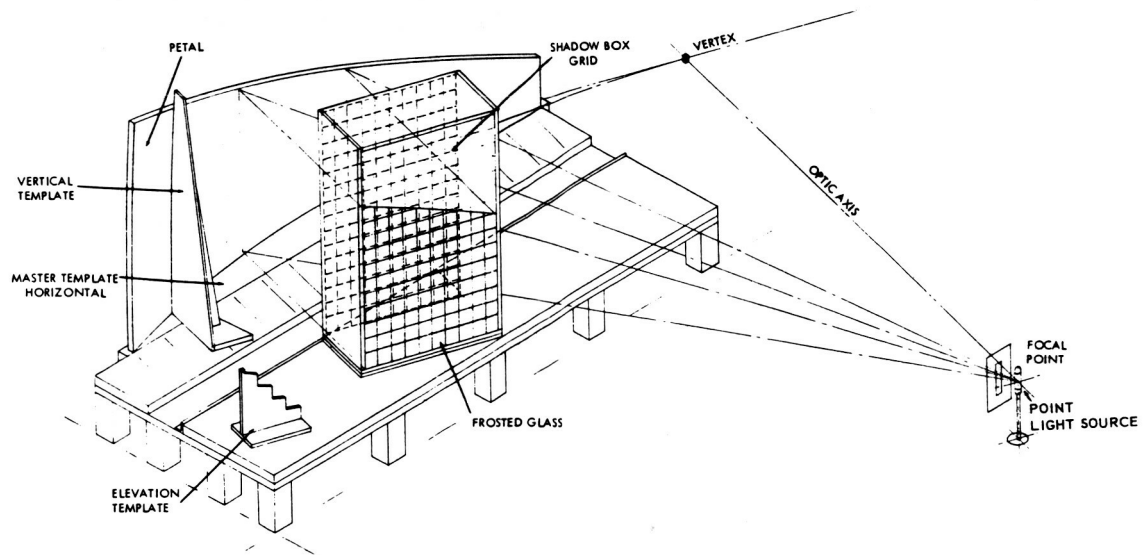


FIGURE 7.3-1

SINGLE SECTOR OPTICAL INSPECTION FACILITY



SUNFLOWER PETAL INSPECTION RIG



ment of the grid shadow on the screen. The shadow box traverses the entire length of the part and photographs are made of the screen to record the deviations. Dimensional measurements are also made and recorded using the template coordinate system.

7.3.3 Sector Optical Inspection Results

A typical grid screen inspection photograph is shown in Figure 7.3-3. It is seen that error deviations in both the radial and circumferential directions can be measured. A composite photograph of sector SPTR-1 is shown in Figure 7.3-4.

Error indications for each increment can be measured. By using a geometric relationship, the gross angular deviation of the surface at each location was plotted as shown in Figures 7.3-5 and 7.3-6 for the radial and circumferential deviations, respectively. Spring back effects can also be seen.

An indication of optical quality can be obtained from this data by relating surface area to the surface deviations. Figure 7.3-7 shows the percentage of collector intercepted area which is within various degrees of quality. The shaded area shows the range of differences between a row of data points along the centerline and those at the edges. The spring back is also shown plotted, and in the worst case would be additive with the gross waviness.

Figure 7.3-6 shows that the measured circumferential errors are large and are an overcurvature of the sector in the short direction. This characteristic was traced to be a permanent set which had occurred in the fabrication tool after several curve heating cycles.

7.3.4 Honeycomb Markoff Inspection Results

The honeycomb markoff, which is typical of the Sunflower collector material, was investigated using the proficorder shown in Figure 5.5-1. This instrument not only plots micro-finish but also can be adjusted to plot waviness profiles. Typical honeycomb - markoff profiles are shown in Figure 7.3-8 for specimens which were actually cut from sector SPTR-1 after solar testing (see section 8.1.1). These show the best and the worst cases of honeycomb markoff which were observed. For SPTR-1, an estimated 40% of the surface had the lower value of markoff, while the remainder was between the 6 minute minimum and the 26.4 minute maximum. With improved process control, it is believed that 95% of the surface would have cell markoff within the lower slope deviation.

Since the surface deviation in a cell varies over the hex (Figure 7.3-8), these typical slopes can be area-weighted. The results are shown in Figure 7.4-1 for the measured data from SPTR-1. Other sectors which were inspected showed similar characteristics.

PROJECTION GRID INSPECTION RESULTS

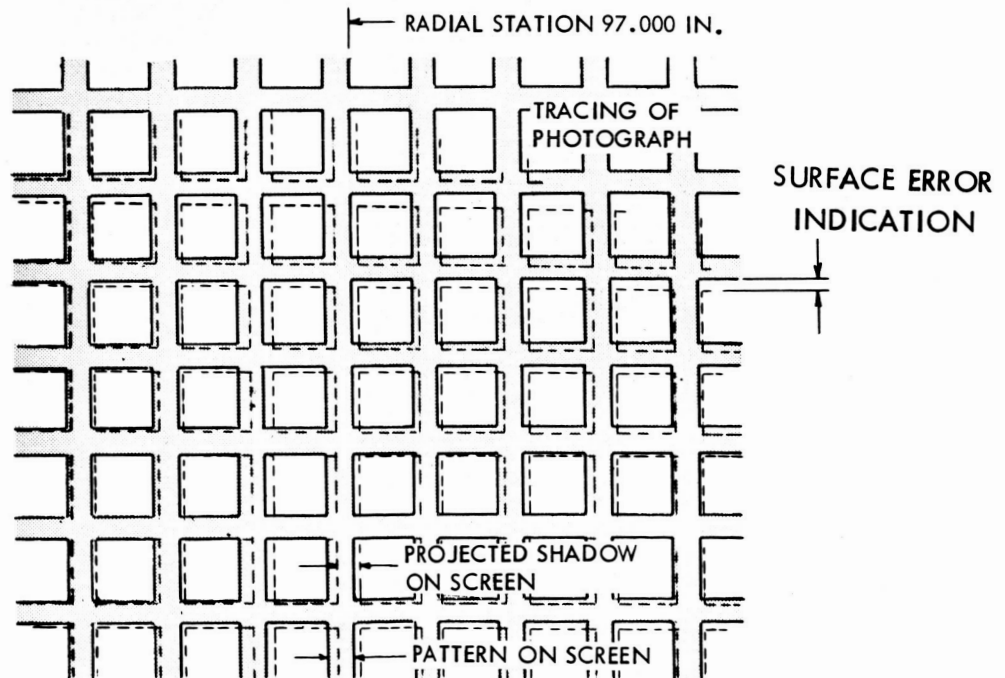
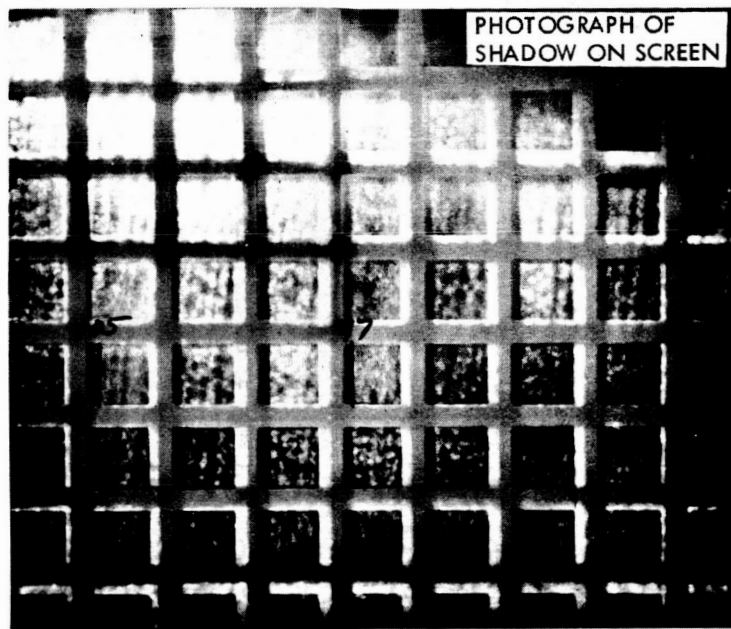
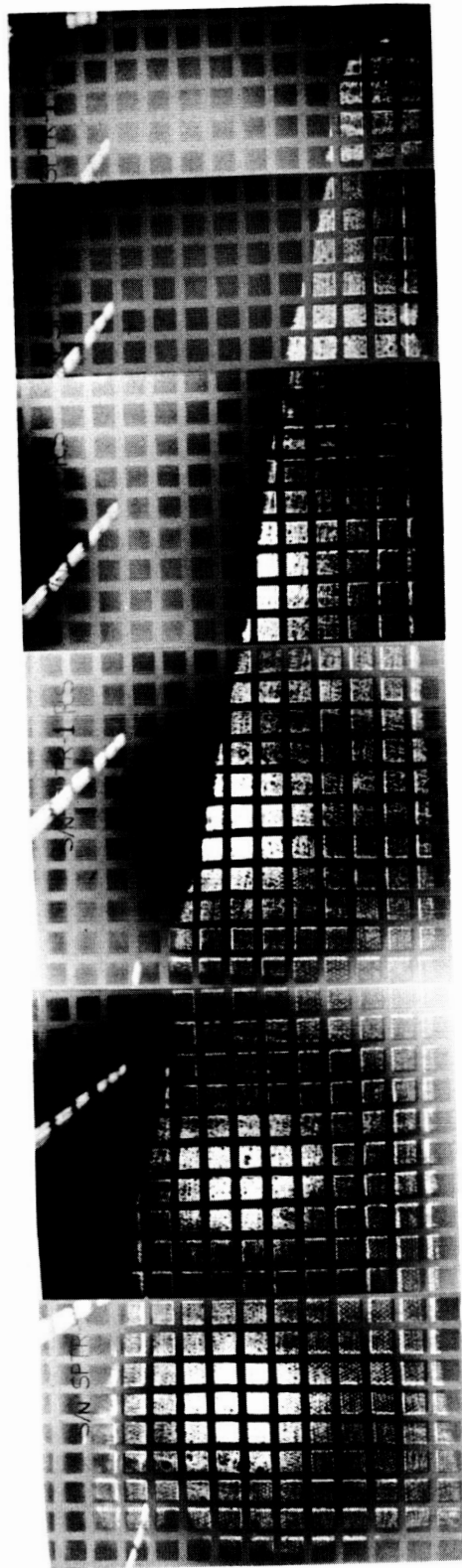


FIGURE 7.3-3



SECTOR SPTR-1

OPTICAL INSPECTION RESULTS RADIAL DEVIATIONS

SPTR 1

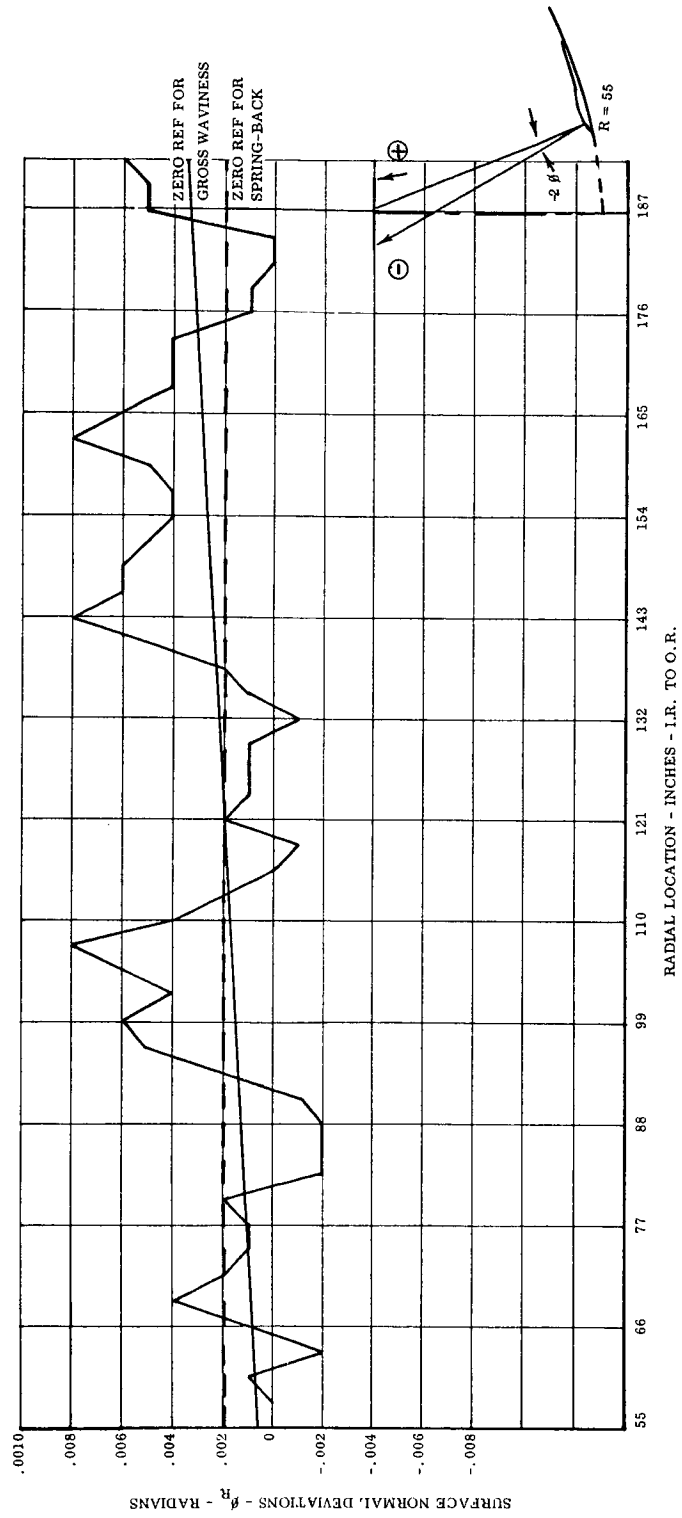


FIGURE 7.3-5

OPTICAL INSPECTION RESULTS CIRCUMFERENTIAL DEVIATIONS

SR-IR-1

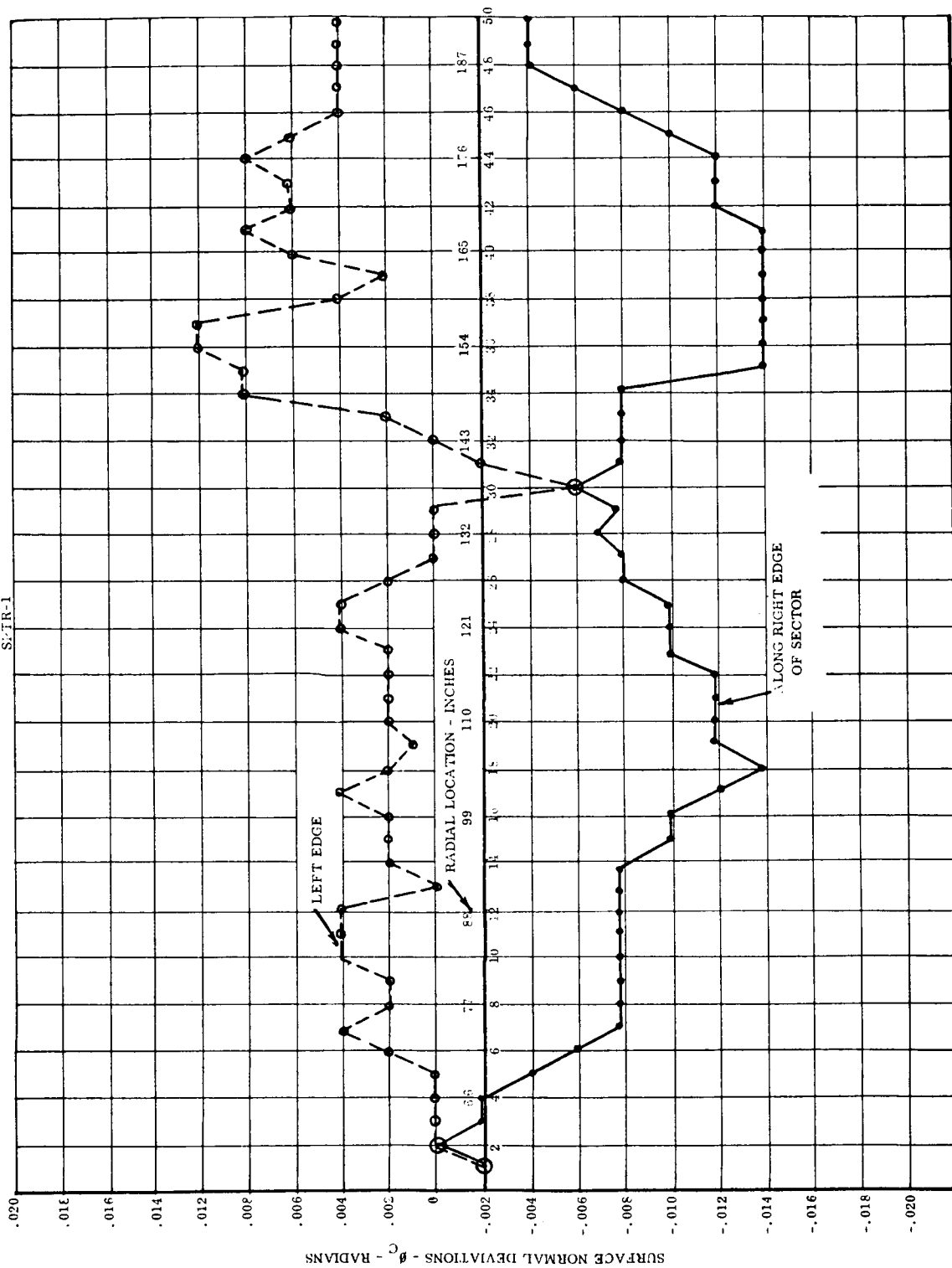


FIGURE 7.3-6

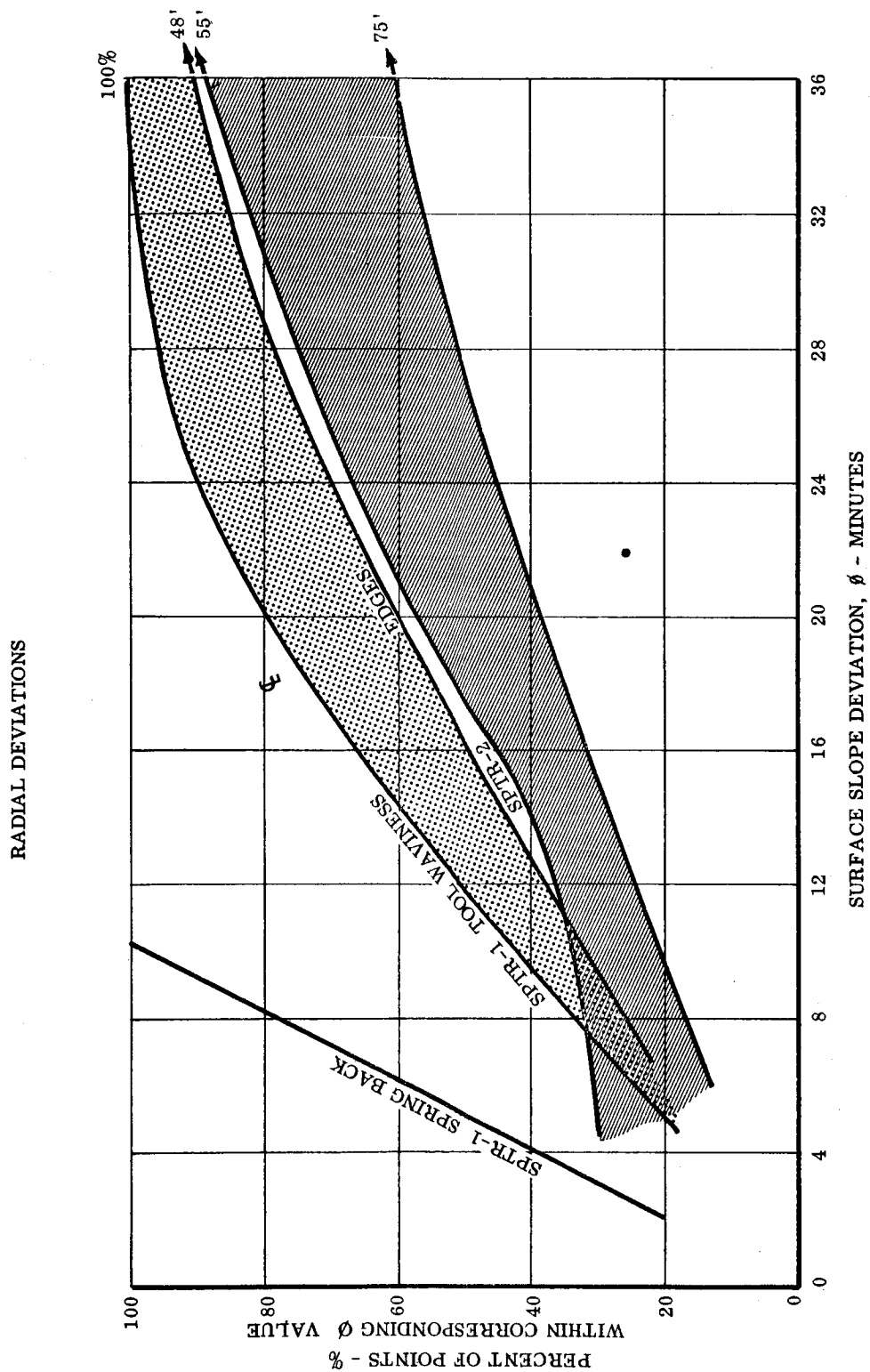


FIGURE 7.3-7

PROFICORDER TRACE OF HONEYCOMB MARKOFF

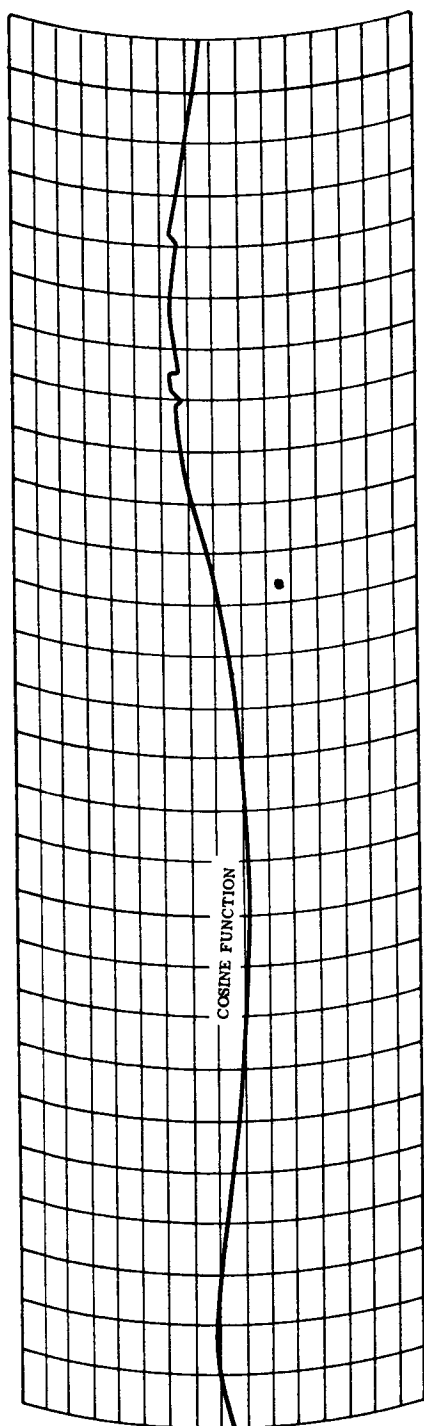


FIGURE 7.3-8a

TYPICAL OF SPTR 1 STATION 171

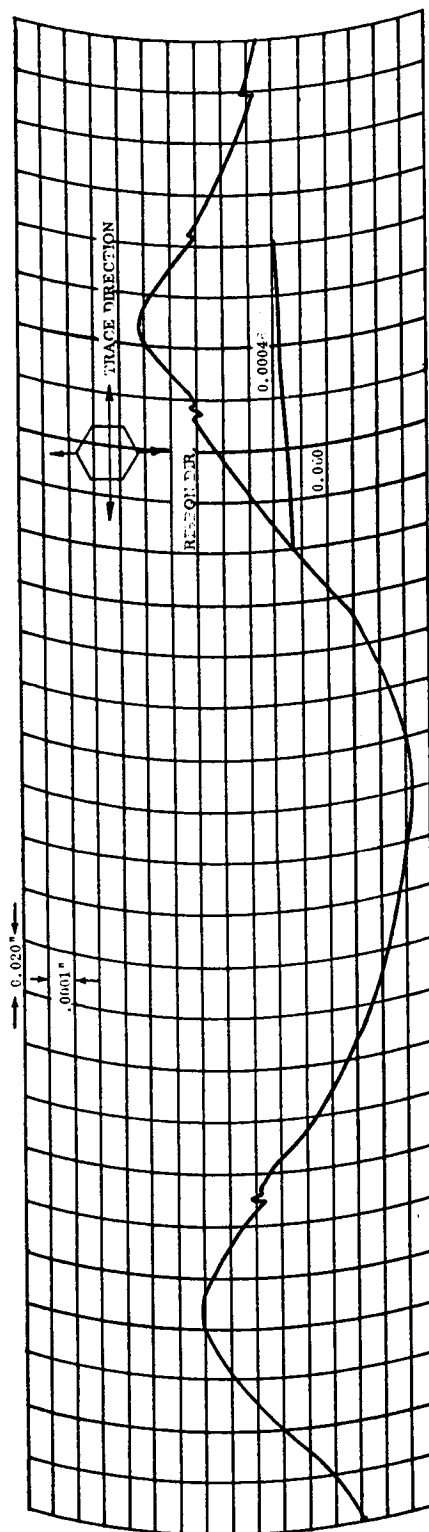


FIGURE 7.3-8b

7.3.5 Reflective Coating Results

Reflectance values of various samples produced during the Sunflower development program were obtained at the Space Technology Laboratory. The STL spectrophotometer has been described by Bevans and LeVantine. Spectral reflectance curves for some samples are reproduced in Figure 7.3-9. Graph number 1 shows the spectral reflectivity of pure aluminum deposited under ideal conditions on fused quartz. It represents the mean of many samples and is quoted as being representative to within $\pm 2\%$ in the ultraviolet range and $\pm 0.5\%$ elsewhere.

Curve number 2 represents STL data of a pure aluminum film evaporated on a 0.002 inch aluminum foil having a 1.5 RMS surface finish. The small reduction in total reflectivity could be assumed to be partially due to the expected tolerance and the effect of the surface finish. Generally it can be stated that the reflectivity decreases with increasing surface roughness; however, this must be tempered by the effect of the magnitude of the surface slope variations.

All other curves show the interference effect of the thin SiO_2 protective coat with their wave pattern. To be non-absorbing, the protective film should be in effect one-half wavelength thick. However, because of the large spectral region covered in the solar spectrum, this condition can only be obtained at a certain wavelength. A reduction in reflectivity over the whole spectrum is therefore unavoidable. By properly selecting the SiO_2 thickness and taking into account the change in optical path length due to the varying surface slope along the radius of the collector, an optimum overall reflectivity can be obtained.

Curve number 4 shows the reflectance loss of a slightly transparent aluminum film, where the losses are substantially greater in the UV range than elsewhere. This points out the dependency of the film thickness on the wavelength for opaqueness.

Curve number 5 indicates the effects of the clear lacquer coat and the aluminum foil on a slightly transparent aluminum film.

Curve number 6 shows the weathering and repeated cleaning effects during prolonged outdoor testing and storage of a sample on the single panel test rig. Again, the reflectance reduction is more pronounced in the UV and visible range than in the infra-red. At 2.0μ wavelength, the reflectivity was the same as the other samples.

7.4 OVERALL GEOMETRIC QUALITY OF THE SUNFLOWER SOLAR COLLECTOR

The geometric quality of the collector surface is a function of the factors listed in Table 7.4-1.

REFLECTIVITY RESULTS

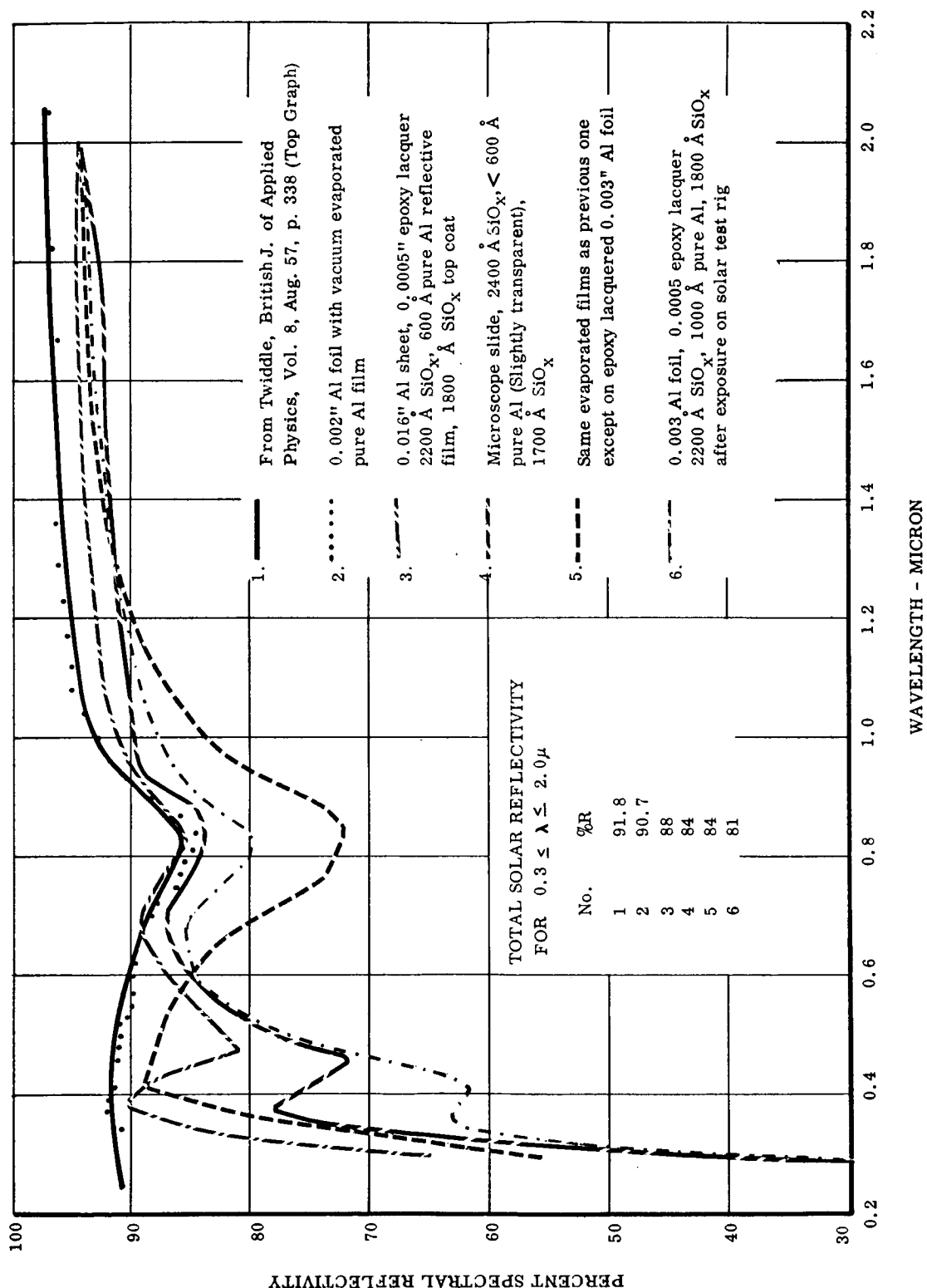


FIGURE 7.3-9

TABLE 7.4-1

<u>TYPE OF DEVIATION</u>	<u>REPRESENTATIVE SURFACE DEVIATION PLOT</u>	
Gross waviness	Figure 7.3-5	(p. 129)
Spring - back	Figure 7.3-5	(p. 129)
Honeycomb markoff	Figure 7.3-8	(p. 132)
Deployment positioning	Figure 8.3-20	(p. 178)
Environmental structural loading	Figure 8.3-23	(p. 181)
Thermal distortion	Figure 4.2-15	(p. 58)

As presented in this report, these factors have been investigated analytically and experimentally. Each factor's individual characteristics are represented in Figure 7.4-1 for comparison. Direct summation of all these curves would give the maximum possible surface deviation; however, a more accurate description of the collector geometric surface deviations was obtained by algebraic summation of the surface normal deviations at each radial location from the curves listed in Table 7.4-1.

This net summation is shown in Figure 7.4-2 and represents the best observed and extrapolated results from the Sunflower solar collector development program. Extrapolations were made to the orbital or flight design case as indicated in the appropriate section's discussion. Also, honeycomb markoff is not included in Figure 7.4-2 since it has a separate distribution which is superimposed over the entire surface area.

From this combined surface error plot, the distribution of error for a single sector was obtained and extrapolated to the entire collector surface area. This is shown in Figure 7.4-3. This extrapolation was made by assuming that the errors from the remainder of the paraboloid would be the same as the single sector, and thus symmetrical about the optical axis. Thus, by summing positive and negative occurrences of the same deviations, the symmetrical distribution for the entire collector is obtained. This then represents the typical distribution of surface errors for the Sunflower solar collector. Comparisons with analytical models were presented in Section 4.1.

INDIVIDUAL CHARACTERISTICS OF SURFACE DEVIATIONS

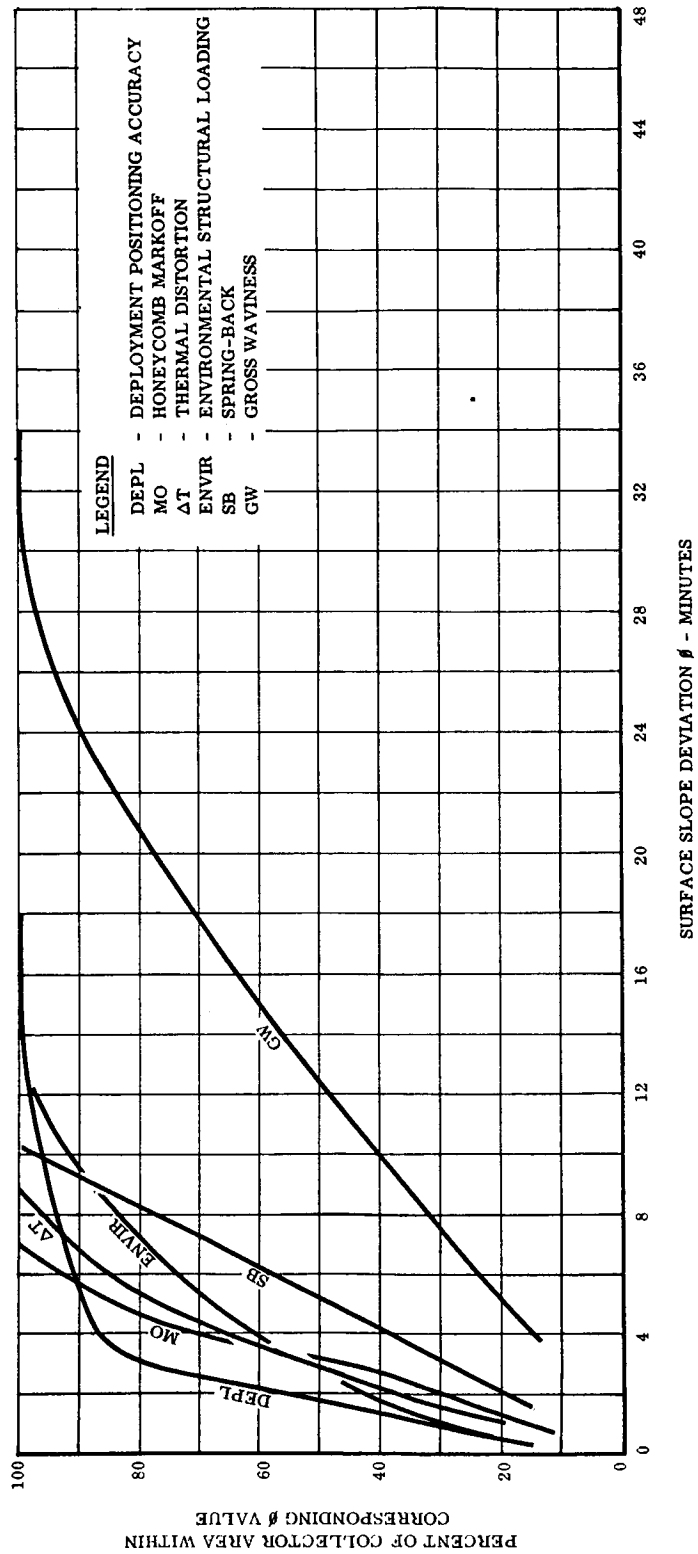


FIGURE 7.4-1

COMBINED SURFACE DEVIATIONS OF THE SUNFLOWER SOLAR COLLECTOR
(RADIAL ERRORS ONLY)

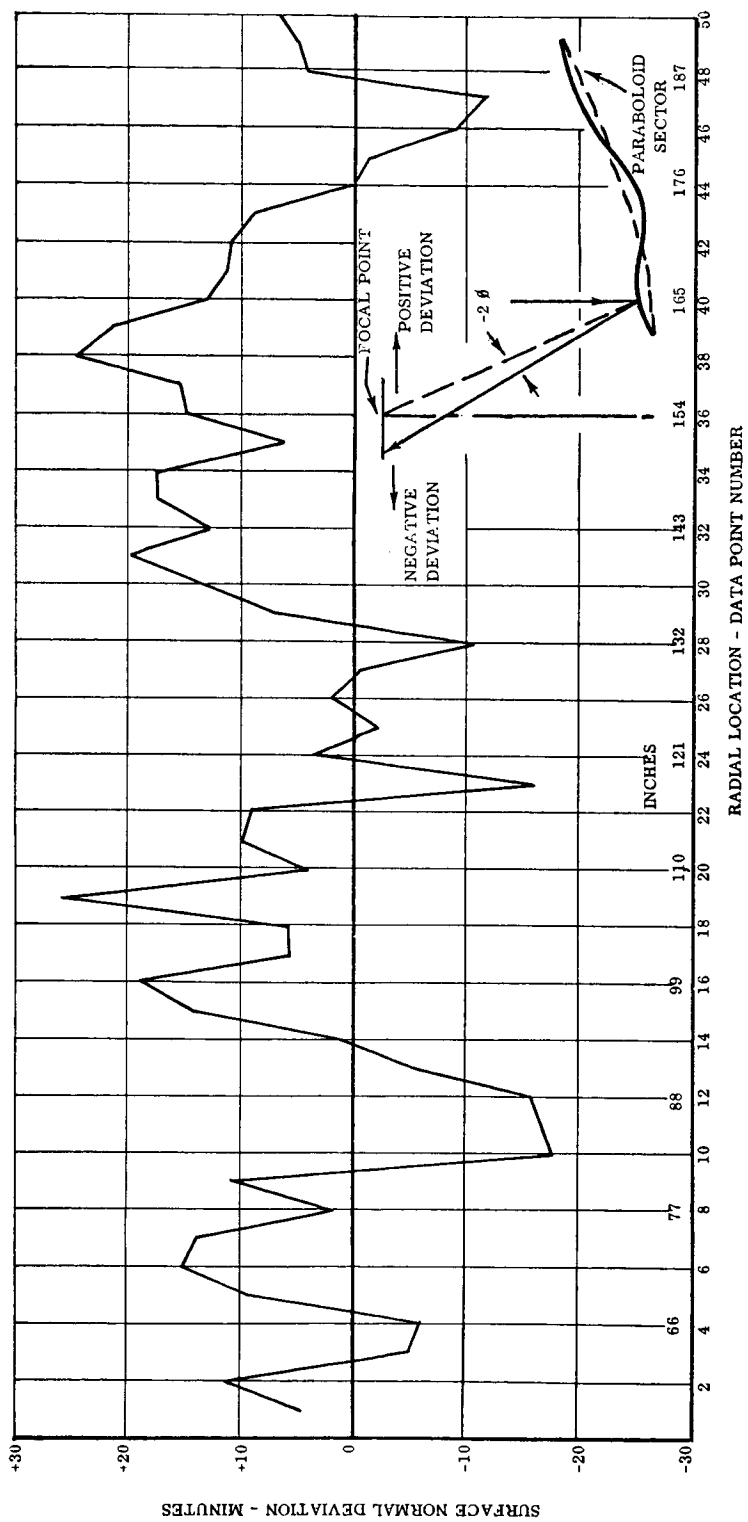


FIGURE 7.4-2

DISTRIBUTION OF RADIAL ANGULAR ERRORS FOR THE SUNFLOWER COLLECTOR

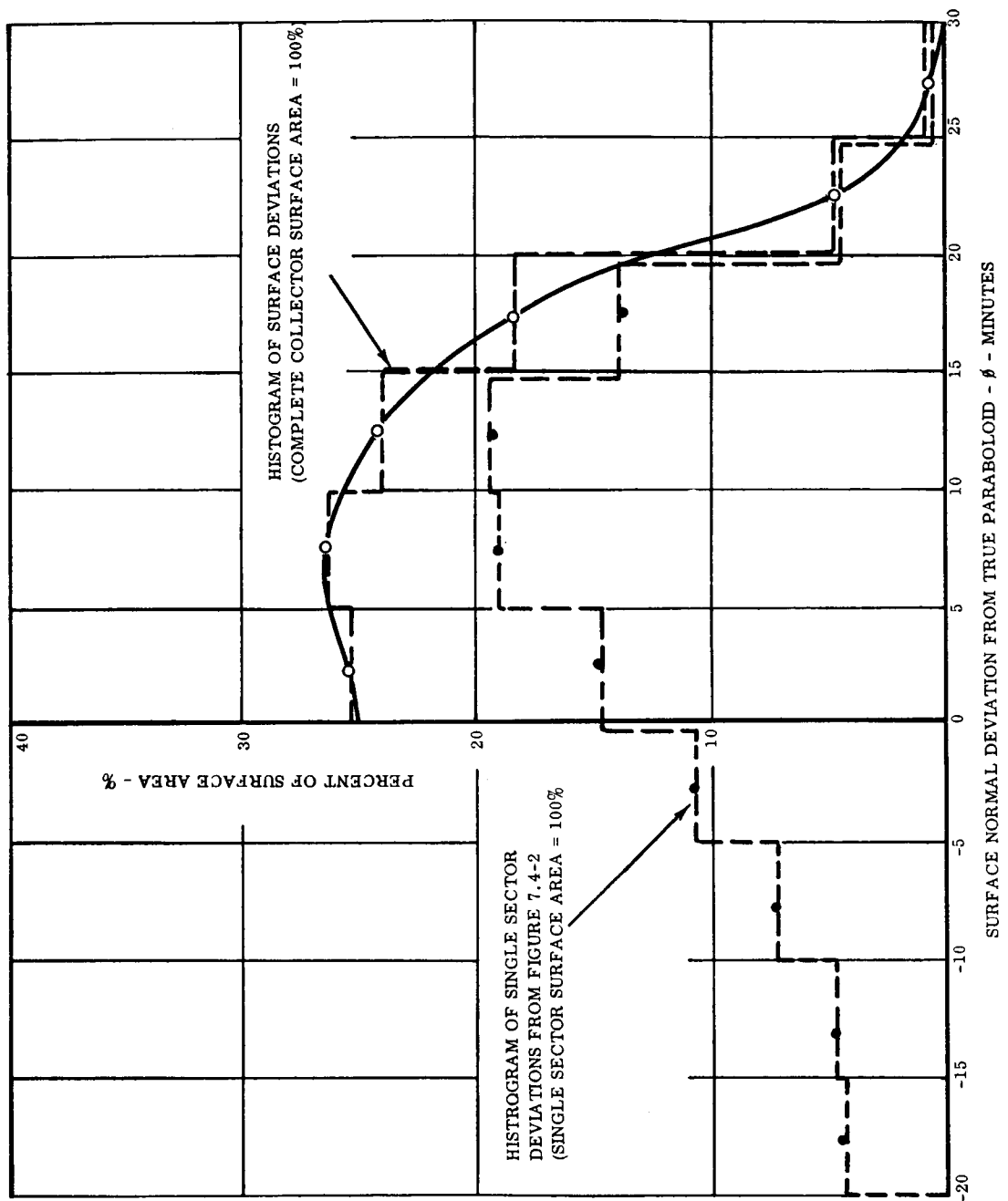


FIGURE 7.4-3

8.0 DEVELOPMENTAL TESTING

Testing was performed during the development program to evaluate and develop a component which was capable of withstanding the operating and nonoperating environments to which the Sunflower system will be subjected. This developmental testing included performance testing, optical inspection, and environmental testing.

8.1 PERFORMANCE TESTING

Performance testing of the Sunflower solar collector consists of calorimetric measurements of collector efficiency when illuminated by solar energy. These tests were performed on a single panel (1/30 of full paraboloid), and plans and a facility were prepared for efficiency tests of a complete full size collector.

8.1.1 Single Panel Performance Testing

The single panel testing was performed on individual collector panels where the sun was used as the energy source.

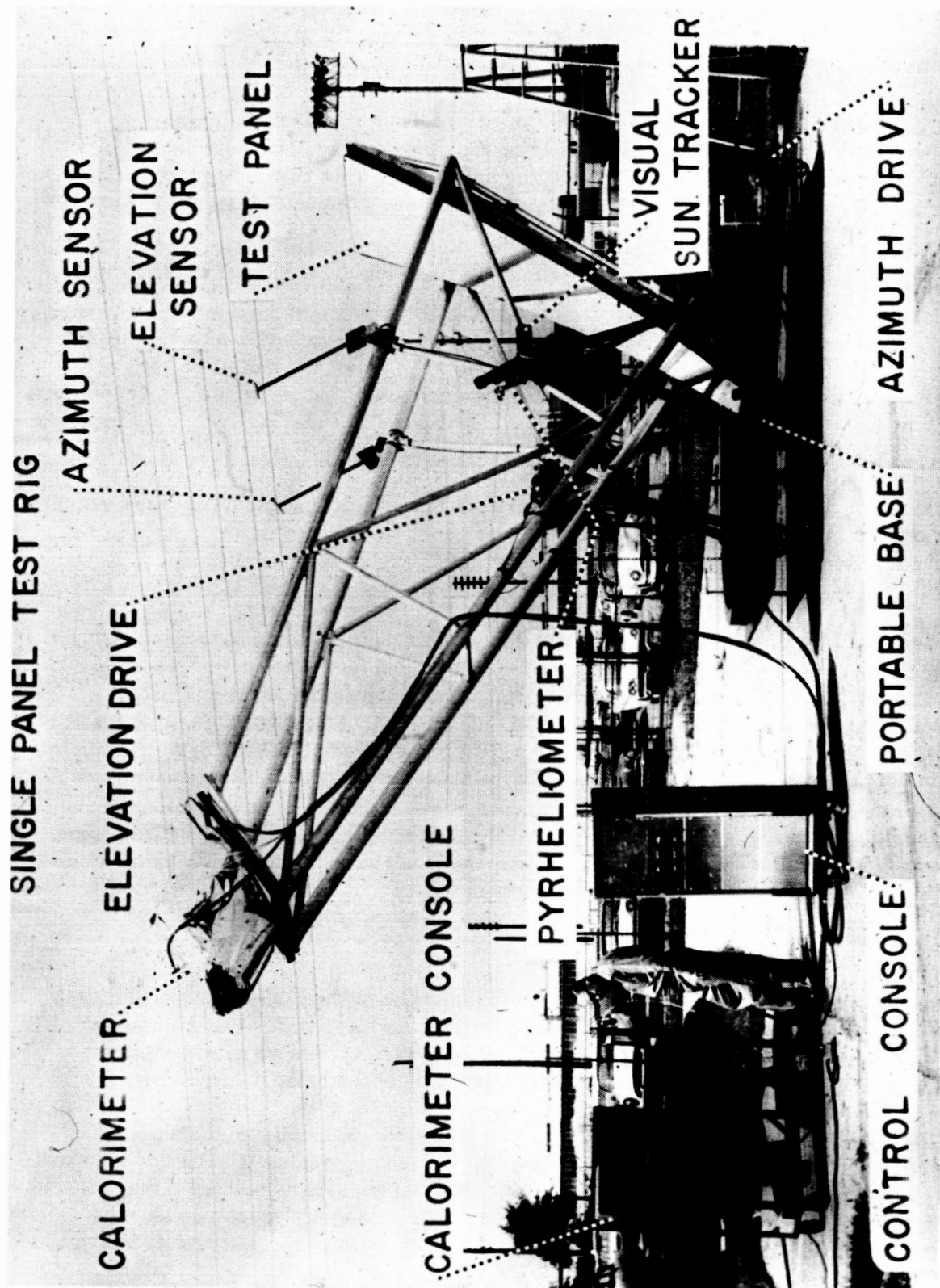
8.1.1.1 Test Rig Description

The test rig which was designed and built specifically for this purpose is shown in Figure 8.1-1. It consists of a structure for holding the test panel in the proper geometric location with respect to the focal point, where the calorimeter is located. This structure is cradled in a pivoting base, thereby providing an altazimuth mounting arrangement. Dc servo motors and gear reductions at each pivot axis drive the rig to keep the optic axis of the collector continually pointed at the sun. The drive motors are controlled by a tracking system which consists of sun sensors, servo amplifiers, and amplidyne generators. With this arrangement, the rig will track the sun automatically or it can be controlled manually. The entire rig is portable so that it can be taken indoors for panel mounting when not testing.

8.1.1.2 Instrumentation

Instrumentation consists of an Eppley normal incidence pyrhelometer mounted directly on the rig to measure the incident solar energy level, an optical tracking scope and a visual alignment target which is calibrated for operating at various misorientations, and the calorimeter for measuring the reflected and concentrated energy.

The calorimeter is a circular cavity type receiver made of aluminum tubing. The exterior is insulated to minimize heat losses. The cavity opening is such that aperture openings of various sizes can be fitted. Water is continuously circulated through the calorimeter tubing and by measurement of the flow rate and temperature rise, the collected energy is calculated and compared with the measured incident solar energy.



TEST RIG FOR PERFORMANCE TESTING OF THE SUNFLOWER SOLAR COLLECTOR

8.1.1.3 Test Description and Results

Single panel performance testing consisted of three specific phases:

- a. Focal plane image investigation
- b. Calorimetric tests
- c. Calorimeter heat loss determination

To investigate the concentrated image, stainless steel plates were placed in the focal plane to intercept all the concentrated energy. Typical high temperature portions of the image are shown in Figure 8.1-2. By the use of temperature sensitive paints, an approximate temperature profile was obtained and is shown in Figure 8.1-3. If this profile is rotated about the optic axis to simulate the opposite symmetric portion of the collector, an estimate of the total flux profile is obtained, being qualified by convection and conduction effects on the steel plate. This is also shown in Figure 8.1-3.

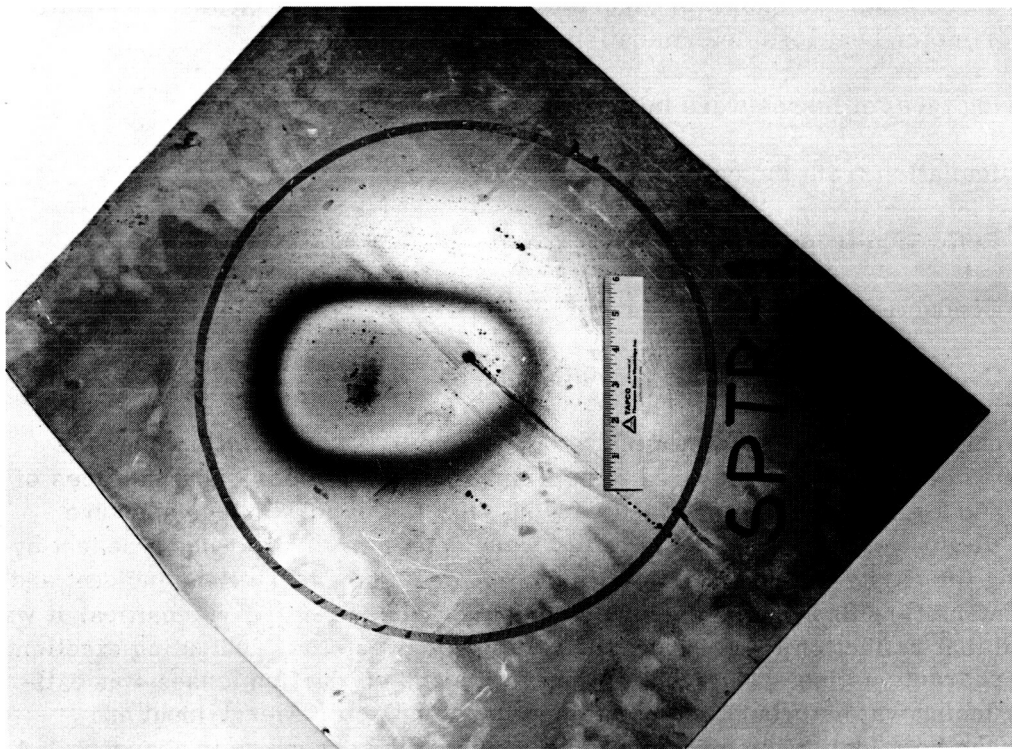
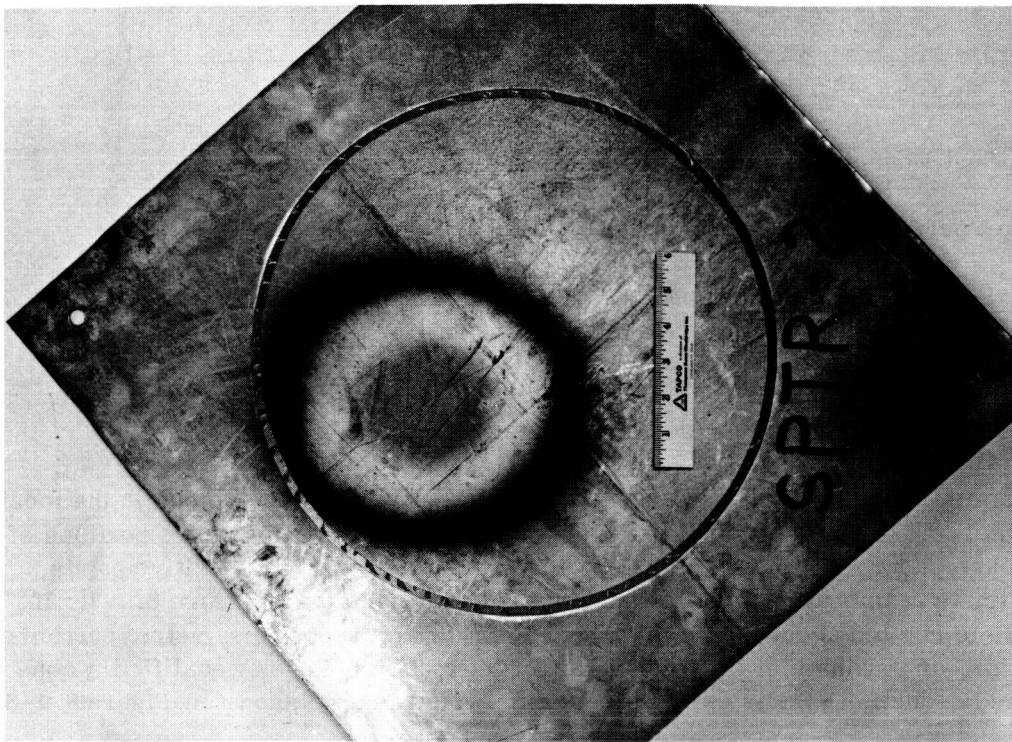
Calorimetric tests were conducted with various aperture sizes to determine the overall performance efficiencies of several typical Sunflower panels.

Results of these tests are shown in Figure 8.1-4. They will be discussed as qualified by the calorimeter heat loss determination phase of testing.

The following types of losses were investigated:

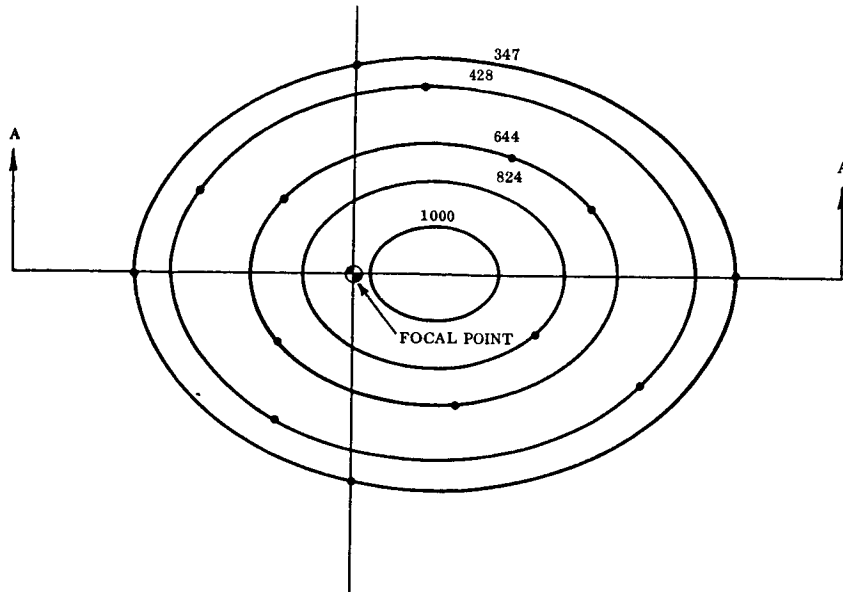
- a. Radiation from the calorimeter cavity
- b. Reflection from the calorimeter cavity
- c. Conduction from the calorimeter
- d. Convection losses around the calorimeter

The combined losses are also shown plotted in Figure 8.1-4. Radiation from the cavity was calculated using measured temperature levels on the internal surfaces of the cavity and a graphically determined varying view factor for various aperture openings. Reflection losses from the cavity were determined in a bench type test by illuminating the cavity with an artificial light source and measuring the incident and reflected intensity with a photometer. By comparing these relative intensities, it was determined that reflection losses from the cavity were very low, indicating excellent blackbody characteristics. The level of convection and conduction losses was estimated by running water through the calorimeter with no solar energy input and measuring the heat lost to the ambient. The combined losses curve in Figure 8.1-4 increases as the aperture decreases. This is mainly due to the conduction and convection which remained relatively constant while the energy entering the cavity de-



FOCAL PLANE IMAGE

TEMPERATURE PLOT IN THE FOCAL PLANE



TEMPERATURE PROFILE ALONG A-A

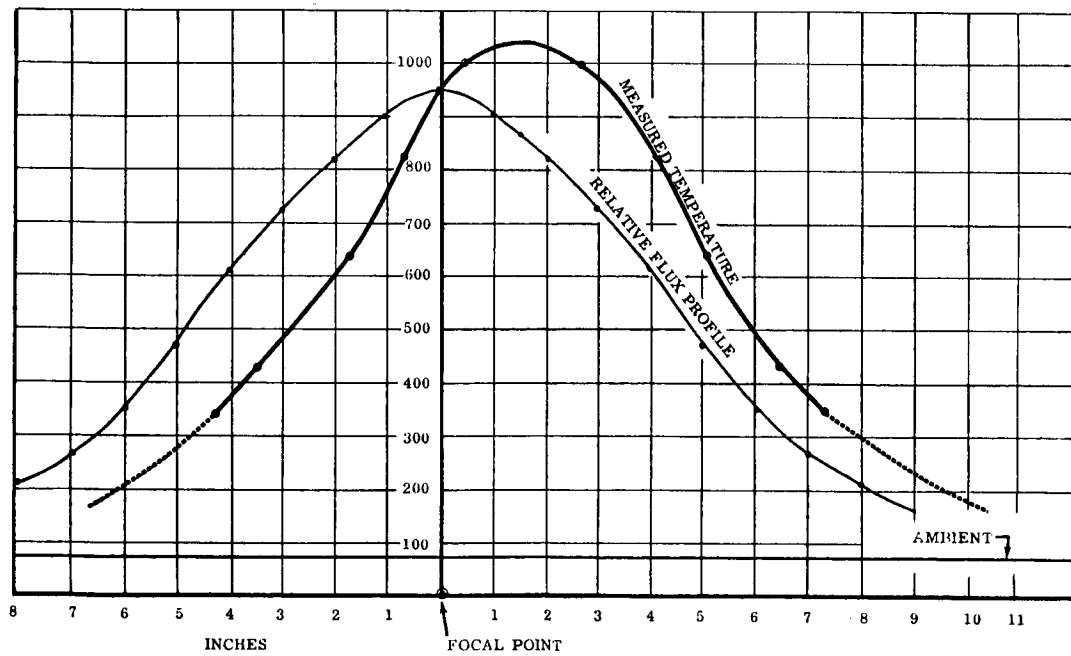


FIGURE 8.1-3

SUNFLOWER COLLECTOR
SOLAR TESTING RESULTS
SINGLE PANEL TEST RIG

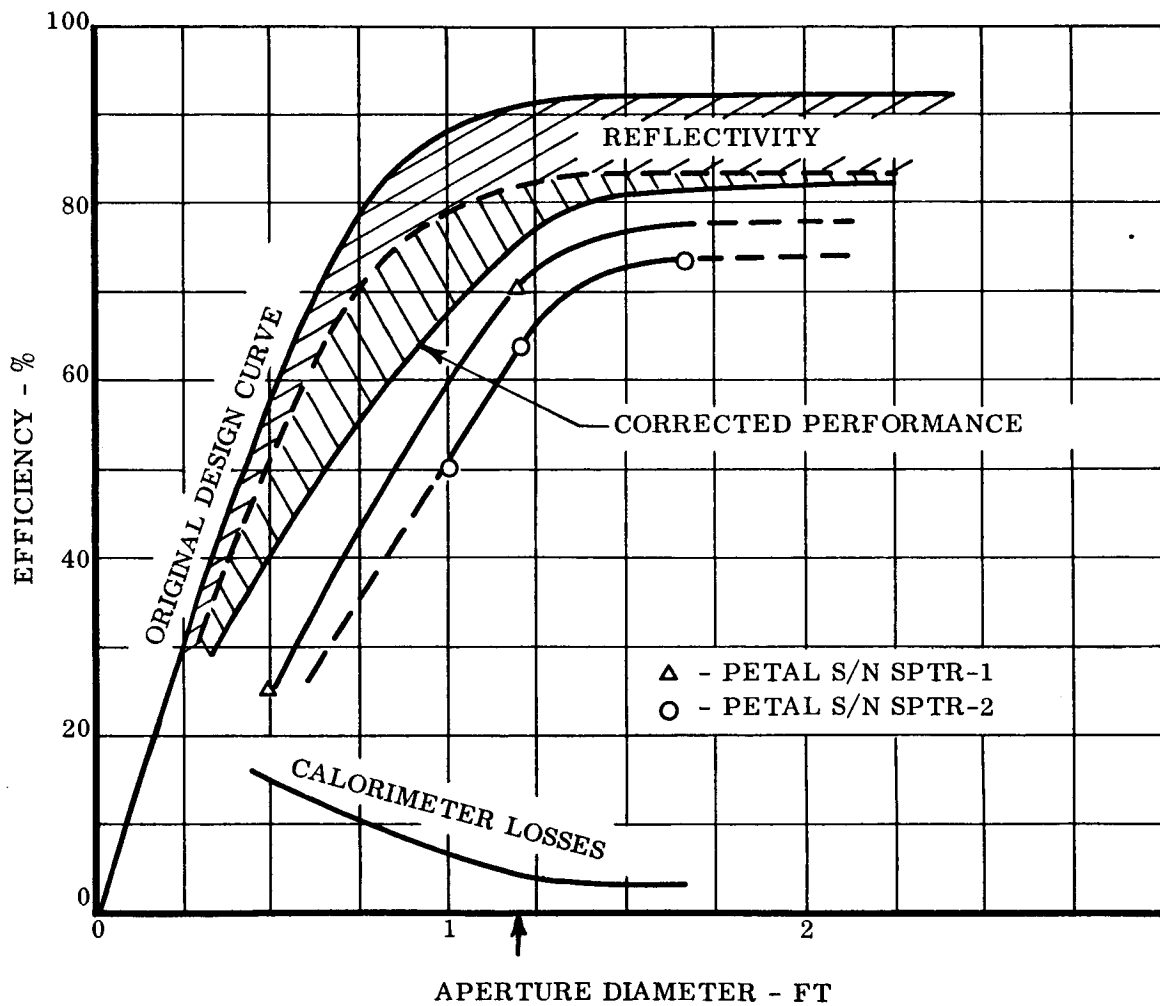


FIGURE 8.1-4

creased, thus becoming a large percentage.

Applying the combined losses correction to the measured data results in the solid curve. This is to be compared to the design curve. However, since the design curve was based upon an ideal reflective aluminum surface, a portion of the difference between design and measured can be attributed directly to reflectivity. Total and specular measurements of reflectivity, as defined in section 5.6, were made of specimens typical of the tested panels. The portion thus accounted for is also shown in Figure 8.1-4.

Due to off center peaking of the temperature profile shown in Figure 8.1-2, the geometric position of the panel was checked after testing and found to be misoriented approximately 0.3° ; however, misorientations of approximately the same magnitude did not result in a measurable change over the test interval.

Additional misorientation performance data was not obtained during this phase of testing, due primarily to lack of sufficiently clear weather during the scheduled test period.

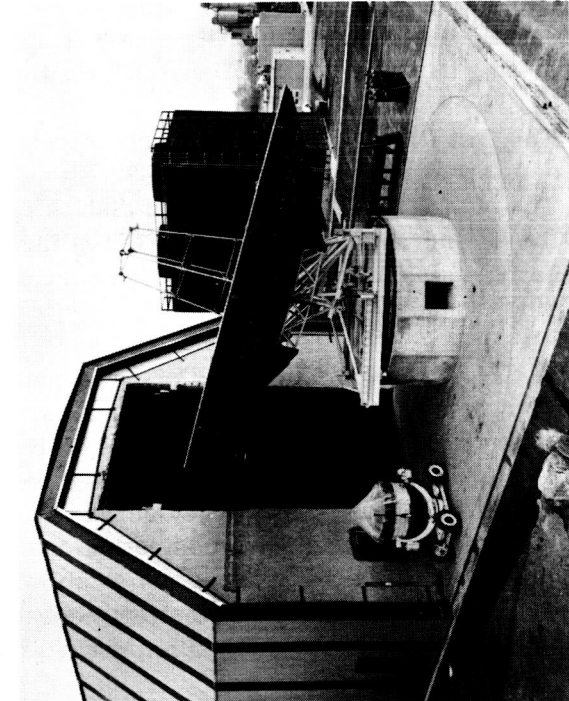
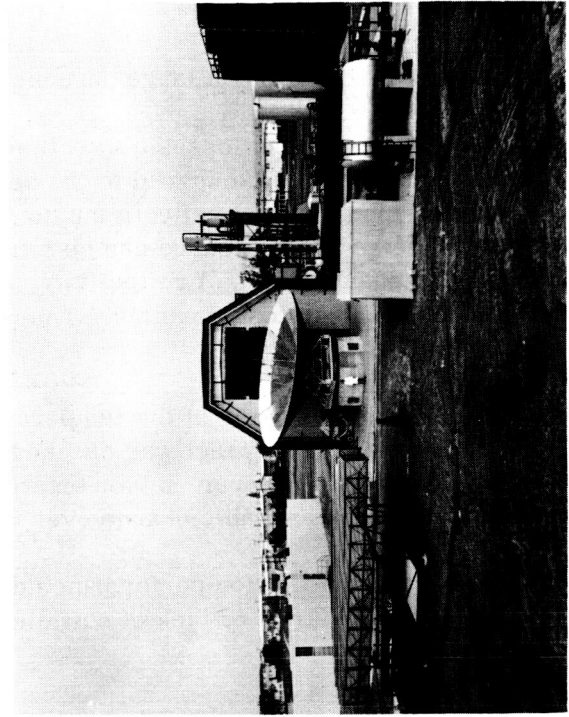
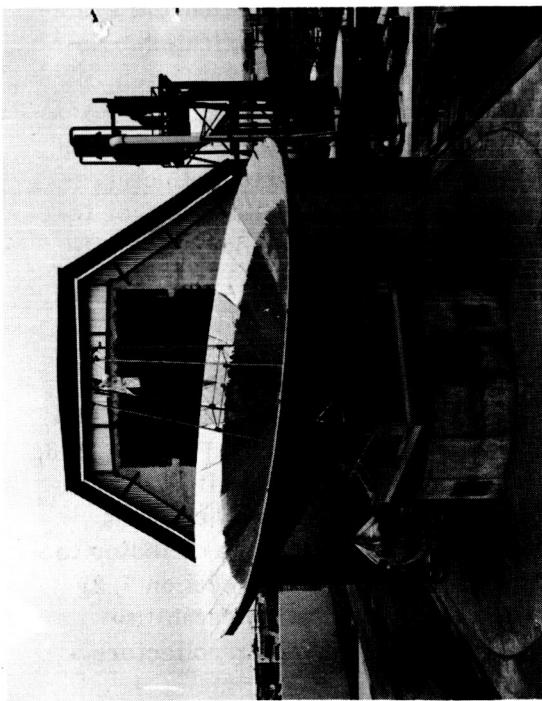
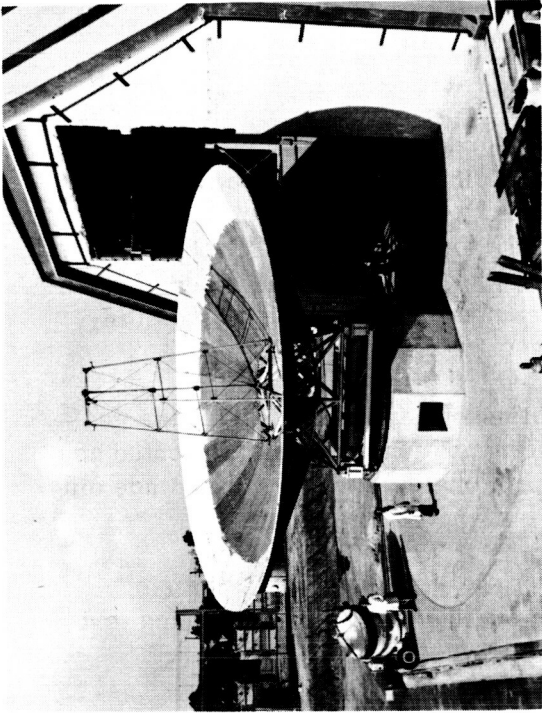
8.1.2 Full Size Sunflower Solar Test Facility

To allow direct experimental determination of full scale collector energy efficiency and to provide the logical developmental step of collector and system integration and evaluation, the solar test facility shown in Figure 8.1-5 was designed and fabricated. No testing has been accomplished during this phase of the development program.

The test facility consists of a rigid forty foot diameter paraboloidal dish which serves as a structural support for the 32.2 foot prototype light weight aluminum collector. The outer four feet of the rigid dish is reflective-coated to supply additional power to the system for various phases of testing. The entire rig will track the sun automatically, using a tracking system similar to that described in section 8.1.1.1 for the single panel test rig.

The rigid dish is fabricated of Kraft paper honeycomb core with resin impregnated fiberglass skins. The fabrication procedure and tooling are similar to that described in Section 6.0 for the preprototype collector. A typical layup is shown in Figure 8.1-6. A finished panel is shown in Figure 8.1-7. The attachment points for the light weight collector can be seen. They serve not only as attachments but also as adjustment points from which desired deviation can be programmed into the prototype collector to simulate zero gravity shape (as established by the procedure outlined in section 7.3) and/or typical thermal distortion modes. This orbital shape simulation capability provides a practical method for ground tests of large, light weight solar collectors.

The entire rig is housed in an electrically actuated movable shelter. This test facility is located at Thompson Ramo Wooldridge's West Coast Laboratory in Inglewood, California.



SOLAR COLLECTOR TEST FACILITY



FABRICATION OF 40 FT. DIAMETER PARABOLOID SECTOR

FIGURE 8. 1-6



COMPLETED SEGMENT OF 40 FT. DIAMETER PARABOLOID

8.2 Optical Tests of the Preprototype Collector

As was mentioned previously, optical testing and inspection of the completely assembled collector was accomplished by a point source-grid screen arrangement. This system, shown in Figure 6.5-1, has the capability of traversing the entire collector surface area. By moving the grid-screen box in radial increments, composite inspection photographs were made of sectors for direct comparison with the single sector zero "g" inspections.

A major problem in determining the optical characteristics of the complete preprototype collector is that the structure is weight-designed for performance in a zero gravity environment and yet can only be tested in the one "g" environment of the laboratory.

Since the assembled collector must be supported by auxiliary support stands to maintain its optics in the gravity environment of the laboratory, a true evaluation of the orbital zero "g" optical characteristics is obtained by a combination of single sector inspection results (see Section 7.3.3) and comparison inspections of the assembled collector before and after various environmental tests. These comparison inspections of the assembled collector are performed with the auxiliary support stands removed and the collector assembly deflected to its dead weight shape. In this way, the collector is not restrained and any shape changes caused by the environmental testing will be observed.

Comparison inspection photographs were obtained during various phases of the developmental testing and typical results will be presented in Section 8.3.4.

8.3 ENVIRONMENTAL TESTING

Environmental testing of the full size preprototype collector consisted of the following tests:

- a. One "g" orbital transfer acceleration loading in the axial direction.
- b. Deployment dynamic loadings.
- c. Launch vibration spectrum in the stowed position.
- d. Orbital transfer vibration spectrum in the deployed position.

The objectives of the environmental testing were to obtain developmental information concerning loads, stress conditions, modes of deflection, and general structural integrity characteristics which would aid in efficient and reliable prototype design. Also to be determined was the relationship of the structure and locks to geometric shape and optical performance. The tests were planned, therefore, to separate the various environmental and performance conditions so that the individual effects could best be determined. For this reason, comparison optical inspections (using the equipment

and procedures described in Section 8.2) follow each test phase to determine any geometric or optical deviations. The collector is not externally supported and is in its dead weight position during inspection.

The following test chronology was used to accomplish the above stated objectives:

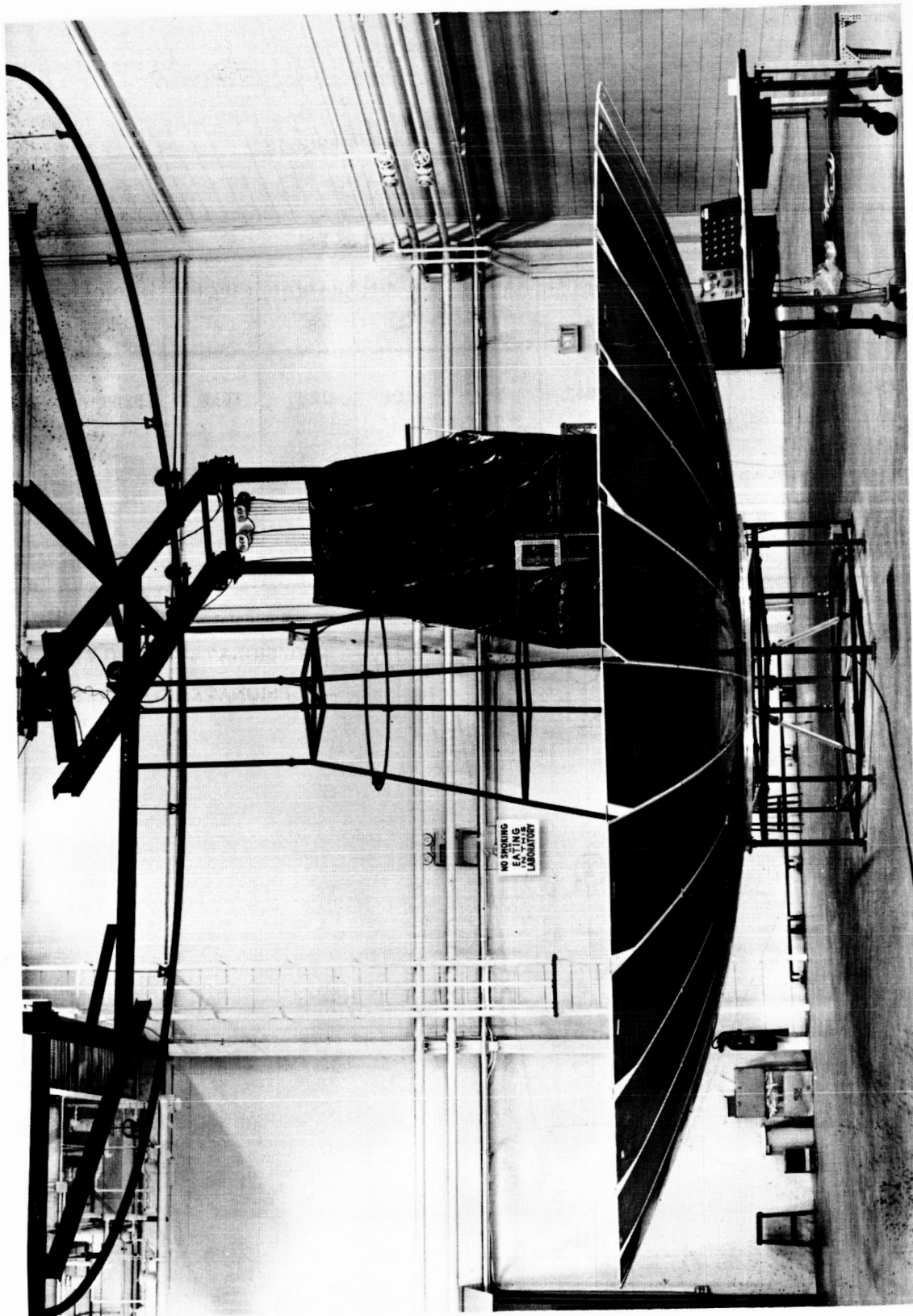
- a. One "g" (dead weight) structural test with rigid rim locks only.
- b. One "g" (dead weight) structural test with rigid rim and intermediate locks.
- c. Optical inspection.
- d. One "g" (dead weight) structural test with prototype rim locks and rigid intermediate locks.
- e. Optical inspection.
- f. Deployment test.
- g. Optical inspection.
- h. Vibration testing.
- i. Optical inspection.

Results of these tests and appropriate comparisons will now be presented.

8.3.1 Dead Weight Structural Testing

To simulate the one "g" orbital transfer acceleration loadings on the deployed collector, the auxiliary support stands used for initial assembly were removed, thereby loading the collector by its own weight. A view of this test set-up is shown in Figure 8.3-1. Note that the collector is supported only at the center mounting ring. Strain gage instrumentation and the optical transit can also be seen.

Surface strain data were obtained at various locations on the collector from which the typical stresses shown in Table 8.3-1 were calculated. Deflection data were also obtained and are shown plotted in Figure 8.3-2. It is seen that the stress levels are appreciably reduced with the addition of the intermediate locks due to the reduction of the bending in the long or radial direction of the sectors. Comparison of the rigid strap locks and the preprototype lock condition shows that the flexibility of the preprototype lock increased the load on the intermediate locks and produced increased deflection and generally higher stresses. Results of optical reference inspections will be presented in Section 8.3.4.

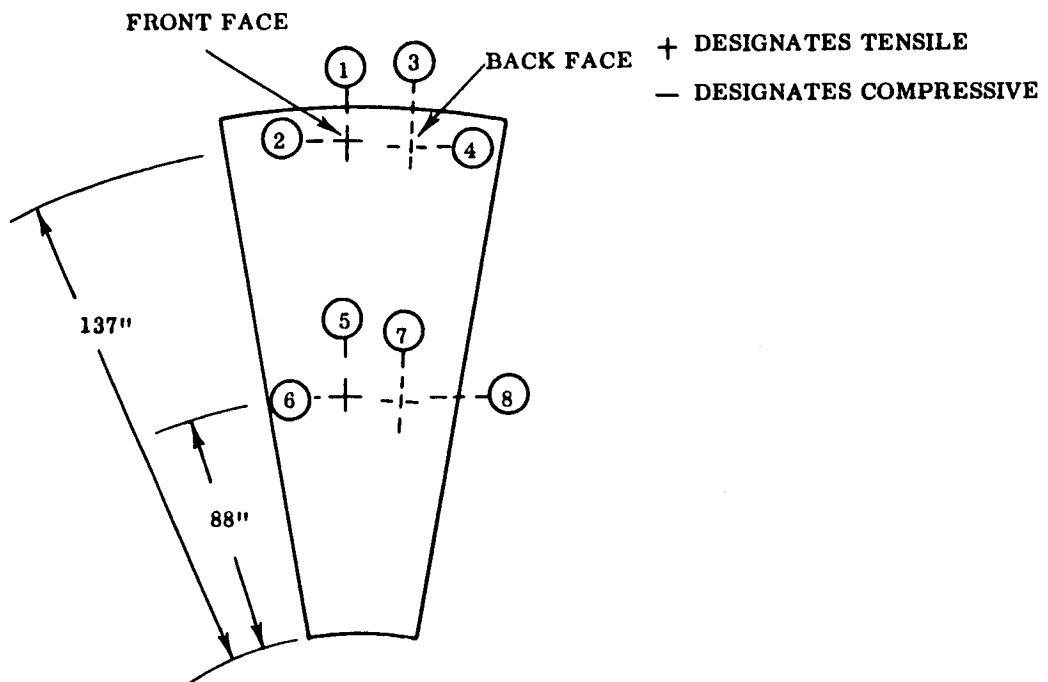


DEAD WEIGHT TEST ARRANGEMENT

TABLE 8.3-1

DEAD WEIGHT STRUCTURAL TEST RESULTS

LOCKING ARRANGEMENT	STRESS PSI							
	RADIAL LOC. 1	CIRCUM. 2	RADIAL 3	CIRCUM. 4	RADIAL 5	CIRCUM. 6	RADIAL 7	CIRCUM. 8
RIM LOCKS ONLY	-173	1863	340	-191	-1285	1588	3209	-1752
RIGID RIM AND INTERMEDIATE LOCKS	-412	263	-186	-260	-224	+244	-224	-147
PROTOTYPE RIM LOCK RIGID INTERMEDIATE LOCKS	-193	941	-250	-227	-78	+530	+224	+454



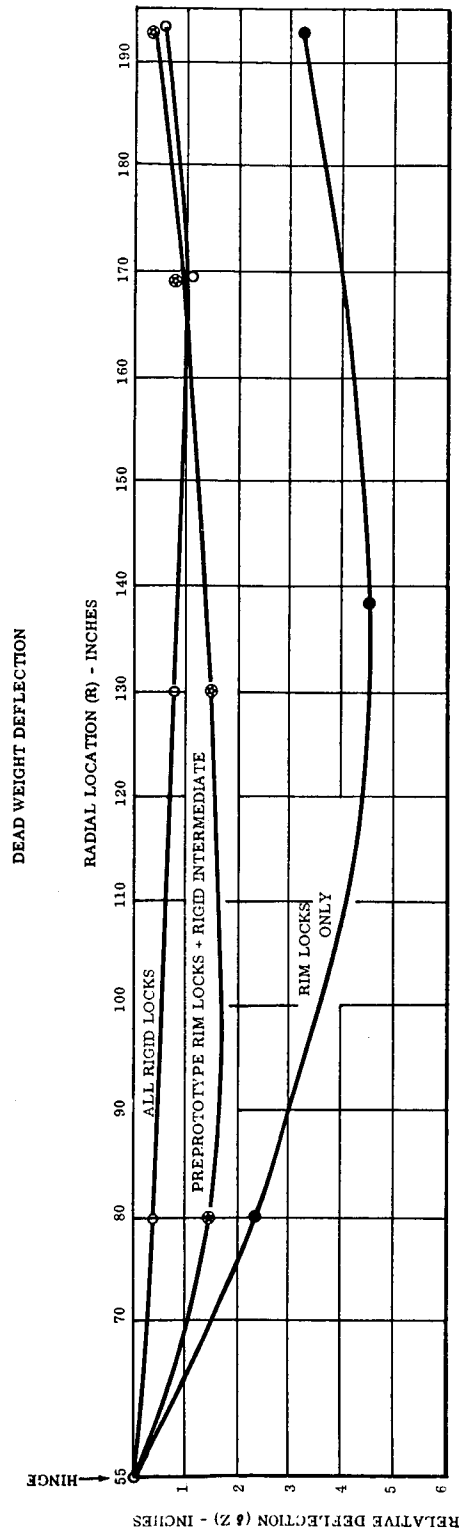


FIGURE 8.3-2

8.3.2 Collector Deployment Testing

As presented in Section 4.2.3, the orbital deployment is actuated by torsion bar springs at the hinges of each sector. To simulate the zero gravity deployment dynamics in the laboratory, a deployment simulation harness was conceived and designed.

8.3.2.1 Deployment Simulation Harness Description

The harness consists of continuous elastic cords around the collector bundle at the lock locations which, when they expand during deployment, counteract the dead weight torque of the sectors, thereby simulating only the net effect of the actuating springs. Figure 8.3-3 shows the elastic cord arrangement during the calibration and adjustment prior to deployment testing. During harness calibrations, the net static torque was measured for various deployment positions. The final calibration plot is shown in Figure 8.3-4. The peaking of the net torque is due to the characteristics of the available elastic cord combinations. However, the net energy input to the sectors simulates quite closely the energy input during an orbital deployment.

8.3.2.2 Deployment Test Instrumentation and Procedure

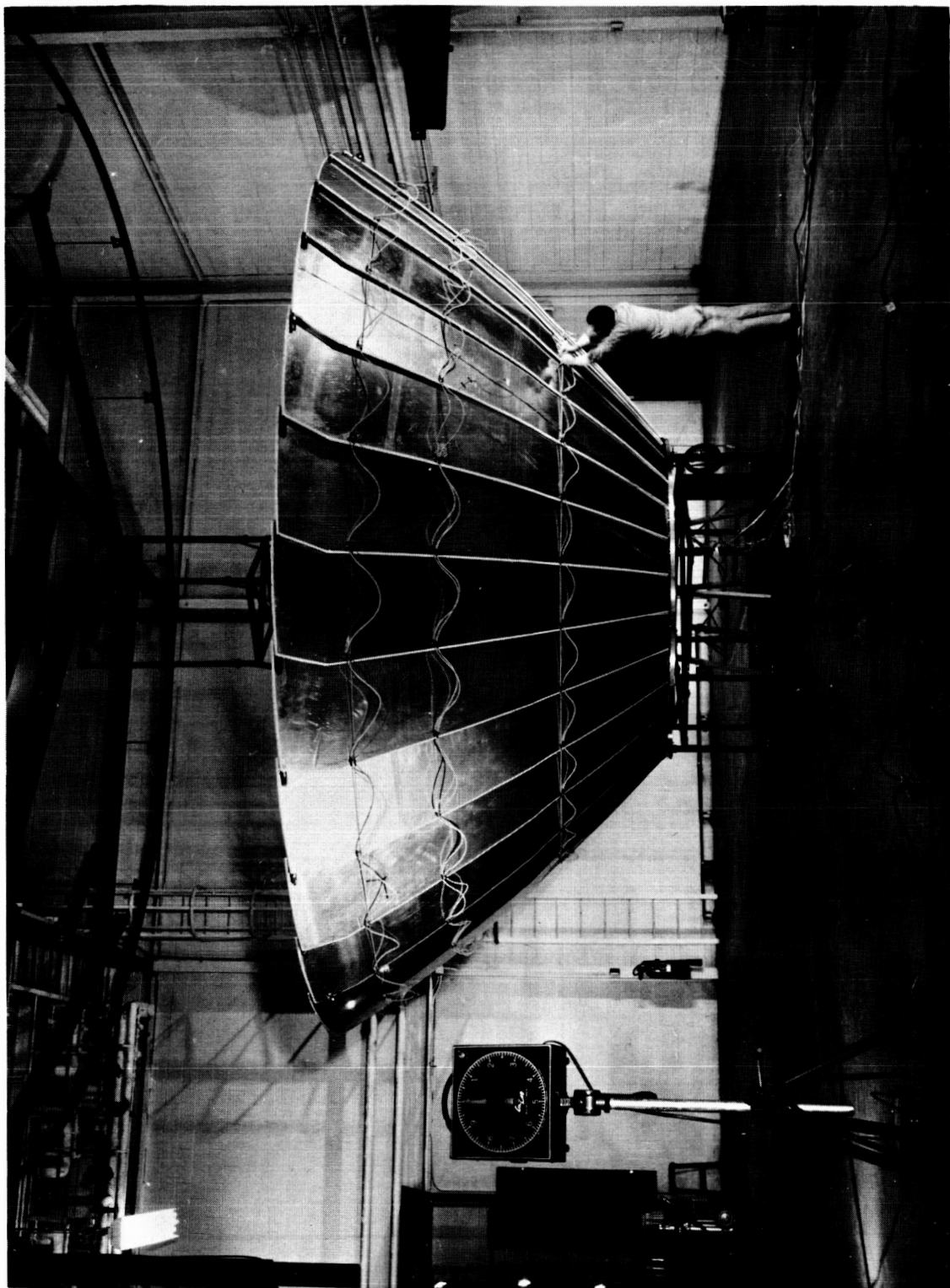
Figure 8.3-5 shows the test setup prior to deployment. The same strain gage arrangement which is shown in the sketch of Table 8.3-1 was used to record surface strains during deployment. An accelerometer which is sensitive to angular position with respect to the vertical was used to record displacement vs time.

To also record dynamics and the symmetry characteristics of the deployment, motion pictures were obtained. A micro-timer is positioned in the picture to provide an accurate time reference.

After final calibration of the deployment harness, the collector bundle is manually opened approximately seven degrees to position the center of gravity of the sector over the vertical. A tethering cord is automatically released to initiate the deployment and data is recorded during the entire sequence.

8.3.2.3 Deployment Test Results

Several preliminary partial deployments were made and two complete deployment tests were conducted. Figure 8.3-6 shows the deployment dynamics as measured by the accelerometer pickup. As mentioned previously, the net energy programmed into the deployment dynamics by the simulation harness closely matches the orbital deployment design. However, original estimates of friction, which were 20 - 30%, are seen to be low. The displacement vs time curve which was calculated for 90% friction fits the observed data. This means that 90% of the energy input to the deployment is absorbed as friction while approximately 10% is converted to kinetic energy of motion.



DEPLOYMENT HARNESS CALIBRATION

FIGURE 8.3-3

DEPLOYMENT HARNESS CALIBRATION DATA

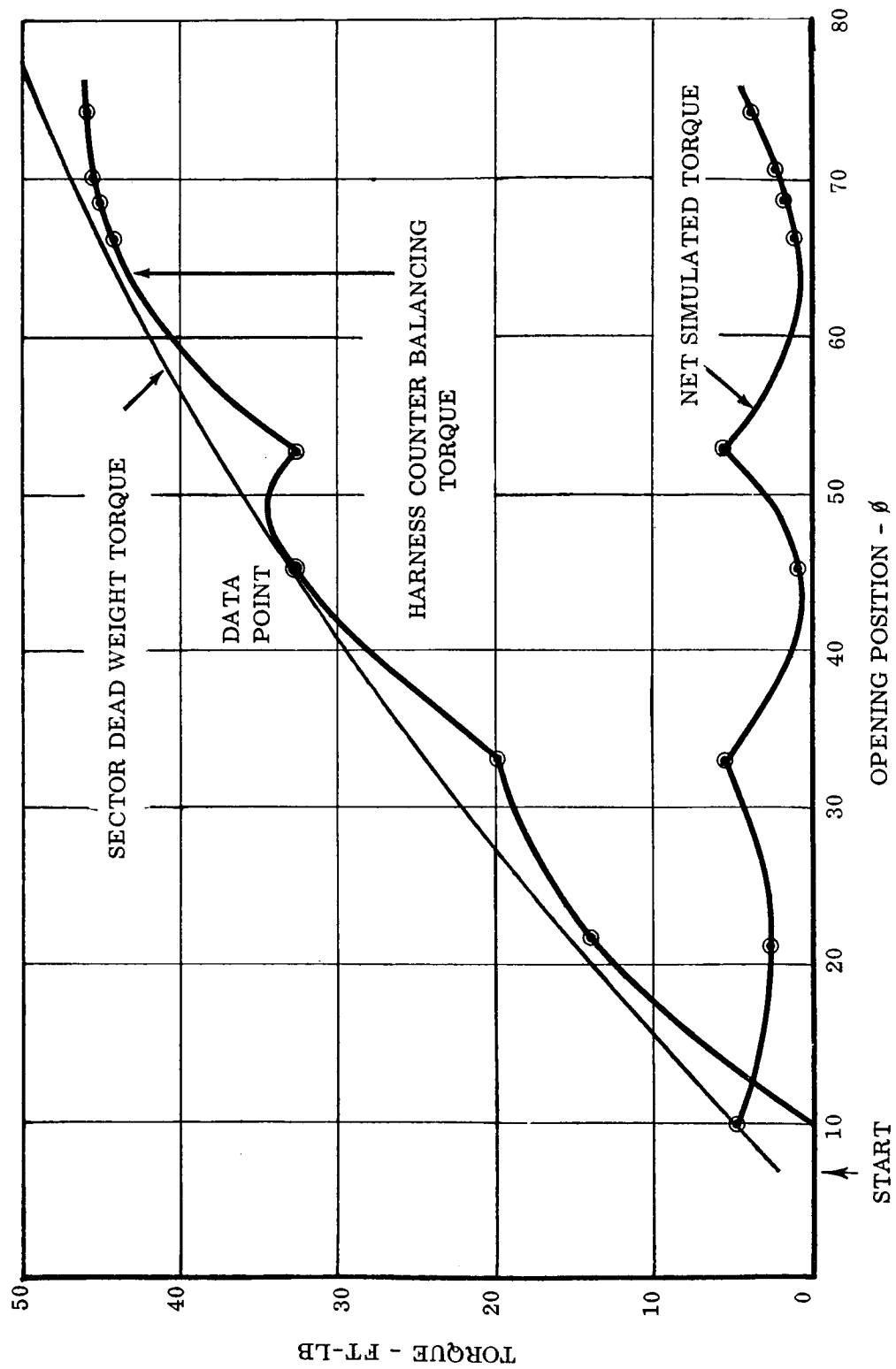
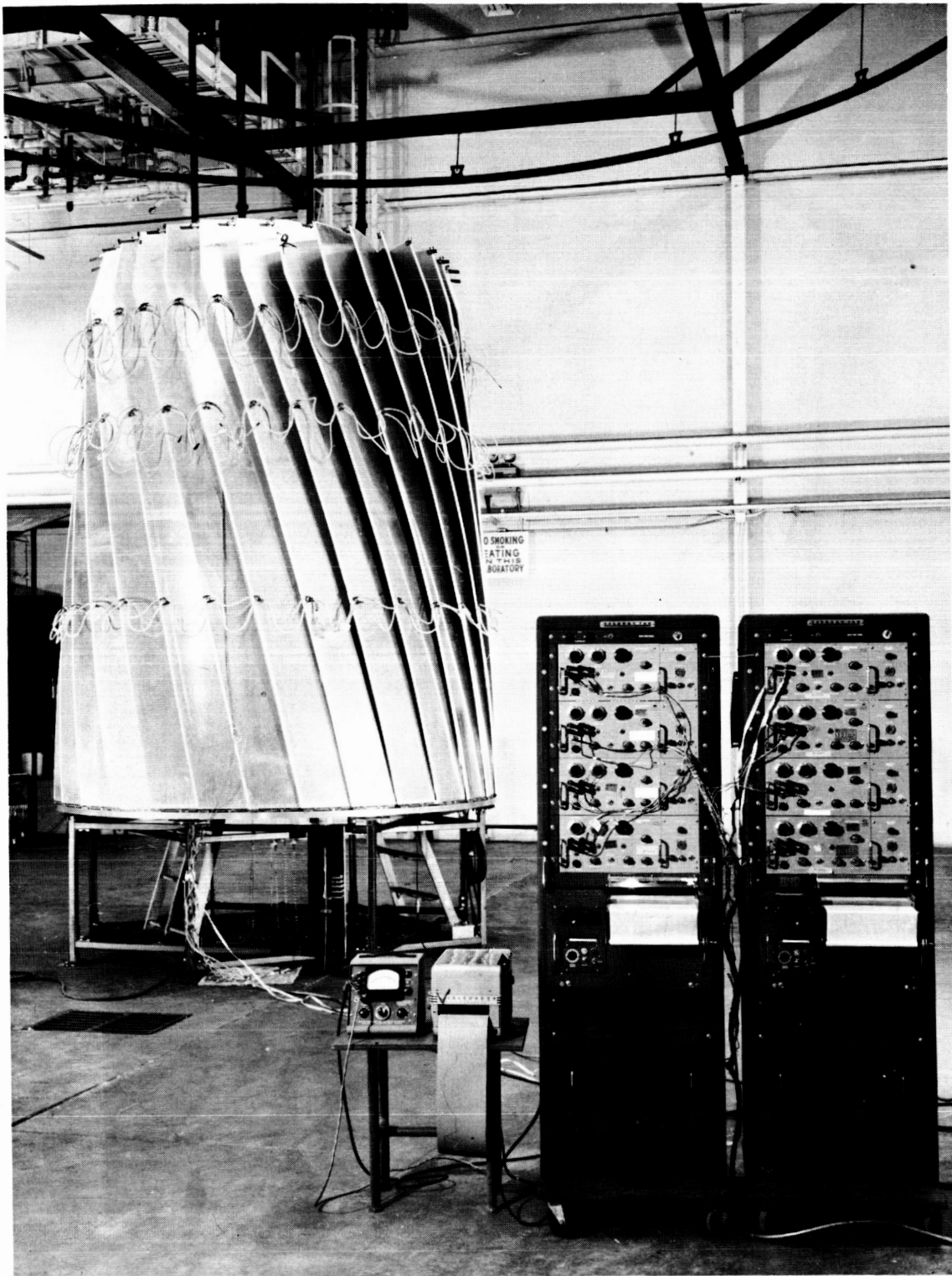


FIGURE 8.3-4



DEPLOYMENT TEST SETUP PRIOR TO DEPLOYMENT

SUNFLOWER COLLECTOR DEPLOYMENT DYNAMICS

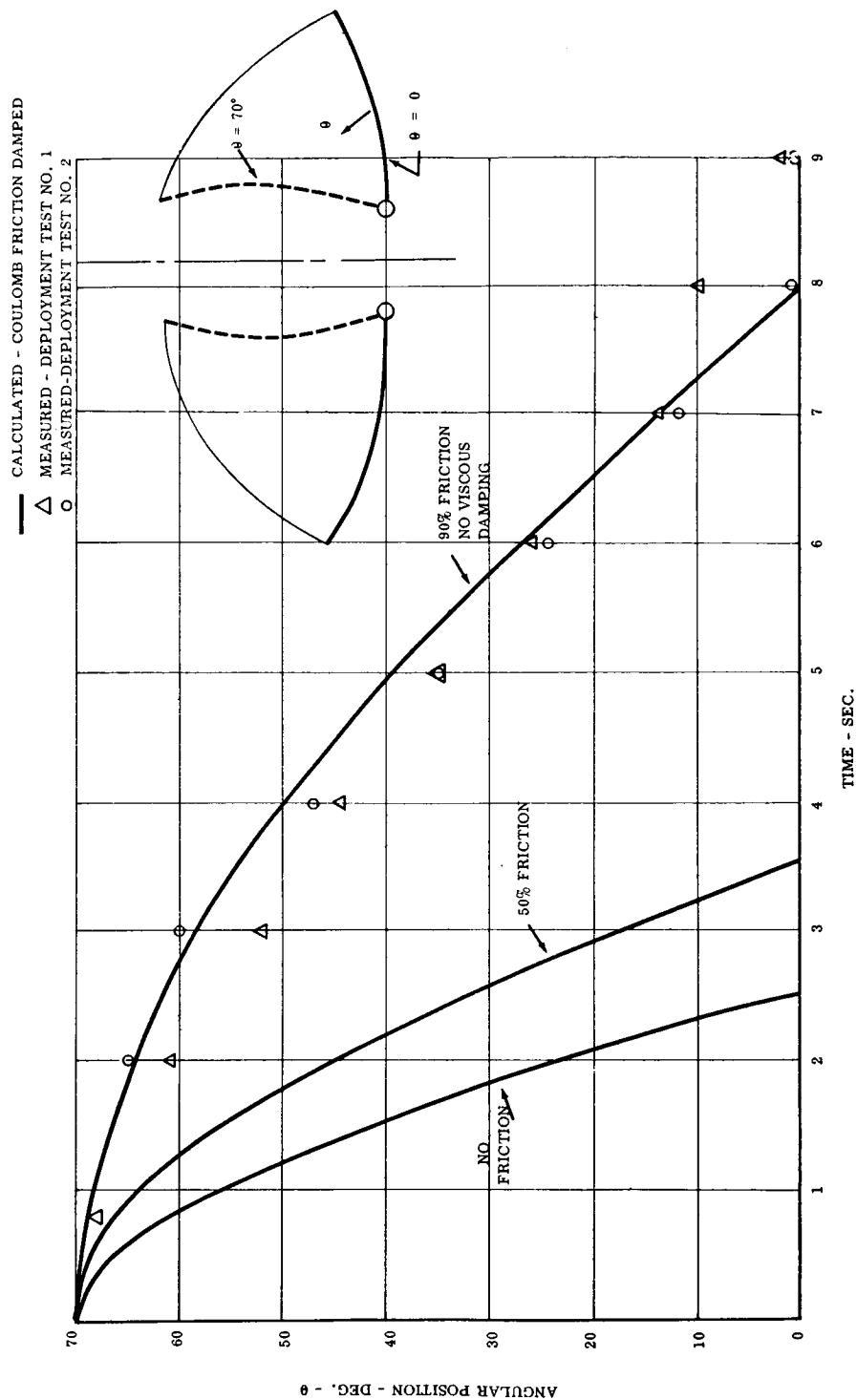


FIGURE 8.3-6

The overall deployment time was approximately 9.2 seconds in both deployment tests. The tail-off between 8 and 9 seconds is due to the locking action.

Motion pictures of the deployments were analyzed and the dynamics compared closely with that shown in Figure 8.3-6. Some non-symmetry in the deployment action was observed and is shown plotted in Figure 8.3-7. It is seen that, in general, the deployment non-symmetry is within 2° of travel for sectors which are directly opposite. This is approximately a 4.5 inch displacement at the rim which would be 0.3 inches per sector for the 15 sectors between the diagonally opposite measured positions. This is within lock piloting funnel capabilities. (Also see Figure 8.3-8.)

Stress levels during deployment were calculated from measured strain values and ranged from 200 psi tension to 200 psi compression during most of the deployment sequence. Momentary peak values of 750 psi compression were measured at the time of lock engagement. Based on the observed stress level in the sectors, it is estimated that they were loaded during deployment between zero stress and one "g" stress conditions. For this reason, the high level of friction previously mentioned can be expected to be reduced during a true zero "g" deployment.

Observation of the locks after deployment revealed that the collector locks had not fully detented. It was found that the piloting length of the probe in the detent was too long for the relative motion which is required near the detenting position. Binding occurs in the lock, which stopped the deployment motion before final detenting. Dry film lubricant was applied to the probes during the second deployment test; however, the final detenting was still prevented by the binding condition. All but one lock engaged (but did not detent) and this lock would also have engaged if a slightly larger funnel, such as the one shown in Figure 5.3-5, were used.

The general conclusions drawn from the deployment testing are:

- a. Measured high levels of inter-sector friction indicate that viscous dampers at the hinge are not required. Simple detent locks have been shown to adequately absorb the stopping loads.
- b. The kinematics of the locking action must be studied more closely to insure a non-binding condition.
- c. Deployment symmetry was observed to be satisfactory.

Results of optical inspections which were performed before and after testing will be presented in Section 8.3.4.

8.3.3 Collector Vibration Testing

Vibration testing of the preprototype collector was accomplished in the TRW test facility shown in Figure 8.3-9. Tests were conducted in both the stowed and de-

SUNFLOWER COLLECTOR DEPLOYMENT NON-SYMMETRY
TEST NO. 2

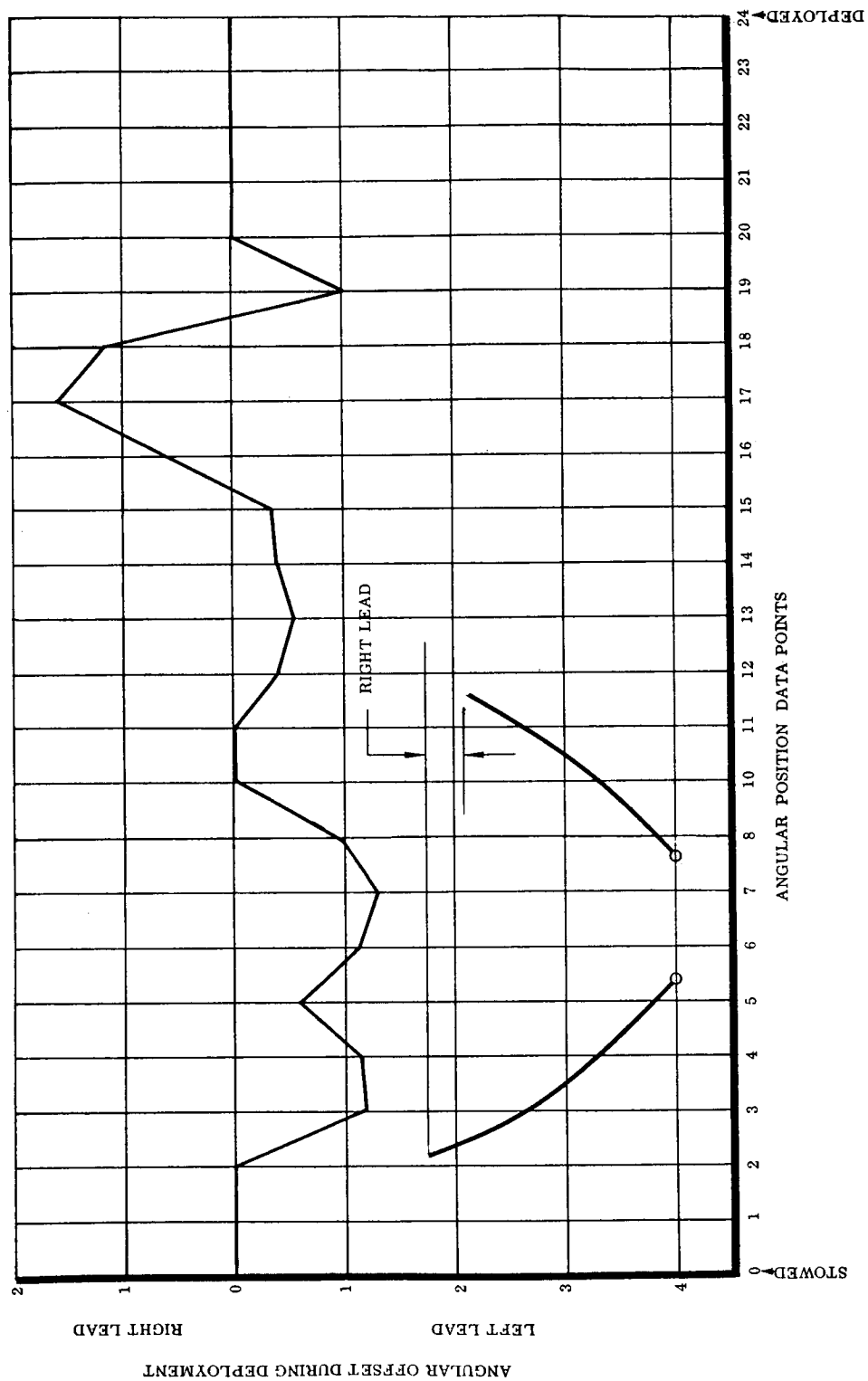


FIGURE 8.3-7

SUNFLOWER COLLECTOR DEPLOYMENT NON-SYMMETRY

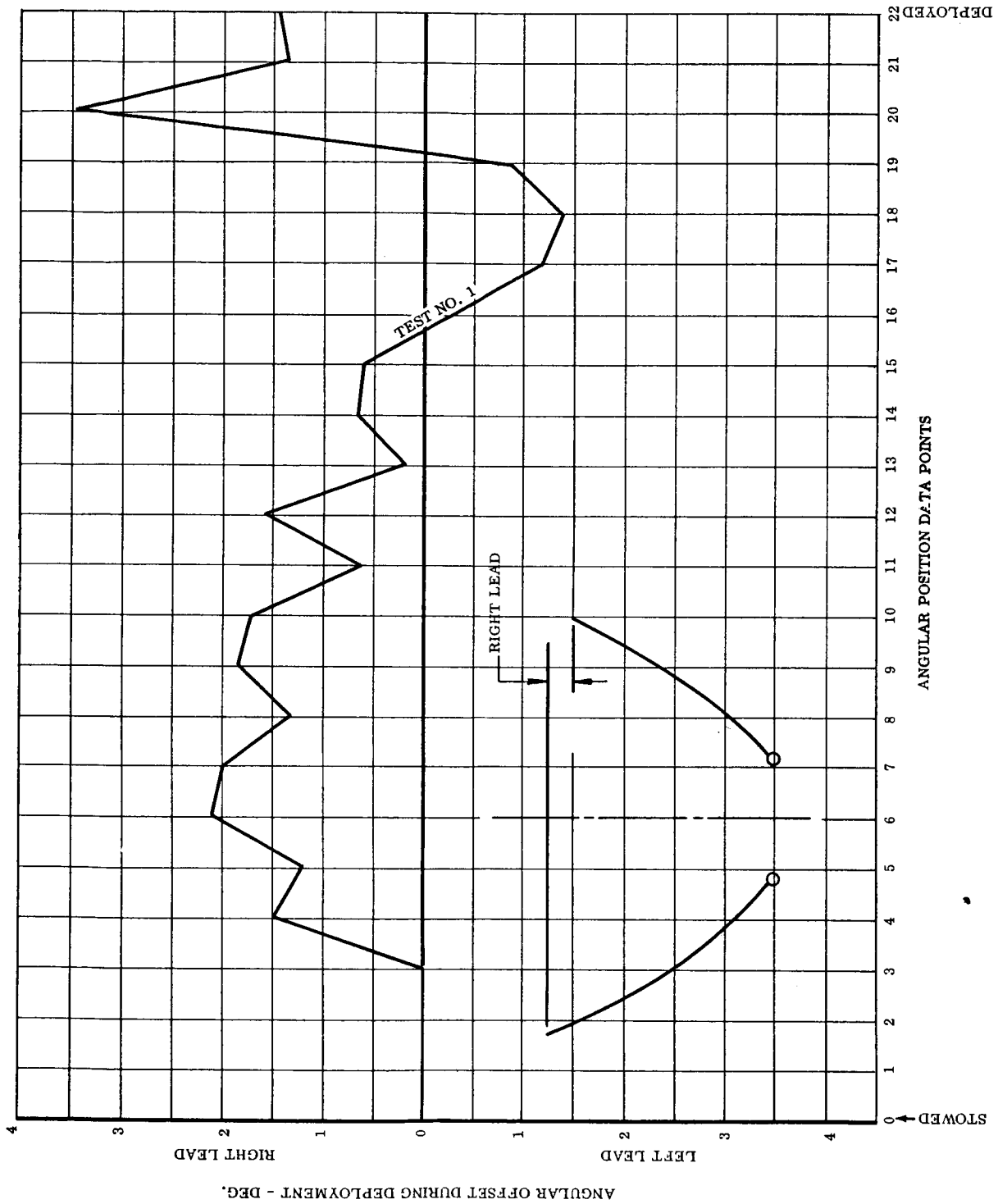


FIGURE 8.3-8

ployed configurations to evaluate response characteristics of the collector to launch and orbital transfer vibration environments.

8.3.3.1 Stowed Collector Vibration Tests

The stowed vibration test set-up is shown in Figure 8.3-10. The collector and quadrupod structure are mounted on an adapter fixture to the C-210 vibration exciter. To best simulate the launch environment, the lower mounting ring is hard mounted to the fixture to simulate the bottomed-out condition of the mounting ring isolators under the 10 "g" launch acceleration loading.

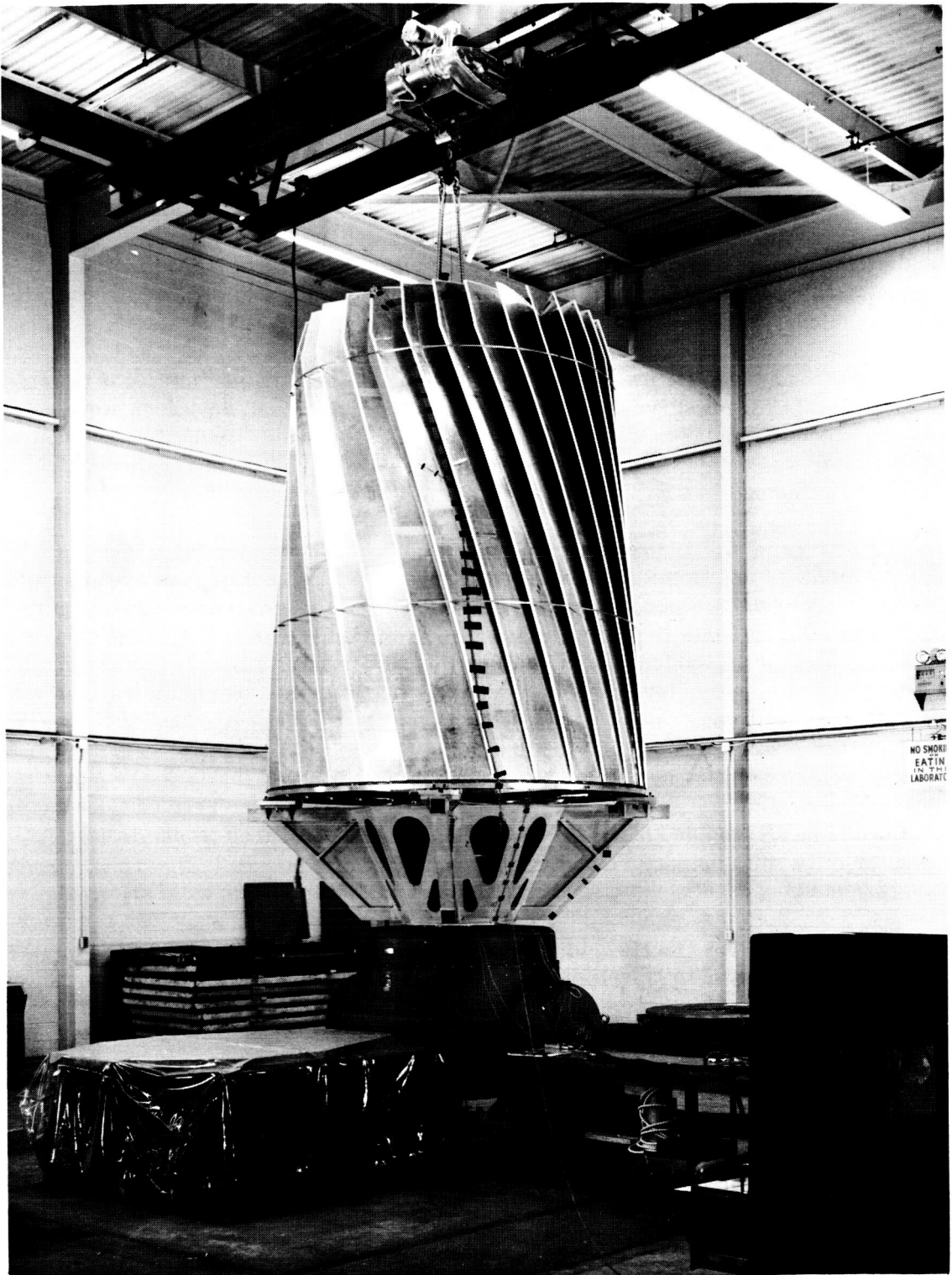
Tests were conducted at a frequency sweep rate of 1.4 octaves per minute in progressively higher "g" level surveys. Accelerometer data at various locations were recorded and motion pictures were taken at times of resonance. Input vibration control of the exciter was based upon the highest of four control accelerometers located on the fixture mounting pads.

The plot in Figure 8.3-11 shows the profile of the actual maximum input level vs frequency which was conducted on the stowed preprototype collector. It is seen that in several areas of the frequency spectrum, the specification environment (see Figure 4.2-2) was not met while in other areas it was exceeded. This is due to the control characteristics of the system which prevented accurate input control at points of resonance or high power levels. With the exception of these points, the revised specifications were imposed.

As mentioned previously (Section 4.2.2), the vehicle vibration inputs to the mounting points of the Sunflower system can be amplified or damped by the response characteristics of the quadrupod and structural mounting rings. Measured transmissive characteristics of the structure and rings are shown in Figure 8.3-12. These curves represent the response of the structure and rings to the input spectrum shown in Figure 8.3-11, and they are actually the input vibrations to the honeycomb sandwich sectors. The stacking ring, which is vibration isolated and structurally damped (see Section 5.3.6), is seen to have a much lower transmissive characteristic. These represent the longitudinal or axial vibration inputs to the sectors; however, lateral vibrations were also observed as response characteristics and will be shown for comparison in the following plots.

Figures 8.3-13 and 8.3-14 show the honeycomb sectors mid span response to the measured vibration condition at the mounting ring. It can be seen that the vibration is highly damped in the axial direction. In the lateral direction (see Figure 8.3-14), the vibration is not as highly damped and in some cases amplification occurs.

Points of resonance which were observed and identified are listed in Table 8.3-2. Approximately fourteen additional minor resonant points were observed over the frequency range; but, as might be expected for such a complex structural arrangement, they could not be specifically identified.



STOWED COLLECTOR VIBRATION TEST INSTALLATION

SUNFLOWER COLLECTOR - STOWED CONFIGURATION VIBRATION TEST, 3-8-63 AND 3-11-63
 PROFILE OF ACTUAL INPUT "G" LEVELS AT COMPONENT MOUNTING PAD (BEST OF 4)

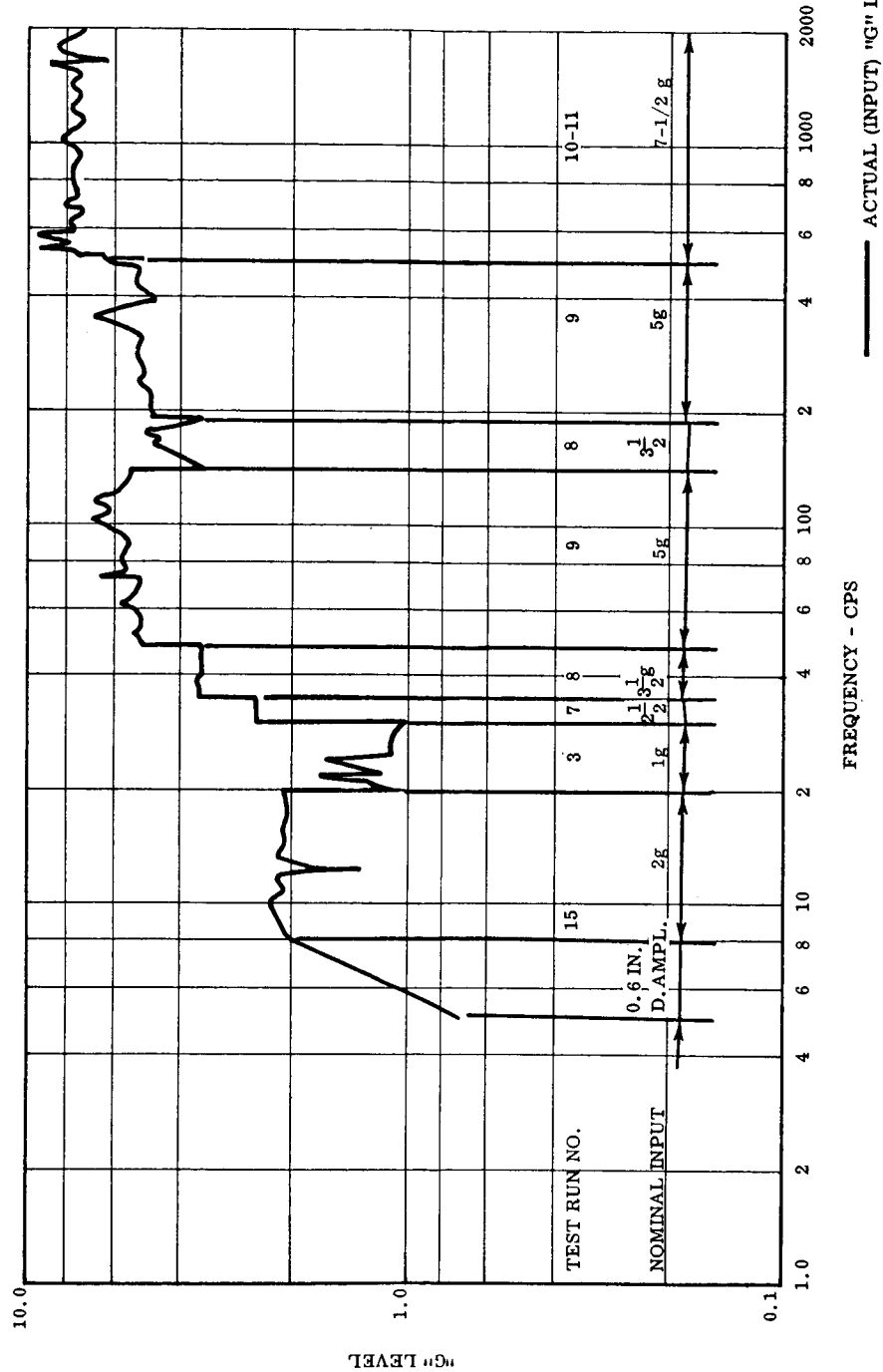


FIGURE 8.3-11

STRUCTURAL SUPPORT RINGS, MID SPAN TRANSMISSIBILITY

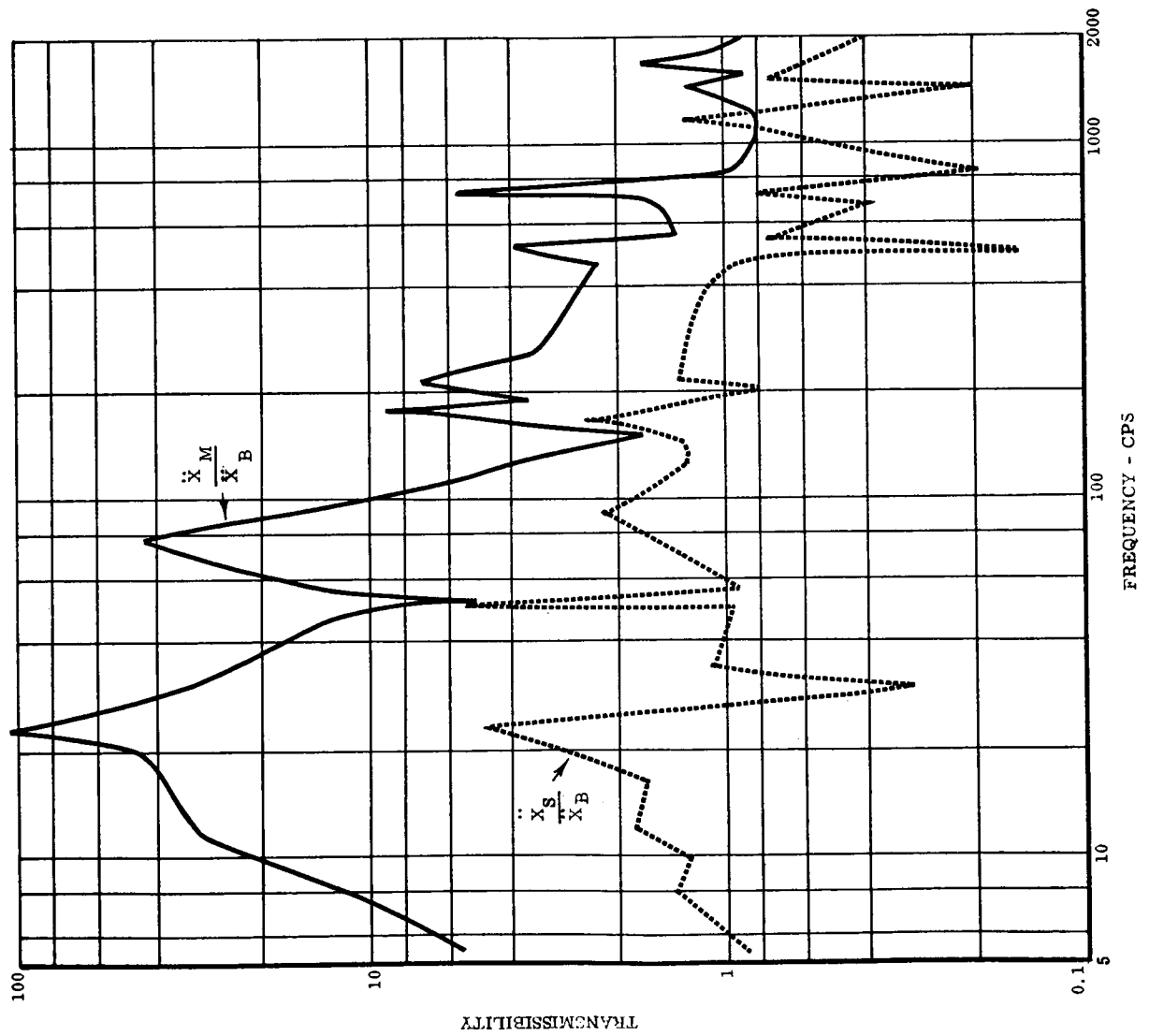
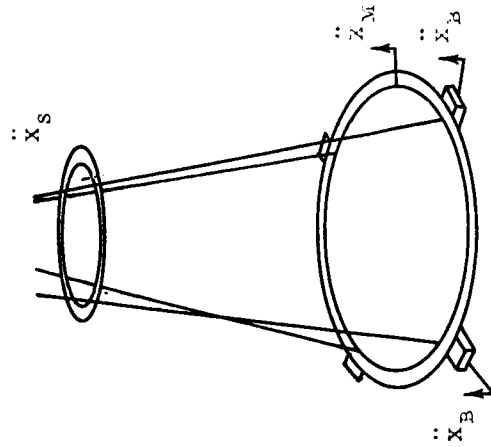


FIGURE 8.3-12



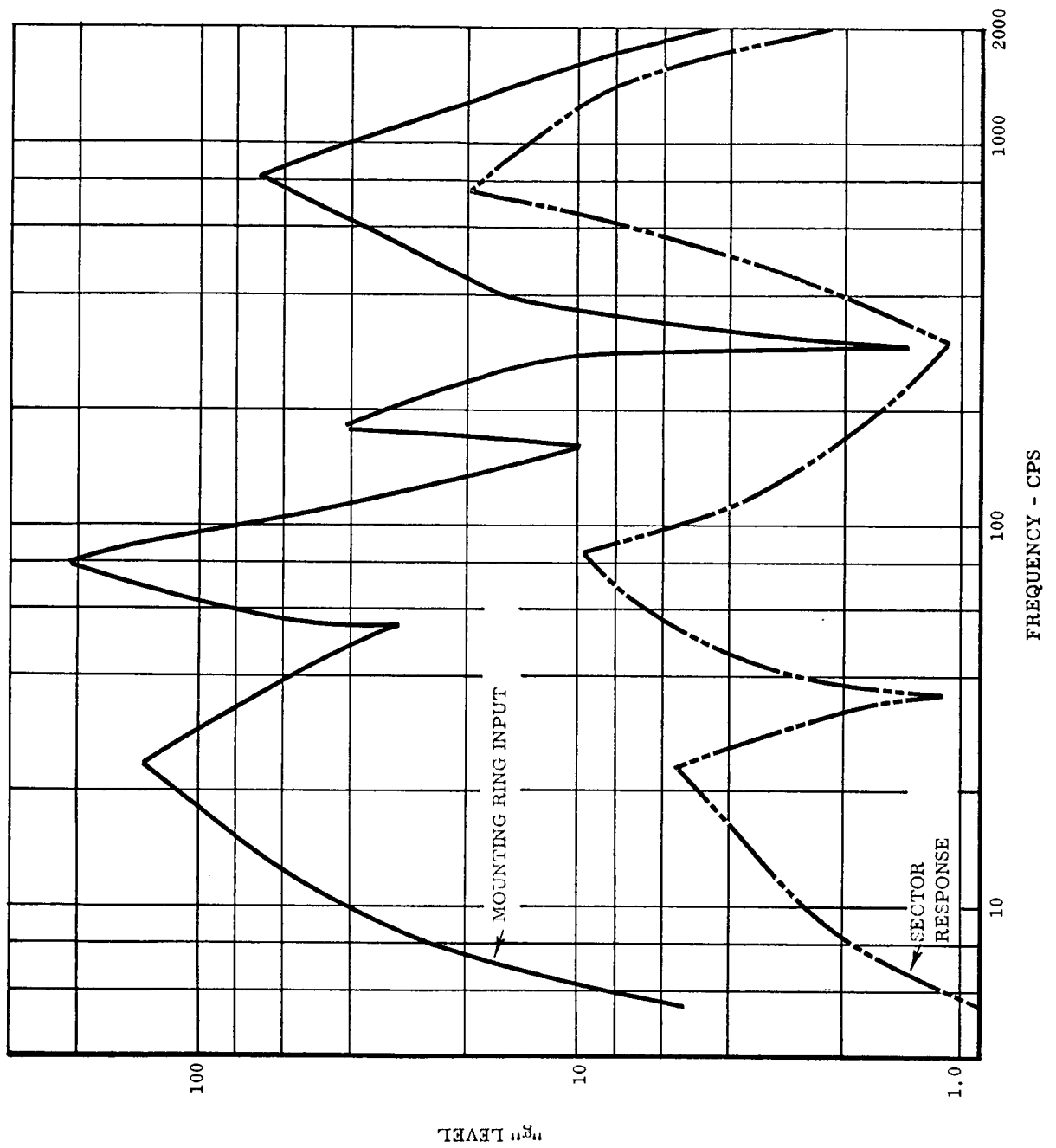


FIGURE 8.3-13

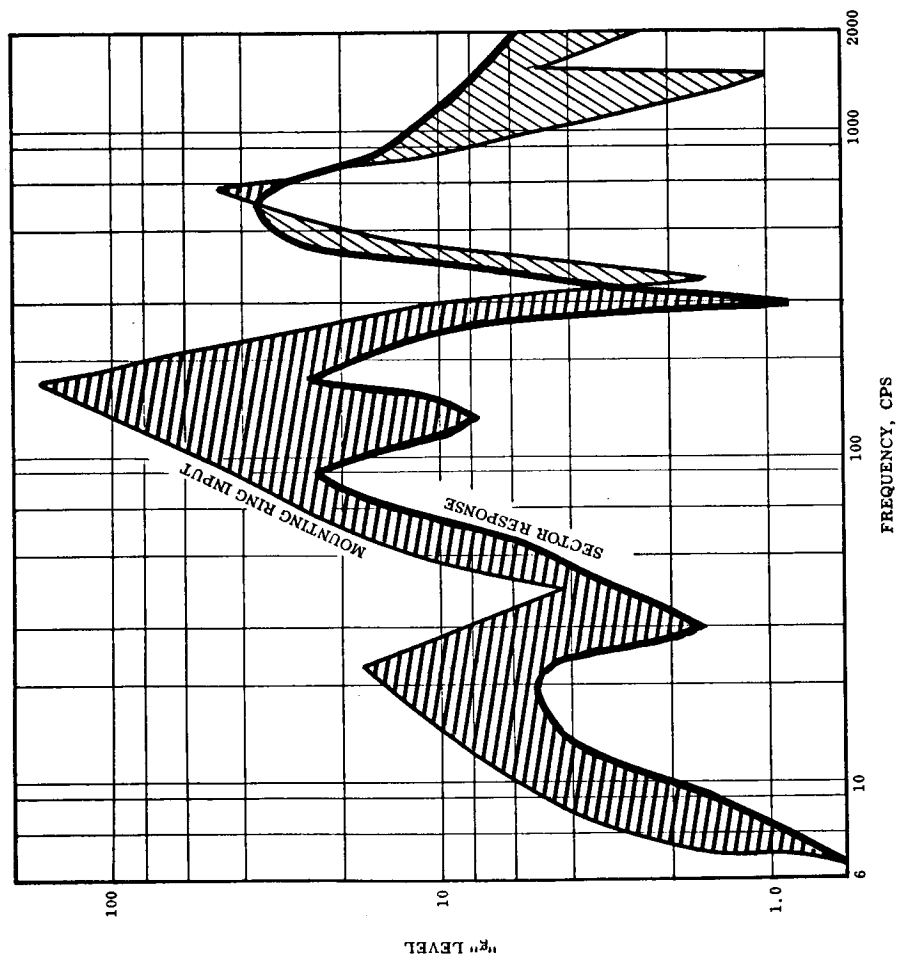


FIGURE 8.3-14

PETAL NO. 13, CENTER Z - Z AXIS

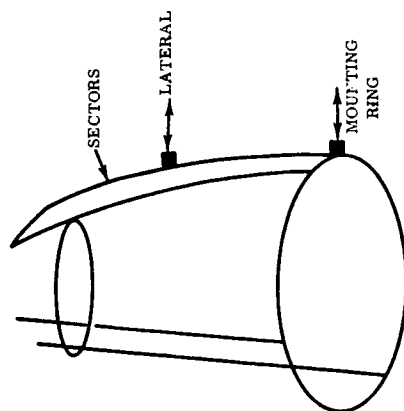


TABLE 8.3-2

STOWED VIBRATION RESONANCE POINTS

Frequency CPS	Type of Resonance	Resonant Member Description		Base Input "g"	Max. Response "g"	Mode Description
		Location	Direction of Primary Resonant Amplitude			
8	Minor	Sector Tip	Tangential	2 Axial	1 Tang.	Bundle Twisting
23	Major	Mounting Ring Mid Span	Axial	1.4 Axial	151 Axial	Mounting Ring Flexural Resonance
50	Major	Stacking Ring Mid Span	Axial	5.4 Axial	31 Axial	Stacking Ring Isolators Natural Frequency
77.5	Major	Mounting Ring Mid Span	Axial	5.6 Axial	247 Axial	Mounting Ring Flexural Resonance
92.5	Major	Sector Tip	Axial, Lateral, and Tangen- tial	5.5 Axial	48.4 Axial 47.2 Tang. 38.4 Lat- eral	Sector Flexural Resonance
175.5	Major	Mounting Ring Mid Span	Radial	5 Axial	200 Radial	Mounting Ring Extensional Resonance
520	Major	Sector Mid Span	Lateral	8.4 Axial	33.2 Lateral	Sector Fluxural Resonance
730	Major	Sector Tip	Axial	7.5 Axial	48.4 Axial	Sector Flexural Resonance

In general, the honeycomb sectors response followed the response of the quadrupod and support rings with isolation and damping over the full frequency spectrum.

8.3.3.2 Deployed Collector Vibration Tests

The deployed vibration test set-up is shown in Figure 8.3-15. The collector was opened and locked while in place on the exciter fixture. The auxiliary support stands which were used for support during opening and lock assembly were pulled back during vibration testing so that the deployed collector was supported only at the center mounting ring. This position combines the orbital transfer environments of one "g" acceleration and the vibration spectrum. Vibration isolators were added to the mounting ring at the mounting pad locations and the tests were conducted similar to the stowed vibration test procedure.

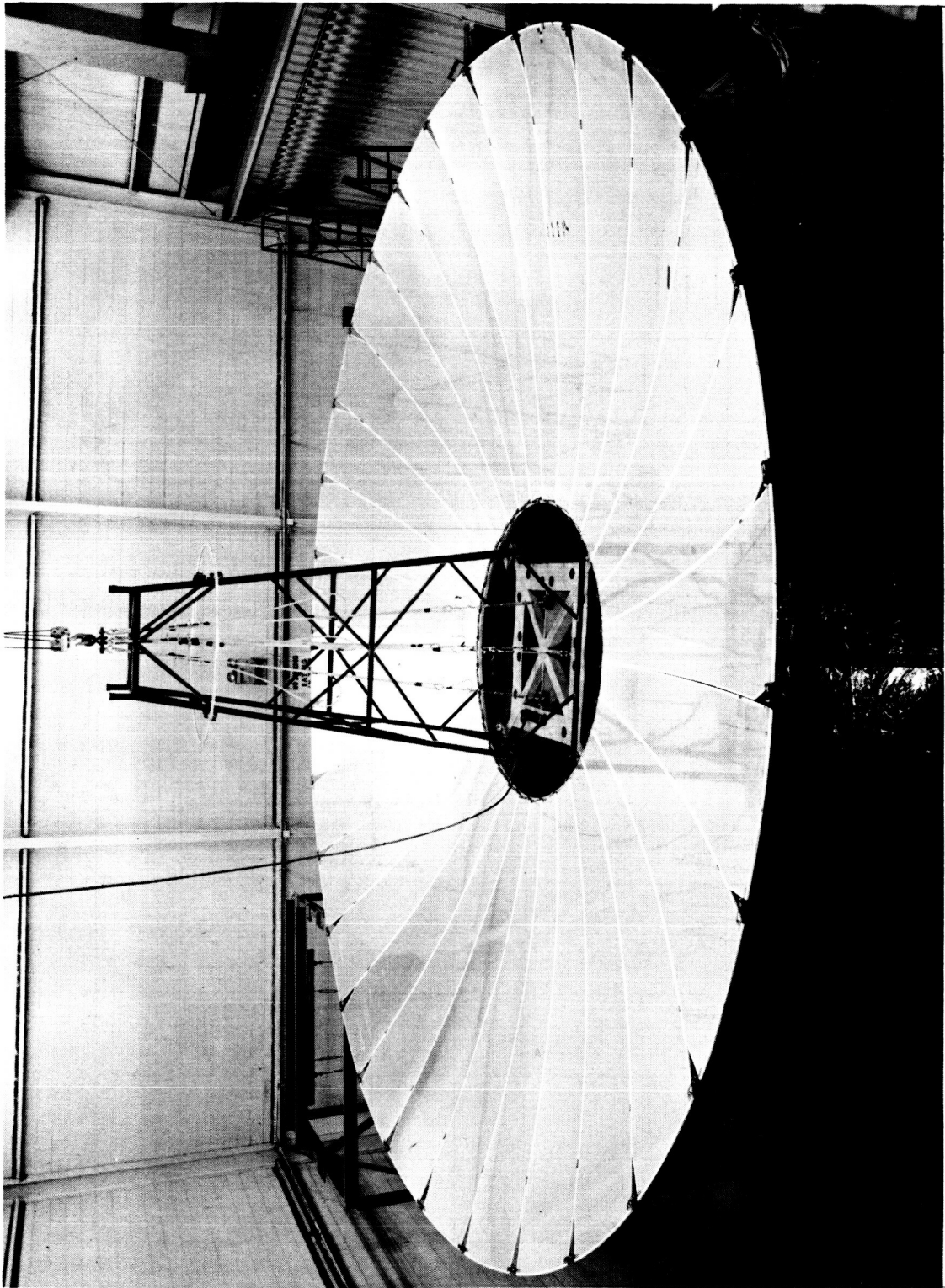
Figure 8.3-16 shows the profile of actual maximum input level which was conducted on the deployed preprototype collector configuration. Again, certain portions of the spectrum were limited by resonances and control capabilities. Also shown in Figure 8.3-16 are the measured response of the mounting ring. It is seen that the isolators damped the vibration in the higher frequency range; however, at the low frequencies, the structural response of the ring produces generally high amplifications of the motion at mid-span. This displays the need for visco-elastic structural damping and additional supports in subsequent mounting ring designs.

Typical honeycomb sector response is shown in Figures 8.3-17 and 8.3-18. It is seen that the honeycomb sandwich material and lock connections produced a general damping characteristic which improved at the collector rim.

The structural response of the honeycomb sectors was monitored by dynamic strain gage measurements at various locations. Typical cyclic stresses at frequencies where apparent large amplitude sector flexure occurred is shown in Table 8.3-3.

This stress is the variation about the dead weight stresses shown in Table 8.3-1 for the prototype rim lock-rigid intermediate lock case. These stresses were observed to cycle about the dead weight stress at the frequency of the base input vibration.

It is seen that the highest stresses occur at the low frequencies. For this reason and since the low frequency vibration specification for the deployed orbital environment is not well defined, higher "g" levels at low frequencies were not attempted. The two other areas where "g" level inputs were reduced (see Figure 8.3-16) are 30 cps due to the mounting ring flexural resonance and approximately 150 cps due to power and control limitations of the C-210 excitor. During the deployed collector vibration testing, a fastener pull-out failure occurred at approximately 2g, 13 cps. The two intermediate lock bonded-in fastener inserts on sector number 11 failed by pulling out of the honeycomb sandwich material. The prototype lock connection was not damaged and the collector came to rest on the auxiliary support stands which were about six inches below.



DEPLOYED COLLECTOR VIBRATION TEST INSTALLATION

SUNFLOWER COLLECTOR - DEPLOYED CONFIGURATION
VIBRATION TEST, 3-14-63 TO 3-16-63

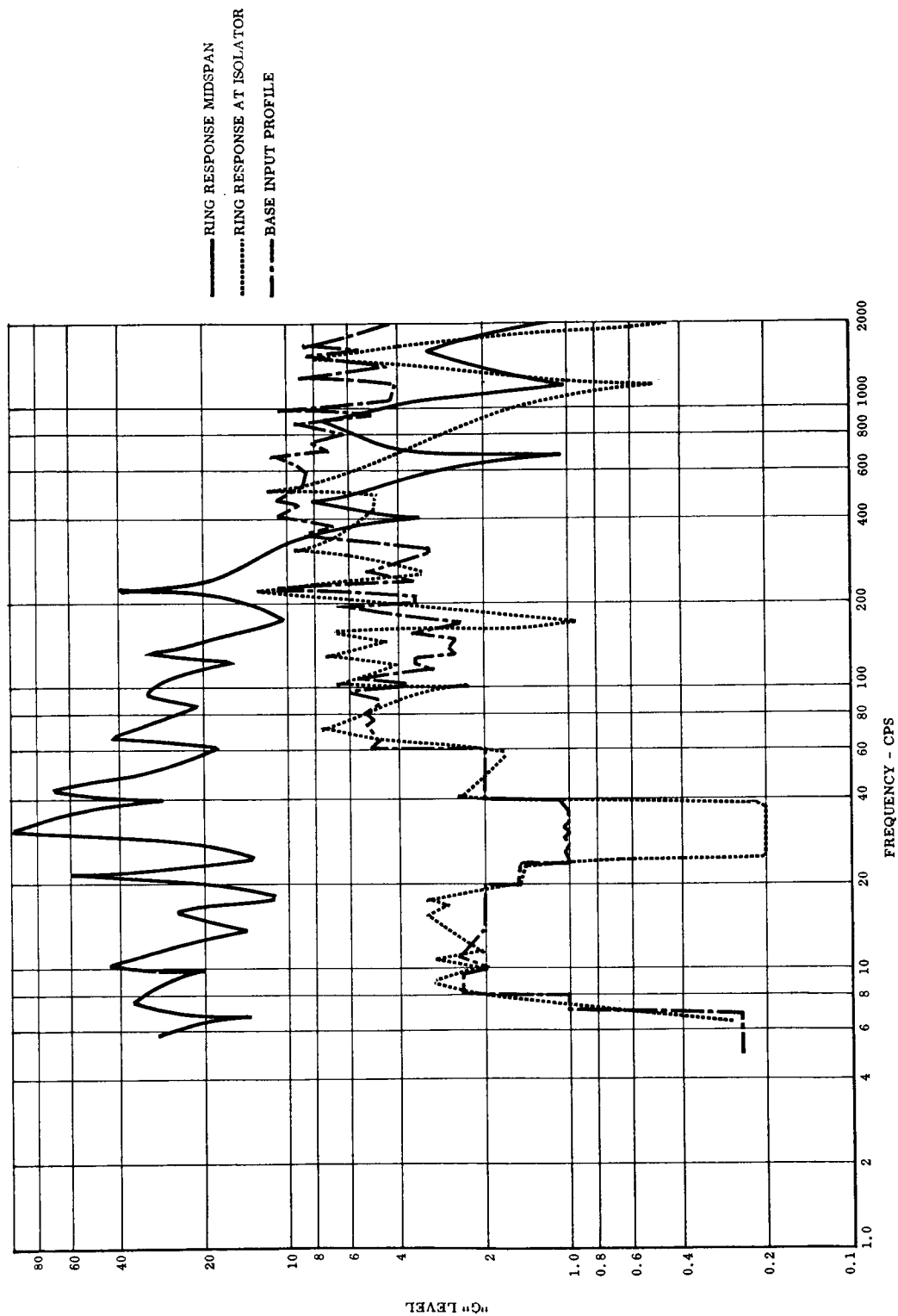


FIGURE 8.3-16

SUNFLOWER COLLECTOR DEPLOYED VIBRATION TEST, 3-14-63 TO 3-16-63
SECTOR RESPONSE AT MID SPAN AXIAL DIRECTION SECTOR NO. 13

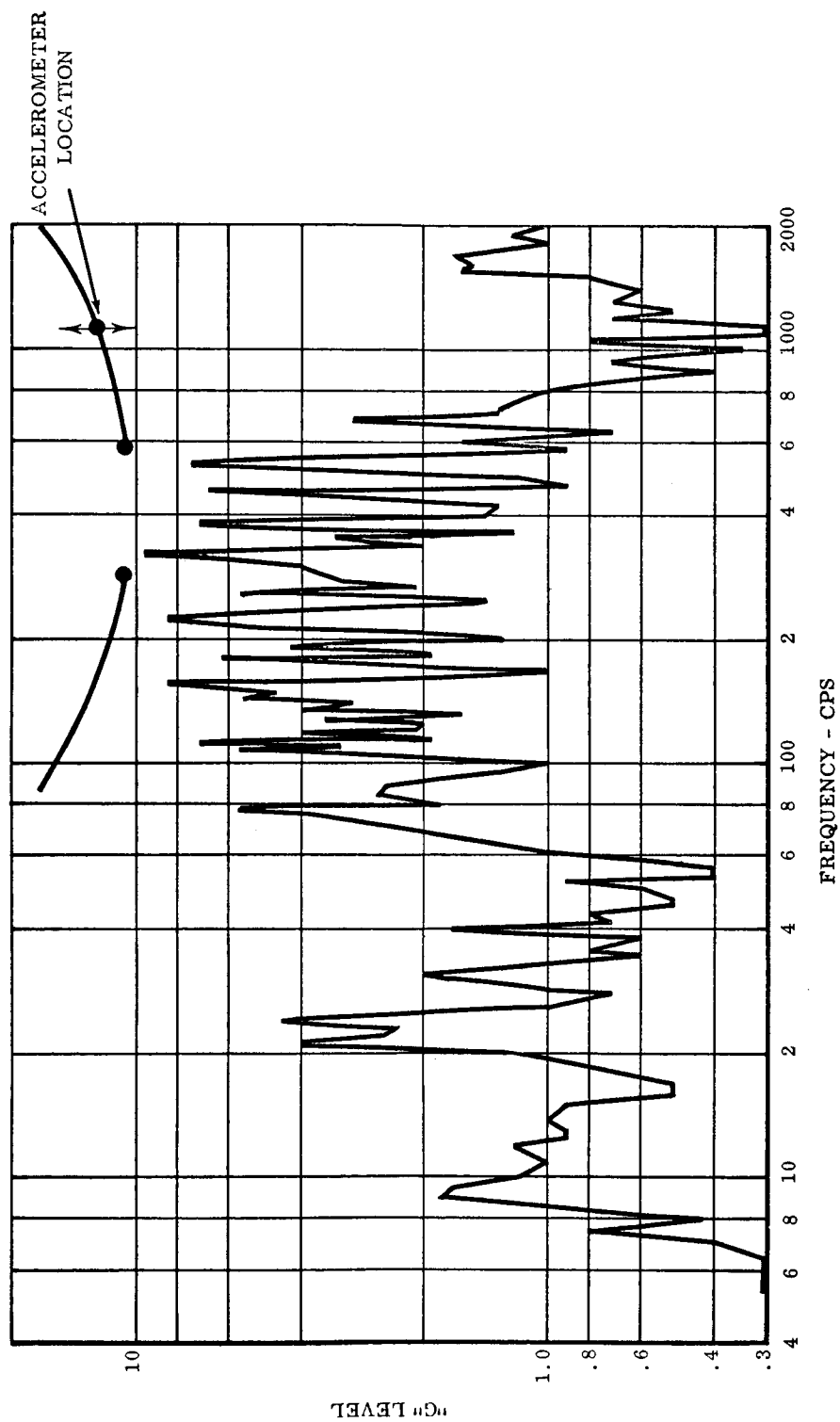


FIGURE 8.3-17

SUNFLOWER COLLECTOR-DEPLOYED VIBRATION TEST, 3-14-63 TO 3-16-63
SECTOR RESPONSE AT RIM AXIAL DIRECTION SECTOR NO. 13

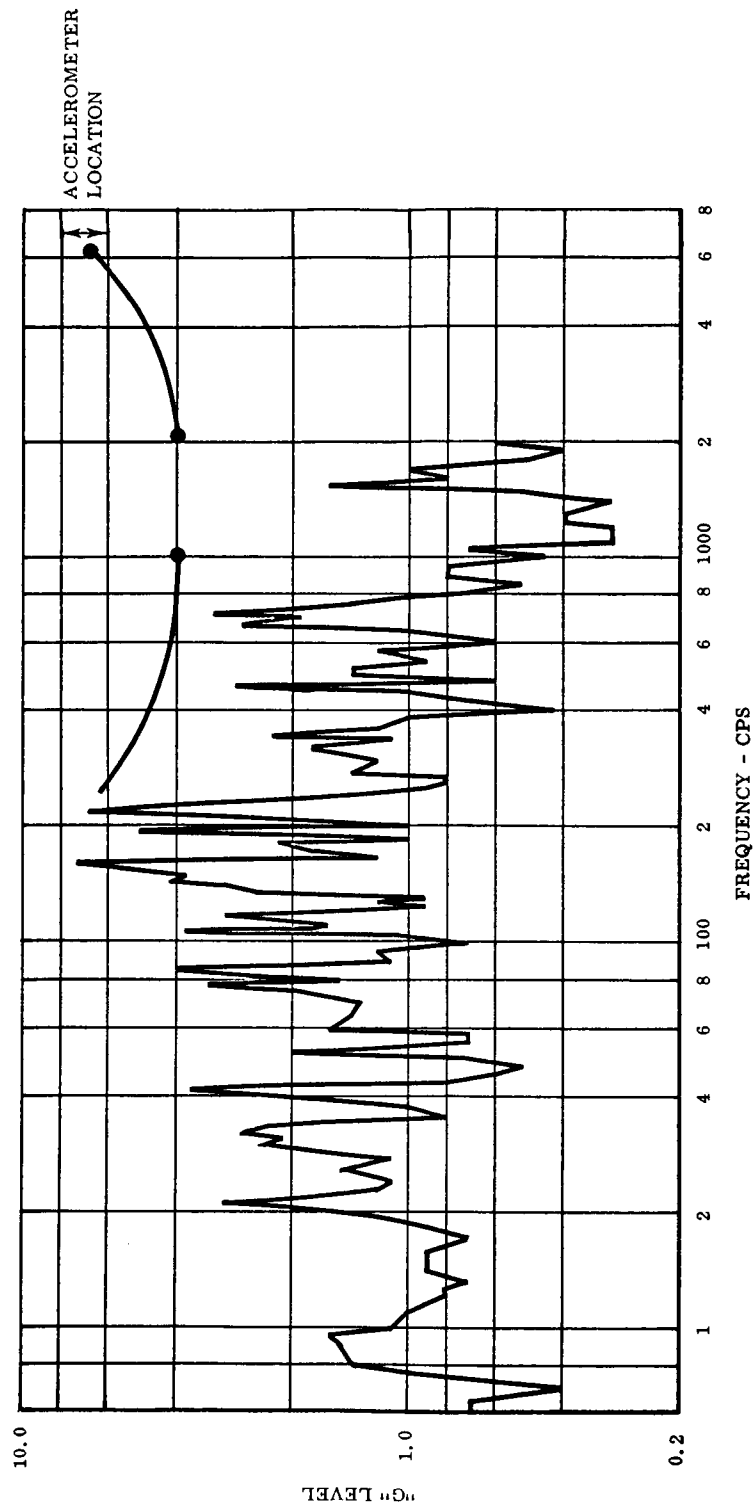
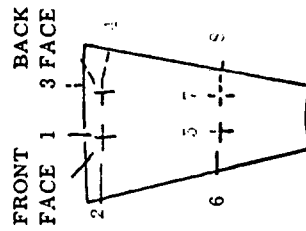


FIGURE 8.3-18

TABLE 8.3-3

CYCLIC STRESSES AT RESONANT POINTS DEPLOYED COLLECTOR VIBRATION

FRE- QUENCY CPS	NOMINAL INPUT "G" LEVEL	CYCLIC STRESS ± PSI							
		RADIAL	CIRCUM.	RADIAL	CIRCUM.	RADIAL	CIRCUM.	RADIAL	CIRCUM.
		LOCATION	1	2	3	4	5	6	7
6	0.25	94	284		215	193	0	0	660
8	2	150	454		208	170	19	57	1208
10	2	94	284		320	360	19	57	692
21.5	1.5	38	113		363	473	147	200	136
42	2	57	170		265	189	102	155	302
60	5	57	170		215	193	0	0	378
75	5	150	454		19	57	320	510	0
112	3.5	11	34		253	215	0	0	287
									195



Upon close examination of the failed fasteners, it was found that the inserts had been bonded improperly; that is, adequate filling of the adjacent core cells had not been accomplished. The sector was repaired and placed back in the assembly and testing was continued. The point at which the failure had occurred was re-run with no structural damage.

8.3.4 Optical and Structural Effects of Environmental Testing

8.3.4.1 Effects of Dead Weight Structural Testing

Typical results of grid-screen optical inspections comparing dead weight deflected shapes of rigid vs preprototype lock conditions is shown in Figure 8.3-19. The absolute slope difference between the two curves is shown plotted in Figure 8.3-20. If this difference is considered to be the effect of the detenting locks upon the deployed position shape under a one "g" environment, then this plot can be extrapolated to the orbital environment specification of 0.001 "g" to estimate the level of possible geometric deviation due to deployment errors. This extrapolation has been plotted in Figures 7.4-1 and 7.4-2 for general comparison with other types of deviations.

8.3.4.2 Effects of Deployment and Vibration Environments

Figure 8.3-21 shows typical results of comparison optical inspections which were obtained from the preprototype collector. Slope changes from these comparisons are shown in Figure 8.3-22. Other sectors which were inspected show similar difference values.

It can be seen from these figures that the general waviness of the sector is not greatly affected, but that the gross deflection of the sectors is changing. Also, the deviations are very small near the collector rim where the preprototype lock is the restraining element. These factors indicate that the primary cause of the observed gross shape changes is due to the variation imposed by the intermediate strap lock bending and fastener hole clearance.

To obtain an indication of any optical changes in the honeycomb sectors themselves, the difference in waviness before and after environmental testing as referenced to the general shape is shown plotted in Figure 8.3-23.

As anticipated from visual observations, the honeycomb sectors shape change due to environmental testing is very small. Although an accurate indication of the effect of prototype locks upon the total paraboloid shape could not be obtained due to the limited design scope and test objectives, it is believed that these changes would also be small as indicated by the previously mentioned small deviations at the collector rim.

Visual inspections of the collector were also made before and after testing to observe any deviations or structural damage which might not be apparent from optical inspections. Damage was observed in the form of skin peels where the adhesive bond to the core had failed. Only 1/3 % of the collector surface areas showed this type of

OPTICAL INSPECTION RESULTS DEAD WEIGHT TESTING

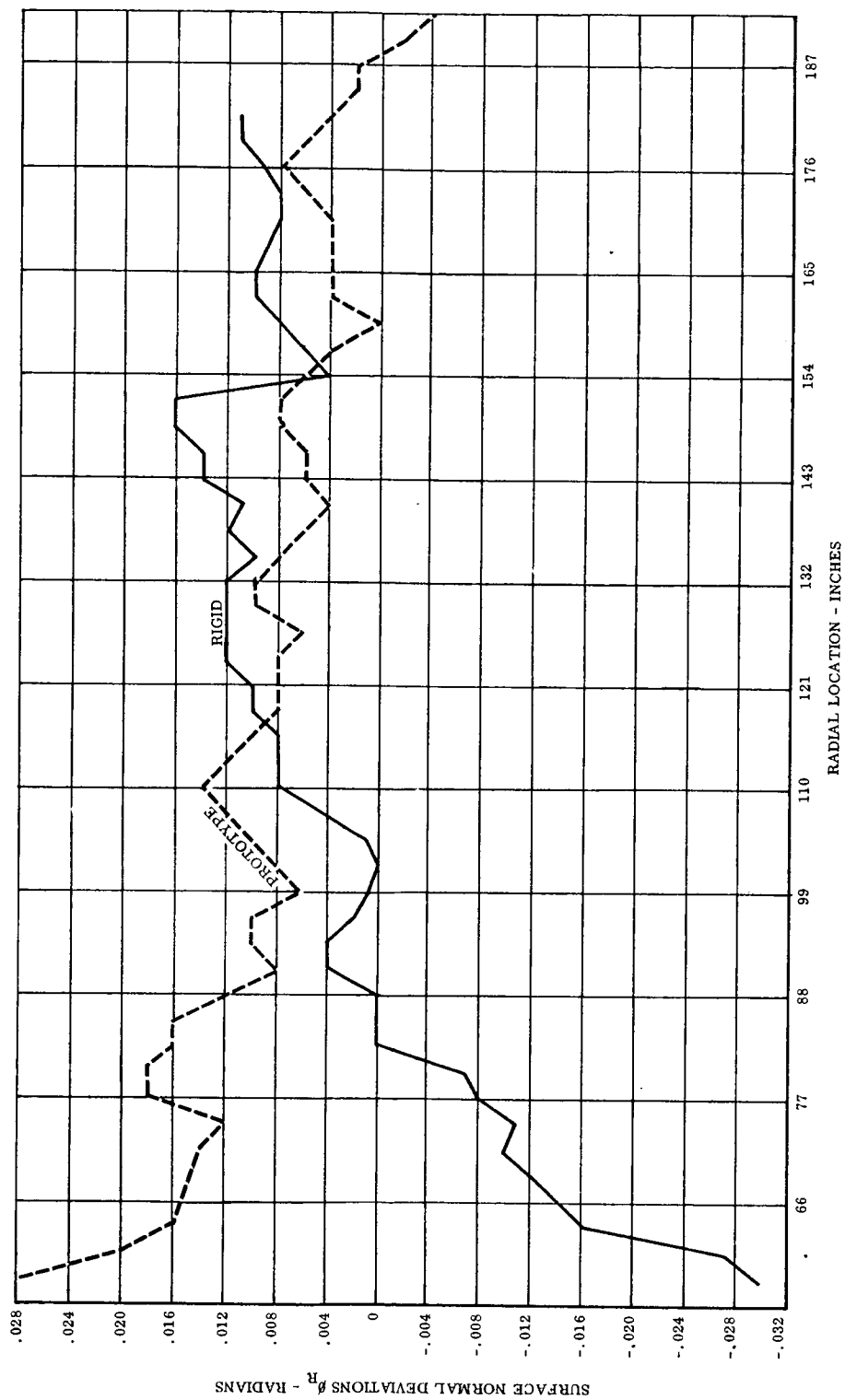


FIGURE 8.3-19

RADIAL SLOPE CHANGES DEAD WEIGHT TESTING

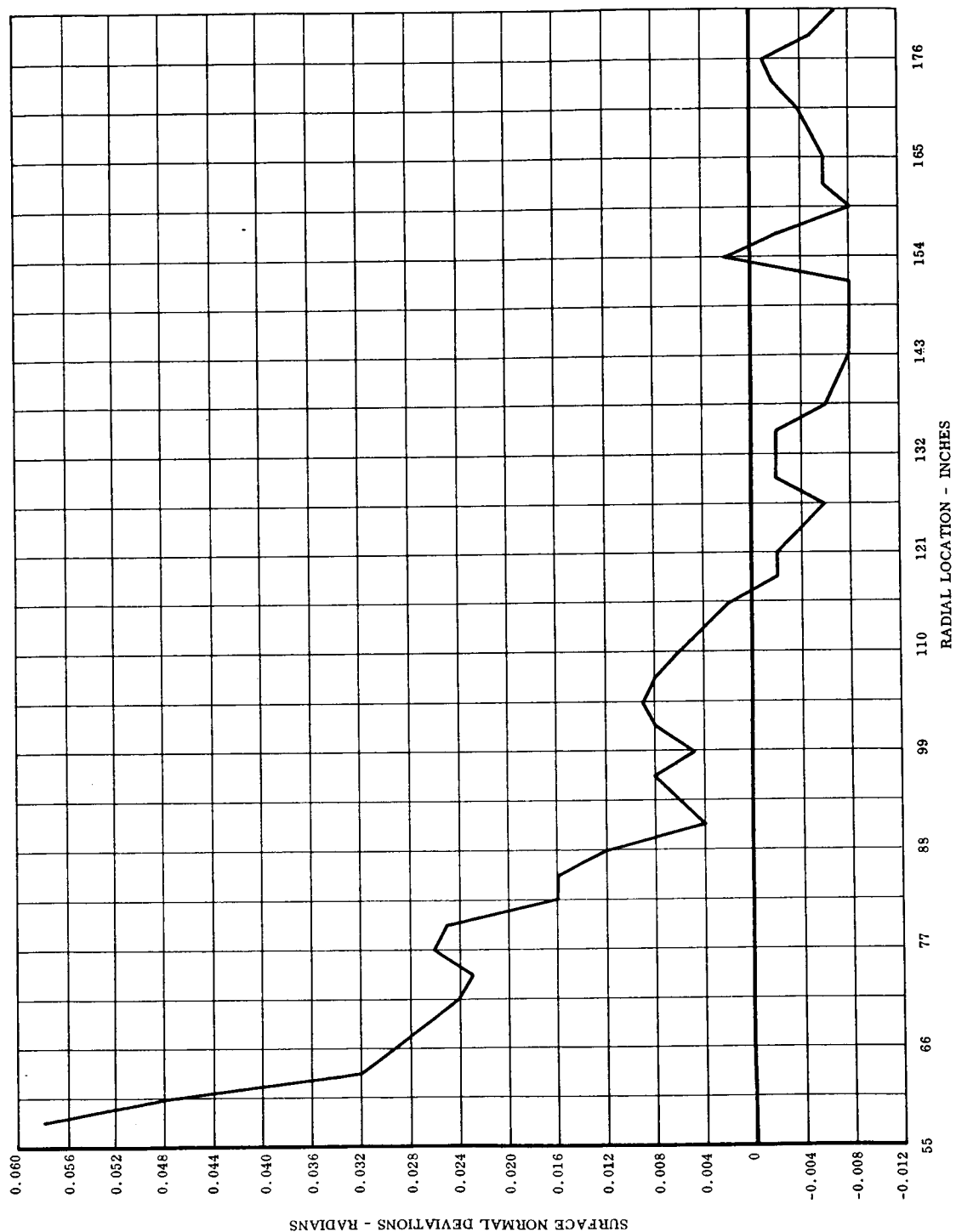


FIGURE 8.3-20

OPTICAL INSPECTION RESULTS BEFORE AND AFTER ENVIRONMENTAL TESTING

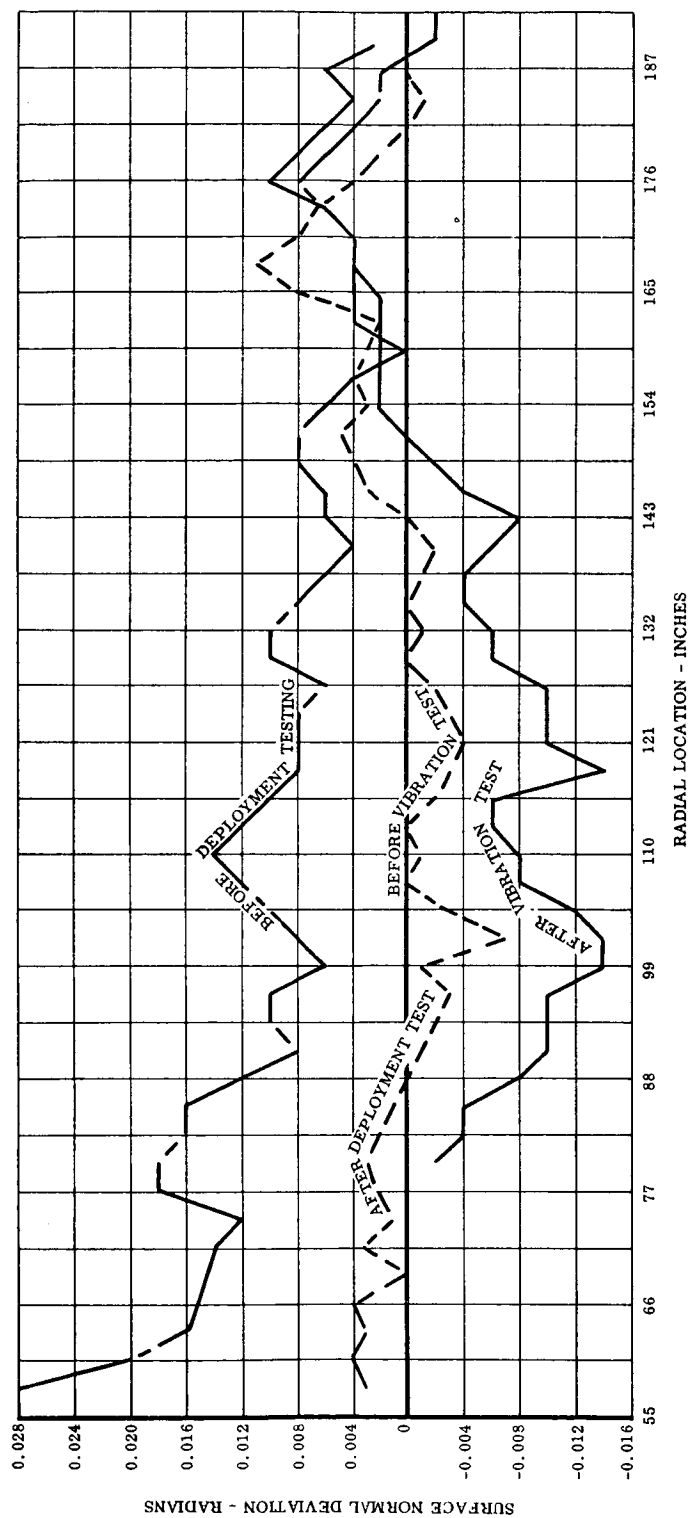


FIGURE 8.3-21

RADIAL SLOPE CHANGES - ENVIRONMENTAL TESTING

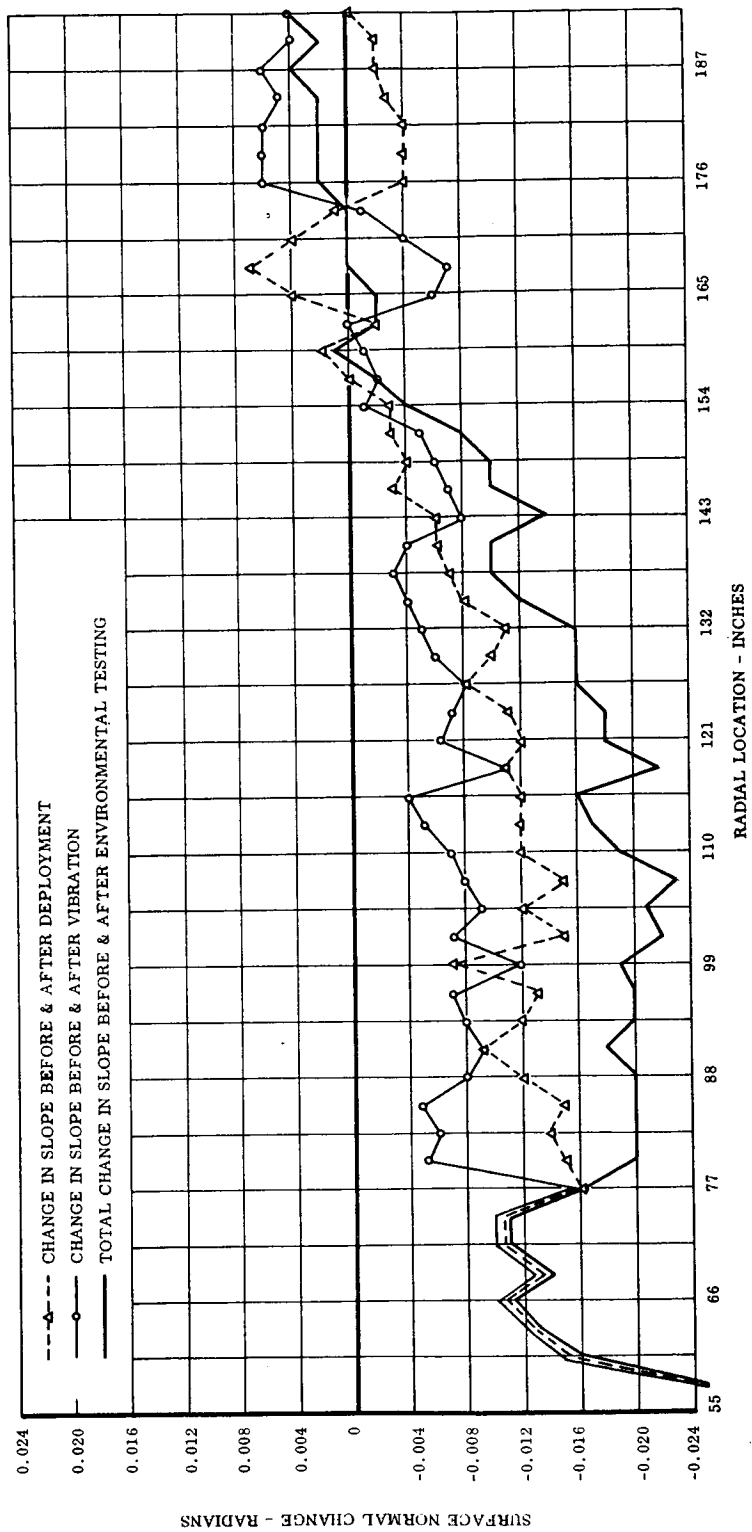


FIGURE 8.3-22

WAVINESS SHAPE CHANGE DUE TO ENVIRONMENTAL TESTING

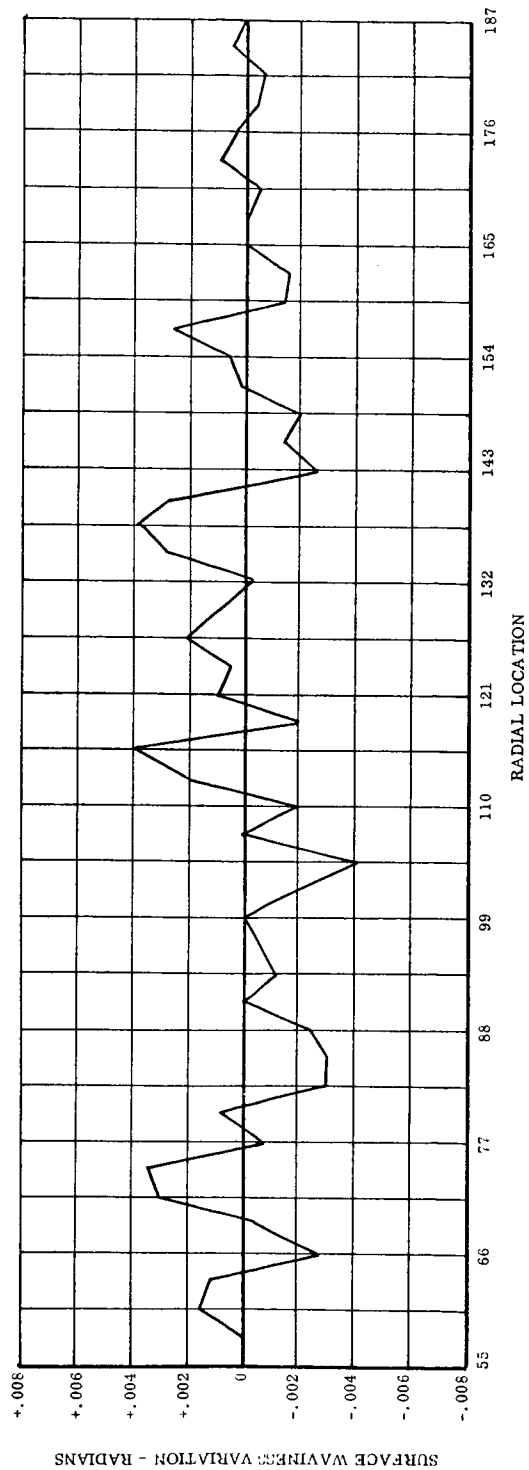


FIGURE 8.3-23

damage, of which less than half was on the optical face. The majority of the observed damage is due to increases in skin peel in areas which were originally peeled, indicating the need for rigid fabrication process control to eliminate weak or completely unbonded areas. Only one sector showed damage in the torsion bar area. This was in the form of skin peeling on the optical face and is believed to have been a fabrication quality problem, since none of the other sectors showed this local peeling condition.

One other form of damage which was observed was abrasion between sectors. After deployment testing, abrasion was apparent on the overlapping portions of adjacent sectors but was caused primarily by the deployment harness calibration technique which required many opening and closing cycles.

Abrasion was also observed on contacting edges of adjacent stowed sectors and at stacking ring locations on each sector due to the relative motion of these parts during vibration testing. Optical surface areas which are involved are small; however, local abrasion padding for both deployment and stowed vibration should be considered in future designs.

In general, no major structural damage was observed during environmental testing. The deviations which were encountered can be eliminated by adequate process and quality control. Optical effects which were observed have been incorporated into the overall geometric quality presentation of Section 7.4.

9.0 CONCLUSIONS

Considerable advancement in solar collector technology and fabrication state of the art has been accomplished during the Sunflower solar collector development program. Collector inspection and test methods have been established as well as analytical procedures to directly utilize this information.

It has been established by test data and correlated by optical inspection results that the normal probability distribution model of surface deviations is more accurate than other models which have been discussed in the literature for paraboloidal concentrators.

Although the preprototype collector was not intended as a high optical quality design, a standard surface deviation of less than $1/2^\circ$ has been demonstrated in single panel performance tests. Based upon the knowledge obtained during the development program, a standard deviation of $1/4^\circ$ including estimated environmental errors can be attained in a prototype design.

The structural integrity of the adhesive bonded aluminum honeycomb sandwich construction used in the Sunflower concentrator has been established as well as the operability of deployment concept in a full size configuration.

Fabrication techniques and tooling concepts have been evaluated and critical factors have been defined. Vacuum deposition processes have been established for the Sunflower collector as well as quality control requirements to obtain a mirror surface.

Many problem areas remain before all the requirements of weight, optical performance, and strength can be attained in a flight-ready concentrator; however, a reliable basis for prototype collector design has been established.

Although much detailed investigation remains before reliability can be verified, the development work performed during this program demonstrates conclusively the feasibility of producing and utilizing large, light weight, foldable solar concentrators for space power conversion systems.

10.0 RECOMMENDATIONS

Utilization of the technology derived from the Sunflower solar collector development program can be accomplished by a continued development effort. Such an effort would result in a completely performance-tested and system-integrated solar power conversion component.

The following three phase program of investigation and development is recommended:

- a. Phase 1. — Developmental Refinements and Tests. This phase is essentially the design period for the prototype collector. Analysis, fabrication, and test information which was obtained during the preprototype collector development would be supplemented by detailed investigation of several specific problem areas, i.e., stretch forming, surface coatings for higher specularity, and silicon oxide stabilization. Also included would be environmental compatibility testing of silicon oxide, structure temperature cycling, and thermal distortion testing.
- b. Phase 2. — Full Size Sector Fabrication and Performance Tests. Single sectors would be fabricated to the design and specifications established during Phase 1. These sectors would then be performance-tested using the existing single panel test rig. In this way, the prototype design would be performance evaluated before fabrication of the complete collector.
- c. Phase 3 — Prototype Collector Fabrication and Performance Tests. The complete full size prototype collector would be fabricated, inspected, and performance-tested. The West Coast test facility would be utilized for complete collector and collector-receiver performance evaluation. The experimental data obtained would provide the information needed for conclusive correlation of optical inspection results and analytical techniques for accurate prediction of collector-receiver performance in a space power system application.

A detailed presentation of this recommended continuation of the Sunflower solar collector development program will be found in "Followon Sunflower Solar Collector Program" (TRW ER-5257, March 1963).

APPENDIX A - REFERENCES

1. Aldrich, C. E., T. P. Kiritsis and E. Bond. "Structural Analysis for Idealized Model of the Sunflower Paraboloidal Solar Collector." General Dynamics/Electric Boat Division, Report U411-62-058, Sept., 1962.
2. Bevans, J. T. and A. D. LeVantine. "Semi-Annual Report on Satellite Materials and Environmental Control Systems Investigations." Space Technology Lab Report STL/TR-60-0000-09195, June 30, 1960.
3. Brozdowicz, Z. "Solar Concentrator Development." JPL Space Programs Summary No. 37-21, pp. 26, 27.
4. Castle, C. H. "Solar Collector Design Procedure (Paraboloidal Concentrator - Cavity Receiver Configuration)." TRW Publication, April 1963.
5. Chen, H., J. E. Cadoret and C. E. Aldrich. "A Matrix Method for Analysis of Complex Structures." General Dynamics/Electric Boat Division, Report U413-61-176, Feb. 1959.
6. Cremer, E., T. H. Kraus and E. Ritter. Z. Electrochem., 62, 9, 1958, pp. 939-941.
7. "Development of Stable Temperature Control Surfaces for Spacecraft." Progress Report No. 1, JPL TR No. 32-340.
8. Dresser, D. L. "Elements of Solar Collector Design." IAS Paper 61-24.
9. Drumheller, C. E. "Properties and Application of Silicon Monoxide." Kemet Corp., Division of Union Carbide Co.
10. Drummeter, L. F., Jr. and E. Goldstein. "Vanguard Emittance Studies at NRL." First Symposium on Surface Effects on Spacecraft Materials. J. Wiley and Sons.
11. Haller, H. C., and C. T. Jaenke. "Sunflower System Heat Transfer Analysis." TRW ER-4978, Jan. 1962.
12. Hass, G. J. Opt. Soc. Am., 45, 11, 1955, pp. 945-952.
13. Hass, G., L. F. Drummeter, Jr. and M. Schlach. J. Opt. Soc. Am., 49, 9, 1959, pp. 918-924.
14. Hass, G. and J. E. Waylonis. J. Opt. Soc. Am., 51, 7, 1961, pp. 719-722.

15. Hanson, J. N. "The Computation of the Flux Distribution Gathered by Solar Collectors." TRW ER-4380, March 1961.
16. Holland, L. J. Opt. Soc. Am., 43, 5, 1953, pp. 376-380.
17. Hukuo, N. and H. Mii. "Design Problems of a Solar Furnace." Journal Sol. Energy Sc. and Engr. April-June 1958, vol. 1, no. 2-3.
18. Jaffe, L. D. and J. B. Rittenhouse. "Evaporation Effects on Materials in Space." JPL Technical Report No. 32-161, Oct. 30, 1961.
19. Kovalcik, E. S. "Idealized Model of the Sunflower Paraboloidal Collector for Structural Analysis." TRW ER-5028, Dec. 1961.
20. Matthews, C. O. and W. L. Finch. "Report on the LMSC Spacecraft Materials Reliability Program." Lockheed Missiles and Space Co., May 7, 1961.
21. Mrazek, W. A., Director of Structures and Mechanics Division, NASA Marshall Space Flight Center, personal communication, Jan. 3, 1961.
22. Sibert, M. E. "Inorganic Surface Coatings for Space Applications." Lockheed Missiles and Space Division Technical Report, August 1961.
23. Silvern, D. H. "An Analysis of Mirror Accuracy Requirements for Solar Power Plants." ARS Paper 1179-60.
24. Stephenson, R. Introduction to Nuclear Engineering. McGraw-Hill, New York, 1958.
25. Thelen, A. "The Use of Vacuum Deposited Coatings to Improve the Conversion Efficiency of Silicon Solar Cells in Space." Energy Conversion for Space Power, Volume 3. Academic Press, New York, 1961.
26. Wahl, N. E. "The Effects of High Vacuum and Ultraviolet Radiations on Non-Metallic-Materials," WADD TR60-125, Part II, April 1961.
27. Winkler, H. et al. "Power Supply for the Tiros I Meteorological Satellite." Energy Conversion for Space Power, Volume 4. Academic Press, New York, 1961.
28. "Sunflower Boiler/Heat Storage." Topical Report, TRW ER-4869, April 1963.

NOMENCLATURE

A_a	=	Receiver aperture area, ft^2
A_c	=	Concentrator intercepted area, ft^2
A_s	=	Receiver interior surface area
a_{sa}	=	Apparent absorptivity of receiver aperture to concentrated solar radiation.
a_{cs}	=	Absorptivity of receiver surface to concentrated solar radiation (while surface is at temperature T_s)
a_{ct}	=	Absorptivity of receiver surface to thermal radiation from other areas of receiver (while surface is at temperature T_s)
CR	=	Area concentration ratio, $(D/d_a)^2$
D	=	Outside diameter of concentrator
d	=	Paraxial image diameter
d_a	=	Receiver aperture diameter
F_r	=	Heat loss factor for receiver
f	=	Focal length of concentrator
$f()$	=	Function of
$F()$	=	Function of
$G()$	=	Function of
Q_c	=	Heat rate into conversion device, BTU/hr
Q_i	=	Intercepted solar flux, BTU/hr
q_s	=	Solar constant at earth radius, BTU/hr. Ft.^2
R	=	Reflectivity (hemispherical) concentrator surface to solar radiation.
r	=	Radial distance in focal plane

T_s	=	Temperature of receiver surface, °R
α	=	Solar disc angle, 32'
α	=	Absorptivity of concentrator materials to solar radiation
δ	=	Translation of concentrator surface away from true mathematical surface, in.
η_C	=	Concentrator efficiency factor
η_{CG}	=	Concentrator geometric efficiency factor
η_{CR}	=	Combined concentrator-receiver efficiency factor
η_E	=	Conversion device efficiency factor
η_R	=	Receiver efficiency factor
η_S	=	Overall conversion system efficiency factor
θ	=	Rim angle, degrees
λ	=	Wavelength of honeycomb core mark-off
μ	=	Ratio of time per orbit period that receiver radiation through aperture occurs to the sun time per orbit period.
ν	=	Angular location on concentrator rim, degrees
σ	=	Stefan-Boltzman constant $0.174 \times 10^{-8} \frac{\text{BTU}}{\text{Ft}^2 \text{ hr. } ^\circ\text{R}^4}$
σ	=	Standard deviation of concentrator surface slope errors
ϕ	=	Surface slope error at concentrator surface, degrees
Ω	=	Misorientation angle of concentrator optic axis from center of solar disc, degrees.
η_{PA}	=	Paraxial concentrator efficiency
b	=	Diameter of nominal ray scattering circle
ϵ	=	Emissivity

T = Temperature

\ddot{X}_B = Vibration acceleration level at the base of the collector

\ddot{X}_M = Vibration acceleration response at the mounting ring mid span

\ddot{X}_S = Vibration acceleration response at the stacking ring mid span

ΔT = Temperature differential